ELECTRICAL RESISTIVITY AND AC SUSCEPTIBILITY STUDIES IN PEROVSKITE MANGANITES

by
Manoranjan Kar

Department of Physics
Indian Institute of Technology Guwahati,
Guwahati-781 039, INDIA
July, 2004

ELECTRICAL RESISTIVITY AND AC SUSCEPTIBILITY STUDIES IN PEROVSKITE MANGANITES

A Thesis Submitted
in Partial Fulfilment of the Requirements
for the Award of the Degree of
DOCTOR OF PHILOSOPHY

by

Manoranjan Kar

Department of Physics
Indian Institute of Technology Guwahati,
Guwahati-781 039, INDIA
July, 2004

STATEMENT

The work contained in the thesis entitled "Electrical Resistivity and AC Susceptibility Studies in Perovskite Manganites" has been carried out by me under supervision of Dr. S. Ravi, Associate Professor, Department of Physics, Indian Institute of Technology Guwahati, Guwahati. This work has not been submitted elsewhere for the award of any degree.

9th July, 2004

(Manoranjan Kar)

Department of Physics,

Indian Institute of Technology Guwahati,

Guwahati - 781039

CERTIFICATE

It is certified that the work contained in the thesis entitled "Electrical Resistivity and AC Susceptibility Studies in Perovskite Manganites" by Mr. Manoranjan Kar, a student of the Department of Physics, Indian Institute of Technology Guwahati, Guwahati for the award of the degree of Doctor of Philosophy has been carried out under my supervision. This work has not been submitted elsewhere for the award of any degree.

9th July, 2004

(Dr. S. Ravi)
Associate Professor
Department of Physics,
Indian Institute of Technology Guwahati,
Guwahati – 781 039

Dedicated

to

my Parents

ACKNOWLEDGEMENTS

I am grateful to my Ph.D. supervisor Dr. S. Ravi for his constant guidance, showing interest in my Ph.D. work, helping me to carryout the experimental works and friendly behaviour throughout my research career at Department of Physics, Indian Institute of Technology Guwahati. I would like to thank him for his encouragement and, introducing me to different subjects, such as experimental techniques, solid state physics, CMR materials, magnetism and many other advanced physics subjects. I am happy to carryout my Ph.D. thesis work under such a kind hearted and intelligent person. I will never forget his company and suggestions throughout my life. I will remain ever grateful to him for teaching physics to me till my thesis submission.

I would like to thank Professor A. Srinivasan, chairman of my doctoral committee and the Head, Department of Physics, Indian Institute of Technology Guwahati, for valuable discussions. I am grateful to him for extending the experimental facilities to me.

I would like to thank my other doctoral committee members, professor A. T. Khan and Dr. Alika Khare for valuable discussions and help whenever I needed.

I would like to thank my course coordinators for teaching me the advanced topics in physics during my course work.

I am grateful to Dr. P. S. Robi**,** Head, Department of Mechanical Engineering, Indian Institute of Technology Guwahati, for extending optical microscope and other experimental facilities. I also offer my thanks to his group for extending their co-operation.

I am grateful to superintendent and technical staff of mechanical workshop, Indian Institute of Technology Guwahati for their help to fabricate cryostat, furnace case, etc.

I am thankful to Mr. Sankaran, Mechanical workshop, Department of Physics, Indian Institute of Technology Madras, for his flawless fabrication of ac susceptibility cryostat as per given design.

I am grateful to Professor M. K. Chaudhuri, Department of Chemistry, Indian Institute of Technology Guwahati, for valuable discussions and extending the facilities for chemical titration. I offer my thanks to his group for their kind co-operation.

I am grateful to Professor Ajay Gupta, centre director, Inter University Consortium for Department of Atomic Energy Facilities, Indore, India for allowing me to carryout magneto-resistivity measurements and for financial support during my stay at IUC-DAEF, Indore.

I am happy to offer my thanks to Dr. Rajeev Rawat for helping me to carry out for magneto-resistivity measurements at IUC-DAEF.

I am grateful to Dr. Alok Banerjee for magnetization measurements.

I would like to thank Dr. R. Maiti for his help to record SEM micrographs and EDAX at Central Research Facility, Indian Institute of Technology Kharagpur, Kharagpur.

I am thankful to Professor A. K. Gogoi, Department of Electronic and Communication Engineering, Indian Institute of Technology Guwahati for extending the coil winding machine.

My special thank is due towards my friends Dr. A. K. Pattanaik and Dr. B. Indrajit Sharma and, my colleagues Pramoda Kumar Nayak and Sankar Moni Borah for their help during my Ph.D tenure.

Here I would like to thank Mr. Sidananda Sarma, Mr. Chandan Borgohain, Mr. Lokesh Chakraborty and Mr. Madan Deka for their co-operation during my Ph.D. tenure.

I would like to thank T. J. Singh, Engineering Section, Indian Institute of Technology Guwahati, for extending his help during installation of electromagnet.

I am happy to be a research scholar in Indian Institute of Technology Guwahati, as I got a very friendly and cordial environment from all departments faculties, non-teaching staff, administrative staff, securities and all others staying inside the campus. So, my heartiest thank goes towards them for giving me a healthy environment during my Ph.D. tenure.

I am grateful to my parents, brothers, sisters, relatives and friends for their constant encouragement and moral support. I would like to offer my thanks to them for their affection, tolerance and support for which I could reach the present stage.

At last but not least I am grateful to Indian Institute of Technology Guwahati for financial support to carry out the present thesis work and providing scholarship to me during my Ph.D. period.

ABSTRACT

Materials based on manganese oxides are generally known as manganites. The manganites $RMnO_3$ (R = Trivalent rare earth elements) and $AMnO_3$ (A = Divalent alkaline earth elements) are known to be insulating with antiferromagnetic (AFM) ordering. Even though the mixed valence manganites, $R_{1-x}A_xMnO_3$ ($x \leq 0.50$) are known to exhibit ferromagnetic (FM) to paramagnetic and metal-insulator transitions as early as 1950, the interest in this type of compounds was renewed only after the discovery of large negative magneto-resistivity in the vicinity of the transition temperature (T_c). The phenomenon of large negative Magneto-Resistivity is called Colossal Magneto-Resistivity (CMR). The above manganites exhibit perovskite crystal structure with mostly cubic, orthorhombic or rhombohedral crystal symmetries. The CMR behaviour can be explored for potential applications in magnetic recording, sensor and switches. These materials have also potential applications as catalysts for automobile exhausts, oxygen sensors and magnetic refrigeration. In addition these materials exhibit very interesting and yet complicated electrical and magnetic properties, which prompted the attention of researchers to understand their basic mechanism. The phenomena of metal-insulator and paramagnetic to ferromagnetic transitions have been explained by Zener double exchange interaction. Later it has been emphasized that in addition to double exchange interaction, a strong electron-phonon interaction has to be taken into account to explain the CMR behaviour.

When I started my Ph.D. work, most of the works in literature were mainly on the study of CMR behaviour in divalent alkaline earth doped (hole doped) manganites and investigations on doping of 'Mn' site with other magnetic and non-magnetic materials to understand the nature of magnetic interactions, etc. I had proposed to study the trivalent 'La' doped (electron doped) $A_{1-x}La_xMnO_3$ ($x \leq 0.50$) compounds in order to understand the electrical and magnetic properties and the interplay of crystal structure on these properties. There were only a few reports on electron doped materials and most of them were on Ca-Mn-O based compounds. I have taken up two series namely $Ba_{1-x}La_xMnO_3$ and $Sr_{1-x}La_xMnO_3$. The large d-electron bandwidth and T_c near room temperature in hole doped regime of these materials ($x \approx 0.67$) are the reasons for choosing the above series. Even though the monovalent alkali ion doped $R_{1-x}A_xMnO_3$ (A = Na, K etc.) compounds are known to exhibit CMR behaviour, the work on other monovalent doped materials are limited.

In the present thesis work I have prepared the following compounds. Most of these compounds were in single phase form.

1. $Ba_{1-x}La_xMnO_3$ x = 0 to 0.80,
2. $Sr_{1-x}La_xMnO_3$ x = 0 to 0.82,
3. $La_{1-x}Ag_xMnO_3$ x = 0 to 0.35,
4. $La_{1-x}Cu_xMnO_3$ x = 0.05 to 0.40,
5. $CaMn_{1-x}Cu_xO_3$ x = 0.05 to 0.40, and
6. $LaMn_{1-x}Cu_xO_3$ x = 0 to 0.40

The first two series are mainly electron doped compounds for 'x' up to 0.50. For the sake of comparison a few hole doped materials were also prepared (x > 0.50). The middle two series (3 & 4) are hole doped materials other than the conventional alkali earth and alkali ion doping. Here monovalent 'Ag' and, 'Cu', which can exist in mono- as well as in di-valent forms are doped in the place of 'La'. The monovalent doping has the advantage of creation of the required concentration of Mn^{3+}/Mn^{4+} ions with relatively small levels of doping. The final two series (5 and 6) are antiferromagnetic parent compounds with 'Cu' doping in place of 'Mn' to understand the magnetic interaction between 'Cu' ions and their influence on electrical transport.

The above samples are characterized by using X-ray diffraction (XRD), optical micrographs, scanning electron micrographs, Energy-dispersive analysis of X-ray and chemical titration. Detailed measurement and analysis of X-ray diffraction patterns, and temperature variations of electrical resistivity, magneto-resistivity on selected samples and ac susceptibility have been carried out.

The present thesis consists of six chapters, namely, (1) Introduction, (2) Experimental Techniques, (3) Electron Doped Materials, (4) Hole Doped Materials, (5) Manganese Site Doped Materials, and (6) Conclusions.

In the first chapter the history of discovery of metal-insulator and paramagnetic to ferromagnetic transitions and colossal magneto-resistivity in manganites have been reviewed. Special emphasis has been given to electrical transport and magnetic studies. The crystal structure of different type of manganites has been reviewed. The highlights of theoretical works and their application in explaining various physical parameters have been also presented. At the end, the motivation behind the present thesis work is given.

In chapter 2, the development of experimental facilities for material preparations, temperature variations of electrical resistivity and ac susceptibility are discussed. The

calibration of indigenously fabricated ac susceptibility apparatus along with measurements carried out on standard magnetic materials have been shown. The details of sample characterization using X-ray diffraction, optical & scanning electron microscope and chemical titration techniques have been discussed.

In chapter 3, the material preparation techniques, experimental results and analysis carried out on electron doped materials, $Ba_{1-x}La_xMnO_3$ and $Sr_{1-x}La_xMnO_3$ have been discussed in detail. For the sake of comparison, the results on a couple of hole doped materials prepared in the same series are presented. These materials are found to be mostly in single phase form except for a few doping concentrations. Metal-insulator transition with CMR behaviour have been observed even in electron doped materials, especially in $Ba_{1-x}La_xMnO_3$ series. The susceptibility measurements demonstrate the presence of ferromagnetic, antiferromagnetic, charge ordering and reentrant spin glass like transitions. The electrical resistivity and ac susceptibility results are found to be in strong correlation with Mn^{3+} concentrations suggesting the domination of double exchange interaction. The electrical resistivity data in metallic regions could be analyzed using various scattering mechanisms such as electron-electron, electron-magnon scattering, etc. The resistivity data in the semiconducting/insulating region were analyzed using Mott variable range hopping, Efros-Shklovskii variable range hopping and small polaron hopping models. The results of the above analysis have been discussed in detail.

Chapter 4 deals with material synthesis, results and analysis of various physical measurements on hole doped $La_{1-x}Ag_xMnO_3$ and $La_{1-x}Cu_xMnO_3$ compounds. Both of the series could be prepared in single phase form upto a certain level of doping. Metal-insulator and paramagnetic to ferromagnetic transitions have been observed upto around 294 K in the former series. The latter series exhibits relatively low T_c (<100 K). The details of XRD analysis using Rietveld method and analysis of electrical resistivity both in metallic and semiconducting regions have been discussed in detail.

In chapter 5, the doping of 'Cu' atoms in the place of 'Mn' on two parent compounds, namely, $LaMn_{1-x}Cu_xO_3$ and $CaMn_{1-x}Cu_xO_3$ have been discussed. Even though 'Cu' doping results in mixed valency of 'Mn' ions, the antiferromagnetic interaction is found to be stronger. Competing FM and AFM interactions have been observed in $LaMn_{1-x}Cu_xO_3$ series. The results of crystal structure analysis and electrical resistivity analysis in terms of variable range hopping and small polaron hopping models have been discussed in detail.

In Chapter 6 the important conclusions drawn from the physical measurements and analysis of all the above six series of compounds are summarized. To highlight a few, (1) in electron doped (Ba, La)-Mn-O series, charge ordering and reentrant semiconducting behaviour at the corresponding temperature have been observed, probably for the first time. (2) The domination of intergranular weak link nature has been observed from ac susceptibility measurements. (3) The large difference between metal-insulator and ferromagnetic transition temperatures in some of the compounds has been explained interms of intergranular weak links. (4) The increase in magneto-resistivity with decrease in temperature in electron doped materials has been attributed to ferromagnetism with competing antiferromagnetic interaction. (5) Most of the above series exhibit structural transition upon doping. (6) The magnitude of saturation susceptibility was found to increase systematically with Mn^{3+} concentrations. This suggests that even in electron doped region, the double exchange interactions play a major role. (7) The mechanism of electrical conduction in metallic region is mostly controlled by electron-electron and electron-magnon scattering. The mechanism of electrical conduction in semiconducting/insulating region is mostly based on Mott variable range hopping (Mott-VRH) or variable range hopping with coulomb interactions of charge carriers (ES-VRH).

CONTENTS

Chapter 2. Experimental Techniques

Chapter 3. Electron Doped Materials

Chapter 4. Hole Doped Materials

LIST OF TABLES

Tables **Page No.**

Chapter 2:

Chapter 3:

Chapter 4:

Chapter 5:

LIST OF FIGURES

Figures **Page No.**

Chapter 1:

Chapter 2:

Chapter 3:

Chapter 5:

Chapter 1

INTRODUCTION

INTRODUCTION

In the periodic classification of the elements, there is a group of metals referred as transition metals. Transition metals use their valence electrons to form compounds such as perovskite structured oxides with interesting electrical and magnetic properties. By structural and compositional tuning, such compounds can be tailored to a large variety of interesting chemical and physical properties. The versatility of perovskite oxides for electronic applications is demonstrated by the fact that, these materials exhibit wide range of conductivity ranging from highly conducting metallic state (even superconducting in some cases) to insulating state. We can find non-magnetic as well as magnetic materials with almost all kinds of magnetic ordering. Hence, among the perovskite oxides, we can find high temperature superconductors, manganites, ferromagnets, ferrimagnets, antiferromagnets and materials with canted spins. The advent of magneto-electronics, or so-called spin-tronics, about a decade ago even more increased the attention to this set of materials. The number of applications are so wide that Physicists, Chemists and Materials scientists have shown a keen interest in these materials. Among the all perovskite oxides, the manganite perovskites have drawn renewed interest in recent years due to their interesting structural, electrical transport, magnetic and large negative magneto-resistivity properties.

1.1. Discovery of Colossal Magneto-Resistivity Materials

The field of manganites was started around 54 years ago with the papers of Jonker and Van Santen [1, 2], where the existence of ferromagnetism in mixed crystals of $LaMnO_3$-$CaMnO_3$, $LaMnO_3$-$SrMnO_3$, and $LaMnO_3$-$BaMnO_3$ was reported. The above compounds are described by a general chemical formula $R_{1-x}A_xMnO_3$, where R is a trivalent rare earth element or 'Bi' and 'A' is a divalent alkaline earth element or 'Pb'. In 1954, Volger [3] reported negative magneto-resistivity with a peak near the Curie temperature of $(La_{0.8}Sr_{0.2})MnO_3$. The magneto-resistivity is defined as, $MR(T) = \frac{\rho(H,T) - \rho(0,T)}{\rho(0,T)}$, where ρ(H,T) and ρ(0,T) are the electrical resistivity measured in the presence and absence of applied magnetic field. Following Volger [3], Searl *et al.* [4, 5] and others [6, 7] reported negative magneto-resistivity in single crystals

of (La,Pb)MnO_3 compounds. Interest in the mixed-valence manganites was revived following the discovery of large negative magneto-resistivity by Kuster *et al.* [8], von Helmolt *et al.* [9] and Chahara *et al.* [10]. Jin *et al.* [11] epitomized the above class of materials as colossal magneto-resistivity (CMR) materials. Thus materials, which exhibit large negative magneto-resistivity in the vicinity of transition from paramagnetic insulator to ferromagnetic metallic state is called CMR materials.

The CMR parent compounds such as $RMnO_3$, $AMnO_3$, etc. are electrical insulators and exhibit antiferromagnetic transition with different Neel temperatures (T_N). For instance, the T_N of $LaMnO_3$ and $CaMnO_3$ are reported to be 141K and 131K respectively from neutron diffraction experiment [12]. In parent compounds 'Mn' ions are either in Mn^{3+} or Mn^{4+} state. The mixed valence oxides, $(R^{3+}_{1-x}A^{2+}_{x})(Mn^{3+}_{1-x}Mn^{4+}_{x})O_3$ can be obtained from the solid solution between end members, such as $RMnO_3$ and $AMnO_3$ with formal valence states $R^{3+}Mn^{3+}O^{2-}_3$ and $A^{2+}Mn^{4+}O^{2-}_3$ respectively. The e_g level of Mn^{3+} ion in $R^{3+}Mn^{3+}O^{2-}_3$ (Mn^{3+} rich) compounds are filled with one electron. The creation of a few holes/vacancies in e_g levels i.e. by doping 'A' elements in place of 'R' is called hole doping, where a few Mn^{3+} ions are oxidized into Mn^{4+} ions. In other way around, induction of a few e_g electrons in $A^{2+}Mn^{4+}O^{2-}_3$ (Mn^{4+} rich) compounds is called electron doping, where a few Mn^{4+} ions are reduced into Mn^{3+} ions. The mixed valent 'Mn' ions (Mn^{3+} & Mn^{4+}) play a major role on CMR properties of manganite perovskites. In addition to the mixed valency, ionic size mismatch, Mn-O bond length, $\angle Mn-O-Mn$ bond angle, etc. play a considerable role on CMR behaviour. The mixed valent manganites can also be obtained by the substitution of mono-valent elements in place of 'R'. One can also get mixed valent manganites by self doping in parent compounds, i.e. by creating vacancy 'Mn' site, 'R' site etc. Such hole doped materials generally exhibit ferromagnetic (FM) behaviour below certain temperature, however the hole doping beyond certain concentration (~50%) results in antiferromagnetic transition. The first clear experimental evidence for positive (ferromagnetic) exchange interaction between $3d^4$ Mn^{3+} and $3d^3$ Mn^{4+} ions was reported by Jonker [13] from magnetization and susceptibility results.

Even before the discovery of CMR behaviour, the charge transport was theoretically described by Zener [14, 15] and it is called Zener double exchange (DE) theory (explained in section 1.3.1 & 1.4.1). Anderson and his group [16, 17] and Goodenough [18] pointed out that ferromagnetism is governed not only by the double

exchange interaction, but also by the nature of the superexchange (SE) interactions. In this context de Gennes [19] superexchange interaction theory is recalled, i.e. Mn^{3+}-O-Mn^{4+} superexchange interaction is ferromagnetic while, both the Mn^{3+}-O-Mn^{3+} and Mn^{4+}-O-Mn^{4+} interactions are antiferromagnetic (AFM). Recently Millis *et al.* [20] have reported that in addition to double exchange interaction, a strong electron-phonon interaction has to be taken into account to explain the CMR behaviour.

1.1.1. Divalent Doped Materials

The widely studied divalent doped materials are $La_{1-x}A_xMnO_3$ (A = Sr, Ca, Ba and Pb). The divalent substituted, $La_{1-x}Ca_xMnO_3$ compounds were the first series to be investigated for ferromagnetic metallic state in 1950s [1]. Later the phase diagram of $La_{1-x}Ca_xMnO_3$ has been constructed by Schiffer *et al.* [21] and Gong *et al.* [22, 23]. The materials for $0 < x < 0.50$ show paramagnetic to ferromagnetic transitions with T_c ranging from 160 to 272K. However, metal-insulator (M-I) transitions were observed for $0.20 < x < 0.50$ with a maximum T_c for $x \approx 0.33$. The maximum MR is found to be around 80% at $T_c \approx 240$K for an applied field of 6T (60kOe) [24]. At $x \approx 0.50$, this compound undergoes paramagnetic to ferromagnetic transition at around 225K and then to a charge ordered antiferro-magnetic phase at $T_{CO} \approx 155$K [21]. Such charge ordering (CO) with hysteresis in electrical resistivity has been reported by Zhao *et al.* [25].

After the pioneering work of Jonker *et al.* [1] and Wollan *et al.* [12] on polycrystalline $La_{1-x}Sr_xMnO_3$ compounds, Urushibara *et al.* [26] carried out detailed study of electrical and magnetic properties on $La_{1-x}Sr_xMnO_3$ crystals for $x = 0$ to 0.60. According to them, no FM transition was observed for $x \leq 0.05$, and for $x \geq 0.10$, these materials exhibit PM to FM transition with T_c ranging from 145K for $x = 0.10$ to 371K for $x = 0.40$. They have observed M-I transitions in the vicinity of FM T_c for $0.175 \leq x \leq 0.40$. In the composition range $0.10 \leq x \leq 0.15$, the M-I transition was followed by a low temperature reentrant semiconducting behaviour. They have reported a magneto-resistivity of about 90% ($x = 0.175$ sample) in the vicinity of $T_{MI} \approx 275$K for an applied field of 15T. Similarly, Zhou *et al.* [27] and Uhlenbruck *et al.* [28] reported M-I transition followed by reentrant semiconducting behaviour for $La_{1-x}Sr_xMnO_3$ crystals with $x \approx 0.12$. Structural transition from orthorhombic to rhombohedral has been reported at $x = 0.175$ in this series[29].

The $La_{1-x}Ba_xMnO_3$ compounds also exhibit M-I & FM transitions above room temperature, i.e. ≈ 340K [13, 30, 31]. Von Helmolt *et al.* [9] reported M-I transition above room temperature on thin film sample of $La_{0.67}Ba_{0.33}MnO_3$ and they have found magneto-resistivity values as high as 60% at room temperature for a field of 5T. Ju *et al.* [32] reported low field (2kOe) magneto-resistivity of 30% at 5kOe on polycrystalline $La_{0.67}Ba_{0.33}MnO_3$. Mandal and Ghosh [33] reported M-I transition at around 270K on $La_{0.8}Ba_{0.2}MnO_3$ crystal and they found reentrant low temperature semiconducting behaviour for $x \leq 0.175$. Other than alkaline earth elements the 'Pb' doped $La_{1-x}Pb_xMnO_3$ compounds are also found to exhibit M-I transition, PM-FM transition and CMR behaviour in the vicinity of room temperature [34-36]. Jia *et al.* [37] reported M-I transition temperature, T_{MI} = 355K and a maximum magneto-resistivity of 65% for 6T field on $La_{0.6}Pb_{0.4}MnO_3$ crystal. Banerjee *et al.* [38] found that T_{MI} values vary from 230 to 275K on polycrystalline $La_{1-x}Pb_xMnO_3$ ($0 \leq x \leq 0.50$). Other rare earth manganites such as $Nd_{1-x}Sr_xMnO_3$ are also found to exhibit M-I & FM transitions at around room temperature [39]. Pattabiraman *et al.* [40] reported the variation of T_{MI} values ranging from 165 to 241K depending upon type of heat treatments on thin film samples of $Nd_{0.67}Sr_{0.33}MnO_3$ and the typical MR at 4.2K is found to around 50% for an applied field of 6.4T. The $Pr_{1-x}Ca_xMnO_3$ ($x = 0.30 – 0.40$) are reported to be charge ordered compounds without any M-I transition, however these materials show M-I transition (150-250K) in the presence of magnetic field [41, 42].

1.1.2. Monovalent Doped Materials

Itoh *et al.* [43] were the first one to demonstrate M-I and FM transitions on mono-valent alkali ion doped, $La_{1-x}A_xMnO_3$ (here A= Na, K, Rb, etc.) compounds and these compounds were known many years ago and tested as oxidation catalyst [44]. According to Itoh *et al.* [43] the FM T_c of 'Na' substituted samples varies from 219 to 336K for $0.04 \leq x \leq 0.12$. The maximum T_c of 'K' and 'Rb' substituted compounds are found to be 330 and 234K respectively. Following Itoh *et al.* [43], a few more groups reported the study of electrical transport and magnetic properties of alkali ion doped perovskite manganites [45 – 49]. Boudaya *et al.* [48] reported the MR value of 40% for an applied field of 5.6T at room temperature on $La_{0.8}K_{0.2}MnO_3$ compound. The detailed crystal structure and magneto-resistivity property of $La_{1-x}Li_xMnO_3$ have been studied by Ye *et al.* [50]. Their

samples for $x \leq 0.15$ showed M-I transition with PM-FM transition. The FM T_c was found to increase from 210 to 240K with increase in 'Li' concentration. Their typical MR was reported to be ≈25% for a field of 0.8T at around T_c. Roy *et al.* [51] studied the 'Na' doped $La_{1-x}Na_xMnO_3$ materials. Their FM T_c value was found to vary from 220 to 330K for the doping concentration of 7% to 40%. They also observed M-I transition in the vicinity of T_c. The maximum MR of 45% was obtained at room temperature for 5T field.

Tang *et al.* [52] and Hien *et al.* [53] studied the magneto-caloric effect of 'Ag' doped $(La_{1-x}Ag_x)MnO_3$ compounds and they reported PM-FM transition near room temperature. Thus, this is an alternative to alkali ions for mono-valent doping. These materials are also found to exhibit CMR behaviour [54, 55]. I have also come across other reports on these materials after the completion of my work [56].

Other than the divalent/monovalent doping, one can also obtain hole doping in $RMnO_3$ compounds by creating vacancy in La or Mn site. These are known as self doped materials. There are a few reports on self doped manganites such as $R_{1-x}MnO_3$ and $RMn_{1-x}O_3$, which are found to exhibit ferromagnetism with CMR properties [57-60].

1.1.3. Electron Doped Materials

Like rare earth manganites $RMnO_3$, the alkaline earth manganites $AMnO_3$ (A = Ca, Sr, Ba) are also basically antiferromagnetic insulators, however, 'Mn' in latter series is in Mn^{4+} state [61, 62]. There are considerable reports on doping of trivalent elements in place of alkaline earth elements, $A_{1-x}R_xMnO_3$ and such materials are called electron doped materials.

$CaMnO_3$ based materials are widely studied by electron doping, i.e. by doping trivalent elements such as 'La' [21, 63 - 65], Bi [66, 67], Y[68, 69], Sm [70-74], and Eu [75] in place of 'Ca'. The magnetic phase segregation (FM & AFM) has been reported in $Ca_{1-x}La_xMnO_3$ compounds [64]. The existence of electronic phase separation has been reported by Kapusta *et al.* [65] from NMR studies on $La_{0.35}Ca_{0.65}MnO_3$ compound. The above materials mostly show CO insulating behaviour without any M-I transition. The maximum CO temperature is found to be around 265K and application of magnetic field results in melting CO phase in $Bi_{1-x}Ca_xMnO_3$ ($x \geq 0.75$) [76]. Chiba *et al.* [66] reported FM moment with large negative magneto-resistivity on $Bi_{1-x}Ca_xMnO_3$ for $0.875 \leq x \leq 0.950$. The reduction in resistivity with increase in 'Bi' concentration was noticed within the above composition. However, no M-I transition is observed. The ferromagnetic

transition temperature T_c was below 200K and it was independent of 'x' in the above range. Bao *et al.* [67] concluded that there is a coexistence of FM and AFM features in the temperature range 150 to 200K on $Bi_{0.18}Ca_{0.82}MnO_3$ single crystal, from their Neutron diffraction study. In $Ca_{1-x}Y_xMnO_3$ compounds ($x \leq 0.18$), enormous reduction of resistivity by several orders of magnitude and increase of the magnetization values with doping were reported [68, 69]. For $x > 0.18$, charge ordering takes place and DE interaction is not effective below the CO temperature, T_{CO}. They found 2.25% of MR at low temperature for $x = 0.10$ sample, at a field of 2.5 kOe. In $Sm_{1-x}Ca_xMnO_3$ compounds metal-insulator transitions were reported at around 110K for a narrow composition range of $0.10 \leq x \leq 0.12$ and the materials exhibit FM transition with weak magnetization in the vicinity of T_{MI} [70].

Unlike $CaMnO_3$ series, there are only limited reports on electron doped $BaMnO_3$ series. Yuan *et al.* [77] were the first one to report M-I transition in electron doped $La_{1/3}Ba_{2/3}MnO_3$ compound. They have explained that the appearance of CMR behaviour at relatively low magnetic field is unlikely due to double exchange interaction but is due to superexchange type of ferromagnetic interaction. Their magneto-resistivity values continuously increase with decrease in temperature without showing any peak in the vicinity of M-I transition. After the completion of my work, I have also come across the work of Raveau *et al.* [78] who have reported that the electron doped $La_{0.35}Ba_{0.65}MnO_3$ compound is generally a mixture of two main phases namely hexagonal $BaMnO_3$ and cubic perovskite $La_{0.65}Ba_{0.35}MnO_3$. According to them, the appearance of metallic conductivity below the M-I transition is mainly due to the presence of cubic perovskite (ferromagnetic phase) above the percolation threshold.

There are a few reports on electron doped materials in $(La_{1-x}Sr_x)MnO_3$ series and they have been studied mostly in the composition range close to $x \approx 0.50$ [79, 80]. Moritomo *et al.* [79] reported, transition from FM to AFM in the temperature range 200 to 250 K for $0.50 < x \leq 0.60$ and in the corresponding temperature, upturn in resistivity was observed. Similar behaviour has been observed by Patil *et al.* [80] for $0.48 \leq x \leq 0.53$. AFM transitions due to charge ordering have been reported by Sundaresan *et al.* [81] and Wakai *et al.* [82] in $La_{0.5}Ca_{0.5-x}Sr_xMnO_3$. Kikuchi *et al.* [62] in their brief report have shown that FM disappears for $x > 0.60$ in $La_{1-x}Sr_xMnO_3$ and the materials exhibit semiconducting behaviour.

Zhao *et al.* [83] studied the electron doped $La_{1-x}Mg_xMnO_3$ ($0.45 \leq x \leq 0.60$) compounds. Their samples exhibit paramagnetic to ferromagnetic transitions without any M-I transition.

In addition to the above perovskites, there is another group of manganite materials with perovskite structure, they are called layered compounds or Ruddleson-Popper phases with chemical formula $(La, Sr)_{n+1}Mn_nO_{3n+1}$ [84-86]. Here n = 1 exhibits semiconducting behaviour with charge ordering, n = 2 exhibits metal-insulator transitions in the temperature range T_{MI} = 110 to 125K and the T_{MI} value of n = 3 is around 150K. Here 'La' can be replaced by other rare earth elements and 'Sr' can be replaced by other alkaline earth elements.

The detailed theoretical and experimental works on manganites have been reviewed by several authors viz. by Ramirez [87], Coey *et al.* [88], Dagotto *et al.* [89], Prellier [90] and Nagaev [91]. The books edited by C. N. R. Rao and Raveau [92], Tokura [93] and authored by Nagaev [94] cover the wide range of CMR materials and their physical properties.

1.1.4. Other CMR Materials

The pyrochlore and spinel structure based materials are also known to exhibit CMR behaviour. These two groups are beyond the scope of the present thesis work. However, a brief review of these materials is given below.

The CMR property on pyrochlore structure based manganite $Tl_2Mn_2O_7$ has been reported by Shimakawa *et al.* [95]. This material exhibits M-I and FM-PM transitions with a T_c at around 142K. This material exhibits metallic behaviour even above T_c. These pyrochlore materials can be synthesized only under high pressure. So only a few reports are available in the literature. Cheong *et al.* [96] have studied the substitution of 'In' in place of Tl ($Tl_{2-x}In_xMn_2O_7$), for $x < 0.25$. According to Subramanian *et al.* [97], unlike perovskite materials, here the CMR behaviour and FM transitions are due to two different origins. The magnetic ordering is explained as superexchange interaction with strong spin fluctuations scattering above Curie temperature. The metallic conductivity is due to the large admixture of Tl-6s band with Mn-3d band. This idea is further supported by band structure calculations [98, 99].

The spinels have general formula HCr_2Ch_4, where H = Fe, Cu & Cd which are tetrahedrally coordinated cation. 'Ch' is a chalcogen, i.e. S, Se, Te [100]. Ramirez *et al.*

[100] reported large magneto-resistivity under high magnetic field in 'Cr' chalcogenide spinels $Fe_{1-x}Cu_xCr_2S_4$.

Like manganite perovskites the above two groups of materials exhibit large drop in resistivity near FM T_c values. However, they have no mixed valant 'Mn' ions.

1.2. Crystal Structure

Basically the CMR parent compounds $RMnO_3$ & $AMnO_3$ (R is a trivalent and A is a divalent element) form an ideal cubic perovskite as shown in the Fig. 1.1. It consists of a three dimensional network of vertex-sharing MnO_6 octahedra and interstitial 'R/A' cations [4]. The ideal cubic perovskite structure is distorted by cation substitutions and/or oxygen off-stoichiometry. It is mainly due to cation size mismatch and Jahn-Teller effect, the electron instability. The ideal cubic structure is modified into a lower symmetry structures such as orthorhombic, rhombohedral, etc. due to the following three mechanism [101, 102], viz. (i) cooperative tilting of MnO_6 octahedra, (ii) displacement of the cations, and (iii) distortions of the MnO_6 octahedra. The tilting of the MnO_6 octahedra is most relevant in deciding the overall space group symmetry of the particular manganite perovskite.

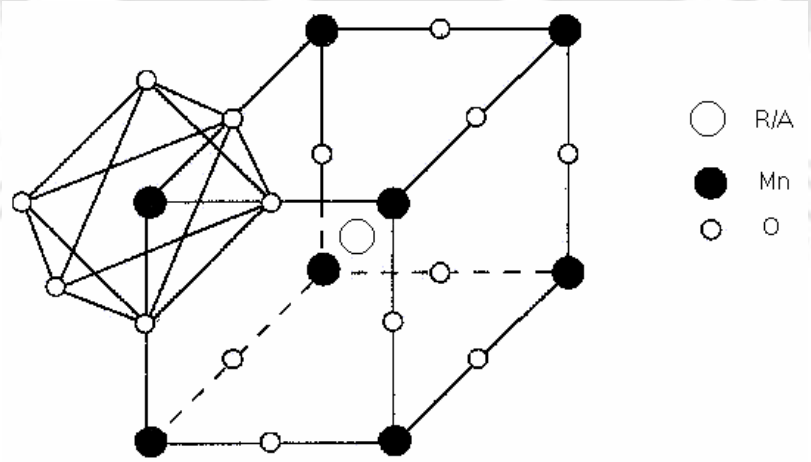

Fig. 1.1: The schematic diagram of an ideal cubic perovskite.

In order to fill the empty space due to size mismatch in 'R/A' site, MnO_6 octahedra rotate co-operatively. This distortion is characterized by the Goldsmith tolerance factor [103],

$$t = {d_{(R/A)-O}}/{\sqrt{2}(d_{Mn-O})} \qquad \text{----------} \qquad (1.1)$$

where $d_{R/A-O}$ and d_{Mn-O} are the average R or A cation-Oxygen and Mn-Oxygen distances respectively. In the case of a cubic perovskite t = 1. Stable perovskite structure is found for t values in the range of 0.8 to about 1.1 [104]. Perovskites containing small cations will lead to t < 1, while large cations will give rise to t > 1. For t ≅ 1, the $R\bar{3}c$ space group is formed with rhombohedral symmetry and for t < 1, the *Pbnm* space group is formed with orthorhombic symmetry. The typical crystal structure of CMR materials is shown in Fig. 1.2. The value of Z, the number of formula units per unit cell are 4 and 2 for orthorhombic and rhombohedral cell respectively.

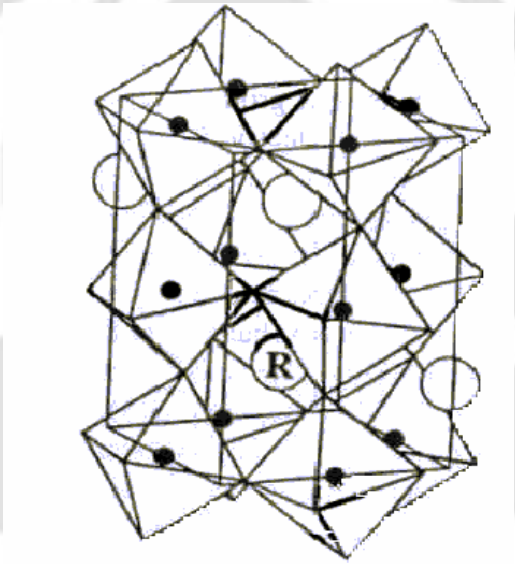

Fig. 1.2: Typical structure of CMR material for orthorhombic structure.

In the cubic environment of the octahedron the hybridization and electrostatic interaction of Mn-3d electron with O-2p electrons will create a crystal field effect. This field lifts the 5-fold degeneracy of d electrons in free 'Mn' ions and split the energy levels into two states namely t_{2g} and e_g. The t_{2g} state is at lower level with triply degenerate and e_g is doublet at higher energy level. The t_{2g} triplet consists of d_{xy}, d_{xz} and d_{yz} orbitals, while the e_g doublet contains the $d_{x^2-y^2}$ and $d_{3z^2-r^2}$ orbitals [105]. The filling of these levels follows Hund's first rule, where parallel spins are energetically favorable due to minimization of Coulomb repulsion energy. In practice, a strong Hund's coupling between the t_{2g} and the e_g states lead to the formation of a high spin state (S = 2) for the four 3d - electrons in the Mn^{3+} ion.

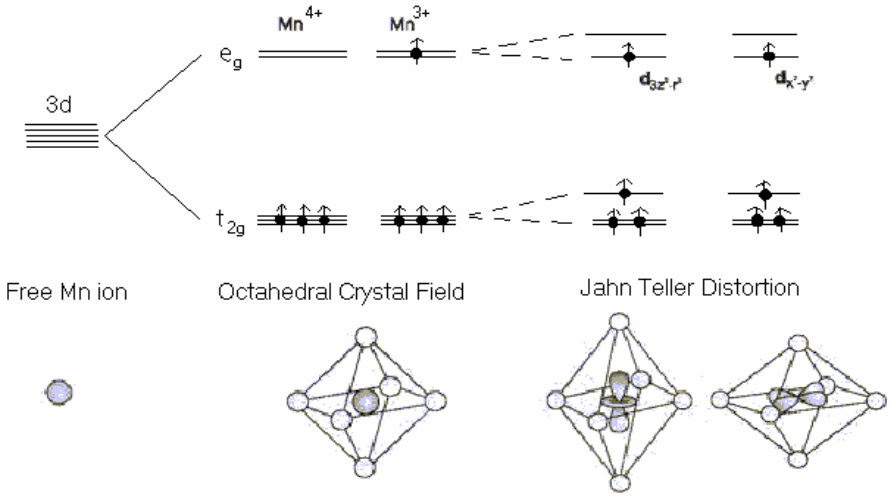

Fig. 1.3: Crystal field lifts the degeneracy of the d^5-electrons of the Mn-ions into t_{2g} triplet and e_g doublet. The Jahn-Teller distortion then further splits the e_g level and favours either the $d_{x^2-y^2}$ or the $d_{3z^2-r^2}$ orbital.

Ions like Cr^{2+} (d^4), Cu^{2+} (d^9) and Mn^{3+} (d^4) in the center of a regular octahedron are known to split the degenerate orbital levels by deforming the cubic symmetry into a tetragonal one. This is the essence of the Jahn-Teller effect [106, 107]. In practice, a lowering of the energy of the $d_{3z^2-r^2}$ orbital is created with the elongation of the O_6 – octahedron along 'z' direction, while the perpendicular plane is compressed. Similarly the $d_{x^2-y^2}$ orbital is stabilized by an inverse elongation/compression (see extreme right of Fig.1.3). Thus the Mn^{3+} ion is Jahn-Teller active and Mn^{4+} is inactive.

The lattice distortions due to ionic size mismatch and Jahn-Teller effect play a role on orbital ordering of Mn-3d electrons [108,109]. It has been also established that the superstructure associated with charge ordering occur at x = 1/8 and 1/2 in $(La_{1-x}Sr_x)MnO_3$ [110], between x = 0.3 and 0.8 in $(Pr_{1-x}Ca_x)MnO_3$ [41] , and x = 1/2., 2/3, 3/4 & 4/5 in $(La_{1-x}Ca_x)MnO_3$ [63]. The charge and orbital orderings are discussed in section 1.4.2

1.3. Electrical Resistivity and Magneto-Resistivity

The CMR parent compounds $RMnO_3$ and $AMnO_3$ are electrical insulators at all temperatures. Here the 'Mn' is either in Mn^{3+} or Mn^{4+} state. The solid solution with general chemical formula $R_{1-x}A_xMnO_3$ (where R is a trivalent rare earth element or Bi and A is divalent alkaline or Pb) shows metal to insulator transition generally for $0.10 < x < 0.50$. These materials consist of Mn^{3+} and Mn^{4+} mixture. The typical M-I transitions in

polycrystalline $La_{1-x}Sr_xMnO_3$ compounds are shown in Fig. 1.4 [26]. The peak temperature corresponds to M-I transition.

The sharpness of the transition often depends on the sample quality. For samples with grain size of the order of 5μm or more, transition is relatively sharp. The temperature dependent resistivity curve can be divided into three regions, high temperature (insulating region), low temperature (metallic region) and critical region (the intermediate region). Critical behaviours are best described by thermodynamic measurements, which couple directly to the magnetic correlation length. High temperature data have been explained by Variable Range Hopping model (VRH), Small Polaron Hopping (SPH) model and simple semiconducting behaviour. The electrical resistivity in the ferromagnetic region has been investigated by several groups [reviewed in ref. 87-94]. In the region just below T_c, ρ falls rapidly. For $T < 0.5T_c$, typically the variation is less rapid, but it is different from what is generally seen in a metallic ferromagnet. Few attempts have been made to understand the critical region by assuming the existence of both insulating and metallic behaviour. Recently the bond percolation theory has been applied to understand the behaviour in entire temperature region.

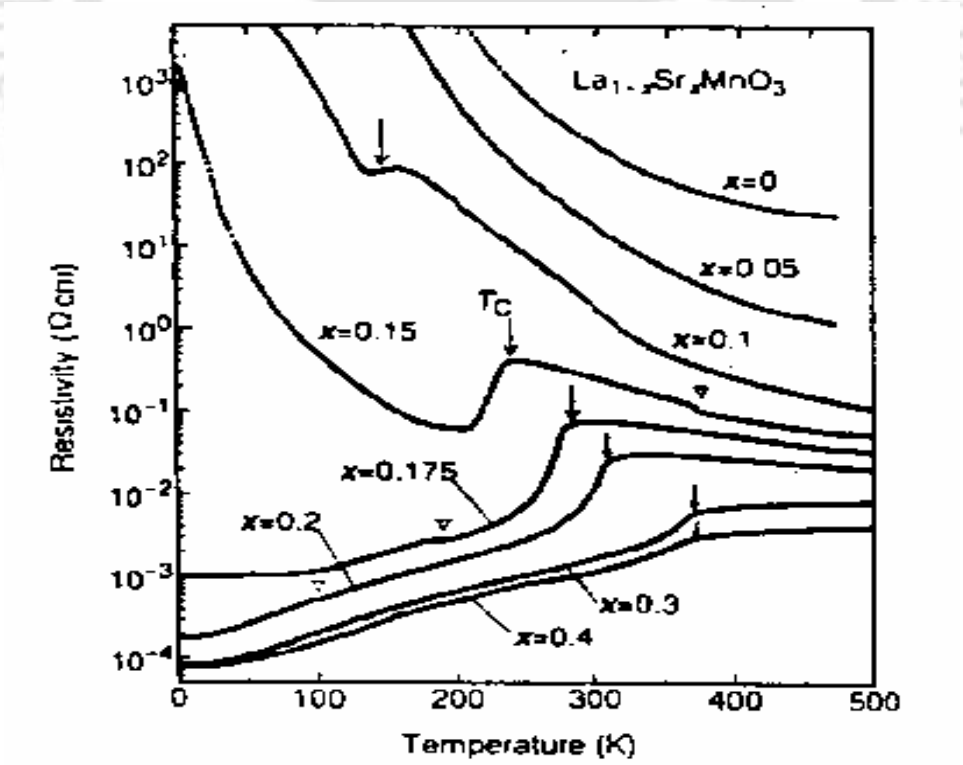

Fig. 1.4: Typical M-I transitions in polycrystalline $La_{1-x}Sr_xMnO_3$. (from Urushibara *et al.* [26]).

Magneto-resistivity (MR) is a measure of the change in electrical resistivity as a function of magnetic field, H and is usually calculated as,

$$MR(T) = \frac{\rho(H,T) - \rho(0,T)}{\rho(0,T)} \qquad \text{----------} \qquad (1.2)$$

where, ρ(H,T) is the measured resistivtiy in the presence of magnetic field and ρ(0,T) is the resistivity in the absence of applied field. The magneto-resistivity arising from different physical origins are given in Fig. 1.5. The electrical resistivity in magnetic materials depends on the direction of the applied magnetic field relative to the orientation of the crystal itself [111], a phenomenon known as anisotropic magneto-resistivity. On the other hand, the ordinary magneto-resistivity (Fig. 1.5(b)), which is related to the Hall effect, originates from the impact of the Lorentz-force on moving charge carriers. In absolute numbers, the magnitudes of the anisotropic and the ordinary magneto-resistivity are moderate and typically not more than a few percentage. In the end of 1980's, it was discovered that multi-layers of magnetic and nonmagnetic metallic materials could show much higher negative magneto-resistivity compared to the previously known MR [112] and it is called giant magneto-resistivity (GMR) (Fig. 1.5 (c)). Only about half a decade later, it was discovered that doped rare-earth manganese oxides by themselves could possess even higher magneto-resistivity (in some cases close to 100%). [9, 10, 11, 113]. The magneto-resistivity values in manganites are found to be even higher than that of GMR and hence the term colossal [9, 90] was used to describe the MR of manganites. The general behaviour of colossal magneto-resistivity is shown in Fig. 1.5(d). In magnetic tunnel junctions, there is another type of magneto-resistivity, known as tunneling magneto-resistivity or junction magneto-resistivity, as shown in Figs. 1.5(e) & (f). The resistivity of a magnetic tunnel junction would be lower for a parallel configuration of magnetization of electrodes. The anisotropic, ordinary and colossal MR can be considered as intrinsic effects of the material, while giant and tunnelling MR depend on extrinsic parameters. The magneto-resistivity in manganite perovskite is associated with a crossover from metallic to insulating state, and accompanied by a magnetic phase transition. The large MR effect is essentially linked to the presence of an adequate amount of Mn^{4+} (around 33%) which can be introduced by cation substitution or cation deficiency [114]. The typical sketch of electrical resistivity in zero field and in the presence of magnetic field in the order of a few Tesla and, magneto-resistivity are shown in Fig.1.6.

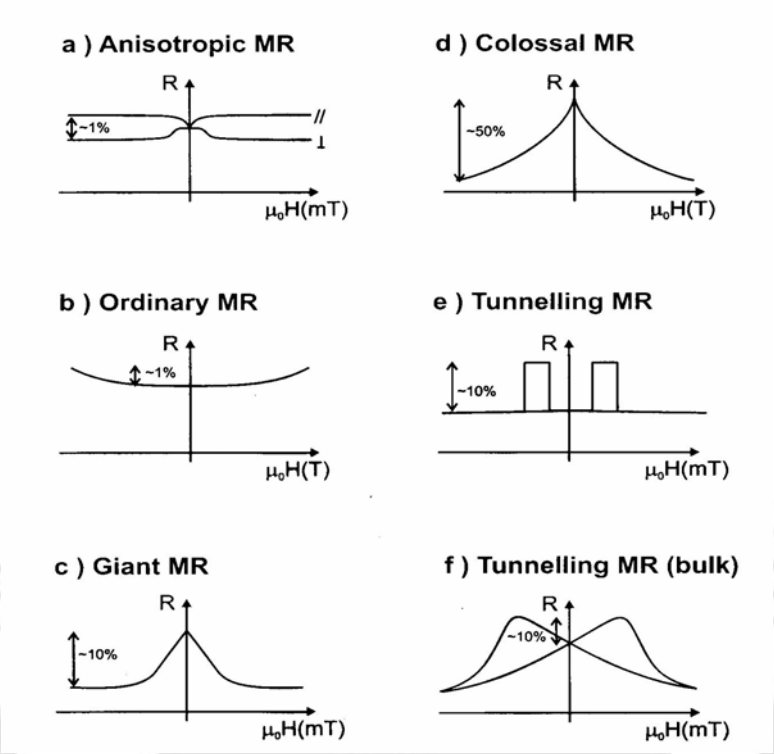

Fig. 1.5: Plots of different types of magneto-resistivity curve.

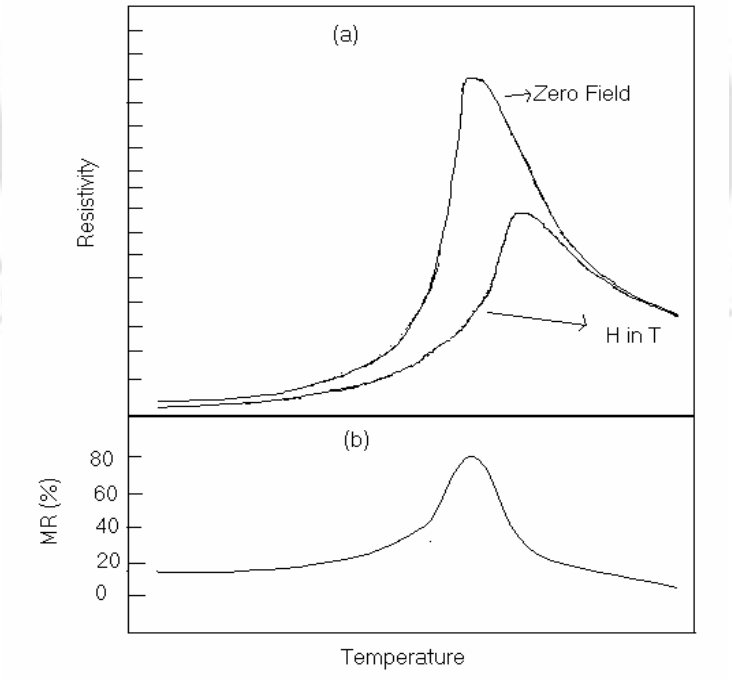

Fig. 1.6: Sketch of (a) ρ versus temperature in zero field and in the presence of field and (b) MR as a function of temperature.

The MR depends upon the applied field. Above T_c, the magneto-resistivity effect is not large in small fields, and the curves are bell shaped. It varies with applied field as, MR α H^2 [37, 115, 116] or MR α M^2 [117]. Here 'H' is the applied field and 'M' is the magnetization. In the vicinity of T_c, the resistivity drops rather sharply at low fields and saturates at higher fields but, at low temperatures, the resistivity is almost independent of field. However, according to Xiong et al. [118], the electrical conductivity is linear in H^2. So, basically the magnetization plays a major role on CMR behavior. On the critical isotherm, M α $H^{1/\delta}$, where $\delta \approx$ 3-5, and hence MR α $H^{2/\delta}$. Below T_c, M depends nonlinearly on H and exponential variation of MR, [exp(-H/H_s)] has been reported by Martinez *et al.* [119]. Snyder *et al.* [120] explained that, a single scaling function MR α exp[-$(M/M_s)^2$] can reproduce the field and temperature dependence of MR both above and below T_c. Here M_s and H_s are the saturation magnetization and the corresponding applied field respectively.

The grain size effects are important in polycrystalline materials. The high-field CMR is almost independent of grain size [24]. Even though polycrystalline materials exhibit low field magneto-resistivity at all temperatures below T_c, such behaviour is absent in single crystals. The low field effect is distinctly different from CMR. It increases with decreasing grain size and grows rapidly at low temperatures. The low field MR effect, which has been observed in polycrystalline ceramics [31, 121] and thin films [122] is attributed to spin-dependent grain boundary scattering.

1.3.1. Theoretical Background

The 'Mn' ions are surrounded by oxygen in manganites as shown in the Fig. 1.1. The 'Mn' ions underlying in such octahedron are subjected to a crystal field splitting of d orbitals as shown in the Fig. 1.3. The crystal field splitting between the t_{2g} and e_g states is about 1eV. In Mn^{3+} based parent compounds, e_g state electrons tend to localize such that Mott insulator is formed. However, the e_g electron can be itinerant by electron vacancies or in otherwords by hole creation in the crystals. Thus the hole doping leads to creation of mobile Mn^{4+} ions in the crystal. Unlike e_g electrons, the t_{2g} electrons are less hybridized with O-2p orbitals and they are stabilized just by crystal field splitting. Thus t_{2g} electrons are localized with a local spin S = 3/2, even in the metallic site. There is a strong coupling between e_g conduction electron spin (S = ½) and t_{2g} localized electron spins (S = 3/2). The exchange energy J_H (Hund's rule coupling energy) is as large as 2-3eV for the manganites

and exceeds the intersite hopping interaction t_{ij}^0 of the e_g electrons between the neighbouring sites, i and j. According to Anderson-Hasegawa [16], in the case of the strong coupling limit, i.e with $J_H/t_{ij} \rightarrow \infty$, the effective hopping interaction t_{ij} can be written as,

$$t_{ij} = t_{ij}^0[\cos(\theta_i/2)\cos(\theta_j/2) + \exp[i(\phi_i - \phi_j)]\sin(\theta_i/2)\sin(\theta_j/2)] \text{ -------- } (1.3)$$

where the core spins are treated as purely classical object and described by unit vectors θ_i, ϕ_i and θ_j, ϕ_j at site i and j respectively. Here θ and ϕ are polar and azimuthal angles. By neglecting the Berry phase term $\exp[(i(\phi_i - \phi_j)]$, one can get,

$$t_{ij} = t_{ij}^0 \cos(\theta_{ij}/2) \quad \text{----------} \quad (1.4)$$

So, the absolute magnitude of the effective hopping depends upon the relative angle θ_{ij} between the neighbouring spins. The ferromagnetic interaction via the exchange of the conduction electrons whose spin shows the on-site (Hund's rule) coupling with the local spin is called "Double-exchange interaction". The ferromagnetic metallic state is stabilized by maximizing the kinetic energy of the conduction electron ($\theta_{ij} = 0$). When temperature is raised close to T_c, the configuration of the spin is dynamically disordered and accordingly the effective hopping interaction is also subjected to disorder and, the average hopping interaction is reduced. This leads to enhancement of the resistivtiy near and above T_c. Therefore, large MR can be expected around T_c, since the local spins are aligned easily by an external field and hence, the randomness of the e_g hopping interaction is reduced. It was the initial explanation of CMR behaviour. However the physics of the CMR behaviour is more complex. In addition to the DE interaction, other interactions such as, the electron-lattice interaction, antiferromagnetic superexchange interaction between the t_{2g} local spins, intersite Coulomb repulsion among e_g electrons, etc. have to be taken into account. Among all the interactions, the electron-lattice interaction frequently occur in manganites, which causes the Jahn-Teller type coupling of the e_g electrons with oxygen displacement. The Jahn-Teller type lattice distortion that lifts the orbital degeneracy and lowers the electronic energy is frequently observed for the orbital degenerate d-electron configuration.

The relation between the electrical conductivity and ferromagnetism can be understood by considering the oscillation of electron between Mn^{3+} and Mn^{4+} ions. According to Zener [14, 15], the magnitude of exchange energy is given by,

$$E = \frac{h\nu}{2} \qquad \text{----------} \qquad (1.5)$$

where, ν is the frequency of oscillation of the electron. The diffusion coefficient of Mn^{4+} ions,

$$D_e \approx \frac{a^2}{t} = \frac{a^2 E}{h} \qquad \text{----------} \qquad (1.6)$$

where, 'a' is the Mn-Mn distance (lattice parameter) and 't' is the time required for a single jump of electron from Mn^{3+} to Mn^{4+} ion. The conductivity equation is

$$\sigma = ne\mu \qquad \text{----------} \qquad (1.7)$$

where 'μ' is the carrier mobility and $n = x/a^3$, the number of Mn^{4+} ions per unit volume. The Einstein relation for carrier mobility is defined as,

$$\mu = \frac{eD_e}{k_B T} \qquad \text{----------} \qquad (1.8)$$

where k_B is the Boltzmann constant and 'T' is the temperature. Now using the above equations the electrical conductivity can be written as,

$$\sigma = \frac{ne^2 D_e}{k_B T} = \frac{xe^2 E}{ahk_B T} \qquad \text{----------} \qquad (1.9)$$

The ferromagnetic Curie temperature T_c is related to the exchange energy by the approximate relation $E = k_B T_c$,

$$\sigma = \left(\frac{xe^2}{ah}\right)\left(\frac{T_c}{T}\right) \qquad \text{----------} \qquad (1.10)$$

The above equation relates the electrical conductivity to ferromagnetic transition temperature T_c and the fraction of Mn^{4+} ions. So, the M-I transition in the manganites is expected to occur at T_c. DE is strongly affected by the structural parameters such as Mn-O-Mn bond angle or Mn-Mn transfer integral.

1.3.2. Electrical Resistivity in the Metallic Region

The low temperature resistivity was first attributed to the electron-electron scattering. Jaime *et al.* [123] showed the existence of electron-magnon scattering. A magnon is a quantized spin wave in a ferromagnetic material. According to Jaime *et al.* [123] the expression for resistivity due to magnon scattering can be written as,

$$\rho(T) = \alpha_\varepsilon T^2 \qquad \text{----------} \qquad (1.11)$$

where,

$$\alpha_{\varepsilon} = \frac{9\pi^3 N^2 J^2 \hbar^5 S}{8e^2 E_F^4 k_F}\left[\frac{k_B}{m^* D}\right]^2 I(\varepsilon) \qquad \text{----------} \qquad (1.12)$$

Here '*NJ*' is the electron-magnon coupling energy. 'D' is the stiffness constant. The effective mass of electron is m^* and $\varepsilon = Dq^2/2k_BT$. The $I(\varepsilon)$ is defined as,

$$I(\varepsilon) = \int_{\varepsilon}^{\infty} \frac{x^2}{\sinh^2 x} dx \qquad \text{----------} \qquad (1.13)$$

The above resistivtiy expression for single magnon scattering event is attributed to absorption or emission of one magnon. Such event is accompanied by an electron spin-flip and the resistivity depends upon T^2. In manganites, several groups [92, 93, 124] analyzed the resistivtiy data interms of the above single-magnon scattering and fitted the experimental data to the expression,

$$\rho(T) = \rho_0 + \rho_2 T^2 \qquad \text{----------} \qquad (1.14)$$

Jaime *et al.* [123] have fitted the low temperature resistivity data to the expression,

$$\rho(T) = \rho_0 + \rho_2 T^2 + \rho_5 T^5 \qquad \text{----------} \qquad (1.15)$$

where, the T^5 contribution arises from electron-phonon process.

The T^2 dependence of the resistivity was established by Mannari [125], in itinerant electron ferromagnets. Jaime *et al.* [123] extended this calculation for the case in which the minority and majority spin sub-bands differ in energy by a constant amount yielding the same T^2 dependence.

A $T^{4.5}$ dependence was observed by Snyder *et al.* [126] and this was attributed to two magnon scattering process as calculated by Kubo and Ohata [127]. However the temperatures involved are too high at which there would be substantial density of states at the Fermi level for the minority spin states and hence single-magnon scattering (the stronger process) can not be ruled out. So, they proposed the expression for resistivity as,

$$\rho(T) = \rho_0 + \rho_2 T^2 + \rho_{4.5} T^{4.5} \qquad \text{----------} \qquad (1.16)$$

The low temperature resistivity of manganites has been calculated separately by Wang and Zhang [128] and by Furukawa [129]. Their calculation yields a temperature dependent resistivity that scales as $T^{2.5}$ above T ~ 60K and contains a $T^{1.5}$ contribution below this temperature. Schiffer *et al.* [21] could successfully fit the low temperature resistivity of their $La_{1-x}Ca_xMnO_3$ sample to the expression,

$$\rho(T) = \rho_0 + \rho_{2.5} T^{2.5} \qquad \text{----------} \qquad (1.17)$$

The above model predicts a significant magneto-resistivity at low temperature, however Hwang et al [121] have not observed any such magneto-resistance on single crystals and thin films.

Furukawa considered the existence of minority spin states created as a result of spin fluctuations leading to a T^3 temperature dependence as,

$$\rho(T) = \rho_0 + \rho_3 T^3 \qquad \text{----------} \qquad (1.18)$$

This model has been used to fit the low temperature resistivity of $La_{1-x}Sr_xMnO_3$ (x = 0.2, 0.3, 0.4) to much lower temperatures than the T^2 fit (i.e. explain the deviation from T^2 at low temperatures).

1.3.3. Electrical Resistivity in the Semiconducting Region

According to Millis *et al.* [20], the existing models based upon double exchange interaction strongly underestimate the magnitude of resistance change during metal-insulator transition. The transition from metallic to insulating phase is described as localization of itinerant electrons as per Mott-transition. The charge transport still occurs in the insulating regime, but the carriers are more localized than in the metallic phase. Already de Gennes [19] demonstrated that for small values of 'x' in $R_{1-x}A_xMnO_3$, local distortions of the antiferromagnetic structure tend to trap the doped charge carrier. Localization of charge carriers will increase their interaction with the surrounding (magnetic) environment and hence a virtual effective mass is added to the hopping electrons. But charge hopping is also connected to the lattice distortions as described by the Jahn-Teller effect. This transport of lattice and spin distortions is usually referred to as magnetic polarons. Several studies have indicated localization of charges and the formation of small polarons in perovskite manganite materials above T_c [130-133]. If the charge carrier with its association to crystalline distortion are less than the size of the unit cell, it is called small polaron. In this case the charge carriers are always found at the lattice site. Further, the temperature variation of resistivity above T_c is mostly found to follow the small polaron model [134], i.e,

$$\rho = \rho_{sp} T^n \exp\left(\frac{E_{sp}}{k_B T}\right) \qquad \text{----------} \qquad (1.19)$$

Here, E_{sp} is the hopping energy, T is the temperature and k_B is the Boltzmann constant. n = 1 corresponds to adiabatic small polaron hopping and n = 3/2 corresponds to non-adiabatic small polaron hopping. According to adiabatic small polaron hopping, the charge carriers

hop more rapidly and each time the carrier hops, the configuration of the vibrating atoms in the adjacent site coincides with that of occupied state. In non-adiabatic case the motion of small polaron is quite slow.

In polycrystalline samples, very thin films and un-annealed samples, i.e. samples with oxygen deficiency, etc. variable-range-hopping (VRH) and non-adiabatic small polaron hopping models are found to explain the data [135-137]. According to Mott variable range hopping (Mott-VRH) model, the expression for electrical resistivity can be written as, [138, 139],

$$\rho = \rho_{0m} \exp\left(\frac{T_{0m}}{T}\right)^{1/4} \qquad \text{----------} \qquad (1.20)$$

Here, ρ_{0m} is the Mott residual resistivity and T_{0m} is the Mott characteristic temperature. The density of states in the vicinity of Fermi level, $N(E_F)$ and, hopping distance $R_{hop}(T)$ and hopping energy, $E_{hop}(T)$ can be written as,

$$N(E_F) = \frac{18}{k_B T_{0m} a^3} \qquad \text{----------} \qquad (1.21)$$

$$R_{hop}(T) = \frac{3}{8} a \left(\frac{T_{0m}}{T}\right)^{1/4} \qquad \text{----------} \qquad (1.22)$$

$$E_{hop}(T) = \frac{1}{4} k_B T^{3/4} T_{0m}^{1/4} \qquad \text{----------} \qquad (1.23)$$

Here 'a' is the localization length. According to VRH model, the charge carriers hop from one localized to another localized state having overlapping electron wave function. The energy required for such hopping is taken from Phonon (lattice vibration). The above Mott -VRH resistivity equation has been derived for 3-dimensional case by neglecting the coulomb interaction between carrier charges. However, Efros and Skhlovskii (ES) have modified the Mott-VRH model by taking into account the coulomb interaction between the charge carriers and the corresponding resistivity expression is,

$$\rho = \rho_{0s} \exp\left(\frac{T_{0s}}{T}\right)^{1/2} \qquad \text{----------} \qquad (1.24)$$

where, ρ_{0s} is the ES residual resistivity and T_{0s}, the ES characteristic temperature is defined as,

$$T_{0s} = \frac{\beta_1 e^2}{k_B a 4\pi\varepsilon_0\varepsilon_r} \qquad \text{----------} \qquad (1.25)$$

Here '*a*' is the localization length, 'ε_r' is the dielectric constant and 'β_1' is a numerical constant = 2.8.

Viret *et al.* [140] found the variable-range-hopping as being the most likely mechanism of charge transport for Ca-doped perovskite manganites with x = 0.30. They found the temperature variation of resistivity as,

$$\rho = \rho_\infty \exp\left[1-(M/M_s)^2/T\right]^{1/4} \quad \text{----------} \quad (1.26)$$

Here M and M_s are the magnetization and the saturated magnetization respectively.

In general, the double exchange interaction still seems to provide the best explanation of the charge transport in the metallic region. Starting from the transfer integral given by Anderson and Hasegawa [16], $t_{eff} = b\cos(\theta/2)$, the expression for resistivity can be written as [141,142],

$$\rho \alpha \exp(-t^2_{eff}) \alpha \exp(-\cos^2(\theta/2)) \quad \text{----------} \quad (1.27)$$

where, the coefficient of proportionality is omitted for simplicity. Since the magnetization is the effective orientation of spins along field direction, $M/M_s \alpha \cos(\theta/2)$ and eqn. (1.27) can be written as,

$$\rho \alpha \exp(-(M/M_s)^2) \quad \text{----------} \quad (1.28)$$

This relation has been verified experimentally for several perovskite manganites. For $M << M_s$, the exponent in Eqn (1.28) can be expanded and hence,

$$\rho(M) = \rho_0(1 - C(M/M_s)^2) \quad \text{----------} \quad (1.29)$$

where, 'C' is a coupling coefficient of the order of unity. It has been shown that the coupling parameter 'C' depends upon the Hund's coupling J_H, the e_g electron bandwidth, W and the doping concentration, x [143]. It has been also demonstrated that eqn.(1.29) is applicable to the resistivity of pyrochlore materials [97]. The magneto-resistivity as defined in eqn. (1.2) can be deduced from eqn. (1.29) and hence,

$$MR = -C(M/M_s)^2 \quad \text{----------} \quad (1.30)$$

For the canonical double-exchange system $La_{1-x}Sr_xMnO_3$ and in the low-M region this expression for MR seems to be accurate [144].

1.3.4. Effective Medium Approach

There are a few manganites where the Tc > T_{MI}. In such cases, both the ferromagnetic insulator and ferromagnetic metallic state co-exists in the mixed valent manganites. Taking this into account, the bond percolation theory has been used to understand the overall temperature dependent resistivity of manganites. So, the resistivity at any temperature can be understood as the effective resistivity of a 3D matrix, where the SE and DE bonds are randomly distributed. The temperature dependence of the resistivity has been designed by taking into account both the metallic and insulating properties. This model is named as effective medium approximation (EMA). The EMA was originally used to understand the electrical conduction in composite materials [145, 146]. Later this theory was applied to understand the electrical resistivity of disordered materials, where there is hopping among localized states well below the mobility edge [147, 148]. The basic idea of this model is that the existence of random mixture of two types of bond with different resistances and the conduction in the composite is essentially studied as a percolation problem. The conduction in such a composite system is decided by the magnitude of the individual resistances and their ratio. The expression for resistivity can be written as,

$$\rho = \frac{4\rho_1\rho_2}{\{(3p-1)\rho_1 + (2-3p)\rho_2\} + [\{(3p-1)\rho_1 + (2-3p)\rho_2\}^2 + 8\rho_1\rho_2]^{1/2}} \quad \text{----- (1.31)}$$

where, ρ_1 and ρ_2 are respectively the nonmetallic and metallic bond contributions in a random mixture. The percolation variable p, is defined as the volume fraction of those bonds which contribute for metallic conduction. The 'p' value decides the type of conduction i.e. either metallic or nonmetallic. The 'p' value at which the resistivity goes from insulating to metallic behaviour is called the percolation threshold value, p_c. This value depends on the dimensionality of the system and for metallic conduction in a 3D matrix, p_c = 1/3. Around this value the effective resistivity ρ is a crucial function of the ratio (ρ_1/ρ_2). On the other hand, if both ρ_1 and ρ_2 are nonmetallic contributions with different functional forms, then the effective resistivity will be predominantly decided by only one of these, on either side of the percolation threshold value. Investigations on the continuous random resistor networks by Kirkpatrick [145] and others [146-150] have proved the success of this EMA model. A similar approach has been adopted to explain magneto-resistivity properties in CMR materials [151, 152].

Recently a parallel contribution theory (both insulating and metallic behaviour) has been proposed to understand the resistivity behaviour. The expression for parallel contribution theory is given as [153],

$$\rho(T) = \left\{ \frac{f(T)}{\rho_{lt}(T)} + \frac{[1-f(T)]}{\rho_{ht}(T)} \right\}^{-1} \qquad \text{----------} \qquad (1.32)$$

where, $f(T) = \{[\exp(T-T_{MI})/\Delta]+1\}^{-1}$ is the fraction of the carriers in the metallic state, T_{MI} is the M-I transition temperature, Δ is the effective width of the transition interval around T_{MI}, $\rho_{lt}(T)$ is the metallic resistivity (below T_{MI}) expression and $\rho_{ht}(T)$ is the semiconducting (above T_{MI}) resistivity expression. Recently Huhtinen *et al.* [154] fitted the resistivity data in the whole temperature range with the above expression for their $La_{0.7}Ca_{0.3}MnO_3$ sample. Here they have taken eqn.(1.16) for $\rho_{lt}(T)$ and eqn.(1.20) for $\rho_{ht}(T)$.

1.4. Magnetic Properties

The mixed valence manganites show paramagnetic to ferromagnetic transition in the temperature range ≈ 100 to 360K depending on the type of materials.

The manganite perovskites exhibit different type of magnetic ordering as shown in the Fig. 1.7 [12]. Out of them 'B' type ordering is the familiar ferromagnetic arrangement, where as, all other arrangements are antiferromagnetic. For instance the parent compound $LaMnO_3$ is an antiferromagnet with Neel temperature (T_N) 141K [12] with 'A' type antiferromagnetic arrangement. Here, the spins in the 'ab' plane are arranged ferromagnetically, while the successive 'ab' planes are coupled antiferromagnetically. There may be a weak ferromagnetic moment along c-axis [155] due to the canted structure of the spin.

In mixed valence manganites, different type of magnetic orderings are observed depending on the concentration of Mn^{3+} & Mn^{4+} ions, which in turn depends on chemical formula. The exchange coupling between pair of 'Mn' ions depends upon their charges (valency), viz. ferromagnetism between Mn^{3+}-Mn^{4+} ions, antiferromagnetism between pair of Mn^{4+} ions and ferro- or antiferromagnetism between pair of Mn^{3+} ions. The ferromagnetic component of magnetization, M appears along c-axis in the presence of Mn^{4+} ions, in hole doped $R_{1-x}A_xMnO_3$ compounds. The FM component increases up to x = 0.33, where the sample is entirely in the ferromagnetic state [12,156]. The coexistence of

antiferromagnetic ordering and FM moment results in spin canting or microscale phase segregation. Two types of antiferromagnetic orderings are generally observed, for further increase in Mn^{4+} concentration, i.e. beyond ~0.35. It is the result of charge ordering of Mn^{4+} & Mn^{3+} ions for certain concentration ratio. For x values close to 1, the ordering transfers to a single type of antiferromagnetic ordering.

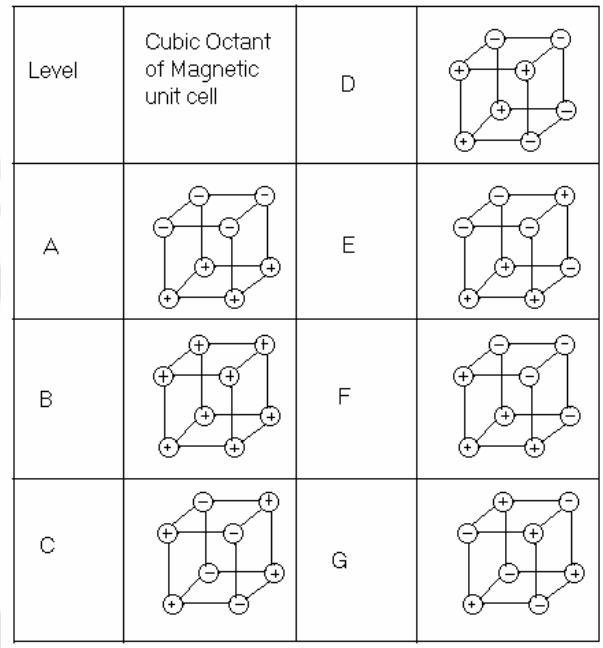

Fig. 1.7: Possible magnetic structures in manganite perovskites and their arrangements.

In certain level of doping, spin-glass type of behaviour with random canting of magnetic spins are observed [157]. Here, as a result of competing interaction between FM ordering with AFM interactions, the spins are frozen in random direction below certain temperatures and it results in sharp fall in susceptibility or magnetization such that their values are quite low. The 'Mn' site substitutions also some time leads to spin-glass behaviour. For instance, replacement of about 20% of the 'Mn' in $(La_{0.67}Ca_{0.33})MnO_3$ compound with 'Cu', results in destruction of ferromagnetic metallic state and leads to thermally activated conduction mechanism with spin-glass order [158]. The substitution of Al [159] and Fe [160] in place of 'Mn' also introduces spin-glass behaviour.

The paramagnetic to ferromagnetic transition temperature (T_c) in mixed valence manganites depends upon the size of the cations. For particular alkaline metal, there is a clear tendency for T_c to increase with increasing atomic radius of the rare earth elements, which is related to e_g band width [161]. Similarly there is a tendency for T_c to increase with increasing tolerance factor, 't' or mean size of the A site cations [70, 113, 162, 163].

This is probably due to increase in Mn-O-Mn bond angle. However, there is no clear trend of T_c variation associated with average atomic weight & electro negativity of the alkali ion. The reduction in Curie temperature was reported on materials prepared by 'Mn' site substitutions such as, Al, Ga, In [164, 165], Cu [166], Fe [167] and Ru [168]. The theoretical magnetic moment with complete spin polarized state is expected to be (4-x) μ_B/fu (x = percentage of A-site cation). However, the experimental values are mostly smaller than the expected values and it is mainly due to the spin canting.

1.4.1. Theoretical Background

The early theoretical work was based upon the experimental works observed in manganite perovskite, where they are assumed to be homogeneous. Even in the present context, Zener's double exchange (DE) is found to explain the experimental magnetic and transport properties [14, 15]. The splitting of d-orbital and filling of d-orbital electrons for Mn^{3+} and Mn^{4+} are shown in Fig. 1.3. For Mn^{3+} ion, three electrons occupy the t_{2g} levels and the remaining one electron occupies the e_g level. A strong Hund's coupling favours the spin alignment of all four electrons. In Mn^{4+} ion the e_g level is vacant. In mixed valent manganites, Mn^{3+} and Mn^{4+} ions are separated by an O^{2-} ion. So, there is a possibility of Mn^{3+} e_g electron hopping to the Mn^{4+} ion via the O^{2-} ion. This motion is governed by the Pauli's exclusion principle and can occur only when an up-spin e_g electron from Mn^{3+} ion replaces the up spin electron of the O^{2-}-2p level. This process is shown in Fig. 1.8. Two simultaneous motions are involved in this process, and so it is called double exchange (DE) interaction. The movement of electron schematically can be written as, $Mn^{3+}_{1\uparrow}O_{2\uparrow,3\downarrow}Mn^{4+} \rightarrow Mn^{4+}O_{1\uparrow,3\downarrow}Mn^{3+}_{2\uparrow}$, where the electrons spins are labeled 1, 2 and 3. Anderson and Hasegawa [16] presented the DE mechanism in detail by visualizing a second order process in which the electron transfer takes as follows $Mn^{3+}_{1\uparrow}O_{2\uparrow,3\downarrow}Mn^{4+} \rightarrow Mn^{3+}_{1\uparrow}O_{3\downarrow}Mn^{3+}_{2\uparrow} \rightarrow Mn^{4+}O_{1\uparrow,3\downarrow}Mn^{3+}_{2\uparrow}$. It has been presented that, the effective hopping integral for the electron to move from one 'Mn' site to another 'Mn' site is proportional to the square of the hoping integral between p-Oxygen and d-Manganese orbitals. If the localized spins (t_{2g}, S = 3/2) are considered as classical objects and if they are canted with an angle θ between the nearest neighbour spins, the effective hopping integral would be proportional to cos(θ/2). For θ = 0, cos(θ/2) attains maximum value 1

and the hopping is maximum and, it corresponds to a ferromagnetic interaction. If θ = 180^0, the cos(θ/2) becomes 0 and it corresponds to antiferromagnetic interaction [16].

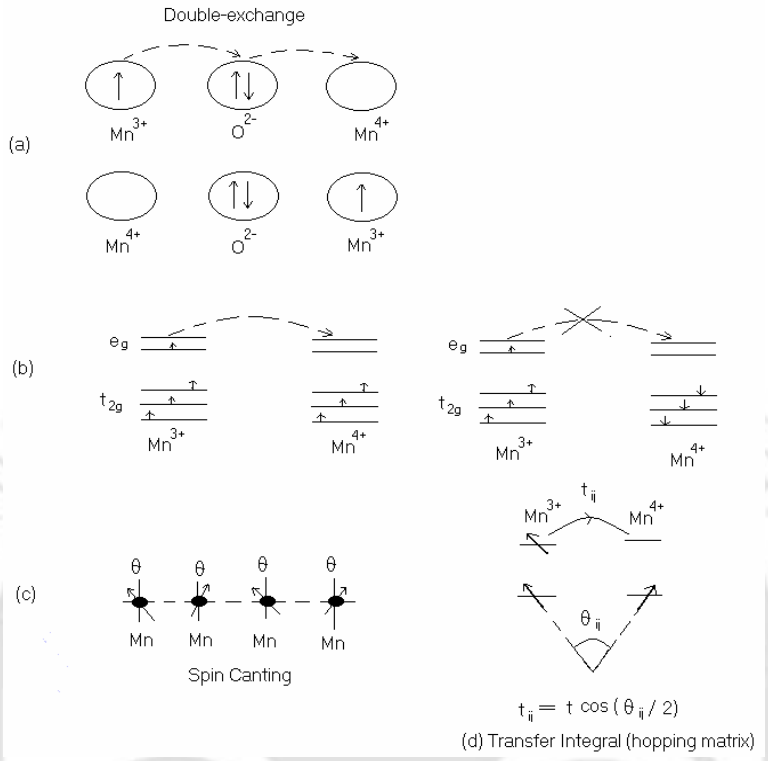

Fig. 1.8: (a) Sketch of the double exchange mechanism which involves two Mn ions and one O ion. (b) The mobility of e_g electrons improves if the localized spins are polarized. (c) Spin-canted state which appears as the interpolation between FM and AFM states in some mean-field approximations. The transfer integral is shown in the Fig. (d).

The quantum mechanical treatment of the DE was reported by Kubo and Ohata in 1972 [127]. The following assumptions were made (i) the two fold degeneracy of the e_g orbitals is ignored, (ii) ions are considered to be held rigidly in the lattice, (iii) the coulomb interaction between the e_g electrons is ignored, (iv) potential fluctuations due to charged impurities are assumed to be averaged out and (v) the number of carriers is small. The magnetization derived within this model was found to fit the temperature dependence of the magnetization curve of $La_{0.62}Pb_{0.38}MnO_3$ [4].

The possible existence of small magnetic or lattice polarons was proposed based on the resistivity, thermopower and Hall effect measurements [156]. In 1995, Millis *et al.* [20] pointed out that the earlier theoretical work was based on only qualitative explanation. It fails to describe quantitatively. In their series of paper [20, 169-173], they argued that the physics of manganites is dominated by the interplay between strong

electron-phonon coupling and the large Hund's coupling. It optimizes the electronic kinetic energy, which is responsible for ferromagnetic phase. The ratio $\lambda = E_{JT}/t$, plays a major role on physical properties of manganites. Here E_{JT} is the static trapping energy at a given octahedron and 't' is the effective transfer matrix element, which is temperature dependent. Following the discussion of double exchange by Kubo and Ohata [127], Millis *et al.* [171] calculated the temperature dependence of the resistivity (ρ) as a function of λ for different carrier concentrations. For all carrier concentrations, it was found that $d\rho/dT < 0$ above T_c, i.e. insulating behaviour. For $\lambda > 1$ a large magneto-resistivity was also observed. Their experimental data follow the above calculation and gives evidence for electron phonon coupling.

1.4.2. Charge and Orbital Ordering in Manganite Perovskite

The study of CMR in $R_{1-x}A_xMnO_3$ has brought yet another novel feature related to the charge ordering in these oxides. It is known as Wigner crystallization, which is driven by interatomic coulomb interactions. For certain particular valencies and concentration of 'Mn' ions, the mobile 'd' electrons in manganites are localized and form a regular lattice. Here the Coulomb interaction between 'Mn' ions is comparable to the conduction electron bandwidth (W) [174]. This effect is supported by small displacement of the oxygen atoms to accommodate the ordered cations. Charge ordering is most likely to occur, when the temperature is low and 'x' is a rational fraction, especially x = 1/8, 1/2, and 3/4. The extra fourth d electrons (e_g electron) can be localized on alternate manganese sites in a plane, as shown in Fig. 1.10(a).

Kanamori [175] pointed out that the carriers in mixed valence manganites may be strongly coupled to local lattice distortions. Orbital ordering can occur at certain carrier concentrations when the 'd' electrons occupy an asymmetric orbital, as shown in Fig. 1.9(b). The driving force is partly due to direct electrostatic repulsion of the charge clouds, however the coupled Jahn-Teller distortions of adjacent octahedral stabilize such effect. Fig. 1.9(c) illustrates the coupled charge and orbital ordering, which is expected for x= 1/2.

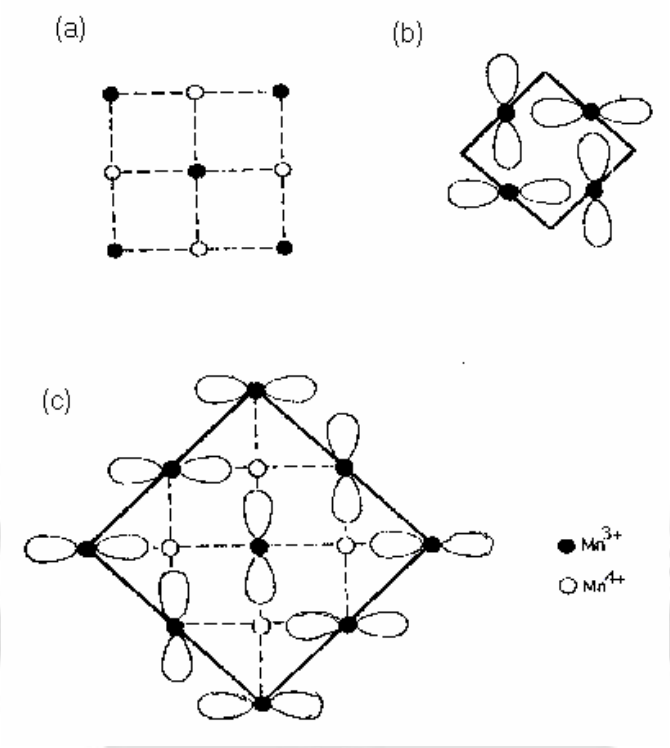

Fig. 1.9: (a) Charge ordering of Mn^{3+} and Mn^{4+} ions in a crystal with x = ½. (b) Orbital ordering of the $d_{3z^2-r^2}$ orbitals of Mn^{3+} and Mn^{4+} when x = 0. (c) Combined charge and orbital ordering when x = ½.

Charge-ordering in manganates is interesting because double exchange gives rise to ferromagnetic metallic state and the charge-ordered state is associated with antiferromagnetic or paramagnetic insulating state. Lattice distortion plays a crucial role in charge-ordering, for instance the orthorhombic distortion stabilizes the charge-ordered state. The charge-ordered state can be melted into a metallic ferromagnetic state, by the application of external magnetic field. The transition from insulating behaviour in the absence of field to metallic behaviour in the presence of field is nothing but a 1st order insulator to metal transition induced by the applied field [6, 176, 177]. The above effect is generally accompanied by considerable hysteresis [177].

Charge ordering in manganites is governed by the width of the e_g band which is directly determined by the weighted average radius of the A-site cations $<r_A>$, or the tolerance factor. This is because a distortion of the Mn-O-Mn bond angle affects the transfer interaction of the e_g conduction electrons (holes). The ferromagnetism and the associated M-I transition can occur without any charge-ordering only when $<r_A>$ is large.

The decrease in $\langle r_A \rangle$ values give rise to transition from ferromagnetic (metallic) state into antiferromgnetic charge-ordered state on cooling. The ferromagnetic metallic state can only be created by the application of the magnetic field in the charge-ordered state, depending on $\langle r_A \rangle$.

Investigations on charge ordering have shown that the lattice distortion localize the charge carriers and initiate charge-ordering. Eventually, the coulomb interaction wins over the kinetic energy of the electrons to form long range CO state. The scale of the energy involved with CO is around 0.5-1eV. This is similar to the unscreened bare nearest neighbour coulomb repulsion. This is also close to the approximate energy required to create ~1% orthorhombic distortion.

1.5. Miscellaneous Physical Properties

Other than the electrical transport and magnetic properties, the manganites perovskites show different interesting physical properties like thermo electrical power, Hall voltage, thermal properties, etc. These properties are beyond the scope of the study in the present thesis work. These properties are reviewed briefly in this section.

1.5.1. Thermo Electric Power (TEP)

Measurement of the electrical field induced by a temperature gradient across a sample provides complementary information to the resistivity. The Seeback coefficient 'S_c' is defined as $\Delta V/\Delta T$. The seeback coefficient of a metal in free-electron model is

$$S_c = \frac{k}{|e|}\left(\frac{kT}{E_F}\right) = 87\frac{kT}{E_F}\mu V K^{-1} \qquad \text{----------} \qquad (1.33)$$

Manganite perovskites generally show a very small thermopower in the metallic state ($S_c < 2\mu VK^{-1}$), with no evidence for temperature dependence [132, 178, 179]. Zhou *et al.* [178] interpreted this as the evidence for vibronic state, where the electrons coupled to the dynamic Jahn-Teller distortion exhibit no dispersion. However, the data below T_c on some $(La_{1-x}Sr_x)MnO_3$ single crystals [180] and $La_{0.67}Ca_{0.33})MnO_3$ thin films [181] exhibit a different behaviour, which is interpreted as a superposition of metallic ferromagnet [182] and phonon drag terms.

When the resistivity is thermally activated, the thermopower may also be expected to show semiconducting-like behaviour. The seeback coefficient for a semiconductor is,

$$S_c = -\frac{k}{|e|}\left(\frac{\Delta}{kT} + B\right) = -87\left(\frac{\Delta}{kT} + B\right)\mu VK^{-1} \quad \text{----------} \qquad (1.34)$$

Where 'Δ' is activation energy, positive for electrons and negative for holes. 'B' is a constant of order 2, which is related to the entropy of the carriers. It is sometimes written as $\ln[2(1-C')/C']$, where C' is the number of carriers per site. The factor 2 is due to spin degeneracy. 1/T variation of thermopower has been observed above T_c. The activation energy 'Δ' inferred from the 1/T variation is smaller by a factor of three to ten, compared to that deduced from resistivity measurements [181]. There is often a broad peak near T_c in samples showing M-I transitions, which is attributed to the coupling of holes and spins, analogous to phonon drag [114]. In many cases, the thermopower changes sign from positive below T_c to negative well above T_c. There is no evidence for $T^{-1/2}$ variation predicted by Mott and Davies [138] in analogy with Mott-VRH in ρ versus T data [181]. There is a strong magnetic field dependence of 'S_c' in the vicinity of T_c, which demonstrates that the carriers are magnetic in character. When a large positive anomaly is observed around T_c, the thermopower is reduced by the applied field. Well above T_c the magnetic field has little effect on S.

1.5.2. Hall Effect

In contrast with normal metals and semiconductors, the Hall resistivity of magnetic materials, contains an additional term, which depends on the magnetization. The expression for Hall resistivity (ρ_{xy}) for magnetic semiconductor is defined as,

$$\rho_{xy} = R_0 B_a + \mu_0 R_E M \quad \text{----------} \qquad (1.35)$$

Where 'μ_0' is the mobility of the charge carrier, 'B_a' is the applied magnetic field, 'M' is the magnetization and, the normal Hall coefficient 'R_0' is 1/ne and the extraordinary Hall coefficient 'R_E' depends on asymmetric electron scattering due to spin-orbit coupling. 'R_E' may be positive, negative or even zero in special cases. In ferromagnets, the second term is larger by an order of magnitude compared to ordinary Hall effect [183]. If one carrier model is assumed, the Hall mobility $\mu_H = R_0/\rho$ may be deduced from measured values of R_0 and the normal resistivity $\rho = \rho_{xx}$.

The sign of the Hall carriers in the ferromagnetic state of mixed valence manganites should depend critically on the Jahn-Teller splitting of the e_g band [184]. If this band is fully split, the expected carrier concentration is 'x' holes ($x < 0.5$), where as, if

it is unsplit, the carrier concentration should be '1-x' electrons. However holes in O-2p band may also contribute to the Hall signal. So, the manganites are complicated materials for Hall effect measurements. The difficulty to achieve magnetic saturation would lead to experimental problem. Another problem arises when the magneto-resistivity is large, any imbalances in the Hall leads would produce extra ρ_{xx} signal and it may mask the Hall contribution and it is necessary to separate the odd and even parts.

1.5.3 Optical Properties

Systematic investigations have been carried out on optical absorption and optical conductivity of $RMnO_3$ perovskites in a wide frequency rang, i.e. from infrared to ultraviolet [185, 186]. The main absorption edge due to charge transfer from $2p(O) \rightarrow 3d(Mn)$ in $LaMO_3$ is found to vary falls from 6eV for M = Sc to zero for M = Ni ($LaNiO_3$ is a metal) [187]. In manganites the above absorption is found to be at around 3.1eV. In addition to that, a weaker absorption fraction at around 1.7eV is observed and it is attributed to the promotion of a t_{2g} electron into a vacant e_g orbital [130,185, 188].

1.5.4 Thermal Properties

The heat capacity of several ferromagnetic manganites has been reported at low temperature [135,189]. The temperature variation of heat capacity follows expression,

$$C = \gamma T + \beta T^3 \qquad \text{----------} \qquad (1.36)$$

Where, γ and β are the constants. Viret *et al.* [140] have reported that, γ = 5-8 mJK^{-2}, which corresponds to the density of states at the Fermi level, $N(E_F) = 4\times10^{28}m^{-3}eV^{-1}$ $(= 3\gamma/(\pi k_B)^2)$. This is relatively a high value for a metal. The value of γ is found to be uncorrelated with the residual resistivity ρ_0, which varies by several orders of magnitude in these compounds. The width of the e_g band is estimated to be 0.9eV with 0.7 electron per formula . e. with the concentration of $1.2\times10^{28}m^{-3}$. Debye temperatures are found to be in the range of 330-400K [135, 189].

Like the resistivity, the thermal conductivity 'κ' exhibits an anomaly in the vicinity of T_c which can be modified by an applied field [190]. An unusual positive temperature coefficient $d\kappa/dT>0$ above T_c is observed and it associated with scattering from large dynamic lattice distortion.

1.6. Objectives and Motivation of the Present Thesis Work

As reviewed above, most of the works in literature were mainly on hole doped materials with divalent atoms. CMR and magnetic properties have been studied to investigate their potential application for magnetic recording and to understand their physical mechanism. There are also reports on substitution of other magnetic ions and non-magnetic ions in place of 'Mn' to understand the nature of magnetic interaction.

Like hole doping, electron doping also gives rise to mixed valent 'Mn' ions, it would be interesting to study these materials to understand their mechanism and possible application. In this context, only Ca-Mn-O based compounds have been studied extensively by electron doping and they mostly show charge ordering with semiconducting behaviour. So, in the present thesis work, I have taken up $BaMnO_3$ and $SrMnO_3$ based compounds for electron doping and to investigate their electrical transport and magnetic properties. The advantage of these two series are that their T_c are close to and even above room temperature in hole doped regime.

As reviewed in this chapter, one can get metal-insulator transitions with CMR behaviour even by doping mono-valent alkali ions such as Li, Na, K, etc. These materials exhibit T_c, close to room temperature. The advantage of mono-valent doping is that one can generate desired ratio of Mn^{3+}/Mn^{4+} ions with relatively low level of doping, i.e. with reduced ionic size mismatch & distortion. It would be interesting to study the effect of substitution of mono-valent atoms, other than alkali ions in place of 'La' (or rare earth). There are couple of reports on 'Ag' doped materials and these are mainly studied in the context of magneto-caloric effect. So, I had proposed to carryout the detailed study of materials prepared by mono-valent doping (non-alkali ions) such as 'Ag' & 'Cu' in place of 'La'.

There are a few reports on doping of 'Cu' in place of 'Mn' ions of CMR materials, such as $(La_{0.67}Ca_{0.33})Mn_{1-x}Cu_xO_3$. The parent compounds of high T_c superconductors ($CaCuO_2$, La_2CuO_4) and CMR materials ($LaMnO_3$, $CaMnO_3$) have several similarities, viz. like crystal structure, mixed valency of 'B' site cation, oxygen off-stoichiometry, etc. So, it was proposed to study the effect of 'Cu' doping on parent compounds of CMR materials, which is expected to produce mixed valency of 'Mn' ions and also interact magnetically with 'Mn' ions. So, in the present thesis work compounds based on following series were prepared.

1. $Ba_{1-x}La_xMnO_3$ (x = 0 to 0.8)
2. $Sr_{1-x}La_xMnO_3$ (x = 0 to 0.82)
3. $La_{1-x}Ag_xMnO_3$ (x = 0 to 0.35)
4. $La_{1-x}Cu_xMnO_3$ (x = 0.05 to 0.40)
5. $LaMn_{1-x}Cu_xO_3$ (x = 0.05 to 0.40)
6. $CaMn_{1-x}Cu_xO_3$ (x = 0 to 0.40)

The first two series (1&2) are mainly electron doped compounds for x upto 0.50. For the sake of comparison a few hole doped materials were also prepared (x > 0.50). The middle two series (3&4) are hole doped materials (other than conventional alkaline earth & alkali ions). In brief, the objectives are

(i) Preparation of above compounds in single phase form.

(ii) To carryout crystal structure analysis.

(iii) To look for possible metal-insulator and ferromagnetic-paramagnetic transitions and colossal magneto-resistivity.

(iv) To investigate the mechanism of electrical conduction by analyzing the experimental resistivity interms of different theoretical models.

(v) To study the correlation between crystal structure, electrical conductivity and magnetic susceptibility results.

Chapter 2

EXPERIMENTAL TECHNIQUES

EXPERIMENTAL TECHNIQUES

The samples for the current investigations were prepared by solid state and nitrate routes. For heat treatments during the material preparations, the indigenously fabricated and also commercial furnaces were used. The details about the design and fabrication of these furnaces are discussed in this chapter. The prepared materials were characterized by using X-ray diffraction to check their phase purity, chemical titration to determine average 'Mn' valency, optical micrographs & scanning electron micrographs to study the microstructure and energy dispersive X-ray analysis for determining sample composition. The electrical transport and magnetic properties were studied by carrying out temperature variation of electrical resistivity, magneto-resistivity and ac susceptibility measurements down to 20K. The ac susceptibility set-up by employing mutual induction bridge method was designed and fabricated and these details along with theoretical background are covered extensively in this chapter.

2.1. Sample Preparation

The samples were prepared from the following starting compounds and elements, such as, Lanthanum Oxide (La_2O_3, 99.9%), Calcium Carbonate ($CaCO_3$, 99.5%), Barium Carbonate ($BaCO_3$, 99%), Strontium Carbonate ($SrCO_3$, 99%), Silver Nitrate ($AgNO_3$, 99.9%), Copper Acetate ($(CH_3COO)_2Cu.H_2O$, 99%), Manganese Acetate ($C_4H_6MnO_4.4H_2O$, 99.5%), Manganese Chloride ($MnCl_2.4H_2O$, 99%) Copper metal (Cu, 99%) and Manganese metal (Mn, 99.9%).

The stoichiometric ratio of starting compounds and/or elements were weighed using an electronic balance supplied by Adair Dutt model no. ADN-200W with an accuracy of ±0.05mg. The weighed compounds were ground under the medium of acetone (99%) using an agate mortar and pestle. The homogeneous mixture of starting compounds was transferred to an alumina crucible and was presintered in the temperature range 800 to 900^0C for over 24hrs followed by furnace cooling to room temperature. The presintered powder was grinded again to get a homogeneous mixture. The presintering was repeated twice. The presintered powder was pressed into cylindrical shape pellets by using a 13mm die and a hydraulic press supplied by Techno Search instruments with a maximum load of 6 Ton/cm^2. The sintering in pellet form was carried out in a step by step process in air at different temperatures with several intermediate grindings and repelletizing. The final

sintering temperatures were different for different series of the samples and these details are discussed in chapters 3, 4 and 5 for respective series of materials.

In nitrate route, the stoichiometric ratio of starting materials were weighed and transferred into separate 250ml Borosil beakers. The starting compounds in the form of oxides, carbonates and metals were dissolved in nitric acid (HNO_3) and required quantity of distilled water was also added to completely dissolve the nitrates. The starting compounds in form of nitrates & acetates were dissolved in distilled water. The nitrate solutions of all compounds were mixed together in a single beaker so that one can get homogeneous mixture. The mixed solution was heated by using a hot plate to evaporate the excess acid and distilled water such that the semi-solid nitrate is obtained. This semi-solid nitrate mixture was heated at 200^0C for 4 hours using a rectangular muffle furnace. Then the temperature was raised to 400^0C and kept for about 4 hours. The resultant dry powder was ground and presintered at 800^0C for over 24 hours. The details about duration and temperature of annealing in pellet form are discussed in chapter 4 for $La_{1-x}Cu_xMnO_3$.

2.2. High Temperature Furnaces

Two furnaces were designed and fabricated, one with maximum operating temperature of 1000^0C and the other with 1200^0C. Other than these two indigenously assembled furnaces, a commercial high temperature furnace with maximum operating temperature of 1400^0C was used for sintering the samples.

A rectangular ceramic muffle of size 10×10×30cm (inner size) was used to fabricate the 1000^0C capacity furnace. The thickness of the muffle was 0.5cm. The block diagram of the furnace is shown in Fig. 2.1. High temperature Kanthal wire was used as heating element. The Kanthal wire (18SWG, 1.22mm diameter) of about 16 meter length was wound over the ceramic muffle. The resistance of the Kanthal wire at room temperature was 34Ω. It was covered with 1 inch width concrete and kept in a drum (diameter = 50cm, length = 55cm) made up of galvanized sheet. High temperature ceramic bricks and ceramic wools were used as thermal insulation. The Chromel-Alumel (Cr-Al) thermocouple and on/off type temperature controller was used for temperature measurement and controlling. The input power to the furnace was regulated using a variac (dimmerstat) of 15A capacity. An external 15A capacity on/off relay was used for controlling the power supply to the heater wire. The relay was triggered using the temperature controller.

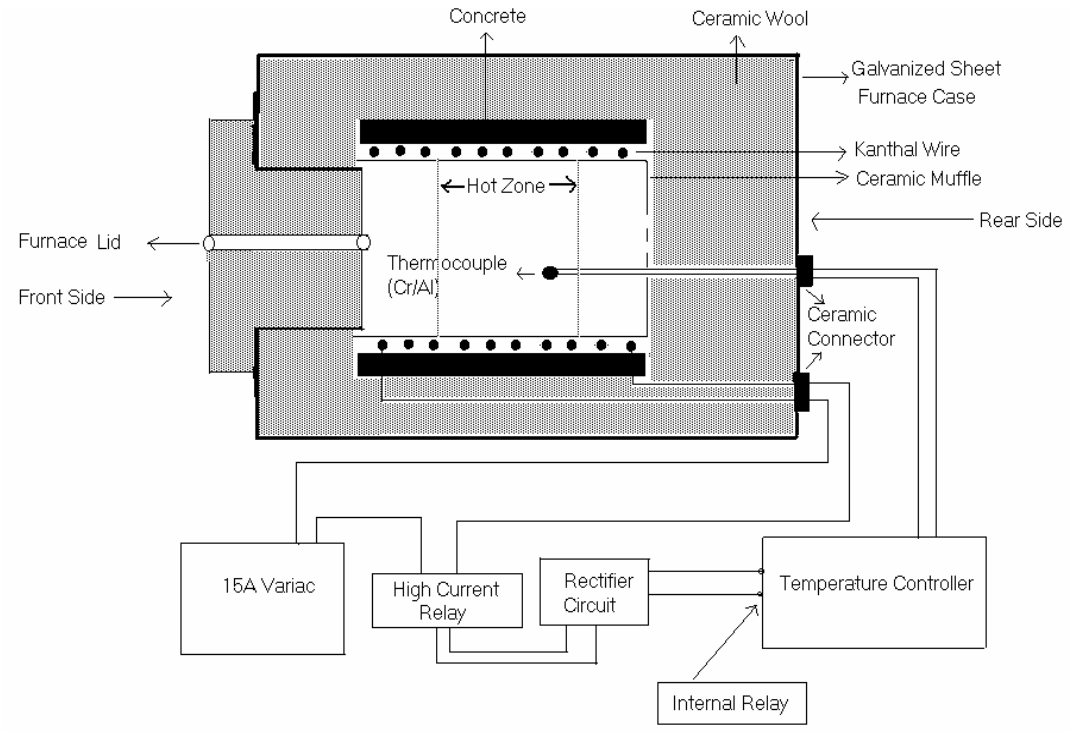

Fig. 2.1: Block diagram of the furnace with maximum operating temperature of 1000^0C.

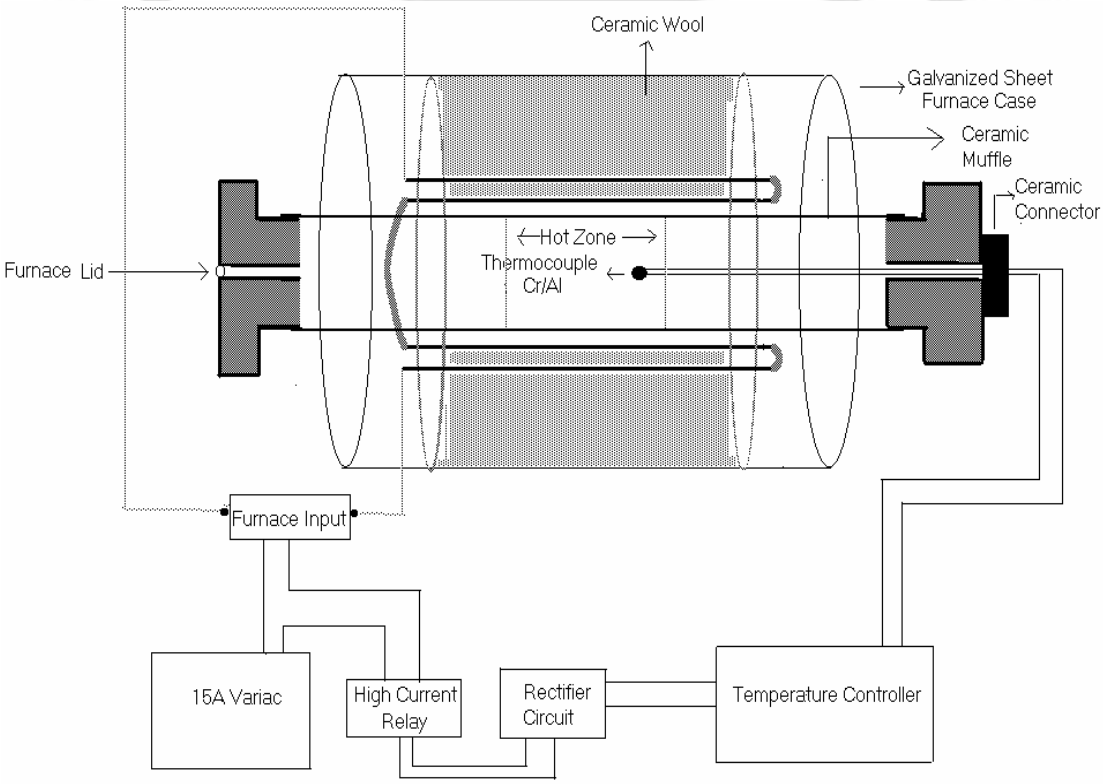

Fig. 2.2: Block diagram of the furnace with maximum operating temperature of 1200^0C.

The furnace with 1200^0C capacity was fabricated using a cylindrical alumina muffle with an inner diameter of 5.8cm and 50cm length. Four silicon carbide rods (length 45cm) were used as heating element. The block diagram of the furnace is shown in Fig. 2.2 along with the external on-off relay circuit.

2.3. X-ray Diffraction

The X- ray diffraction technique has been used to study the phase purity and crystal structure of the prepared compounds. Powder X-ray diffraction (XRD) measurements were carried out at room temperature using a commercial X-ray diffractometer supplied by Seifert (model no. 3003TT) by employing CuK_α radiation (1.5418Å). In the present investigation, all the XRD data were collected with the setting of 30mA current and 40kV voltage for X-ray generator. The instrument is based on the Bragg-Brentano geometry as shown in Fig. 2.3. In this geometry, the source to sample distance and the sample to detector distance are kept equal. A perspex sheet with rectangular groove was used for sample mount where the powder sample was filled uniformly in the groove. The data were collected in an usual θ-θ scan with an angular speed $1\text{-}2^0$/minute and a step size of $0.01\text{-}0.05^0$.

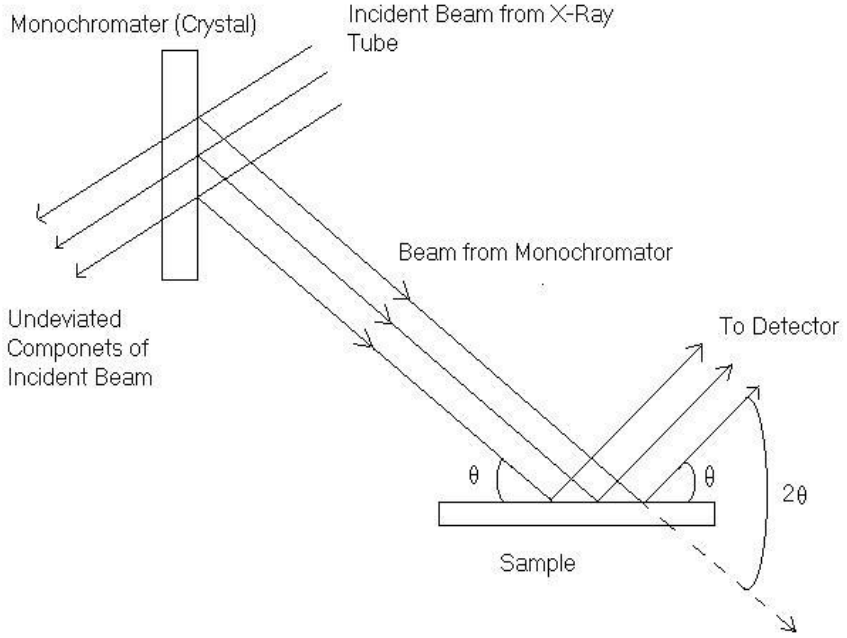

Fig. 2.3: Ray diagram of X- ray diffractometer.

The obtained XRD patterns were analyzed by employing the Rietveld profile refinement [191] with the help of Fullprof program to determine the crystal structure parameters. The lattice parameters, occupancy, atomic positions, scale factor, half-width parameters etc. were varied at the time of refinement.

Inter atomic distances (bond length) and bond angles were calculated using the refined fractional coordinates and lattice parameters as follows. Let us consider two position vectors A (x_1,y_1,z_1) and B(x_2,y_2,z_2), referred to the same base system consisting of three non-coplanar vectors r_1, r_2 and r_3, and they can be written as,

$$A \cdot B = \left(x_1 r_1 + y_1 r_2 + z_1 r_3\right) \cdot \left(x_2 r_1 + y_2 r_2 + z_2 r_3\right) \quad \text{---------} \quad (2.1)$$

Equation 2.1 can be written as,

$$A \cdot B = \begin{bmatrix} x_1 & y_1 & z_1 \end{bmatrix} \begin{bmatrix} r_1 \cdot r_1 & r_1 \cdot r_2 & r_1 \cdot r_3 \\ r_2 \cdot r_1 & r_2 \cdot r_2 & r_2 \cdot r_3 \\ r_3 \cdot r_1 & r_3 \cdot r_2 & r_3 \cdot r_3 \end{bmatrix} \begin{bmatrix} x_2 \\ y_2 \\ z_2 \end{bmatrix} \quad \text{---------} \quad (2.2)$$

The above equation can be written in simple form as,

$$A \cdot B = A' G B \quad \text{----------} \quad (2.3)$$

Here A' is a transpose matrix of A, and G is a matrix tensor. The elements $g_{ij} = r_i \cdot r_j$ are the scalar product of the base vectors. Let us assume that A = B, so that the equation 2.3 will be,

$$A \cdot A = |A| \cdot |A| = A' G A \quad \text{----------} \quad (2.4)$$

$$\Rightarrow |A| = \sqrt{A' G A} \quad \text{----------} \quad (2.5)$$

The scalar product of two vectors can be written as,

$$A \cdot B = |A||B|\cos(\theta) \quad \text{----------} \quad (2.6)$$

where, θ is the angle between the vectors A and B. Using eqns. 2.5 and 2.6, we can get,

$$\cos(\theta) = \frac{A' G B}{\sqrt{A' G A} \cdot \sqrt{B' G B}} \quad \text{----------} \quad (2.7)$$

Eqns. 2.5 and 2.7 are generally used to obtain the vector lengths and the angles between the vectors. In crystallography, the vectors r_1, r_2, r_3 can be replaced by lattice parameters a,

b & c (translation vectors). The inter atomic bond length, 'd' can be obtained using the following matrix product,

$$d^2 = \begin{bmatrix} \Delta x & \Delta y & \Delta z \end{bmatrix} \begin{bmatrix} a\cdot a & a\cdot b & a\cdot c \\ b\cdot a & b\cdot b & b\cdot c \\ c\cdot a & c\cdot b & c\cdot c \end{bmatrix} \begin{bmatrix} \Delta x \\ \Delta y \\ \Delta z \end{bmatrix} \quad \text{----------} \quad (2.8)$$

Here x, y, z and x+Δx, y+Δy and z+Δz are the positions of two atoms forming the bonds in fractional coordinates. For an orthorhombic system ($a \neq b \neq c$ and $\alpha = \beta = \gamma = \pi/2$), the bond length is found to be,

$$d = \sqrt{a^2\Delta x^2 + b^2\Delta y^2 + c^2\Delta z^2} \quad \text{----------} \quad (2.9)$$

Similarly for a hexagonal system ($a = b \neq c$, $\alpha = \beta = \pi/2 \neq \gamma = 2\pi/3$),

$$d = \sqrt{a^2\Delta x^2 + b^2\Delta y^2 + c^2\Delta z^2 - ab\Delta x\Delta y} \quad \text{----------} \quad (2.10)$$

Typical XRD patterns for the polycrystalline samples of $SrMnO_3$, $LaMnO_3$ and $La_{0.85}Ag_{0.15}MnO_3$ are shown in Figs. 2.4, 2.5 and 2.6 respectively along with the Rietveld fitting. The '+' signs represent experimental points and solid lines represent Rietveld refined data. The dotted lines show the difference between experimental & refined data. The observed peaks for $SrMnO_3$, $LaMnO_3$ and $La_{0.85}Ag_{0.15}MnO_3$ samples can be indexed to $P6_3$, *Pbnm* and $R\bar{3}c$ space groups respectively. The input files for Rietveld analysis (PCR file) are given in Appendix A for the above samples. The typical values of reliability factors R_p, $R_{\omega p}$, R_{exp}, R_{Bragg}, R_F and χ^2 are respectively 11.6, 15.2, 10.3, 16.0, 13.6 and 1.83 for the sample $SrMnO_3$.

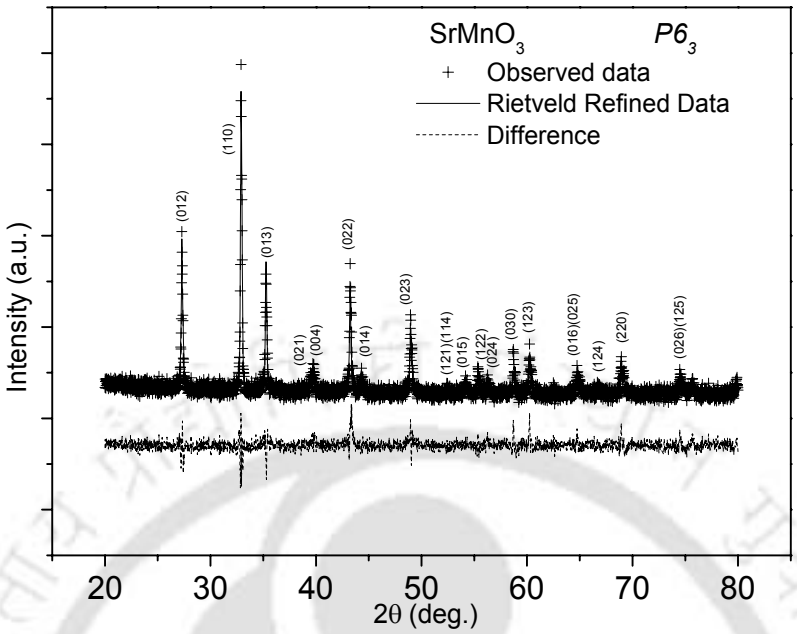

Fig. 2.4: XRD pattern for the sample $SrMnO_3$. The '+' signs represent experimental points and solid line represents Rietveld refined data. The dotted lines show the difference between experimental & refined data.

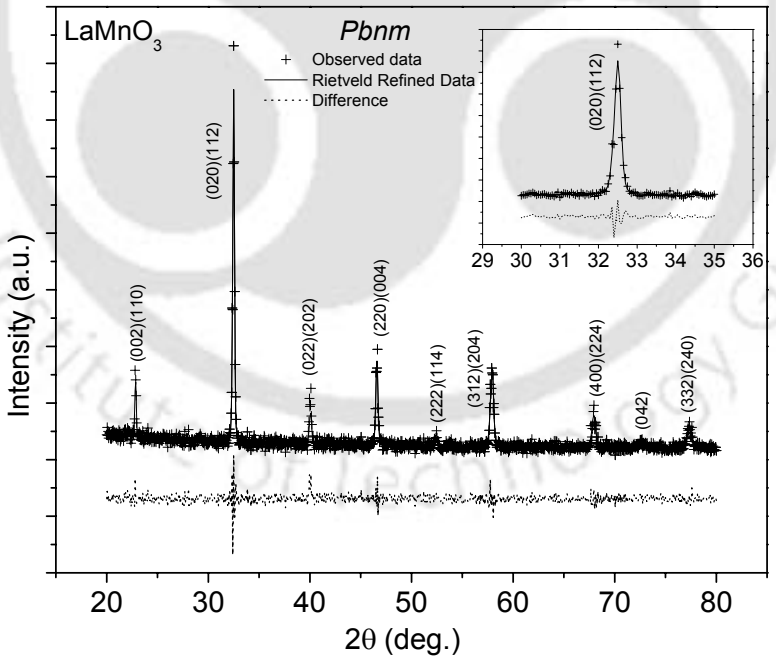

Fig. 2.5: XRD pattern for the sample $LaMnO_3$. The '+' signs represent experimental points and solid line represents Rietveld refined data. The dotted lines show the difference between experimental & refined data. The inset shows expanded view of (020) (112) peaks.

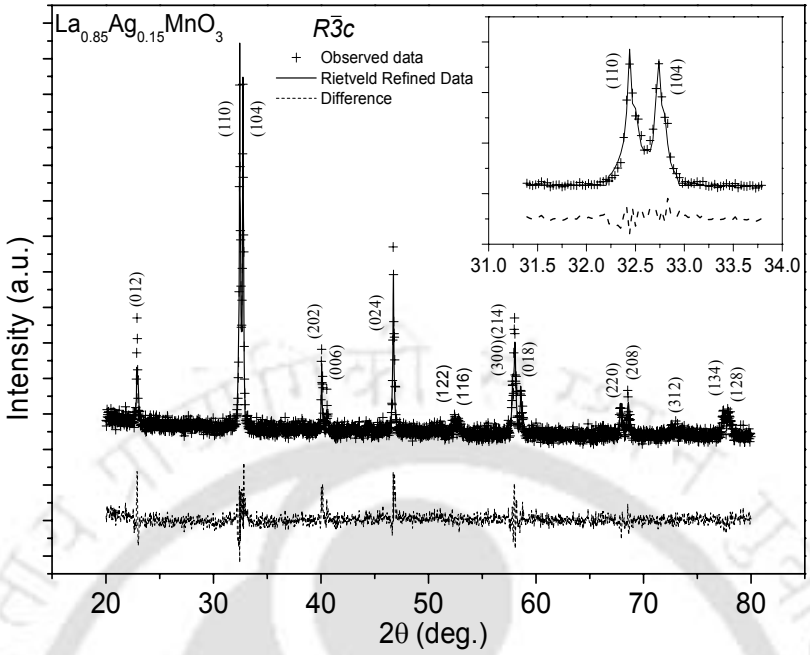

Fig. 2.6: XRD pattern for the sample $La_{0.85}Ag_{0.15}MnO_3$. The '+' signs represent experimental points and solid line represents Rietveld refined data. The dotted lines show the difference between experimental & refined data. The inset shows expanded view of splitting of (110) & (104) peaks.

The average particle size (S_G) has been calculated from the peak broadening by using the Scherrer's formula [192]

$$S_G = \kappa\lambda / \beta\cos\theta \qquad \text{----------} \qquad (2.11)$$

where, constant 'κ' depends upon the shape of the particle(grain) size. Here it is taken as 0.89 by assuming the circular shape of particle, β = Full Width at Half Maximum (FWHM) of intensity versus 2θ profile, 'λ' is wavelength of the CuK_α radiation and 'θ' is the Bragg's diffraction angle.

2.4: Chemical Titration

The oxidation state of 'Mn' was determined by a chemical titration method, in which the samples were dissolved in dilute sulphuric and phosphoric acids with an addition of excess amount of Mohr salt, $Fe(NH_4)_2(SO_4)_2.6H_2O$ and were titrated against self-indicating potassium permanganate, $KMnO_4$ solution [193, 194]. Here, the valency of 'Fe' and 'Mn' are +2 and +7 respectively. During titration Fe^{2+} is oxidized to Fe^{3+} and Mn^{7+} is reduced to Mn^{2+}. The reaction is as follows,

$$MnO_4^- + 8H^+ + 5Fe^{2+} \rightarrow Mn^{2+} + 5Fe^{3+} + 4H_2O \quad \text{----------} \quad (2.12)$$

$$Mn^{7+} + 5e \rightarrow Mn^{2+}$$

$$5Fe^{2+} - 5e \rightarrow 5Fe^{3+}$$

$$Mn^{7+} + 5Fe^{2+} \rightarrow Mn^{2+} + 5Fe^{3+} \quad \text{----------} \quad (2.13)$$

The normality of Mohr salt and $KMnO_4$ was kept constant during the titration. The normality (N) for any solution is defined as,

N = M × number of reduced valency or oxidized valency ---------- (2.14)

Here 'M' is the molarity of the solution. The molarity of a solution is '1' when the solution is prepared by adding amount of molecular weight of the sample in 1000ml of water. To prepare 250ml solution of 'y' molar concentration, one has to add 'z_1' gm (z_1 = molecular wt. × 250 ×y/1000) of material into 250ml of water.

Generally, fresh solutions were prepared to perform the titrations. Molecular weight of Mohr salt and $KMnO_4$ are 392.13gm and 158.04gm respectively. In a 250ml volumetric flask, z_1 = 49.016gm (1/8 of the molecular weight) of Mohr salt was taken and deionized water was added up to the mark on the volumetric flask. It was shaken thoroughly at the time of adding water and it leads to a molarity of 0.5M (0.5N). Similarly, in another 250ml volumetric flask, z_1 = 3.95gm (1/40 of the molecular weight) of $KMnO_4$ was taken alongwith added deionized water up to the mark of the volumetric flask. It leads to a molarity of 0.1M (0.5N). So, the normality of the above two solutions was equal. 20ml of Mohr salt solution was taken in a conical flask with the help of a 20ml pipette. 2ml of dilute phosphoric (H_3PO_4) and 2ml of dilute sulphuric (H_2SO_4) acids were added to it. $KMnO_4$ solution was taken in a burette and was titrated against Mohr salt solution and, was shaken at the time of adding. At the end point, faint pink colour of Mohr salt solution was turned into a straw colour i.e. all iron was oxidized. The quantity of $KMnO_4$ solution added was determined from the initial and final burette readings. Titration was repeated two times, and the average value has been taken for finding the equivalence of $KMnO_4$ solution (say 'u_1' ml) for 20ml of Mohr salt solution. Let 'u_2' ml of $KMnO_4$ solution is equivalent to '1' ml of Mohr salt.

To standardize the titration procedure, commercially supplied MnO_2 (Mn^{4+}) and, standard mixed valent materials $La_{0.7}Ca_{0.3}MnO_3$ and $La_{0.7}Sr_{0.3}MnO_3$ were used. For determining the valency of 'Mn' in MnO_2, a small amount of known weight of MnO_2 was

added into the 20ml of Mohr salt solution before titration. As a result of the addition of MnO_2, some of the Fe^{2+} ions are oxidized to Fe^{3+} ions. The Mohr salt solution containing MnO_2 was titrated against $KMnO_4$ solution. The consumption of $KMnO_4$ solution (say 'u_3' ml) was found to be less than the value obtained from the earlier titration, i.e. titration against pure Mohr salt solution. The difference between the equivalent Mohr salt solution (u_1) and the consumption of $KMnO_4$ solution (u_3) can be found and, this quantity of Mohr salt solution is called consumed Mohr salt solution (say 'u_4' ml). The reduced valency (R_v) of 'Mn' in MnO_2 was calculated using the formula,

$$R_v = \frac{x_1 y_2}{x_2 y_1} \quad \text{----------} \quad (2.15)$$

where, x_1 and x_2 are the atomic weight of 'Mn' and 'Fe' respectively. y_1 is the mass of 'Mn' present in the MnO_2 compound added to the Mohr salt solution in gram. y_2 is the mass of 'Fe' present in the consumed Mohr salt solution, i.e. in 'u_4' ml of Mohr salt solution. So, the actual valency can be calculated as,

$$\text{'Mn' Valency} = 2 + R_v \quad \text{----------} \quad (2.16)$$

Similar procedure was followed for $La_{0.7}Ca_{0.3}MnO_3$ and $La_{0.7}Sr_{0.3}MnO_3$ samples. The above titration results are given in Table 2.1. One can see that the values of 'Mn' valency in the above compounds are close to the expected value. The above titration method was used to determine the 'Mn' valency of all the samples studied in the thesis.

Table 2.1: Results obtained from the chemical titration for standard 'Mn' based samples.

Parameters → / Samples ↓	Wt. Of the Compound added (gm)	Initial Burette Reading	Final Burette Reading	Difference	R_v	Experimental valency	Expected valency
Bare	---	0	19.2	19.2	---	---	
Bare	---	19.2	38.4	19.2	---	---	
MnO_2	0.1258	0	13.7	13.7	1.98 ±0.01	3.98	4.00
$La_{0.7}Ca_{0.3}MnO_3$	0.0382	13.7	30.8	17.1	1.30 ±0.01	3.30	3.30
$La_{0.7}Sr_{0.3}MnO_3$	0.0963	30.8	44.7	13.9	1.28 ±0.01	3.28	3.30

2.5. Optical Microscope

Optical microscopes are instruments to produce magnified photographic images of small objects. Fig. 2.7 shows the general principle of magnification of an object using a lens.

The general view of Axiotech^{vario}100HD microscope is shown in the Fig. 2.8. Here different magnifying glasses are used to record the photograph. The image was captured by using a PC installed with the software KS300.

The samples for taking the photograph are mounted using a commercially supplied hydraulic specimen mounting press, supplied by BUEHLER (Siplimet 2). Here the transoptic powder was used to mount the sample. The view of the mounted samples on a mold is shown in Fig. 2.9.

The mold was polished using Ecomet-6 variable speed grinder and polisher. The samples were polished with Ecomet emery paper of grid size 200 and 600. After that it has been polished using METADI II diamond paste supplied by Buehler. The microscope photograph was recorded for magnifications of 20 and 100.

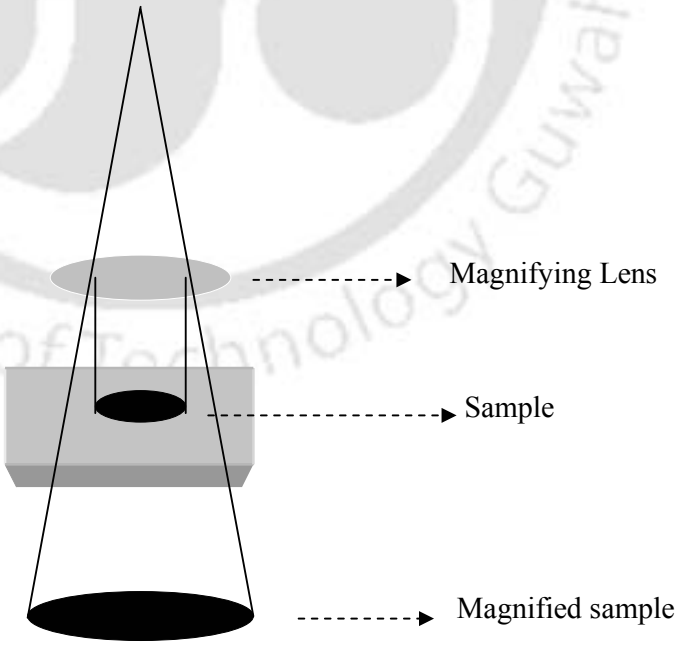

Fig. 2.7: Magnification by a thin lens.

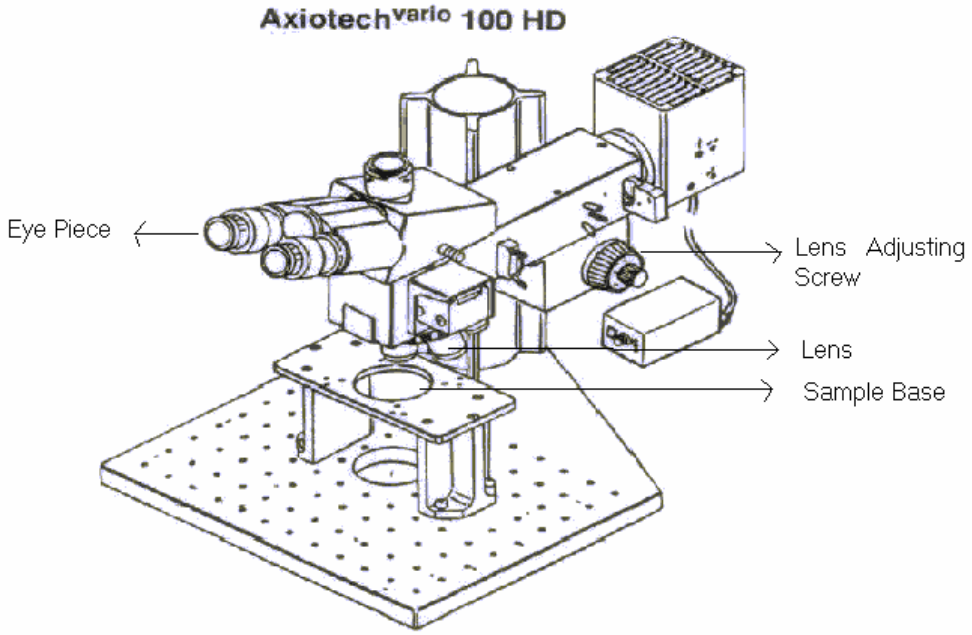

Fig. 2.8: Overall view of Axiotech^{vario}100HD optical microscope.

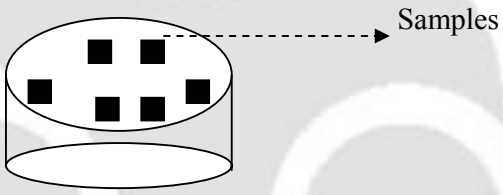

Fig. 2.9: View of samples mounted on a mold.

2.6. Scanning Electron Microscope (SEM)

The composition of bulk samples could be analyzed using a Scanning Electron Microscope (SEM) with Energy Dispersive X-ray analysis (EDAX) accessory. EDAX analysis of the composition of the sample is based on the following principle. When an electron beam strikes a solid surface, electrons and X-rays are emitted from the surface (Fig. 2.10). The X-ray photon may be absorbed by an atom resulting in the ejection of one of the bound electrons of that atom. The energy distribution of emitted X-rays and electrons are shown in Fig. 2.10 (a) and 2.10(b) respectively.

Compositional analysis was carried out on a few samples using a commercial SEM-EDAX instrument (JEOL, JSM-5800) at Central Research Facility (CRF), Indian Institute of Technology Kharagpur, Kharagpur. Both spot and overall analysis were

performed on the samples. The SEM-EDAX was operated with an acceleration potential of 20kV and each spectrum was collected for about 100s.

The SEM photograph has been taken for few selected samples to find out the average particle size. A typical SEM optical microscope photograph is shown in Fig. 2.11 for the sample $Ba_{0.5}La_{0.5}MnO_3$. The average particle size can be determined from the observed grains. For the present sample, the average particle size was found to be 3.3μm.

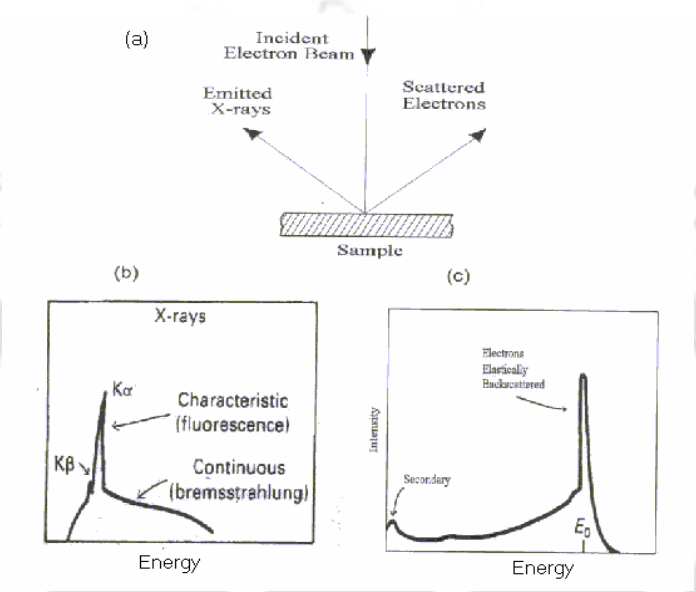

Fig. 2.10: (a) The scattering process of an electron beam in a SEM. The energy distribution of (b) X-rays and (c) electrons, after emission from the sample surface.

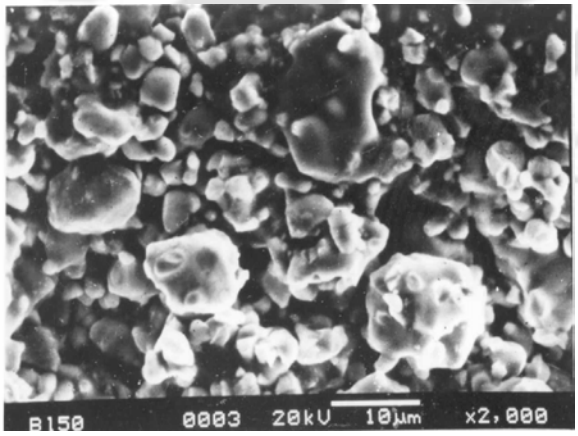

Fig. 2.11: SEM photograph of a typical manganite sample ($Ba_{0.05}La_{0.05}MnO_3$). The magnification is used 2,000. The average particle size is 3.3μm.

2.7. AC Susceptibility Set-up

AC susceptibility technique can be used for studying the magnetic properties of the materials [195-199] and it has advantage over other techniques in terms of cost and one can get additional information such as loss components, etc. The ac susceptometer with temperature variation down to 20K has been designed and developed by me and, the details are given as follows. It is basically designed by employing mutual inductance bridge method [200]. It consists of a primary coil and coaxially wound two identical secondary coils as shown in Fig. 2.12. One secondary coil is used for mounting the sample and is called sample secondary and the other one is reference coil. The primary coil is energized using a sinusoidal signal of desired frequency and voltage, $E = E_0 e^{i\omega t}$. Magnetic field, $H = H_0 e^{i\omega t}$ is generated along the axis of the solenoid (primary coil) corresponding to applied voltage in the primary. In the absence of the sample, the induced voltage in each secondary coil would be almost equal and its differential output would be close to zero. When sample is inserted into sample secondary coil, the induced emf, '*e*' is a measure of susceptibility of the material, as given in the following expression,

$$e = (\alpha n_s V_s \omega \mu_0 H_0)\chi \qquad \text{----------} \qquad (2.17)$$

where, 'n_s' is the number of turns per unit length in the secondary coil, 'ω' is the angular frequency of input signal to primary coil and 'V_s' is the volume of the sample. The filing factor coefficient, 'α' depends on the geometry of the sample and secondary coils. 'χ' is the susceptibility of the material.

The outline of the mutual inductance coil assembly is shown in Fig. 2.12. The primary coil was wound with 27SWG (diameter 0.4166mm) insulated copper wire on a nylon cylinder of inner diameter 52mm, outer diameter 58mm and length 65mm. The number of turns in the primary coil was 2187 and its resistance at room temperature was 36.6Ω. Two identical secondary coils of length 10mm each were wound with 39SWG (diameter 0.1312mm) insulated copper wire on a perspex tube of outer diameter 15mm and inner diameter 10mm.

For temperature variation down to 20K in ac susceptibility measurements, a Helium exchange gas cooled top loading closed cycle Helium refrigerator (CCR) of CTI make (model no. 22) was used. The schematic diagram of CTI cryostat is shown in Fig. 2.13. The position of mounting of primary coil is also shown.

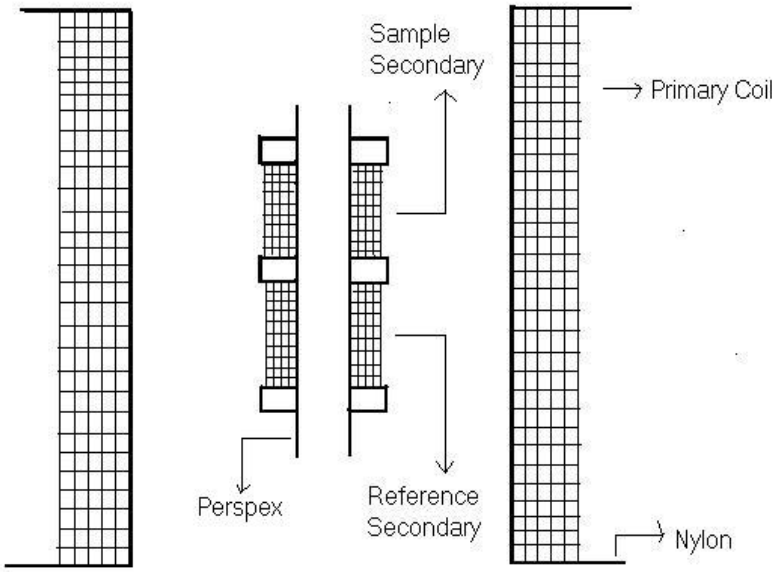

Fig. 2.12: Block diagram of primary and secondary arrangement of the three coil system.

A sample insert assembly and secondary coil loading assembly have been designed and fabricated for quick loading & unloading of samples. The schematic diagram of the sample holder is shown in Fig. 2.14. The non magnetic thin walled stainless steel (SS) tube with outer diameter 10mm and length 550mm is coupled to the sample holder made up of nylon rod of length 100mm. The bottom part of nylon rod was made into a plane surface to load the sample and temperature sensor. At the top of the SS tube one electrical feed through was mounted for electrical connections to the temperature sensor kept near the sample. Electrical feed through attached to aluminium flange was used for connecting the secondary leads. The position of sample holder can be adjusted with the help of Wilson nut arrangement. A platelet type Pt-100 sensor was mounted in the vicinity of sample position as shown in the Fig. 2.14. The Pt-100 sensor was calibrated down to 20K against the calibrated silicon diode sensor supplied by LakeShore.

The block diagram of the ac susceptibility set-up is shown in Fig. 2.15. The primary coil is connected to the oscillator output of a dual phase lock-in amplifier supplied by Perkin–Elmer, model no. 7265. The maximum oscillator output of lock-in amplifier is 5V (rms). The magnetic field was calculated using the standard relation of the solenoid,

$$H = \frac{NI}{l} \text{ (A/m)} \qquad \text{----------} \qquad (2.18)$$

or,

$$H = \frac{NI}{l} 4\pi \times 10^{-3} \text{ (Oe)} \quad \text{----------} \tag{2.19}$$

Here, 'N' is the total number of turns in the primary coil, 'I' is the amplitude of current flowing through the primary in Ampere and 'l' is the length of primary in meter. The maximum amplitude of magnetic field in the present set-up was found to be around 12Oe. The output of both the secondary coils is connected to the differential input (A-B) of the lock-in amplifier, which can measure the in-phase and out of phase components of ac susceptibility signal simultaneously. The Pt-100 sensor is connected to the 'B' channel output of the temperature controller for measuring the sample temperature. For controlling the temperature a silicon diode sensor, which follows the standard LakeShore DT-470 curve was used. This sensor was mounted at the cold tip of the CCR, where a heater wire of 50Ω resistance was also installed. Four leads of the controlling sensor are connected to the 'A' channel of the temperature controller. Both the temperature controller and the lock-in amplifier were connected to a personal computer equipped with a GPIB board for data acquisition. The necessary software in the language of Quick Basic was developed for running the temperature variation of ac susceptibility. The accuracy of temperature measurement was ±50mK.

To completely separate the real and imaginary components, appropriate reference phase angle needs to be set, in the lock-in amplifier. The phase angle 'ϕ' was obtained by adjusting the reference phase in the lock-in amplifier such that the signal of the out of phase (loss/imaginary component) component is zero above the ferromagnetic transition temperature, i.e. in the paramagnetic region. One can also numerically separate the real and imaginary components, by measuring the susceptibility in zero phase and using the following expressions [201],

$$\chi' = \chi_0' \cos\phi + \chi_0'' \sin\phi \quad \text{----------} \tag{2.20}$$

$$\chi'' = \chi_0'' \cos\phi - \chi_0' \sin\phi \quad \text{----------} \tag{2.21}$$

Where χ_0' and χ_0'' are the measured susceptibilities before phase adjustment (at zero phase).

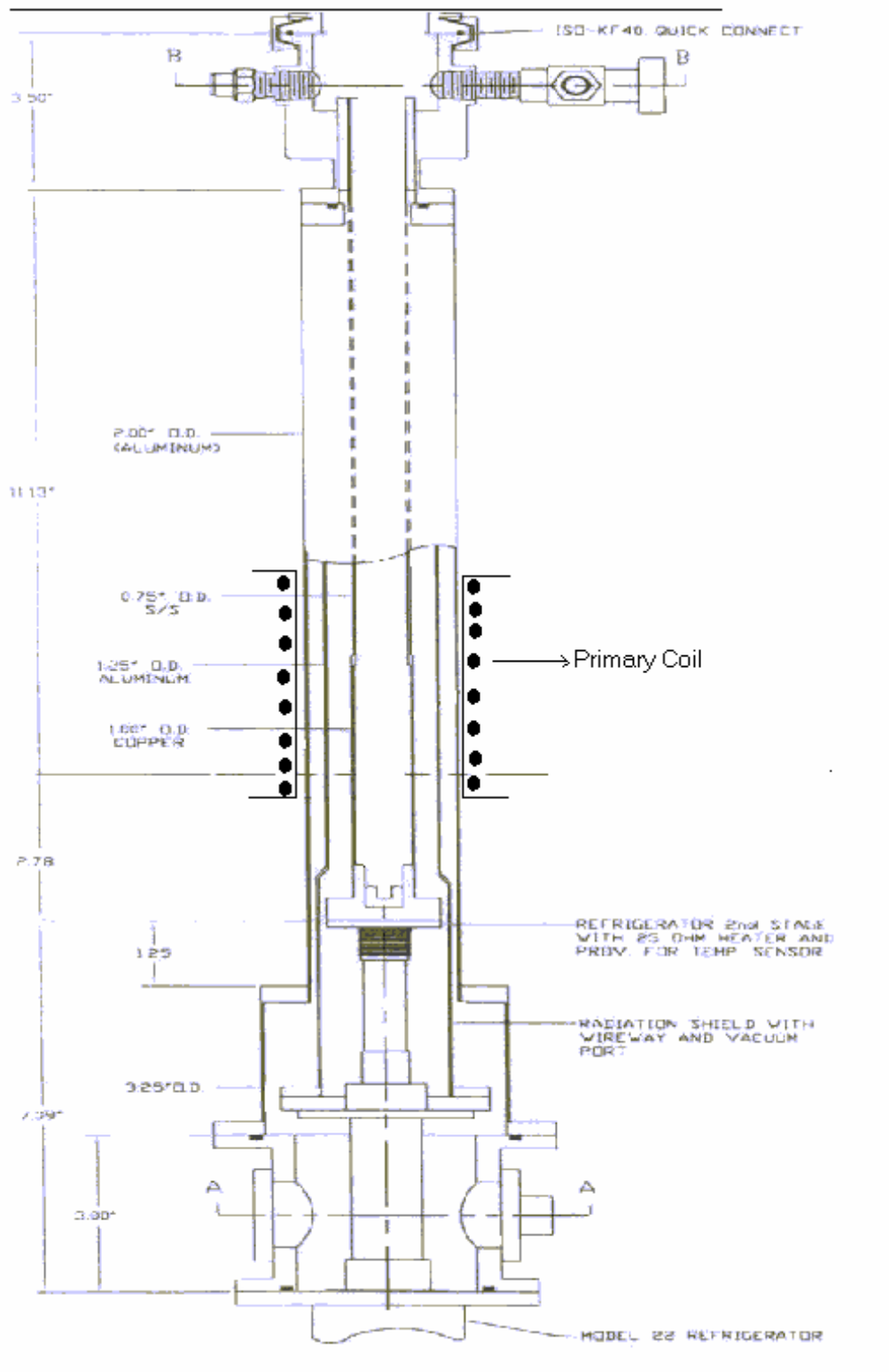

Fig. 2.13: Block diagram of CCR cryostat.

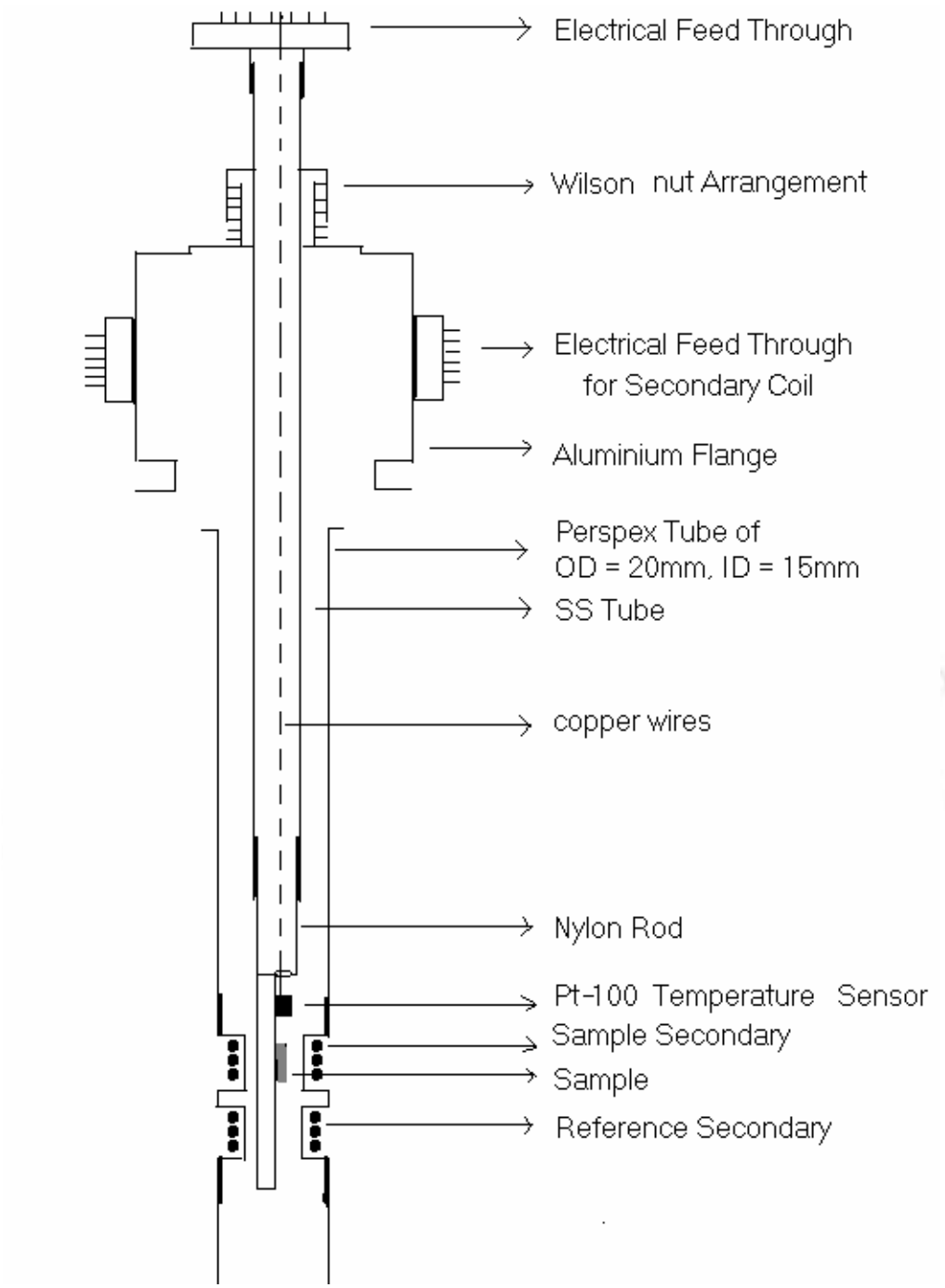

Fig. 2.14: Fabricated susceptibility sample holder attached to the CCR cryostat.

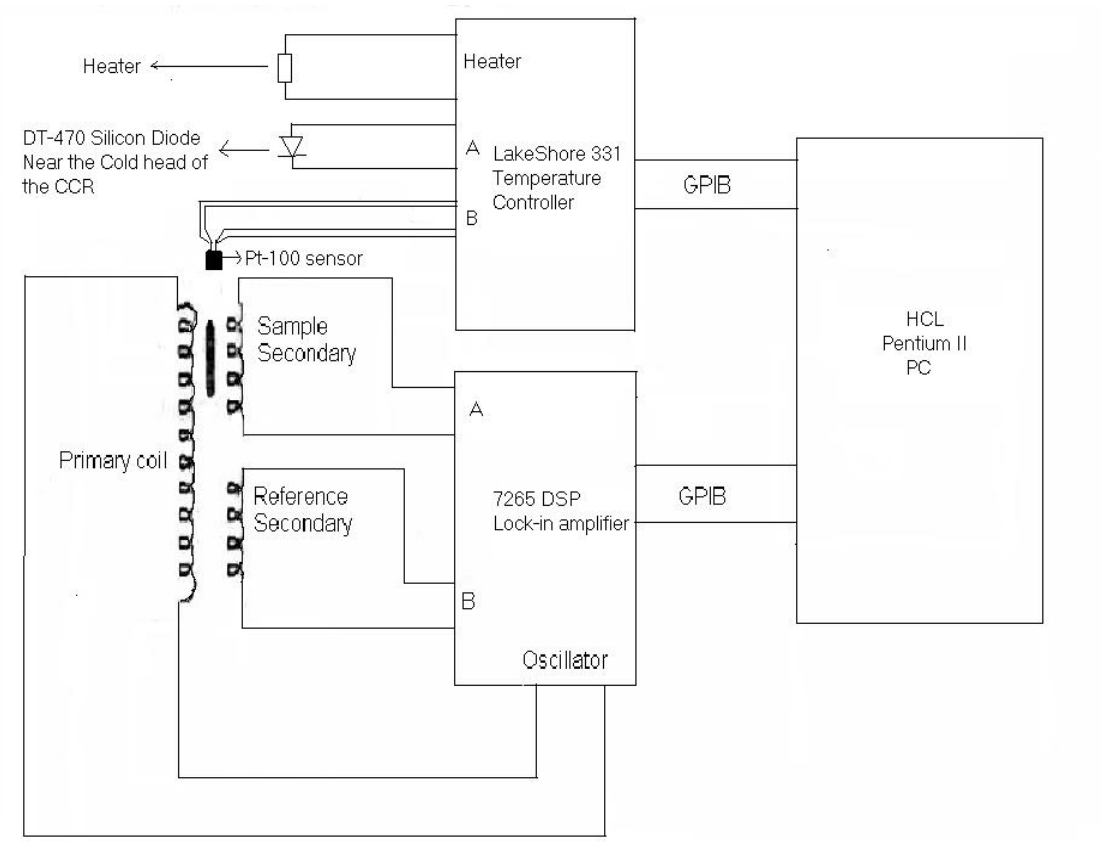

Fig. 2.15: Block diagram of ac susceptibility set-up.

Calibration of the ac susceptometer was carried out by using the standard paramagnetic salts [202]. Here Mohr salt ($Fe(NH_4)_2(SO_4)_2.6H_2O$) was taken as the standard and its temperature dependent gram susceptibility is given as, [203]

$$\chi = \frac{9500}{1+T} \times 10^{-6} \text{ c.g.s} \qquad \text{----------} \qquad (2.22)$$

Here, T is in Kelvin. The Mohr salt powder was pressed into a cylindrical pellet of ≈ 13mm diameter and 4-5mm thickness. A parallelepiped shaped sample with dimension 3.2×2.4×10mm was cut from the pressed pellet. The above piece was used for calibration. The ac loss for above paramagnetic salt was found to be zero. The temperature variation of in-phase signal, $e^{/}$ was measured and was converted into the unit of μV/gmOe and, it is shown in Fig. 2.16. The experimental data could be fitted to Curie-Weiss law, [204]

$$\chi = \frac{C}{T-\theta} \qquad \text{----------} \qquad (2.23)$$

where, 'C' is the Curie constant and 'θ' is the Curie temperature and the fit is shown in the inset of the Fig. 2.16 as solid line. The fitted parameters are -θ/C = -0.057±008 and 1/C = 0.00782±0.00007.

By comparing the above experimental data with the standard value (calculated using the eqn. 2.22), the calibration constant is determined and it is found to be 1μV/gmOe = (67.0±1.8)×10^{-6} emu/gmOe.

The above calibration constant is used for calculating the susceptibility in terms of emu/gmOe from measured signal in the unit of μV/gmOe. To confirm the validity of the above calibration constant, another two standard paramagnetic salts namely Mercury Thio Ciano Cobaltate(III) cyanide [$HgCo(SCN)_4$] [205] and copper sulphate [$CuSO_4$].5H_2O [203] were measured using the above calibration constant. The temperature variations of standard susceptibility for the $HgCo(SCN)_4$ and [$CuSO_4$].5H_2O are given as,

$HgCo(SCN)_4$, $\chi = \frac{4981}{10+T} \times 10^{-6}$ c.g.s. ---------- (2.24)

[$CuSO_4$].5H_2O, $\chi = \frac{1758}{T} \times 10^{-6}$ c.g.s. ---------- (2.25)

The temperature variations of $1/\chi'$ for $HgCo(SCN)_4$ and [$CuSO_4$].5H_2O are shown in Figs. 2.17 and 2.18 respectively. Here circles represent the measured susceptibility and solid lines represent the standard values. As can be seen from the Figs. 2.17 and 2.18, the experimental susceptibility follows the literature value. Fig. 2.19 shows the temperature variation of χ' (circles) and χ'' (solid line) for a standard CMR sample, $La_{0.7}Ca_{0.3}MnO_3$. This material shows paramagnetic to ferromagnetic transition with T_c = 254K. The Tc value and the saturation susceptibility value are comparable to those reported in the literature [206].

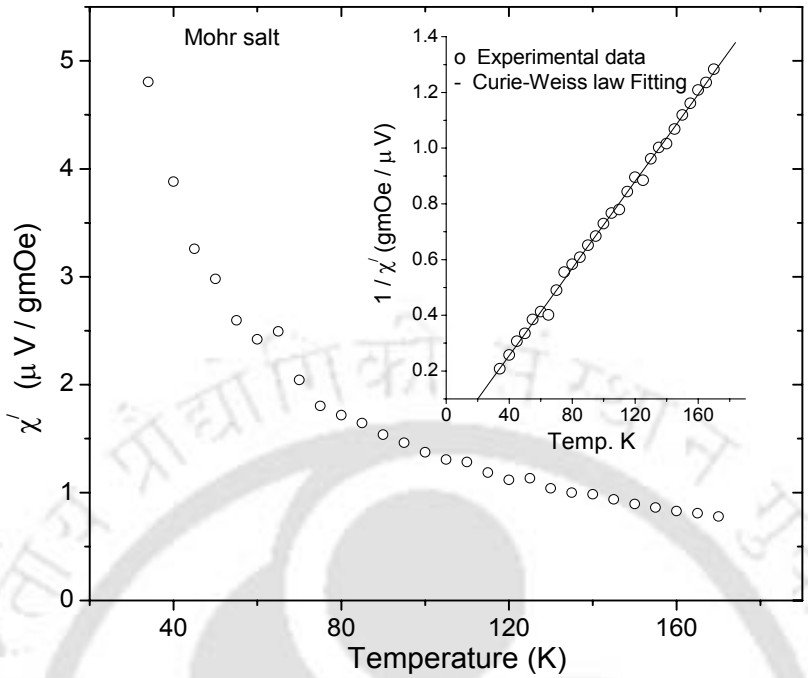

Fig. 2.16: Temperature variation of ac susceptibility (χ') in μV/gmOe for Mohr salt. Inset shows the $1/\chi'$ vs. Temperature plot. Circles represent the experimental data and solid line represents the fit to Curie-Weiss law.

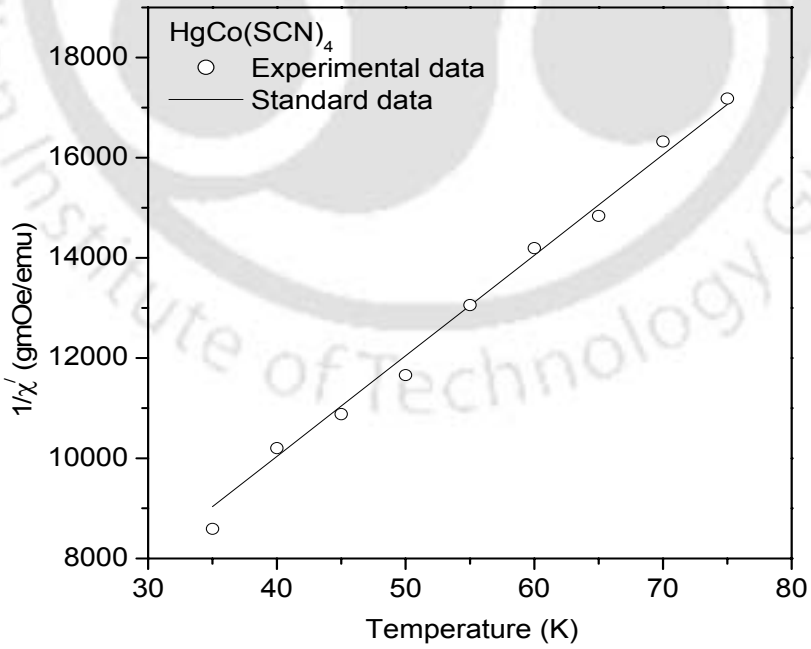

Fig. 2.17: $1/\chi'$ (gmOe/emu) versus temperature for the sample $HgCo(SCN)_4$. The solid line represents the standard literature value.

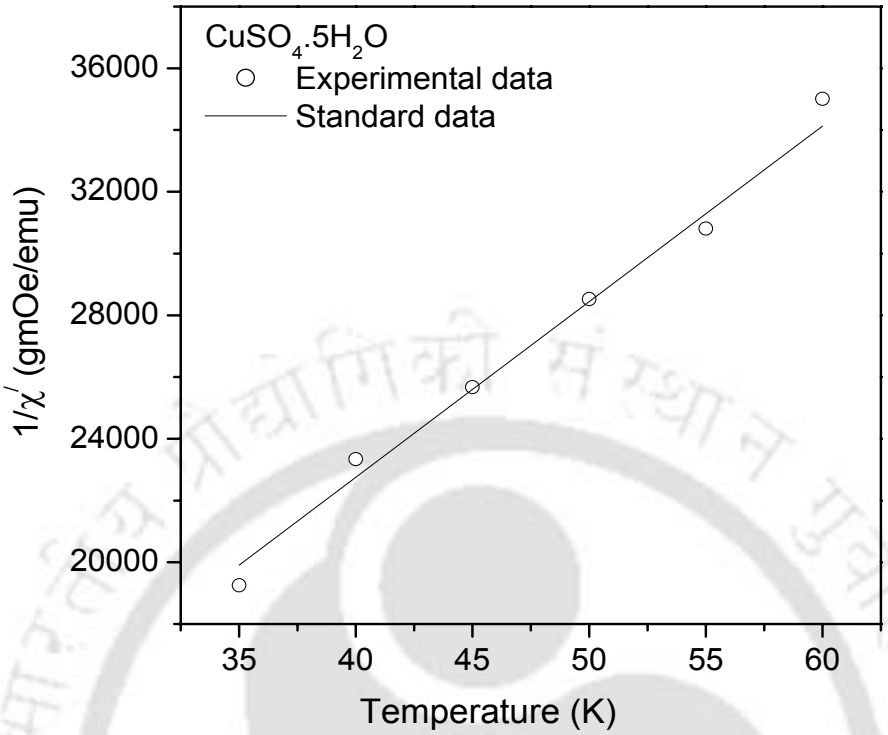

Fig. 2.18: $1/\chi'$ (gmOe/emu) versus temperature for the sample $CuSO_4.5H_2O$. The solid line represents the standard literature value.

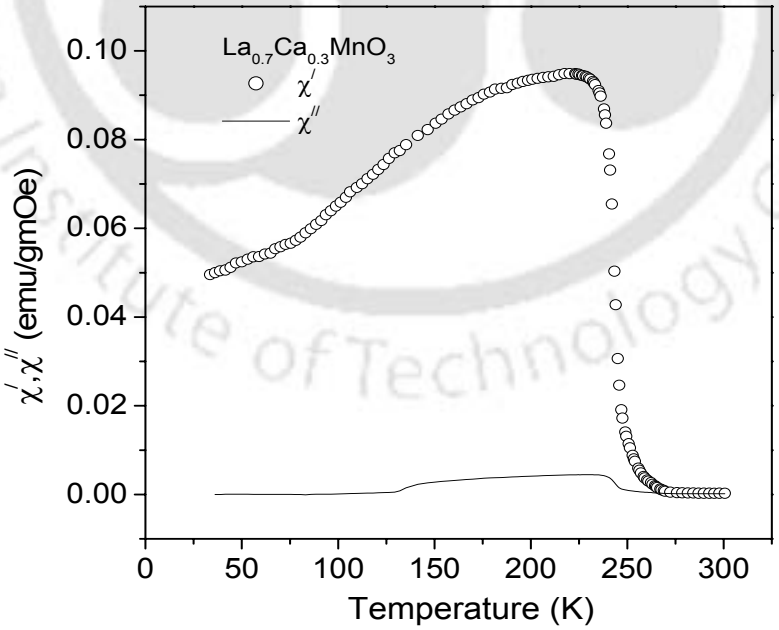

Fig. 2.19: Temperature variation of χ' (circles) and χ'' (solid line) of the sample $La_{0.7}Ca_{0.3}MnO_3$.

2.8 DC Electrical Resistivity Set-up

Temperature variation of dc electrical resistivity measurements down to 20K were carried out to study the electrical transport on manganite perovskites. The temperature variation was achieved using a commercially supplied APD make CCR. The schematic diagram of the Cryostat is shown in the Fig. 2.20. A copper sample holder (27×22×6mm) was fabricated. It was mounted on the cold tip of the cryostat to load the sample. The temperature variation was achieved by using a heater wire wound in the vicinity of the cold tip.

The top view of sample holder is shown in Fig. 2.21. The sample holder was made up of copper block of dimension 27×22×6mm. A groove of 10mm length and 3mm diameter was made in the copper block to mount the Pt-100 sensor for sample temperature measurement. The controlling sensor is Si-diode which was mounted at the cold tip, where the heater wire of 37Ω resistance is installed. To electrically insulate the sample from the copper sample holder, a thin mica sheet was used. Electrical contacts on the sample were made with the help of silver paint and/or Indium soldering. A printed circuit board (PCB) with four copper strips was mounted on the sample holder. The copper wires of 32SWG (0.2743mm) were used for electrical connection between PCB and sample. Standard linear four probe technique was used to eliminate contribution of contact resistance and lead resistance coming into picture. Current through the sample was passed using outer two leads and a programmable Keithley constant current source, model no. 224. The voltage drop across the sample was measured using Keithley nanovoltmeter, model no. 2182. To eliminate the thermo-emf generated across the voltage leads, measurements were carried out for both positive and negative current. The experimental data were collected using a personal computer equipped with GPIB card. The block diagram of the resistivity set-up is shown in Fig. 2.22. The necessary software in quick Basic language was developed for temperature controlling and data acquisition using a personal computer.

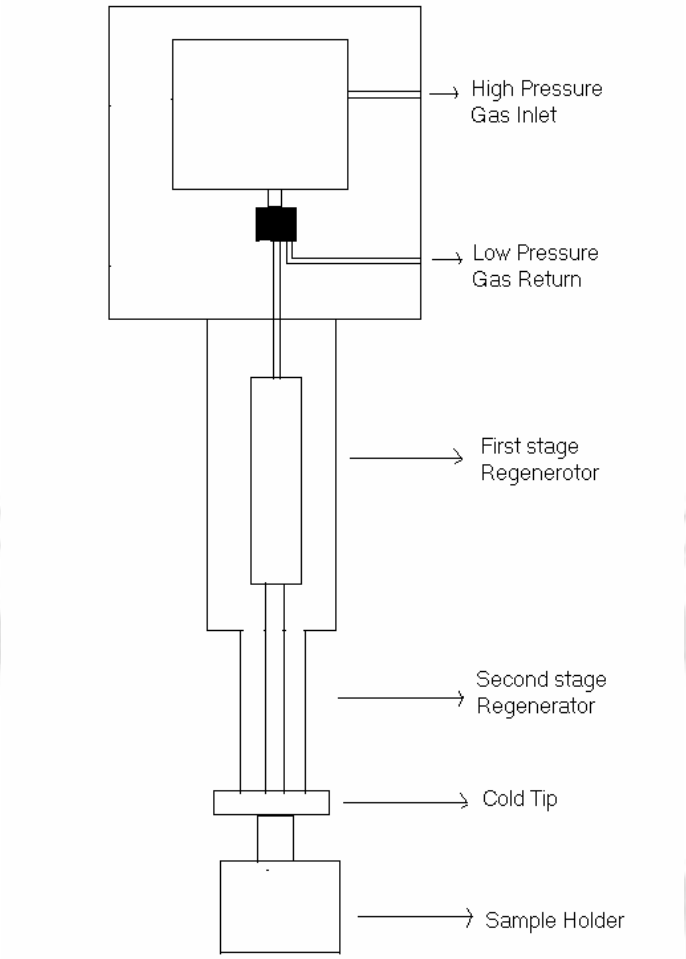

Fig. 2.20: Block diagram of APD Cryostat.

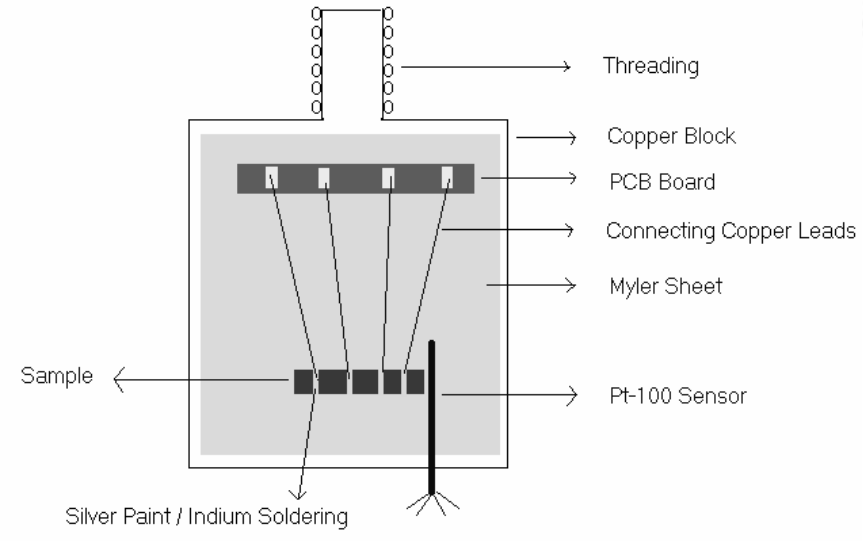

Fig. 2.21: Top view of sample holder for resistivity measurement.

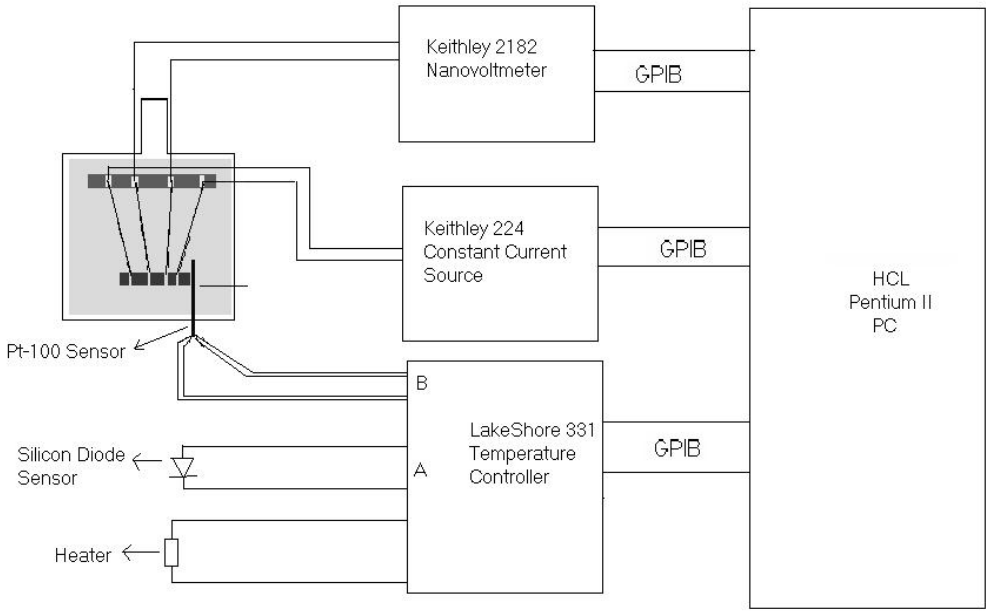

Fig. 2.22: Block diagram of electrical resistivity measurement set-up.

2.9. Magneto-Resistivity Measurement

Longitudinal Magneto-resistivity have been measured on a few samples, using the facility at "Inter University Consortium for Department of Atomic Energy Facilities, Indore, India". To generate high magnetic field at low temperature environment, a commercial superconducting magnet with power supply (Oxford, Spectromag^{2000}) was used. This system consists of a superconducting solenoid, which can produce maximum magnetic field up to 80 kOe at the center of the solenoid. Dip stick type sample holder was used to load the sample into the superconducting magnet. For temperature measurement, a calibrated Cernox temperature sensor (model no. CX-1050-SD) is fixed on the sample holder with the help of GE7031 varnish. LakeShore temperature controller (DRC-93CA) was used for measuring and controlling the temperature of the sample. At a time 16 samples can be loaded in the sample holder. So for selecting the different samples Keithley Switching System (model 7002) was used. A nanovolt scanner card (model 7168) was used for switching between the voltage leads of different samples and a general-purpose scanner card (model 7056) was used for switching between the current leads. Keithley constant current source (model 2400) and nanovoltmeter (model 182) were used for sending current through the sample and measuring voltage drop across the sample. All the instruments were connected to a HP486 PC for online data collection.

For some of the samples, I have carried out magneto-resistivity measurements in our lab, where a Walker electromagnet (model HV-10H, $10^{//}$ to $3^{//}$ tapered pole diameter.) with a maximum field strength of 15kOe for 2.5inch air gap was used. CTI (Fig. 2.13, model no 22) CCR was used for temperature variation down to 20K. The details about the magneto-resistivity measurement are given below.

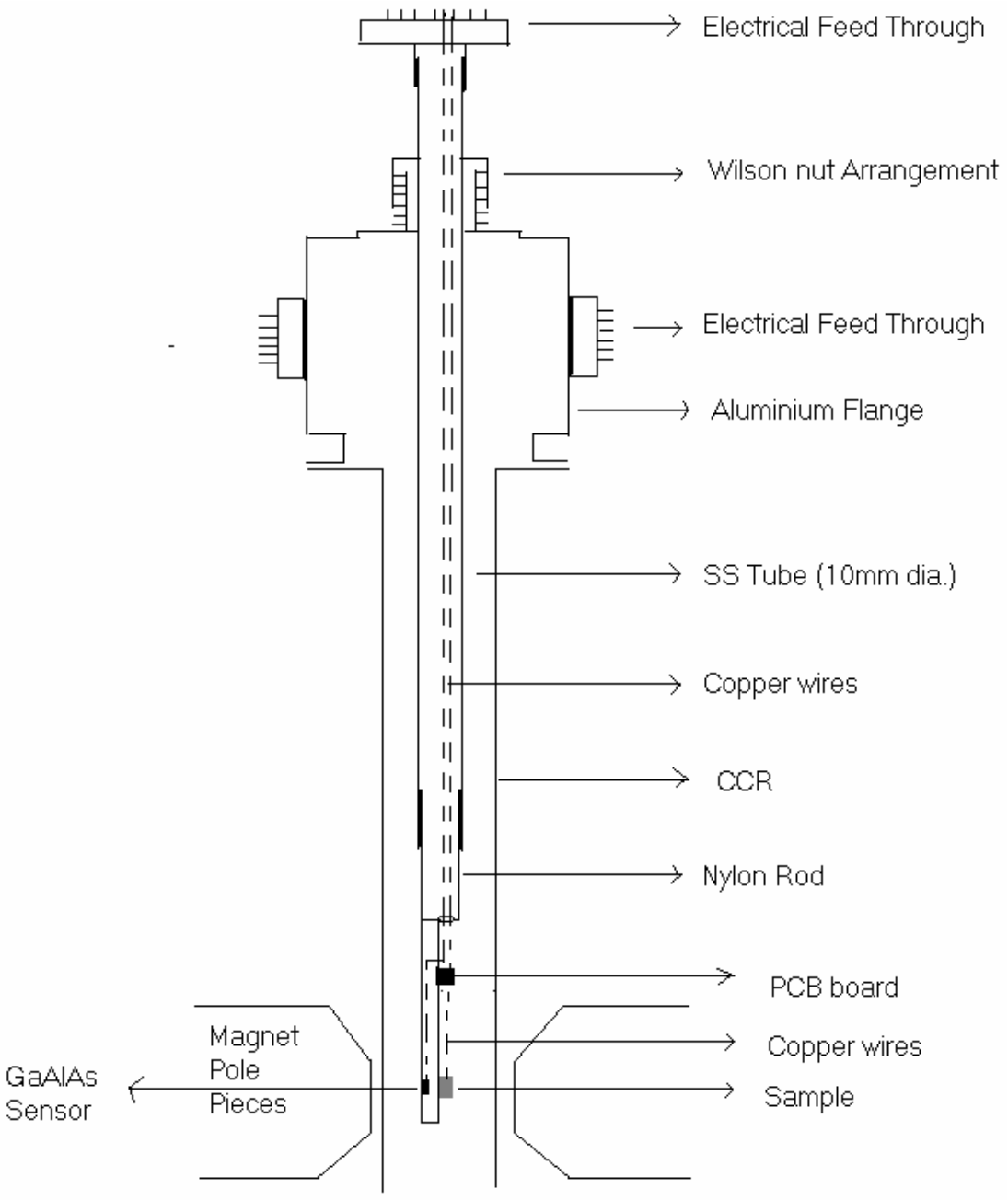

Fig. 2.23. Fabricated magneto-resistivity sample holder attached to the CCR cryostat.

A sample insert assembly has been designed and fabricated similar to that of ac susceptibility set-up for quick loading & unloading of the samples. The schematic diagram of the sample holder is shown in Fig. 2.23. Separately the sample holder is shown in Fig. 2.24. A LakeShore calibrated GaAlAs diode sensor was used for temperature measurements. The sensor is mounted just opposite side of sample position on the nylon rod as shown in Figs. 2.23 and 2.24.

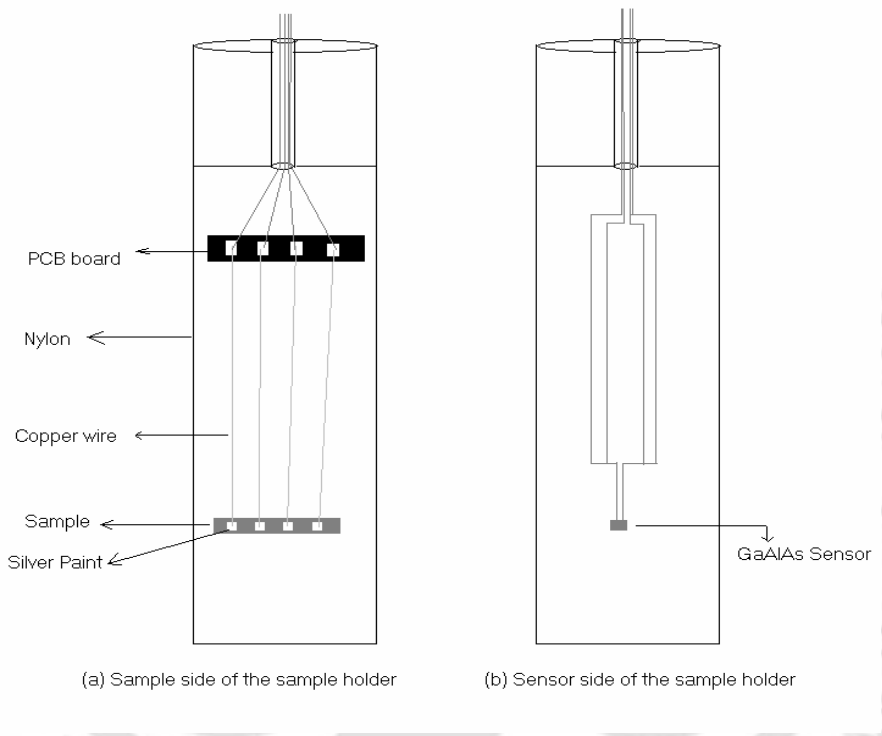

Fig. 2.24: Expanded view of magneto-resistivity sample holder. (a) Sample side of the sample holder and (b) Sensor side of the sample holder.

The details about electrical contacts on the sample, online data recording etc. are discussed in the section 2.8.

2.10. Magnetization Measurement

DC magnetization as a function of temperature on a selected few samples was measured down to 77K using the facility at Inter University consortium for Department of Atomic Energy Facilities, Indore, India.

Chapter 3

ELECTRON DOPED MATERIALS

ELECTRON DOPED MATERIALS

As discussed in the introduction, $BaMnO_3$ and $SrMnO_3$ are the electrical insulators at all temperatures with the antiferromagnetic ordering. The valency of 'Mn' is 4+ in both the materials. Partial replacement of divalent 'Ba' and 'Sr by trivalent 'La' with the chemical formula $Ba_{1-x}La_xMnO_3$ and $Sr_{1-x}La_xMnO_3$, lead to the mixture of Mn^{4+} and Mn^{3+} ions. In this process e_g electrons are created. These are basically Mn^{4+} rich compounds and they are called electron doped materials. This chapter deals with the study of crystal structure, electrical transport and magnetic properties on the above two electron doped series. For the sake of comparison, a few hole doped materials in these series were also prepared and analyzed in the light of above physical properties.

3.1. $Ba_{1-x}La_xMnO_3$ (x = 0 to 0.80) Compounds

The materials for x = 0 to 0.80 were prepared for the present work. For the range of compositions $0 < x < 0.50$, the materials are in the electron doped regime and for $0.50 < x \leq 0.80$, they are in the hole doped regime.

3.1.1. Preparation

$Ba_{1-x}La_xMnO_3$ compounds were prepared for x = 0, 0.05, 0.10, 0.15, 0.20, 0.25, 0.30, 0.40, 0.50, 0.60, 0.70 and 0.80 by conventional solid state route. Stoichiometric ratio of starting compounds such as Barium Carbonate ($BaCO_3$, 99%), Lanthanum Oxide (La_2O_3, 99.9%) and Manganese Chloride ($MnCl_2.4H_2O$, 99%) were weighed. The above compounds were mixed and grinded under acetone using agate mortar and pestle. The mixture was presintered at 800^0C for 25 hours with intermittent grindings at room temperature. The sintering in pellet form was carried out at 900^0C for 10hours, 1000^0C for 10 hours and 1100^0C for 20 hours. The pellets were crushed and grinded into a fine powder and repelletized after annealing at each temperature. The final sintering in pellet form was performed at 1200^0C for 35 hours. All the above heat treatments were carried out in air and the samples were furnace cooled after final sintering.

3.1.2. Characterization

X-ray diffraction (XRD) patterns recorded at room temperature are shown in Fig. 3.1 for the samples x = 0, 0.15, 0.20, 0.25, 0.30, 0.40 and 0.50. The XRD pattern of the parent compound (x = 0), $BaMnO_3$ is found to be in single phase form. It could be indexed to hexagonal symmetry with the space group of $P6_3mc$. The lattice parameters are found to be a = b = 5.664Å and c = 4.786Å and they are comparable to those reported by Hardy [207]. The samples in the composition range x = 0.05 to 0.15 are found to be in mixed phase form with hexagonal and orthorhombic symmetry phases, where the former corresponds to parent compound. The typical XRD is shown for x = 0.15. For x ≥ 0.20, the materials are found to be essentially in single phase form as can be seen from Fig. 3.1. For x = 0.20 - 0.30, they could be indexed to orthorhombic cell with *Pbnm* space group. The patterns for x = 0.40 and 0.50 could be indexed to rhombohedral cell with $R\bar{3}c$ space group. Generally these electron doped materials are difficult to prepare in single phase form and most of the time they form as mixed phase with parent compound as impurity [78, 208]. However, by following the present preparation technique, I have shown that the electron doped materials (for x ≥ 0.20) can be prepared in single phase form. The impurity due to parent compound is not observed, which can be seen by comparing the XRD pattern of x = 0 sample with that of electron doped materials (x ≥ 0.20).

XRD patterns of hole doped materials, i.e. for x = 0.60, 0.70 and 0.80 are shown in Fig. 3.2. It is found that the samples are essentially in single phase form. All the observed peaks could be indexed to rhombohedral symmetry with $R\bar{3}c$ space group. Thus the 'La' doped materials, $Ba_{1-x}La_xMnO_3$ exhibit a structural change from orthorhombic to rhombohedral symmetry with increase in doping. Such structural transitions are widely observed in these types of materials [209, 210].

The XRD patterns were analyzed using Rietveld refinement with the help of Fullprof program [191]. The background was refined using a polynomial function. Pseudo-Voigt function was chosen for peak shape. The global parameters, such as coefficients of background polynomial, scaling factor, half width parameters (u, v, w) and lattice parameters (a, b, c) were mainly varied during the refinement. In addition to that nuclear structure variables such as fractional atomic co-ordinates (x, y, z), isotropic displacement (temperature) parameters and occupancy values were varied. Here, occupancy is the chemical occupancy normalized to the multiplicity of the general

position of the group. The occupancy of oxygen was taken as '1' for all the refinements and it was not varied during the refinement. The quality of the refinements are known based on the values of reliability factors such as, R_p, R_{wp}, R_{exp}, R_{Bragg}, R_F and χ^2 and they are defined as follows.

$$\text{Profile factor, } R_p = 100\frac{\sum_{i=1,n}\left|y_i - y_{c,i}\right|}{\sum_{i=1,n} y_i} \quad \text{----------} \quad (3.1)$$

Here 'y_i' is the observed point (experimental) and '$y_{c,i}$' is the calculated point and n represents the number of data points.

$$\text{Weighted profile factor, } R_{wp} = 100\left[\frac{\sum_{i=1,n}\omega_i\left|y_i - y_{c,i}\right|^2}{\sum_{i=1,n}\omega_i y_i^2}\right]^{1/2} \quad \text{---------} \quad (3.2)$$

Here $\omega_i = \frac{1}{\sigma_i^2}$, σ_i^2 is the variance of observation y_i.

$$\text{Expected weight factor, } R_{\exp} = 100\left[\frac{n-p}{\sum_{i=1,n}\omega_i y_i^2}\right]^{1/2} \quad \text{--------} \quad (3.3)$$

Here (n – p) is the number of degrees of freedom. 'n' is the total number of experimental points and 'p' is the number of refined parameters.

$$\text{Reduced chi-square, } \chi^2 = \left[\frac{R_{wp}}{R_{\exp}}\right]^2 \quad \text{----------} \quad (3.4)$$

$$\text{Bragg factor, } R_B = 100\frac{\sum_{h}\left|I_{obs,h} - I_{calc,h}\right|}{\sum_{h} I_{obs,h}} \quad \text{----------} \quad (3.5)$$

Here 'h' is the vector which levels the Bragg reflections. The $I_{obs,h}$ is the observed integrated intensities and $I_{calc,h}$ is the calculated intensities.

$$\text{Crystallographic } R_F \text{ factor, } R_F = 100\frac{\sum_{h}\left|F_{obs,h} - F_{calc,h}\right|}{\sum_{h} F_{obs,h}} \quad \text{----------} \quad (3.6)$$

Here $F_{obs,h}$ and $F_{calc,h}$ are the observed and calculated structural factors respectively.

The typical refinement of XRD pattern for x = 0.30 sample is shown in Fig.3.3. Here the experimental data are shown as crosses (+) and the calculated intensities are

shown as solid line. The dotted lines represent the difference between experimental and calculated intensities. We can see that the experimental intensity closely follow the calculated intensity for *Pbnm* space group. The typical lattice parameters for this sample are found to be a = 5.470Å, b = 5.521Å and c = 7.763Å. The typical values of atomic positions, isotropic displacement (temperature) parameters and occupancy values for different elements and reliability factors are tabulated in Table 3.1 for the sample x = 0.30.

Similarly the XRD patterns of samples with x ≥ 0.40 could be refined using $R\bar{3}c$ space group and the typical pattern along with refinement are shown in Fig. 3.4 for x = 0.50 sample. The inset shows the expanded view of splitting of (110) and (104) peaks. The refined data mostly follow the experimental pattern. The typical values of atomic positions, isotropic displacement (temperature) parameters and occupancy for different elements etc. are shown in Table 3.2 for the sample x = 0.50. The Rietveld refinement of one of the hole doped materials, i.e. for x = 0.70 is also shown in Fig. 3.5 along with experimental intensity.

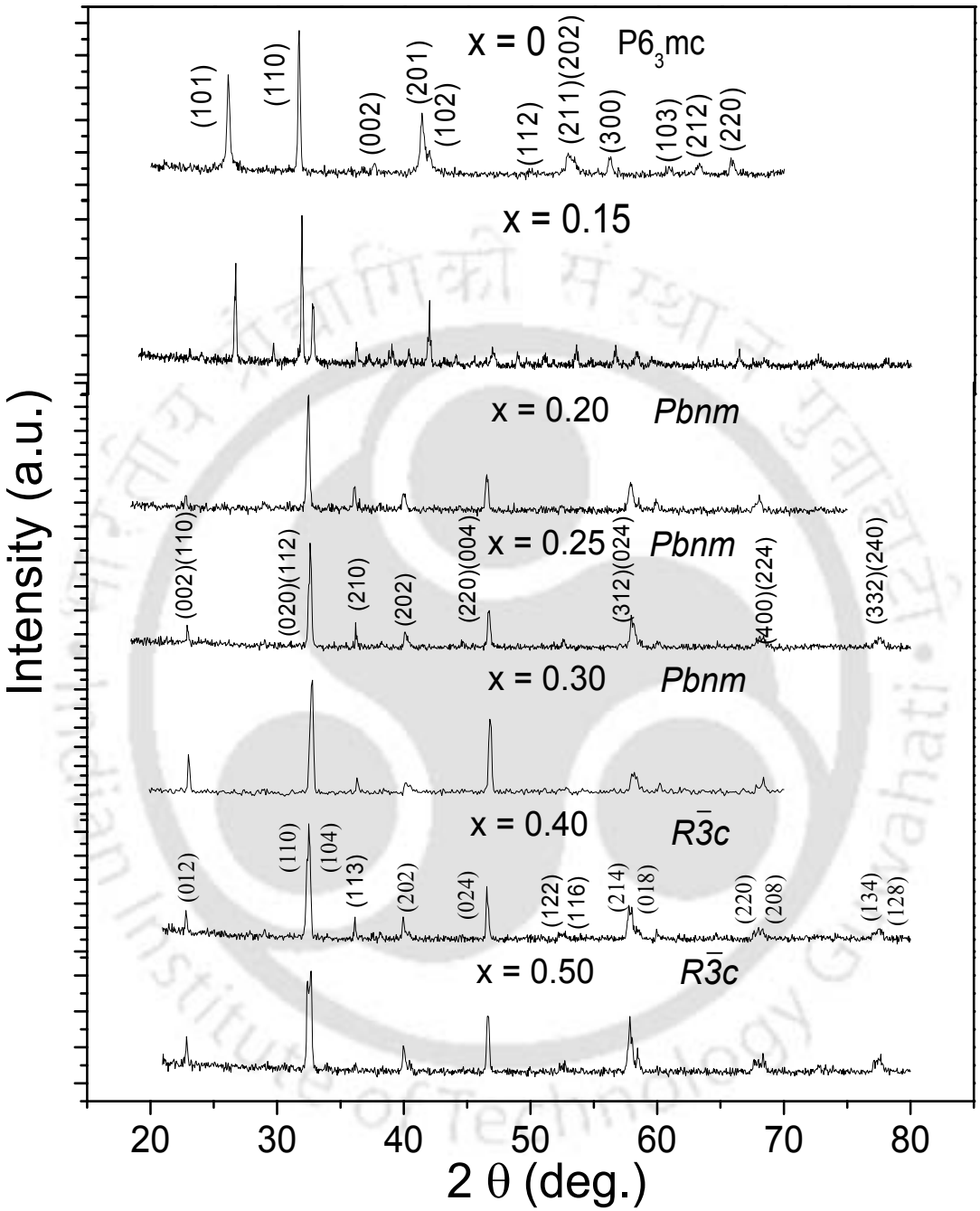

Fig. 3.1: XRD patterns of $Ba_{1-x}La_xMnO_3$ sample for x = 0, 0.15, 0.20, 0.25, 0.30, 0.40 and 0.50.

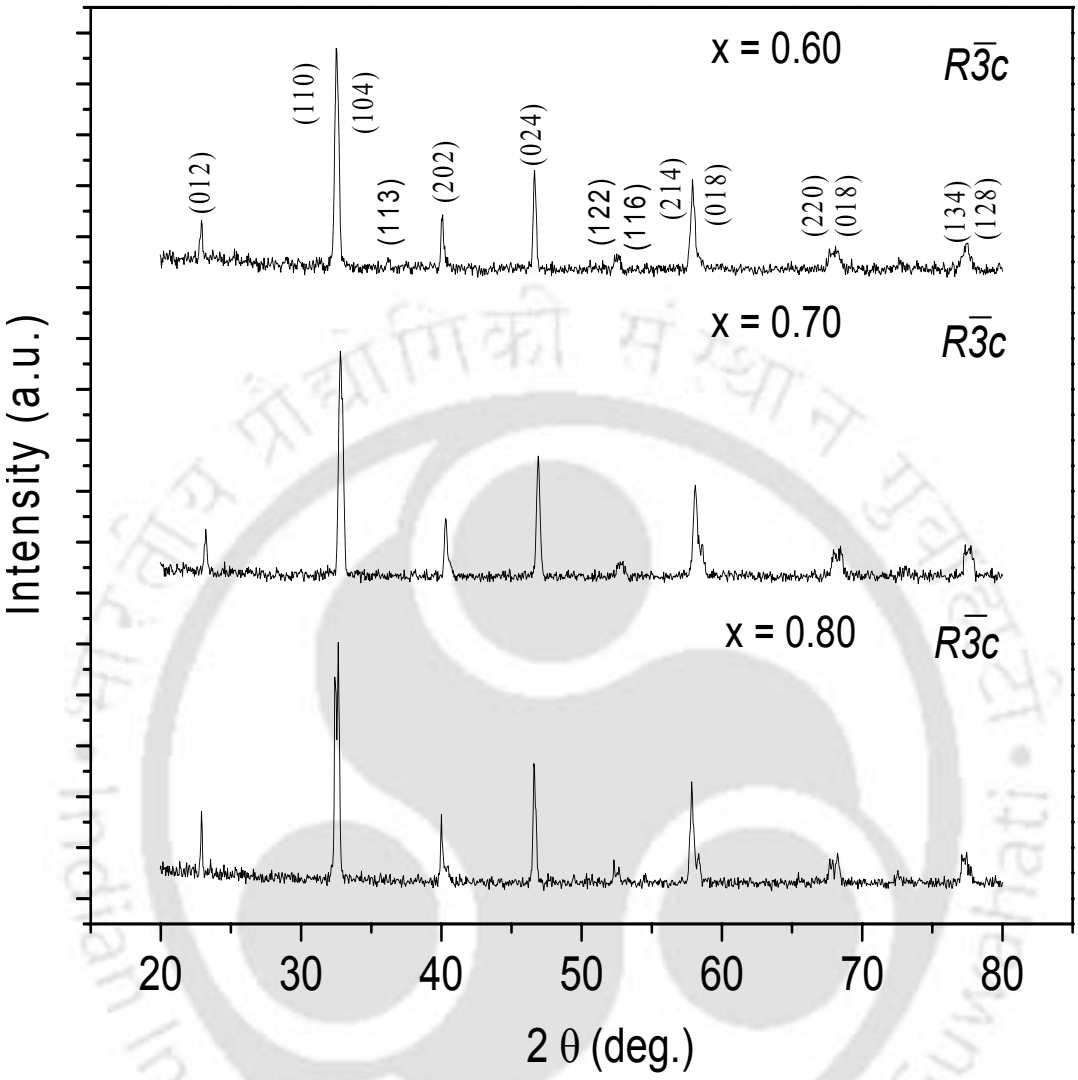

Fig. 3.2: XRD patterns of $Ba_{1-x}La_xMnO_3$ for x = 0.60, 0.70 and 0.80.

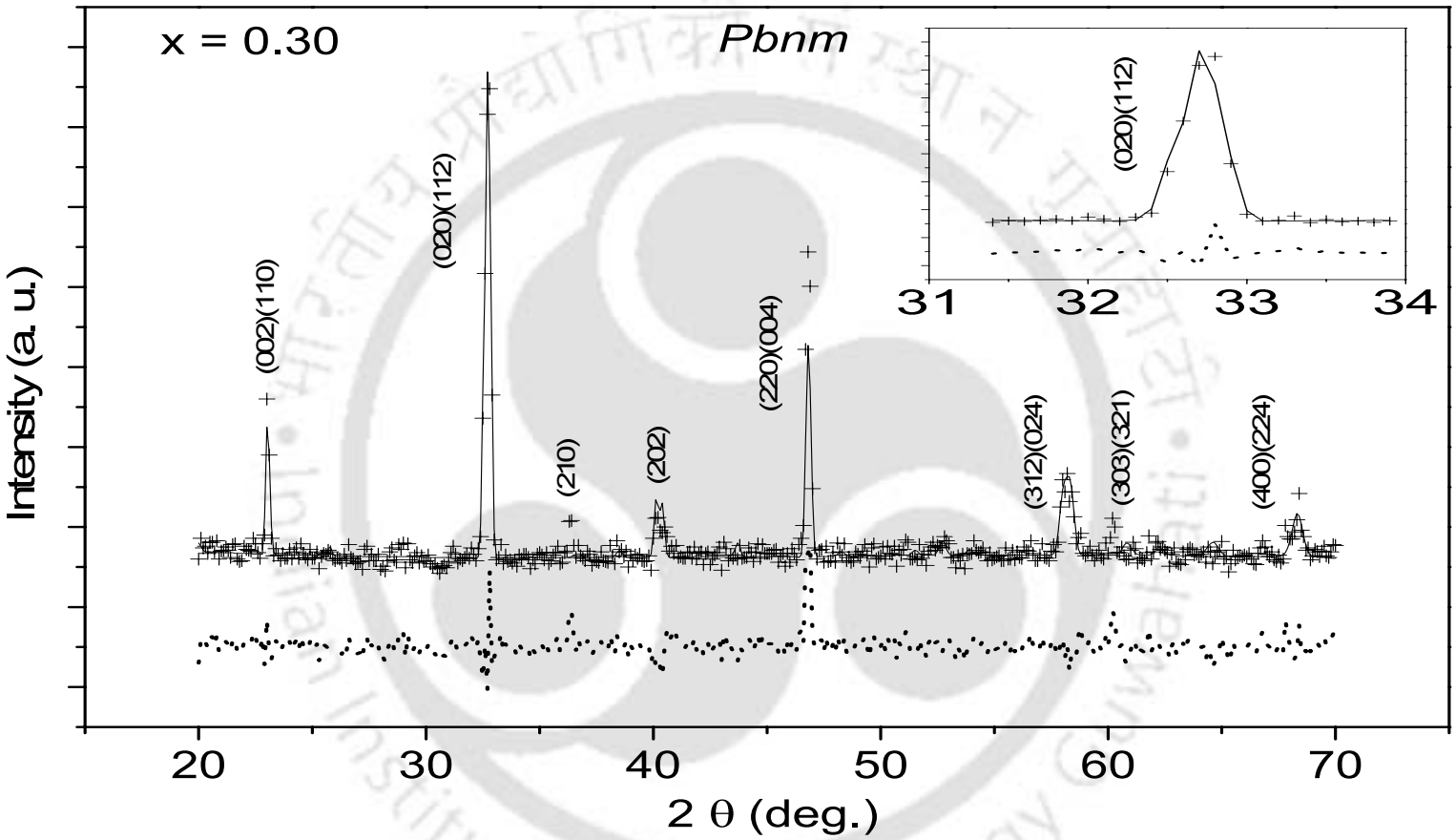

Fig. 3.3: XRD pattern alongwith Rietveld refined data for the sample $Ba_{0.7}La_{0.3}MnO_3$ (x = 0.30). The '+' signs represent experimental points and solid line represents Rietveld refined data. The dotted lines show the difference between experimental & refined data. The inset shows expanded view of (020) (112) peaks.

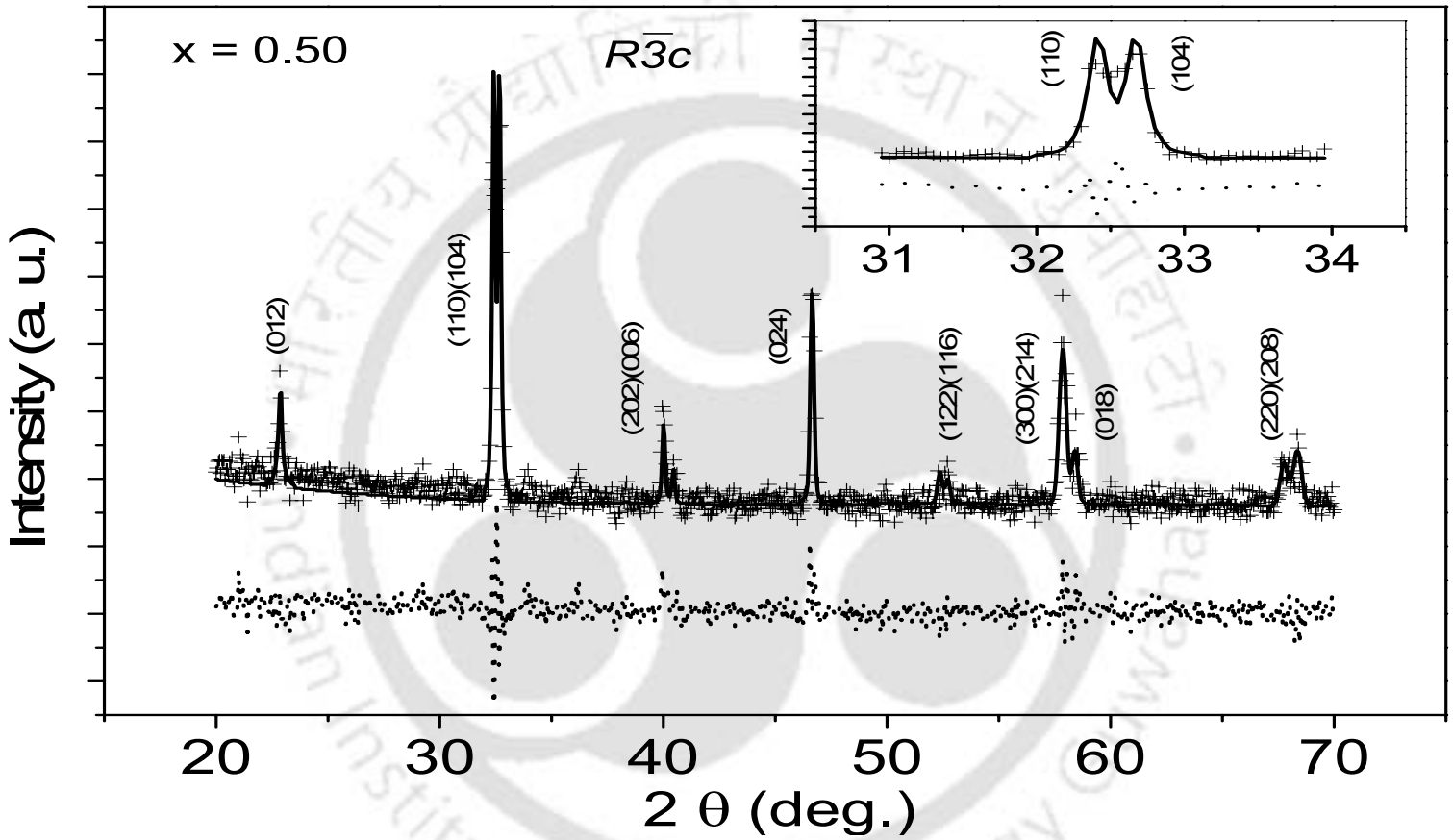

Fig. 3.4: XRD pattern alongwith Rietveld refined data for the sample $Ba_{0.5}La_{0.5}MnO_3$ (x = 0.50). The '+' signs represent experimental points and solid line represents Rietveld refined data. The dotted lines show the difference between experimental & refined data. The inset shows splitting of (110) and (104) peaks.

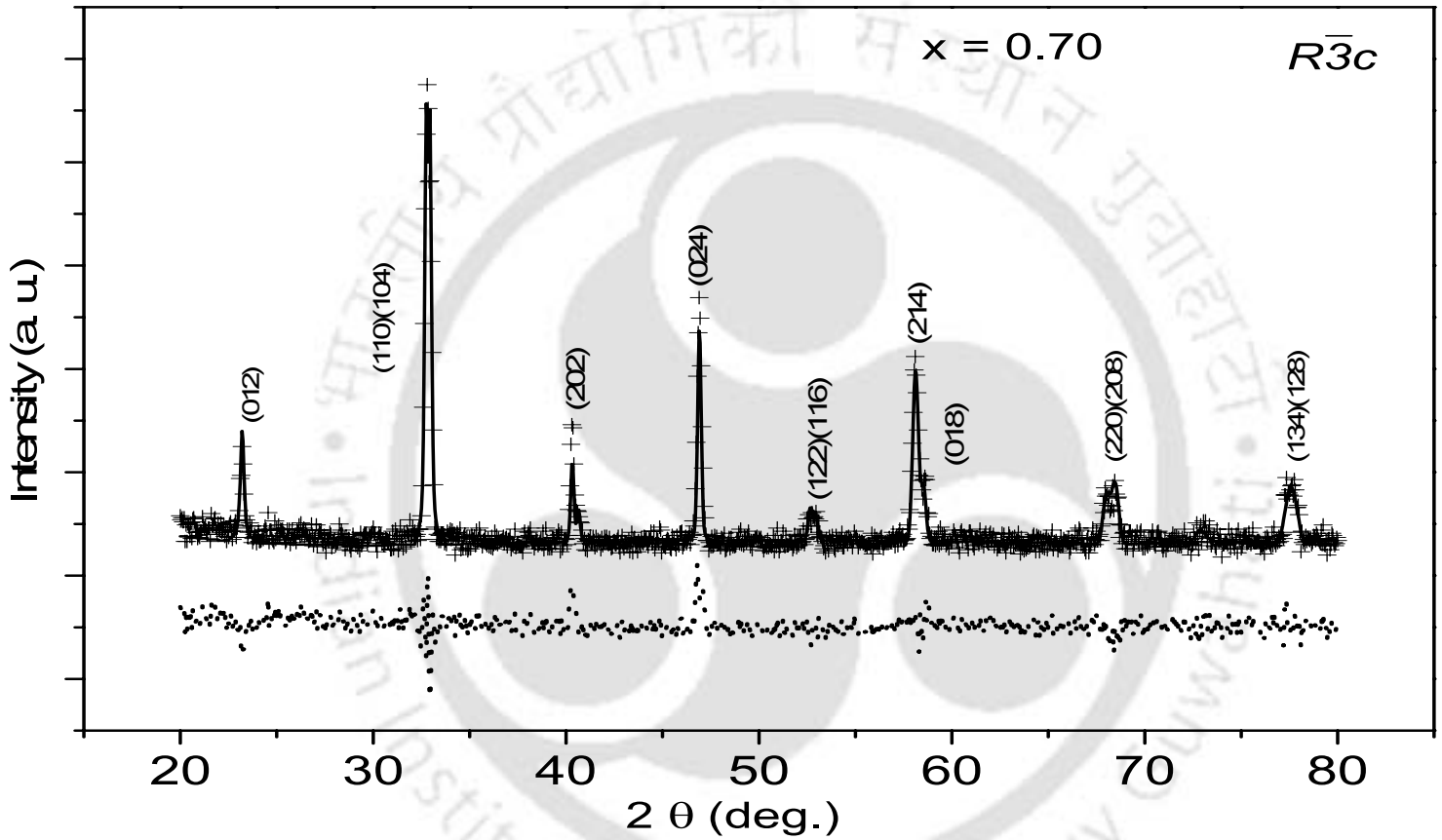

Fig. 3.5: XRD pattern alongwith Rietveld refined data for the sample $Ba_{0.3}La_{0.7}MnO_3$ (x = 0.70, hole doped). The '+' signs represent experimental points and solid line represents Rietveld refined data. The dotted lines show the difference between experimental & refined data.

The Mn-Mn and Mn-O bond lengths and Mn-O-Mn bond angles have been calculated from the refined values of atomic positions & lattice parameters and, by using the eqns. (2.9) and (2.10). The particle size has been calculated using Scherrer's formula (eqn. 2.11). The lattice parameters, volume of the unit cell, particle size, bond length and bond angles for different samples (x = 0.20 to 0.80) are tabulated in Table 3.3. Occupancy values for different elements and reliability factors of fitting are given in Table 3.4. The lattice parameters are comparable to those reported by Dabrowski *et al.* [209] and Mukovskii *et al.* [211] in this series. We can see from Table 3.3 that the lattice parameters mostly increase with 'La' doping baring a few anomalies. Even though, the ionic size of 'La' is less than that of 'Ba', the increase in lattice parameters with 'La' can be visualized as the increase in concentration of Mn^{3+} ions. In addition to that as 'La' concentration increases, the material reaches towards stable higher symmetry crystal structure, where the buckling of Mn-O octahedral co-ordination is reduced. As the buckling is reduced, the lattice parameters can increase marginally. This can be further confirmed from the decrease in values of Mn-O bond length as we approach towards hole doped regime (for $x \geq 0.40$) and correspondingly the Mn-O-Mn bond angle approaches towards 180^{o}. The unit cell volume increases with doping and is in correlation with lattice parameters. The particle size estimated from XRD patterns uniformly increases with doping. The occupancy values of 'Ba' and 'La' are mostly comparable to the doped concentration. We can see that the 'La' occupancy values increase with doping. The 'Mn' site shows some vacancy in most of the prepared compositions.

The values of average valency of 'Mn' ions determined from the chemical titration for the above compounds are listed in Table 3.5. As the doping concentration of 'La' increases the average valency decreases due to electron doping. For the doping range $x < 0.50$, the average valency is greater than 3.5. Thereby Mn^{4+} concentration is dominant on the other hand for $x > 0.50$, the Mn^{3+} concentration is found to be dominant. For $x = 0.50$, the concentration of Mn^{3+} is found to be marginally higher. Even though, the Mn^{3+} concentration increases continuously with doping as expected, the actual concentrations marginally differ from the expected values and this could be mainly due to oxygen off-stoichiometry. Such oxygen off-stoichiometry in mixed valence perovskite manganites have been reported by other groups [209, 212]. The minor discrepancy between XRD analysis and the valency from chemical titration is mainly due to the fixing of oxygen

occupancy in the refinement. Since the scattering power of oxygen for X-ray relatively weak, one can not get consistent values of occupancy in the refinement.

Table 3.1: Parameters obtained from the Rietveld analysis of XRD pattern of the sample $Ba_{0.7}La_{0.3}MnO_3$ (x = 0.30). The XRD pattern has been fitted to *Pbnm* space group. The lattice parameters are a = 5.470Å, b = 5.521Å and c = 7.763Å. Biso is the isotropic displacement (temperature) parameter and Occ is the occupancy number.

Parameters → / Atoms ↓	Fractional coordinates			Biso Å^2	Occ
	x	y	z		
Ba	0.9861	0.0053	0.2500	3.70	0.637
La	0.9861	0.0053	0.2500	3.70	0.271
Mn	0.5000	0.0000	0.0000	0.62	0.883
O1	-0.0378	0.4399	0.2500	0.37	1.000
O2	0.6528	0.3129	-0.0136	0.37	1.000

Table 3.2: Parameters obtained from the Rietveld analysis of XRD pattern of the sample $Ba_{0.5}La_{0.5}MnO_3$ (x = 0.50). The XRD pattern has been fitted to $R\bar{3}c$ space group. The lattice parameters are a = b = 5.534Å and c = 13.400Å. Biso is the isotropic displacement (temperature) parameter and Occ is the occupancy number.

Parameters → / Atoms ↓	Fractional coordinates			Biso	Occ
	x	y	z		
Ba	0.0000	0.0000	0.2500	3.83	0.497
La	0.0000	0.0000	0.2500	3.83	0.508
Mn	0.0000	0.0000	0.0000	4.03	0.988
O1	0.5550	0.0000	0.2500	1.91	1.000

Table 3.3: Parameters obtained from the XRD analysis of the samples $Ba_{1-x}La_xMnO_3$ (x = 0.20, 0.25, 0.30, 0.40, 0.50, 0.60, 0.70 and 0.80). 'S_G' is the average particle size obtained from the line broadening of the XRD pattern.

Samples → / Parameters ↓	x = 0.20	x = 0.25	x = 0.30	x = 0.40	x = 0.50	x = 0.60	x = 0.70	x = 0.80
Space Group	*Pbnm*	*Pbnm*	*Pbnm*	$R\bar{3}c$	$R\bar{3}c$	$R\bar{3}c$	$R\bar{3}c$	$R\bar{3}c$
a (Å)	5.499	5.487	5.470	5.523	5.534	5.531	5.543	5.543
b (Å)	5.528	5.514	5.521	---	---	---	---	---
c (Å)	7.776	7.761	7.763	13.409	13.400	13.448	13.458	13.447
Volume (Å^3)	236.4	234.8	234.4	354.2	355.4	356.2	358.2	357.8
Mn-Mn (Å)	3.899	3.889	3.886	3.894	3.898	3.901	3.910	3.907
Mn-O_1 (Å)	1.953	1.958	1.979	1.984	1.973	1.961	1.956	1.954
Mn-O_2 (Å)	2.042	2.091	2.043	---	---	---	---	---
$\angle Mn-O_1-Mn$ (deg.)	173.7	166.7	158.0	157.7	162.2	168.2	175.7	179.1
$\angle Mn-O_2-Mn$ (deg.)	146.7	137.1	144.1	---	---	---	---	---
S_G (nm)	23	23	24	25	31	31	32	37

Table 3.4: Parameters obtained from the XRD analysis of the samples $Ba_{1-x}La_xMnO_3$ (x = 0.20, 0.25, 0.30, 0.40, 0.50, 0.60, 0.70 and 0.80). G_{Ba}, G_{La} and G_{Mn} are the occupancy of respective elements obtained form the Rietveld analysis. R_p, $R_{\omega p}$, R_{exp}, R_{Bragg}, R_F and χ^2 are the reliability factors.

Samples → / Parameters ↓	x = 0.20	x = 0.25	x = 0.30	x = 0.40	x = 0.50	x = 0.60	x = 0.70	x = 0.80
G_{Ba}	0.808	0.744	0.637	0.599	0.497	0.399	0.299	0.193
G_{La}	0.229	0.258	0.271	0.365	0.508	0.585	0.708	0.793
G_{Mn}	0.988	0.978	0.883	0.986	0.988	0.981	0.950	0.999
R_p	10.1	14.3	11.5	11.7	14.3	13.0	14.1	13.8
$R_{\omega p}$	13.5	18.0	14.7	14.9	17.9	16.3	17.6	17.5
R_{exp}	11.3	13.4	11.5	12.1	14.8	13.89	13.9	14.1
R_{Bragg}	16.0	23.1	20.4	11.4	12.0	9.1	12.8	11.8
R_F	17.6	26.9	22.2	9.9	9.7	7.3	8.6	8.4
χ^2	1.43	1.81	1.64	1.53	1.46	1.38	1.61	1.54

The typical picture of optical micrograph for x = 0.30 sample is shown in Fig. 3.6 for a magnification of 40. The morphology of the sample is found to be uniform throughout the material. The material is found to be quite porous.

The SEM photographs have been taken for the samples x = 0.30 and 0.50. The typical SEM micrographs for x = 0.30 with the magnification of 2,300 and 5,000 are shown in Figs. 3.7 and 3.8 respectively. We can see that the morphology of the grains is almost uniform. Not much variation in the shape and size of the grains are observed and it suggests the monophasic nature of the sample. The average grain size is found to be 2.1 μm and 3.3 μm for x = 0.30 and 0.50 samples respectively. The grain size is found to increase with increase in 'La' concentration and it is in correlation with the trend observed from XRD analysis. However their magnitudes differ and this could be mainly due to the assumption of circular grain in Scherrer's formula. Such variation has been reported in literature [213].

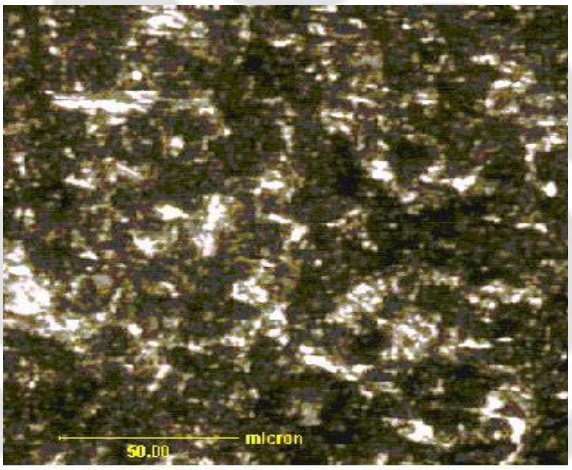

Fig. 3.6: Microscope photograph (magnification-40) of the sample $Ba_{0.7}La_{0.3}MnO_3$.

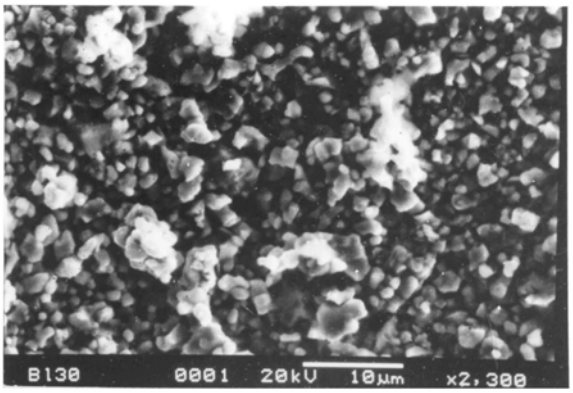

Fig. 3.7: SEM photograph of $Ba_{0.7}La_{0.3}MnO_3$ (x = 0.30) with magnification-2,300.

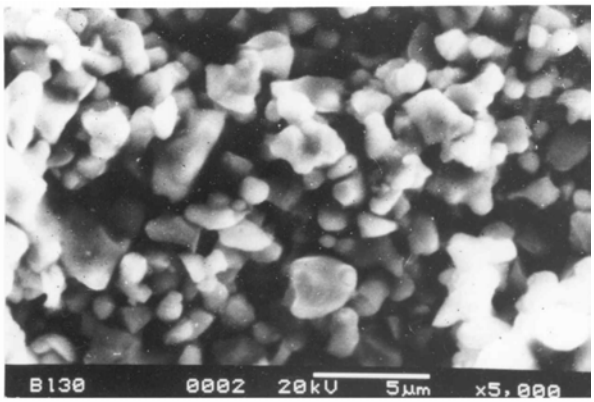

Fig. 3.8: SEM photograph of $Ba_{0.7}La_{0.3}MnO_3$ (x = 0.30) with magnification-5,000.

3.1.3. AC Susceptibility Study

The temperature variation of ac susceptibility in electron doped materials, i.e. for x = 0.20, 0.25, 0.30, 0.40 and 0.50 are shown in Fig. 3.9. Here the measurements were carried out in zero field cooled (ZFC) condition in the temperature range 30 to 420K. The samples were generally taken in a shape of parallelepiped with approximate dimension ≈ 10mm length, 2mm to 3mm width and 1 to 2mm thick. The amplitude of magnetic field was 4.9Oe with a frequency of 233Hz. No demagnetization correction was applied. The magnetic field was applied along the length of the sample. So the demagnetization factor is expected to be quite small. We can see from the Fig. 3.9 that all the materials exhibit paramagnetic to ferromagnetic transition. The transition onset, T_{on} systematically decreases with increase in 'La' doping. On the otherhand, the saturation susceptibility $\chi_s^{/}$ i.e. the susceptibility value at the end of ferromagnetic transition increases with 'La' doping. The increase in $\chi_s^{/}$ value can be understood as a result of enhanced Mn^{3+} concentrations, which in turn results in more Mn^{3+}/Mn^{4+} pairs, and these pairs take part in double exchange interaction. The T_{on} values are in strong correlation with Mn-O-Mn bond angles given in Table 3.3. As 'La' concentration increases in electron doped materials (x ≤ 0.50), the Mn-O-Mn bond angles decreases, in other words, they deviate from 180^0. Such deviation results in reduced double exchange interaction and thereby T_{on} decreases with 'La' doping. The ferromagnetic transition temperature, T_c was taken as the temperature (T) corresponding to peak in $\left|\frac{d\chi^{/}}{dT}\right|$ versus T plot. These values along with T_{on} are tabulated in Table 3.5.

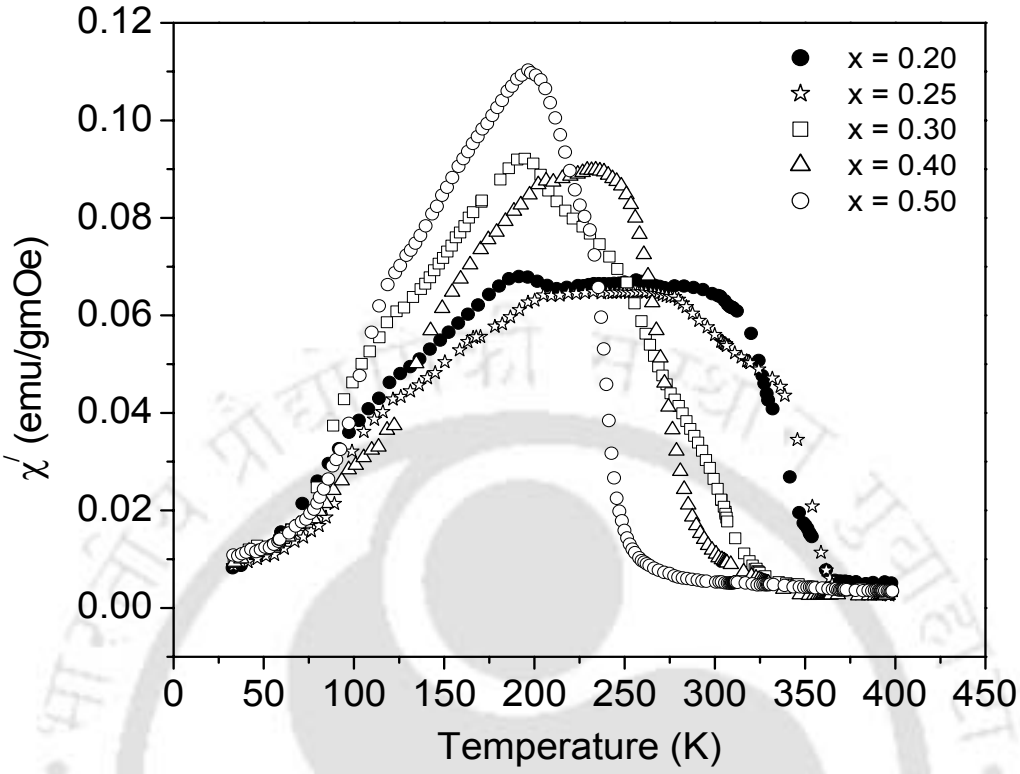

Fig. 3.9: Temperature variation of in phase ac susceptibility (χ') of samples $Ba_{1-x}La_xMnO_3$ for x = 0.20, 0.25, 0.30, 0.40 and 0.50.

Table 3.5: Parameters obtained from the chemical titration and ac susceptibility measurements of the sample $Ba_{1-x}La_xMnO_3$ (x = 0.20 to 0.80). The T_{on}(K), T_c(K) and χ'_s(emu/gmOe) are noted for ZFC measurement. T_f is the reentrant spin glass freezing temperature taken from ZFC measurement. The error in T_{on} is ±2K, T_c is ±1K and T_f is ±1K.

Samples → / Parameters ↓	x=0.20	x=0.25	x=0.30	x=0.40	x=0.50	x=0.60	x=0.70	x=0.80
'Mn' Valency	3.67	3.63	3.61	3.60	3.42	3.36	3.28	3.19
T_{on}(K)	364	364	326	283	256	364	363	299
T_c(K)	347	345	280	266	240	265	269	280
χ'_s(emu/gmOe)	0.066	0.066	0.093	0.090	0.110	0.114	0.154	0.130
T_f (K)	116	106	100	140	99	116	117	119

The χ' versus T plot of x = 0.30 sample is reproduced in Fig. 3.11 up to 300K. Even though, the material is found to be in single phase form as per XRD, it exhibits a complex magnetic behaviour like a magnetic multi phase. A secondary rise in susceptibility at around 280K followed by a change of slope at around 245K is observed. Similar behaviour of secondary rise in susceptibility has been observed by other groups in electron doped manganites [71, 83], however no explanation was given. The transition at 280K is attributed to ferromagnetic weak links at grain boundaries with relatively low T_c compared to the main ferromagnetic phase. The above argument is based on the χ' versus temperature measured on powdered sample as explained in the next paragraph. The change of slope observed below 245K can be attributed to the charge ordering (CO) present in this material. Generally the charge ordering in $R_{0.5}A_{0.5}MnO_3$ type of compounds occur in the temperature range 160 to 270K depending on the type of rare earth (R) and alkaline earth (A) materials [144]. The susceptibility value is found to saturate (peak) at around T_s = 194K, and then start decreasing with decrease in temperature. Such decrease in susceptibility below FM transition in low field measurement is not surprising. As the temperature is lowered, the FM ordering increases gradually and to keep the magnetic energy minimum, more and more domains are formed, and the applied field will not be enough to align all the domains and as a result the χ' decreases with temperature. In other words, there is a loss of long range ferromagnetic ordering due to magnetic anisotropy. Such susceptibility variations have been reported by other groups in manganites especially at low magnetic field [83, 214]. A sharp fall in susceptibility is observed at around 100K and in the same temperature region χ'' versus temperature exhibits broad peak (Fig. 3.10(a)). The ferromagnetic ordering competes with random antiferromagnetic interaction and as a result the magnetic moments are frozen in random direction and, it is called reentrant spin glass (RSG) behaviour [215]. Thus the temperature corresponding to sharp fall in χ' versus T plot below the FM transition can be attributed to RSG state and the corresponding temperature is called freezing temperature, T_f of RSG state. To confirm this, I have carried out χ'' versus temperature measurement for a few frequencies viz. 233, 1133 and 3333Hz. We can see from Fig. 3.10(a), the peak observed in χ'' versus temperature in the vicinity of sharp fall in χ' versus temperature shifts towards higher temperature i.e from 100K for 233Hz to 104K for 3333Hz and this is a manifestation of RSG state.

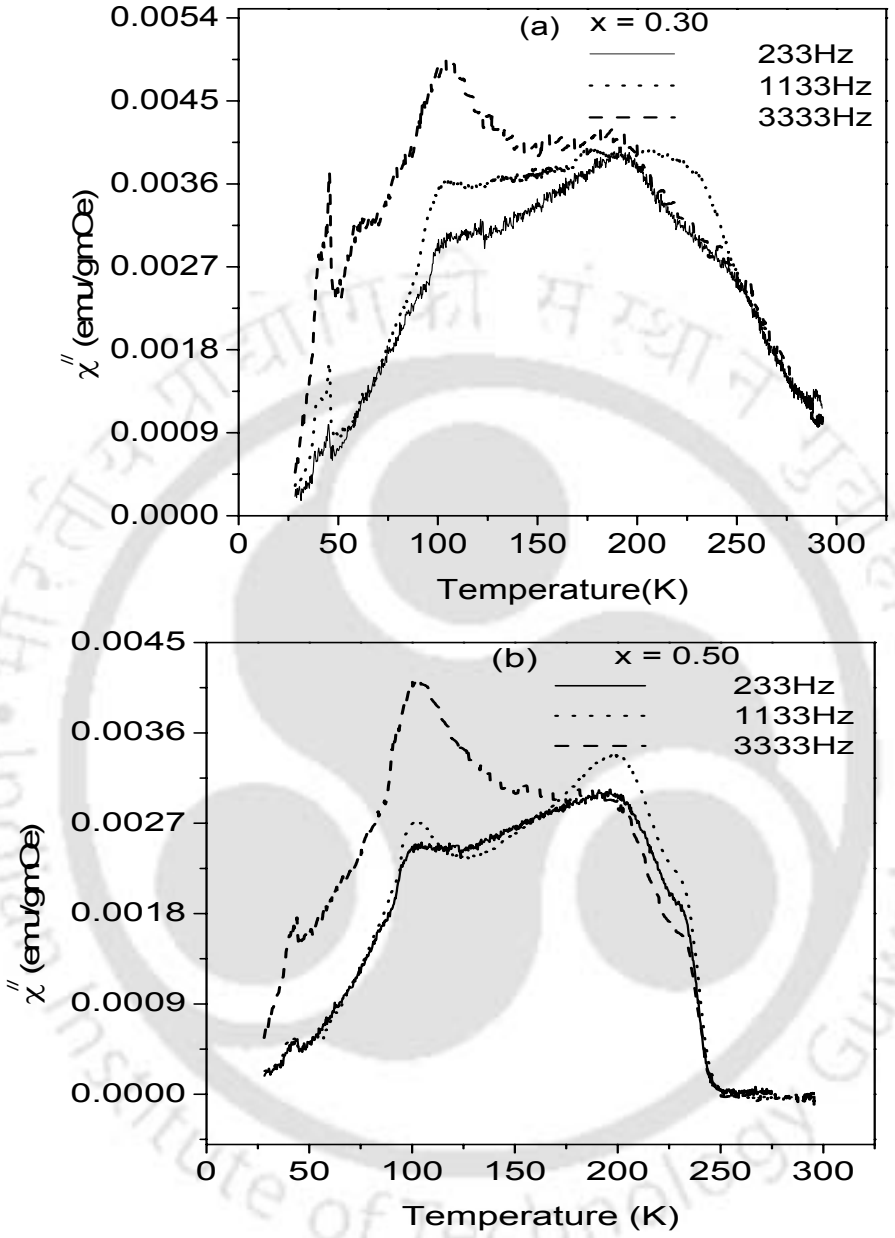

Fig. 3.10: Temperature variation of out of phase ac susceptibility ($\chi^{//}$) of samples $Ba_{1-x}La_xMnO_3$ for (a) x = 0.30 and (b) 0.50.

To study the intergranular behaviour, I have also measured temperature variation of susceptibility on powdered sample, i.e. by crushing the solid sample from the same pellet. $\chi^{/}$ versus T plot for such powdered sample is shown in Fig. 3.11 for x = 0.30 (triangles). One can see a large reduction in magnitude of susceptibility, i.e. for about 60%

reduction in the region of saturation susceptibility and it emphasizes the presence of considerable intergranular weak links in the present sample. The domination of intergranular region could be mainly due to smaller grains observed in these types of materials. As the grain size decreases, the number of grain boundaries and the corresponding weak link networks increase. The low temperature FM transition (280K) and CO transition (245K) appeared on solid sample almost disappeared on powdering. Thus the above two transitions were mainly due to intergranular weak link structure. The magnetic anisotropy induced loss of long range ferromagnetic ordering is also vanished. However, the powdered sample also exhibits a sharp fall in susceptibility at low temperature and with a small peak at 118K. Thus, the RSG behaviour is due to the intrinsic property of the material rather than the weak links. As a result of small concentration of Mn^{3+} ions, there is a possibility of AFM superexchange interaction between Mn^{4+} ions.

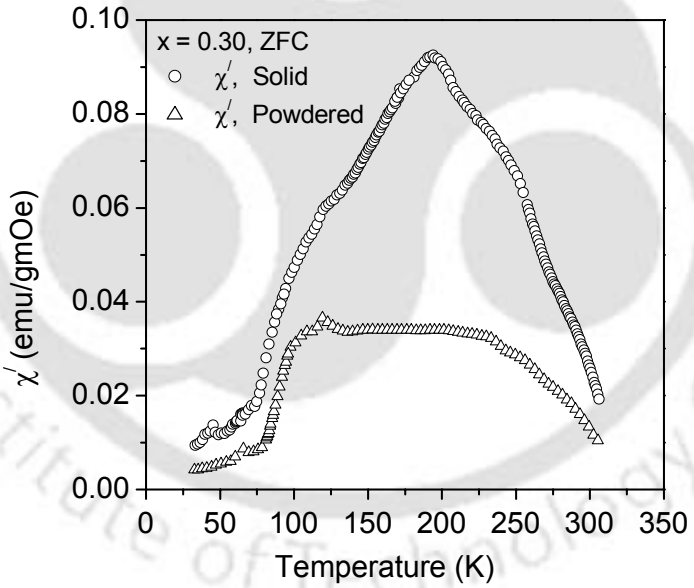

Fig. 3.11: AC susceptibility (χ') as a function of temperature for $Ba_{0.7}La_{0.3}MnO_3$ (x = 0.30) sample. Circles and triangles represent for solid and powdered samples respectively.

To study the irreversibility behaviour, the susceptibility measurements were carried out in zero field cooled (ZFC) and field cooled (FC) conditions. Typical plots of χ' versus T for ZFC and FC cases are shown in Fig. 3.12 for x = 0.40. The ZFC curve is comparable to that of x = 0.30 sample except that the present sample shows no trace of

CO. As can be seen from the figure, there is an appreciable difference between ZFC and FC curve especially below T_f. The increase in χ' value in FC condition is mainly due to the stabilization of FM state rather than AFM. In the presence of magnetic field H, the FM state can gain a free energy (-MH) rather than the AFM state (M = 0) [83, 216]. The freezing temperature, T_f is also reduced considerably under FC condition. In the temperature region $T > T_f$ (ZFC), there is no appreciable difference between ZFC and FC data.

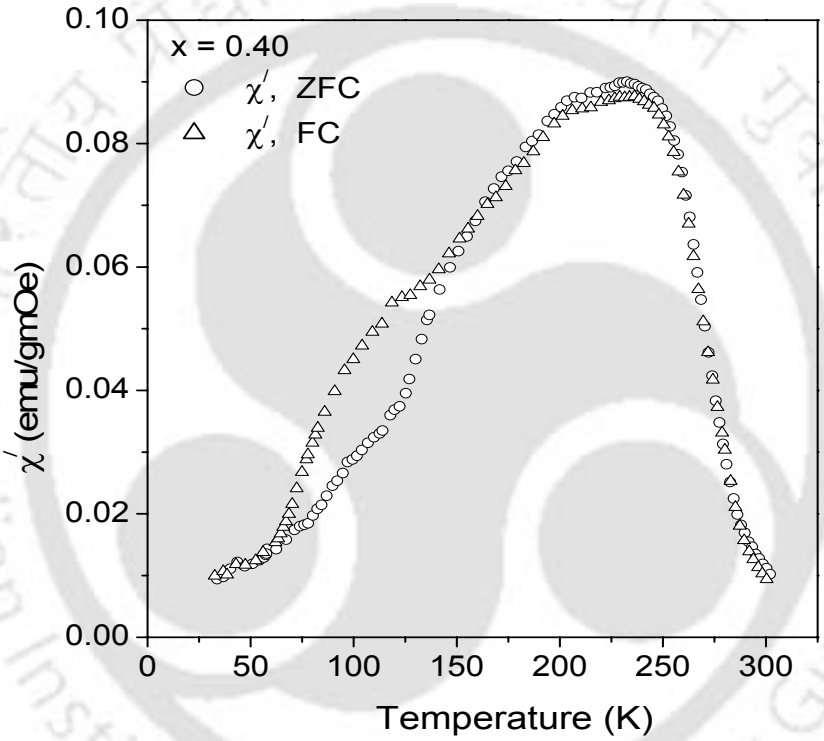

Fig. 3.12: AC susceptibility (χ') as a function of temperature for $Ba_{0.6}La_{0.4}MnO_3$ (x = 0.40) sample. Circles and triangles represent ZFC and FC data respectively.

Temperature variations of χ' in solid and powdered sample of x = 0.50 are also shown in Fig. 3.13. Unlike other materials, in this compound a sharp FM transition with onset temperature at around 256K is observed. The FM transition is followed by CO and RSG behaviour. The RSG behaviour is confirmed from the shifting of peak observed in χ'' versus T plot from 99K for 233Hz to 103K for 3333Hz (Fig. 3.10(b)). Unlike x = 0.30 sample, CO transition is observed even in powdered sample and this suggests that CO is intrinsic property of x = 0.50 sample. The observation of charge ordering in x = 0.50

sample as an intrinsic property is not surprising because in this material most of grains would be having equal concentrations of Mn^{3+} and Mn^{4+} ions. The onset of CO temperature is at around 225K. The saturation susceptibility is reduced to about 50% upon powdering and this suggests that the intergranular region play a considerable role on the magnetic properties of polycrystalline perovskite.

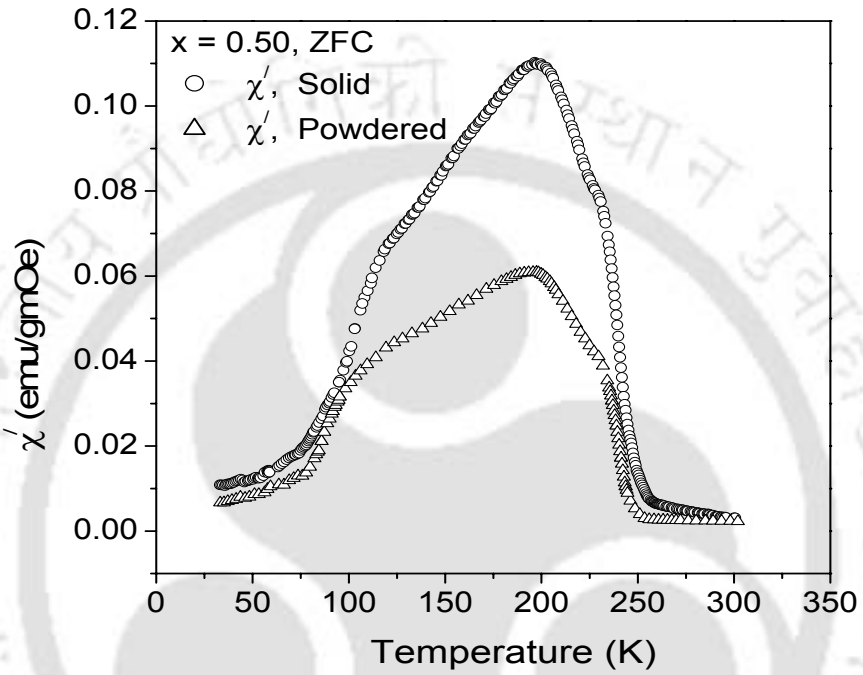

Fig. 3.13: AC susceptibility (χ') as a function of temperature for $Ba_{0.5}La_{0.5}MnO_3$ (x = 0.50) sample. Circles and triangles represent susceptibility for solid and powdered samples respectively.

χ' versus T plots for the hole doped materials are shown in Fig. 3.14. Here hollow circles, triangles and squares represent for the samples x = 0.60, 0.70 and 0.80 respectively. Unlike electron doped materials, here no multiple magnetic transitions are observed. The FM onset temperatures, T_{on} are found to be above the room temperature and they are listed in Table 3.5. The typical value for x = 0.70 is 363K and it is comparable to that reported by Raveau *et al.* [78]. The saturation susceptibility for x = 0.70 sample is found to be maximum. Further rise in 'La' concentration, i.e. for x > 0.70, results reduction in saturation susceptibility. Thus x = 0.70 is found to be the optimum doping for maximum double exchange interaction, where the ratio of concentration of Mn^{3+}/Mn^{4+} are approximately 70%/30%. In Fig. 3.15, χ' versus T plots for solid (circles) and powdered

(triangles) samples of x = 0.70 are shown. We can see a large reduction in magnitude of susceptibility for powdered samples like electron doped case. It illustrates the presence of considerable concentration of intergranular weak link networks even in the hole doped materials. These materials also exhibit a loss of long range ferromagnetic ordering due to magnetic anisotropy. A minor fall in susceptibility at around 117K has been observed. The ZFC and FC data of hole doped materials almost coincide each other without any noticeable difference as shown in Fig. 3.16 for x = 0.60. This is in contrast to what observed in electron doped materials. This is mainly due to lack of significant AFM interaction in hole doped materials.

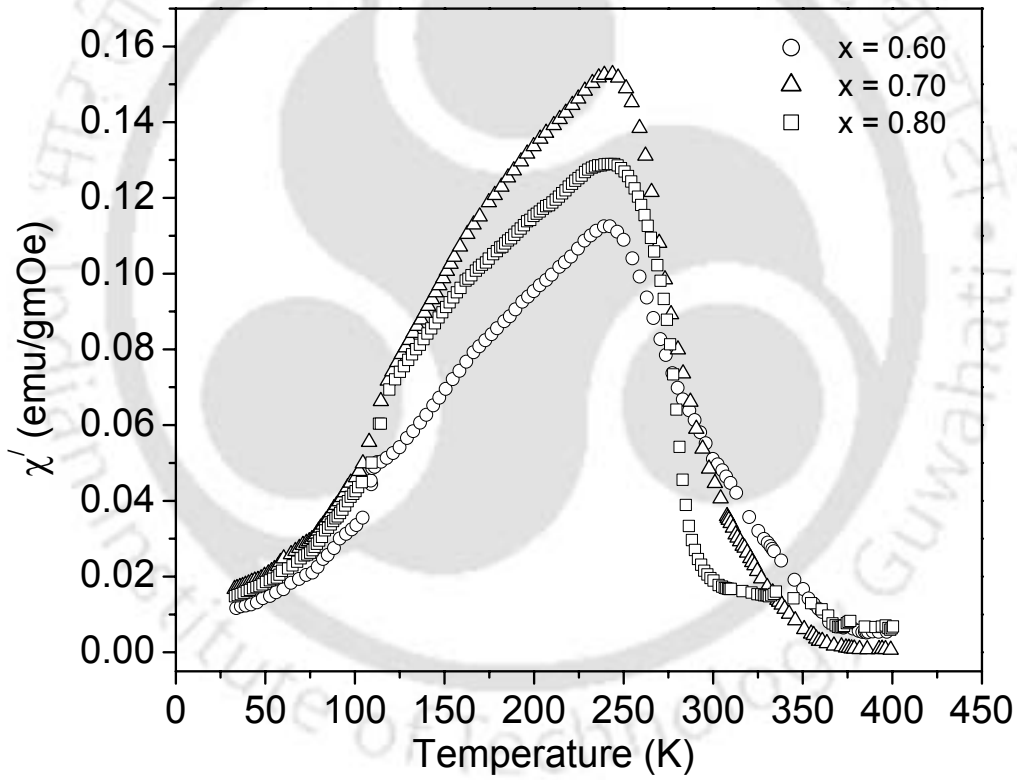

Fig. 3.14: Temperature variation of in phase ac susceptibility (χ') of samples $Ba_{1-x}La_xMnO_3$ for x = 0.60 (circles), 0.70 (triangles) and 0.80 (squares).

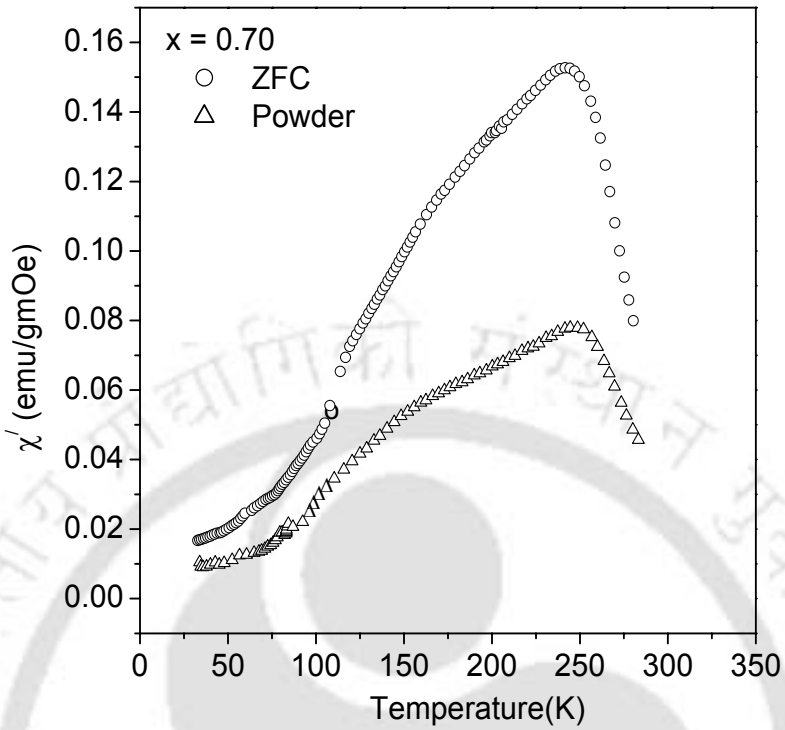

Fig. 3.15: AC susceptibility (χ') as a function of temperature for $Ba_{0.3}La_{0.7}MnO_3$ (x = 0.70) sample. Circles and triangles represent susceptibility for solid and powdered samples respectively.

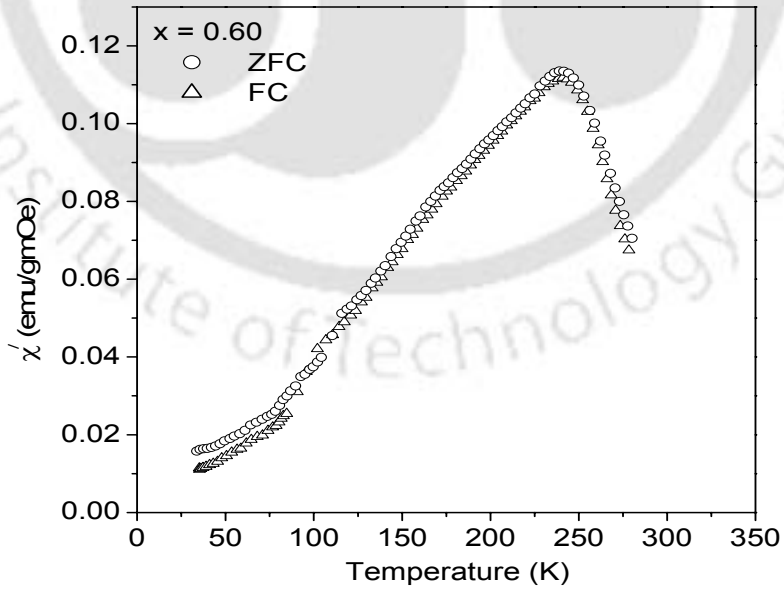

Fig. 3.16: AC susceptibility (χ') as a function of temperature for $Ba_{0.4}La_{0.6}MnO_3$ (x = 0.60) sample. Circles and triangles represent zero field cooled (ZFC) and field cooled (FC) data respectively.

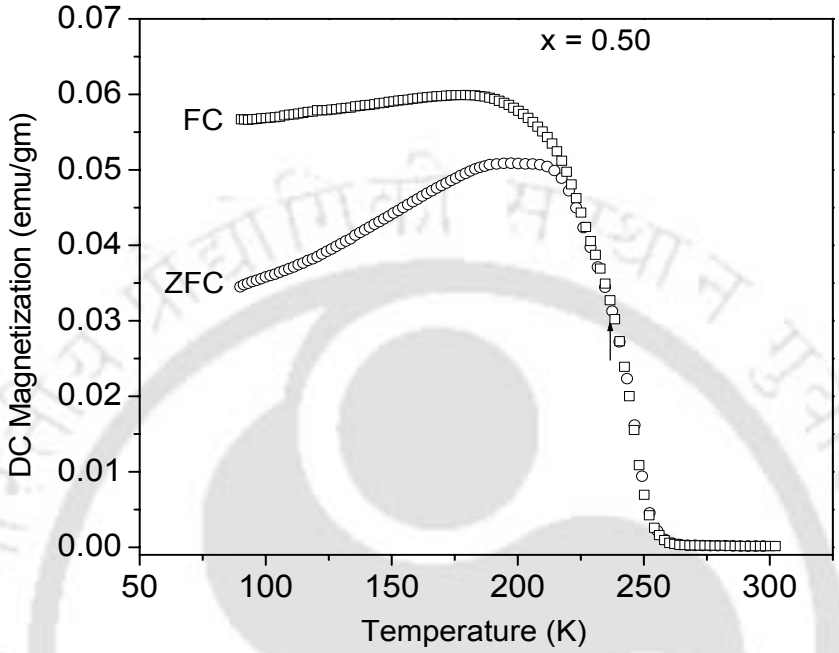

Fig. 3.17: Plot of temperature variation of DC magnetization of $Ba_{1-x}La_xMnO_3$ (x = 0.50) sample for ZFC (circles) and FC (squares) conditions.

For a comparison, the temperature variation of dc magnetization (M) was measured down to 80K for a magnetic field of 25Oe. Typical plots of M versus T for x = 0.50 sample in the ZFC (circles) and FC (squares) conditions are shown in Fig. 3.17. The T_{on} value is found to be 257K, which is comparable to that measured from ac susceptibility (256K). By looking at the graph carefully, we can see a change of slope at around 234K due to charge ordering and it is comparable to that observed in χ' versus T plot. The ZFC data exhibit decrease in susceptibility due to magnetic anisotropy induced loss of long range FM ordering. However, the magnetization data show constant saturated value in the FC condition. In the process of field cooling, the applied field aligns all the moments before the domain formation. However, in the ZFC process the magnetic domains are formed when the material is cooled to low temperature and the field applied later is insufficient to align all the domains.

3.1.4. Electrical Resistivity and Magneto-Resistivity Studies

The temperature variation of dc electrical resistivtiy measured in zero field for the electron doped materials such as x = 0.20, 0.25, 0.30, 0.40 and 0.50 are shown in Fig. 3.18. For the convenience of comparison of ρ versus T plots of different samples, ρ values are shown in logarithmic scale. We can see that all the samples exhibit metal-insulator transition. The temperature corresponding to peak is taken as the metal-insulator transition temperature. Even though, x = 0.30 and 0.50 samples in electron doped regime are reported, probably for the first time to my knowledge metal-insulator transition is reported in the entire electron doped region, i.e. for $x \geq 0.20$. For low concentration of 'La' (x = 0.20 & 0.25), large difference between T_{MI} and T_c values are observed. This can be attributed to the intergranular tunneling, where the T_c of intergranular weak links are quite small compared to main ferromagnetic phase. The FM transition in most of the electron doped materials is found to be quite broad and this may also play a role in difference between T_c and T_{MI}. Such a difference between T_c and T_{MI} has been reported by other authors [30]. A minor anomaly at around 240K is observed in the resistivity curve of x = 0.30 sample and it can be compared with the intergranular charge ordering observed in the χ' versus T plot of the same sample. In addition to that, we can notice that below 100K the rate of fall of resistivity decreases and ρ versus T graph exhibits small upturn. This can be compared with the RSG state observed in χ' versus T measurements. Thus the setting of RSG state gives rise to increase in resistivity. The x = 0.40 sample shows double peak and such behaviour can be explained as a result of intergranular tunneling. Several authors have reported such double M-I transitions both in electron and hole doped materials. The magnitude of resistivity decreases systematically with increase in Mn^{3+} concentrations or in other words, the increase in Mn^{3+} concentration results in enhanced intensity of double exchange interaction.

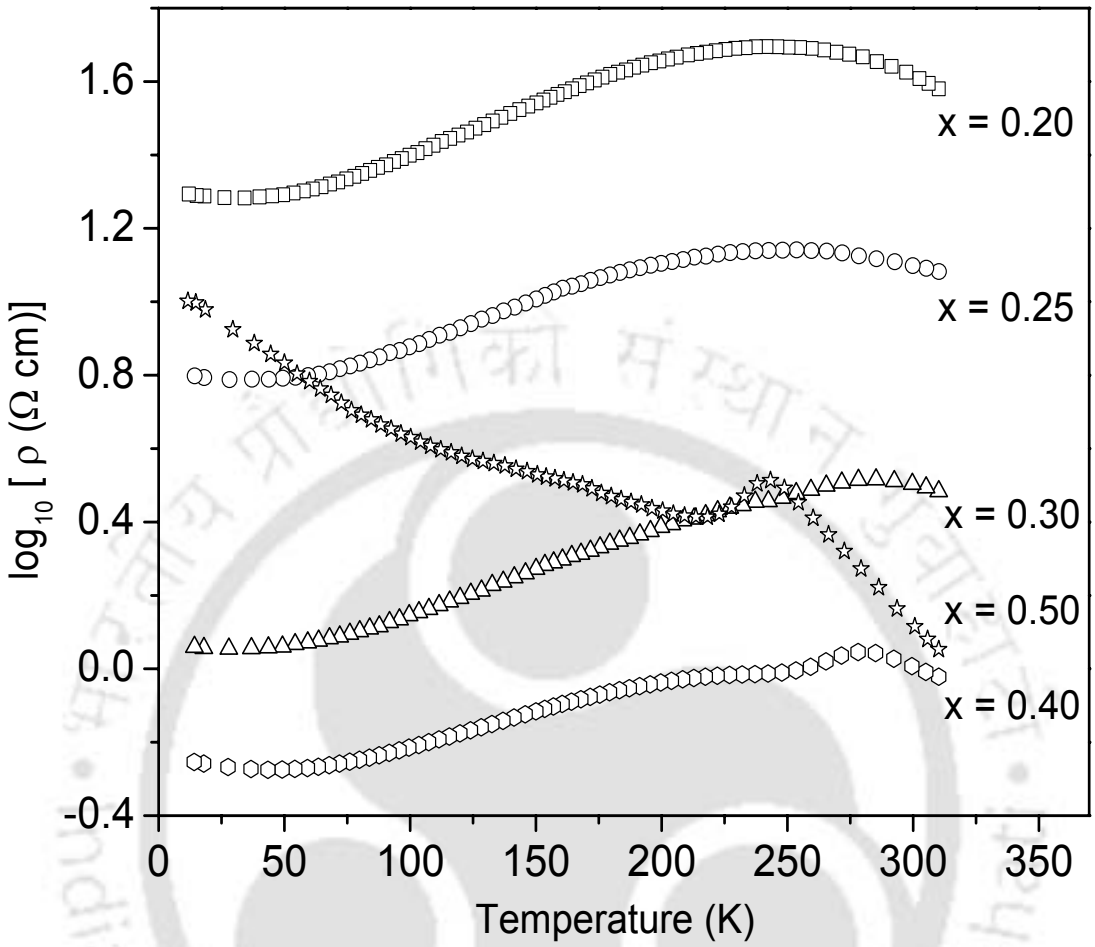

Fig. 3.18: Temperature variation of electrical resistivity for $Ba_{1-x}La_xMnO_3$ (x = 0.20, 0.25, 0.30, 0.40 and 0.50) samples. For clarity resistivity data have been shown in logarithmic scale.

The ρ versus T plot of x = 0.50 shows interesting behaviour. In addition to M-I transition, a reentrant semiconducting behaviour with onset temperature at around 222K (negative peak) is observed. Interestingly this temperature is in correlation with CO observed in susceptibility measurement. Thus at this temperature, the kinetic energy of 'e_g' electrons are overcome by coulomb interaction of ordered 'Mn' ions and the materials behave like AFM. At low temperature, i.e. at around 100K, a further sharp rise in resistivity with decrease in temperature has been observed and this temperature is in correlation with RSG state observed in χ' versus T plot. So the freezing of magnetic moments in random direction results in secondary rise in resistivity.

The temperature variations of electrical resistivity in the presence of magnetic fields, H = 10 and 50kOe were carried out on electron doped materials. These plots are shown along with zero field data in Figs. 3.19 - 3.23 for samples x = 0.20 - 0.50. The magnitude of resistivity decreases and T_{MI} values shift towards higher temperature with the application of magnetic field. This is a result of enhanced double exchange interaction in the presence of magnetic field. The low temperature upturn in ρ versus T plots disappear in the presence of magnetic field. As the magnetic field is applied, the FM interaction enhances and it results in shifting of freezing temperature of RSG state to further low temperature. This results in suppression of upturn in ρ versus T plots. The magneto-resistivity is calculated using the relation $MR = \frac{\rho(H,T) - \rho(0,T)}{\rho(0,T)}$, where ρ(H,T) and ρ(0,T) are the resistivity measured in the presence and absence of magnetic field. The plot of negative MR versus T for x = 0.20 - 0.50 samples are shown in Figs. 3.24 - 3.28. For x ≤ 0.30, no peak at around T_{MI} is observed and the magnitudes of MR increase with decrease in temperature. Such a trend of magneto-resistivity has been reported by Yuan *et al.* [77] and Trukhanov *et al.* [210]. The increase in MR at low temperature could be due to the presence of magnetic anisotropy and competing antiferromagnetic interaction (RSG) as a result of magnetic phase separation. As the applied magnetic field tends to stabilize the FM state rather than AFM state and also tends to increase the domain size by reducing the anisotropy, increase in MR with decrease in temperature is observed. The lack of appearance of peak at around T_{MI} could be mainly due to the fact that T_{MI} values are quite away from bulk FM transition onset. On the other hand, MR of samples with x ≥ 0.40 exhibit peak at around T_{MI}, because in these samples T_{MI} values are quite close to the bulk T_c. The values of magneto-resistivity at minimum temperature (15K) and the corresponding values in the vicinity of T_{MI} are tabulated in Table 3.7.

Typical plot of temperature variation of electrical resistivity in the absence of field for the hole doped material, x = 0.70 is shown in Fig. 3.29. The M-I transition temperature is found to be 340K and it is comparable to that reported in literature [26]. All the hole doped samples exhibit M-I transitions. The M-I transition temperature, T_{MI} and ρ_{300K} are tabulated in Table 3.6. ρ_{300K} is found to be minimum at x = 0.70.

The electrical resistivity data in the metallic region for electron doped samples (0.20 ≤ x ≤ 0.40) for H = 0, 10kOe and 50kOe fields were analyzed using various models

discussed in the introduction (section 1.3.2). In the metallic region, it could be mostly fitted to the empirical relation (eqn 1.14), $\rho = \rho_0 + \rho_2 T^2$ by following Schiffer et al. [21]. Here ρ_0 is the temperature independent resistivity due to impurity, grain boundaries, etc. and ρ_2 is proportionality constant. The parameters ρ_0 and ρ_2 are tabulated in Table 3.8. The estimated error for each parameter is also given. The error has been estimated by varying the range of fit and by repeating the fits. The chi^2 was found to be constant within the error value given in the Table 3.8. This analysis suggests that the electrical transport is mostly controlled by electron-electron scattering [126]. According to Snyder et al. [126], n = 2 corresponds to intrinsic behaviour of rare earth manganites. The fitted data are shown as solid lines in Figs. 3.19 - 3.22 for x = 0.20 - 0.40. Typical plots of ρ versus T^2 are also shown in Fig. 3.30 for H = 0, 10 and 50kOe fields. We can see that they exhibit linear behaviour. They were fitted to the linear relation $\rho = \rho_0 + \rho_2 T^2$ and the fitted data are shown as solid lines. The fitted data closely follow the experimental data. From the above analysis we can conclude that resistivity in the metallic region is controlled by electron-electron scattering mechanism irrespective of the presence of magnetic field. The fitted values of ρ_0 and ρ_2 are given in Table 3.8. We can see that the ρ_0 value decreases in the presence of magnetic field and it could be due to enhancement of ferromagnetic domain size in the presence of magnetic field.

The resistivity data of hole doped materials below T_{MI} were also fitted to the empirical relation, $\rho = \rho_0 + \rho_2 T^2$. So the resistivity mechanism is unchanged in the metallic region for hole doped materials. The resistivity data above T_{MI} for the sample, $x \geq 0.50$ is analyzed using the Mott-VRH (eqn. 1.20), ES-VRH (eqn. 1.24) and SPH (eqn. 1.19) models as discussed in the section 1.3.3. Mott-VRH model gives the better fit compared to other models. The fitted data are shown as solid lines in the Fig. 3.29 for the sample x = 0.70.

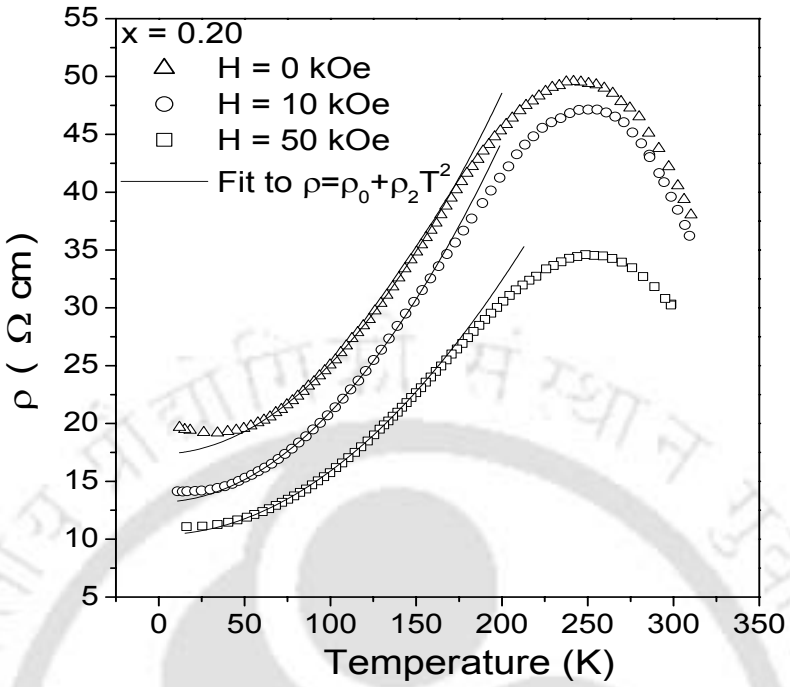

Fig. 3.19: Electrical resistivity as a function of temperature for $Ba_{0.8}La_{0.2}MnO_3$ (x = 0.20) sample. The experimental data corresponding to zero, 10kOe and 50kOe magnetic fields are shown as triangles, circles and squares respectively. The fitted data to the equation $\rho = \rho_0 + \rho_2 T^2$ are shown as solid lines.

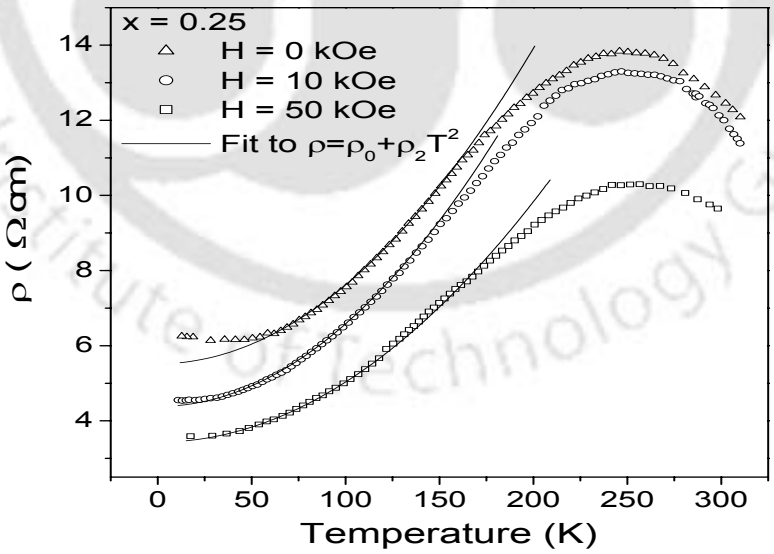

Fig. 3.20: Electrical resistivity as a function of temperature for $Ba_{0.75}La_{0.25}MnO_3$ (x = 0.25) sample. The experimental data corresponding to zero, 10kOe and 50kOe magnetic

fields are shown as triangles, circles and squares respectively. The fitted data to the equation $\rho = \rho_0 + \rho_2 T^2$ are shown as solid lines.

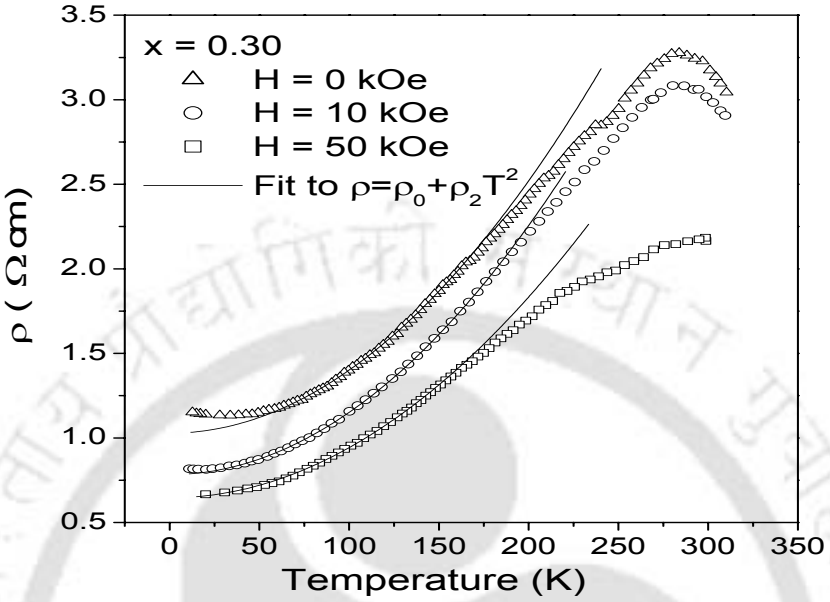

Fig. 3.21: Electrical resistivity as a function of temperature for $Ba_{0.7}La_{0.3}MnO_3$ (x = 0.30) sample. The experimental data corresponding to zero, 10kOe and 50kOe magnetic fields are shown as triangles, circles and squares respectively. The fitted data to the equation $\rho = \rho_0 + \rho_2 T^2$ are shown as solid lines.

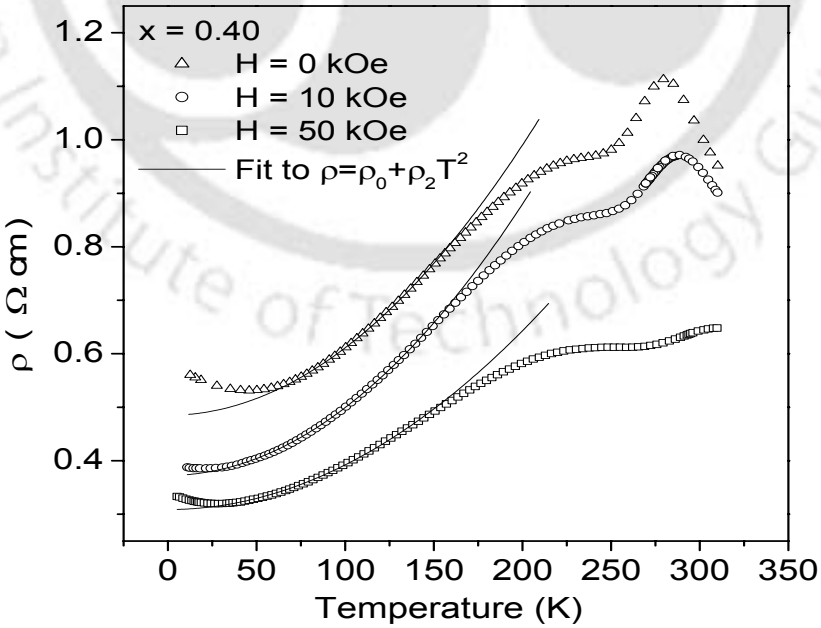

Fig. 3.22: Electrical resistivity as a function of temperature for $Ba_{0.6}La_{0.4}MnO_3$ (x = 0.40) sample. The experimental data corresponding to zero, 10kOe and 50kOe magnetic fields are shown as triangles, circles and squares respectively. The fitted data to the equation $\rho = \rho_0 + \rho_2 T^2$ are shown as solid lines.

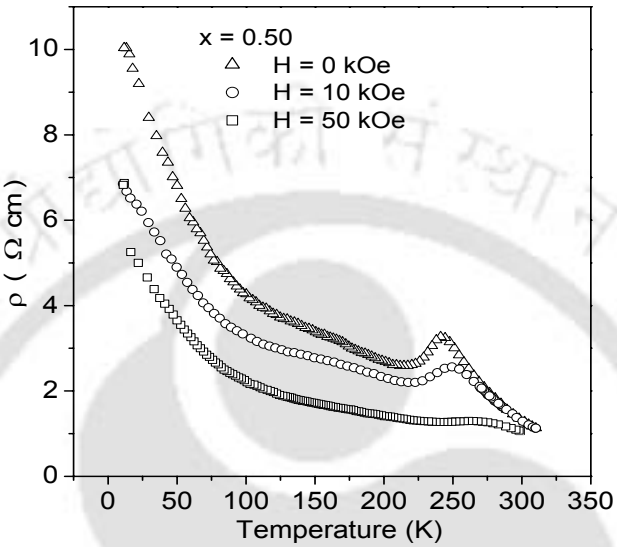

Fig. 3.23: Electrical resistivity as a function of temperature for $Ba_{0.5}La_{0.5}MnO_3$ (x = 0.50) sample. The experimental data corresponding to zero, 10kOe and 50kOe magnetic fields are shown as triangles, circles and squares respectively.

Table 3.6: Parameters obtained from electrical resistivity measurement. T_{MI} is the metal-insulator transition temperature. ρ_{300K} is the resistivity at 300K in the absence of magnetic field. The error in T_{MI} is ±2K.

Parameters → / Samples ↓	T_{MI} (K)			ρ_{300K} (Ωcm)		
	0kOe	10kOe	50kOe	0kOe	10kOe	50kOe
x = 0.20	245	257	259	41.31	39.32	30.34
x = 0.25	255	261	262	12.50	12.00	9.65
x = 0.30	285	287	298	3.19	3.01	2.11
x = 0.40	281	290	304	1.02	0.94	0.64
x = 0.50	243	250	275	1.31	1.21	1.05
x = 0.60	340	---	---	0.29	---	---
x = 0.70	340	---	---	0.20	---	---
x = 0.80	275	---	---	0.56	---	---

Table 3.7: Parameters obtained from magneto-resistivity measurements. MR% (T_{MI}) and MR% (T_{15K}) are respectively the negative magneto-resistivity in the vicinity of T_{MI} and at minimum temperature (15K).

Parameters → / Samples ↓	-MR% (T_{MI}) (10 kOe)	-MR% (T_{MI}) (50kOe)	-MR% (T_{15K}) (10 kOe)	-MR% (T_{15K}) (50 kOe)
x = 0.20	5	30	28	43
x = 0.25	5	26	28	42
x = 0.30	6	35	29	42
x = 0.40	15	44	31	44
x = 0.50	24	61	33	47

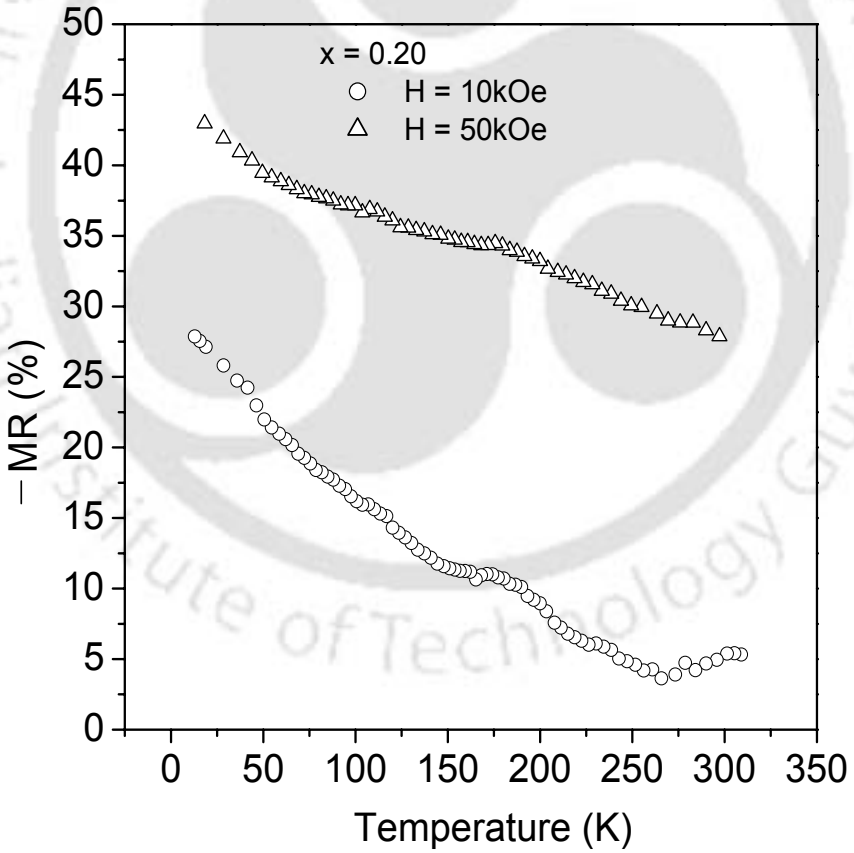

Fig. 3.24: Temperature variation of negative magneto-resistivity measured at 10kOe (circles) and 50kOe (triangles) fields for $Ba_{0.8}La_{0.2}MnO_3$ (x = 0.20).

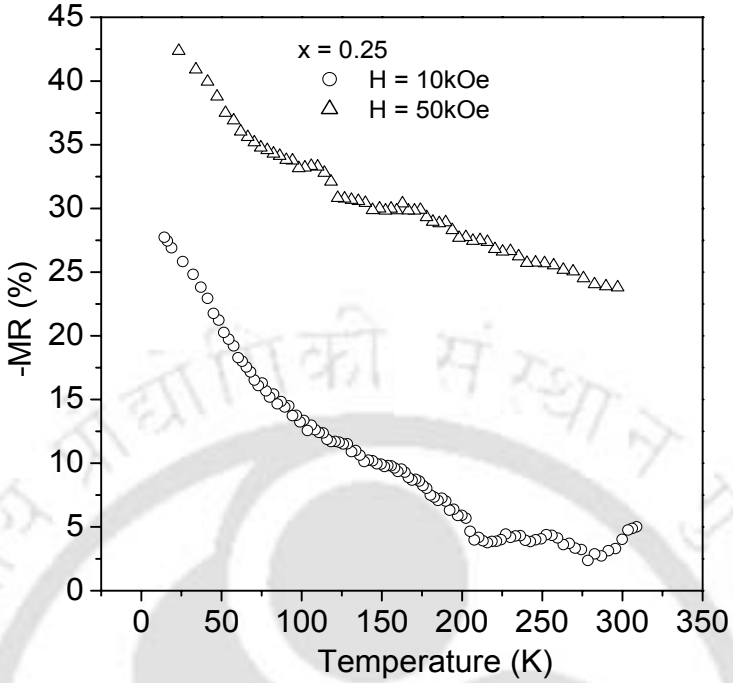

Fig. 3.25: Temperature variation of negative magneto-resistivity measured at 10kOe (circles) and 50kOe (triangles) fields for $Ba_{0.75}La_{0.25}MnO_3$ (x = 0.25).

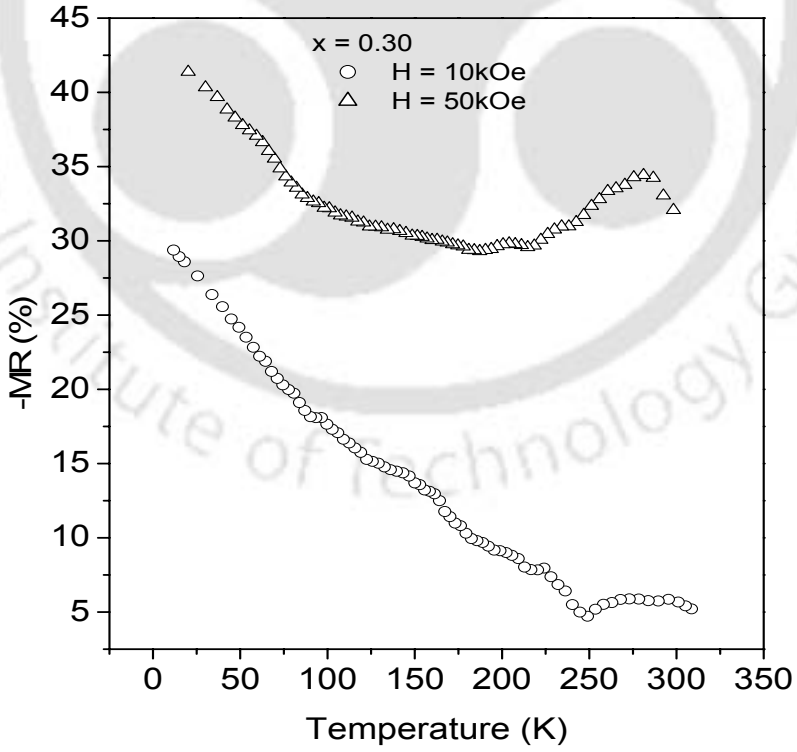

Fig. 3.26: Temperature variation of negative magneto-resistivity measured at 10kOe (circles) and 50kOe (triangles) fields for $Ba_{0.7}La_{0.3}MnO_3$ (x = 0.30).

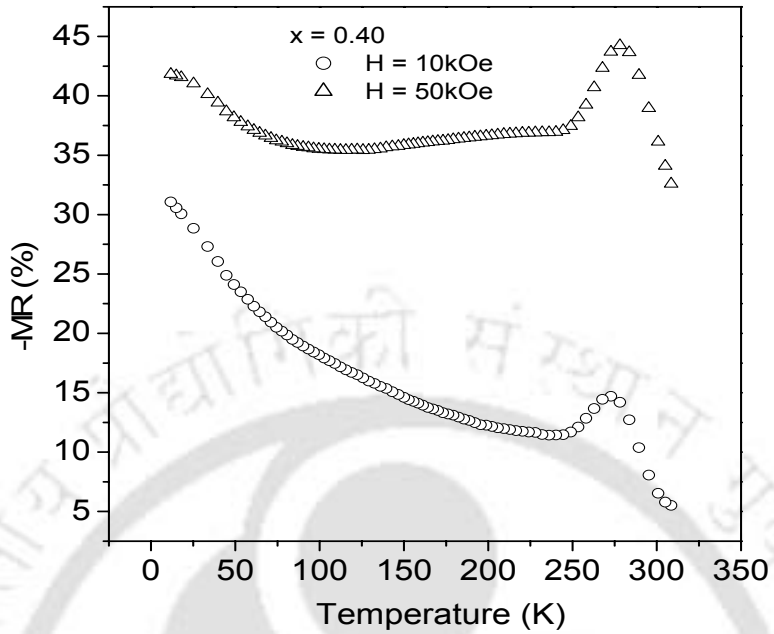

Fig. 3.27: Temperature variation of negative magneto-resistivity measured at 10kOe (circles) and 50kOe (triangles) fields for $Ba_{0.6}La_{0.4}MnO_3$ (x = 0.40).

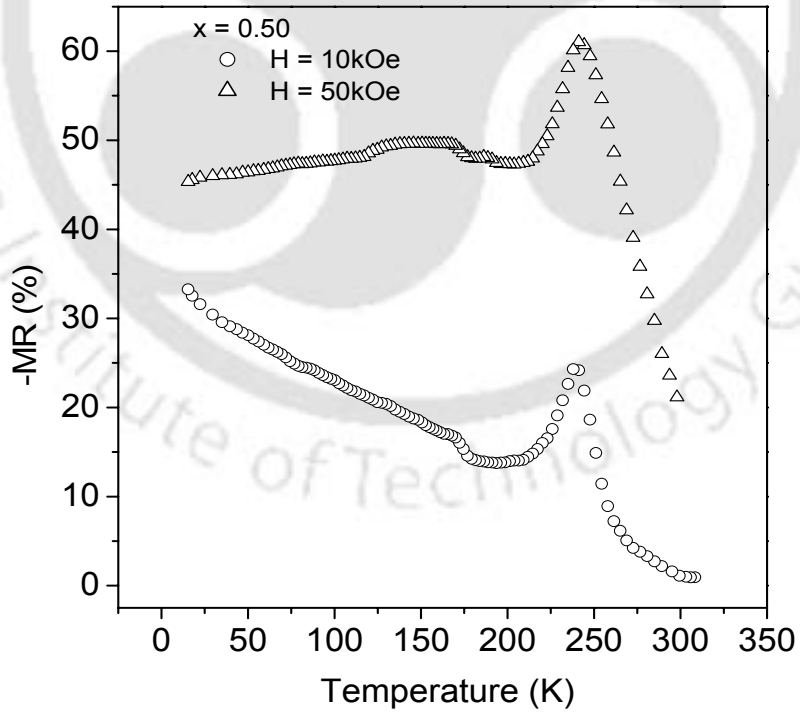

Fig. 3.28: Temperature variation of negative magneto-resistivity measured at 10kOe (circles) and 50kOe (triangles) fields for $Ba_{0.5}La_{0.5}MnO_3$ (x = 0.50).

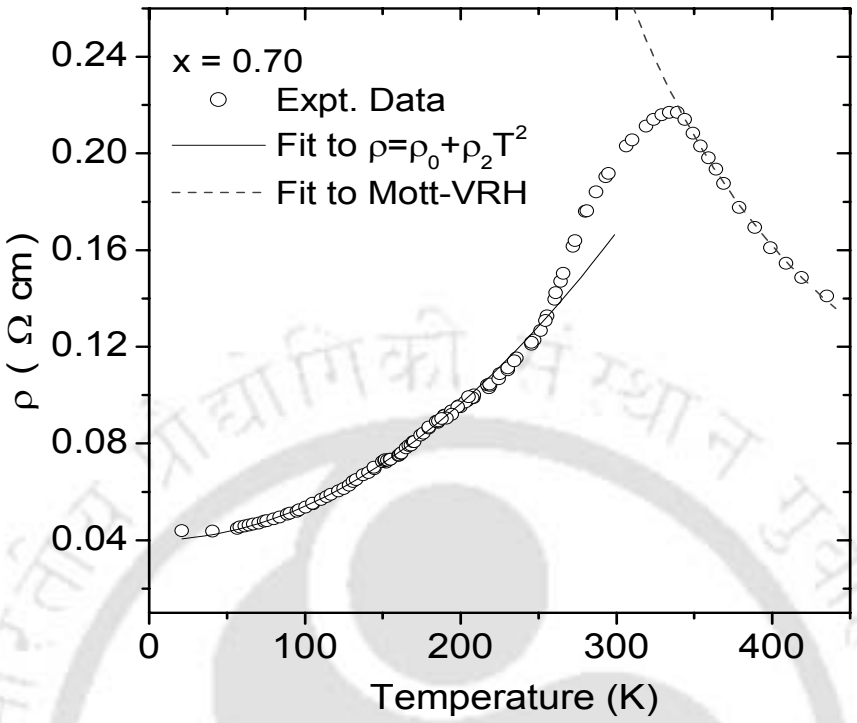

Fig. 3.29: Electrical resistivity as a function of temperature for $Ba_{0.3}La_{0.7}MnO_3$ (x = 0.70) sample. The experimental data are shown as circles. Solid line represents the fit to eqn. $\rho = \rho_0 + \rho_2 T^2$ and dotted lines represent the fit to Mott-VRH model.

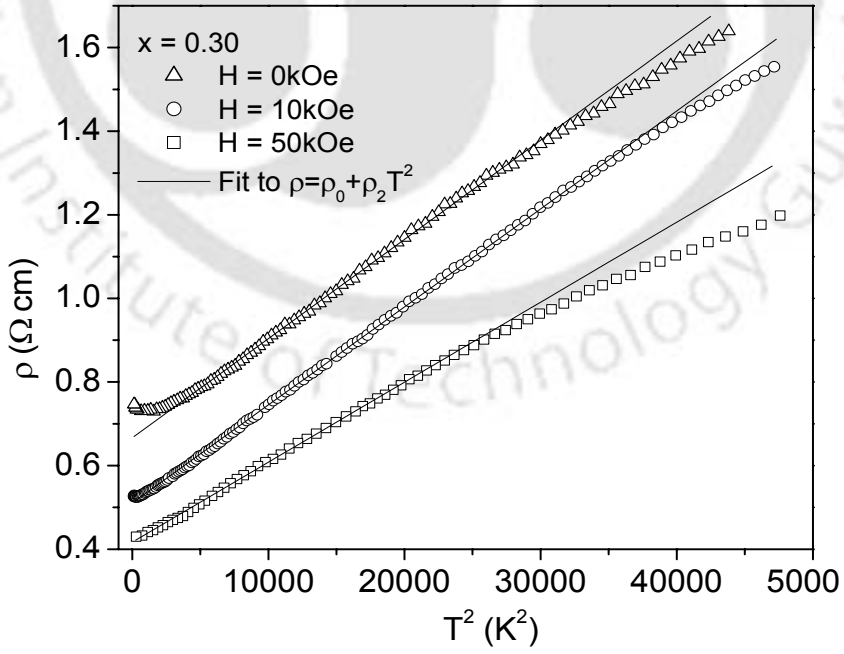

Fig. 3.30: Electrical resistivity as a function of T^2 for $Ba_{0.7}La_{0.3}MnO_3$ (x = 0.30) sample for 0, 10 and 50kOe fields. Solid lines represent the fit to eqn. $\rho = \rho_0 + \rho_2 T^2$.

Table 3.8: Parameters obtained from electrical resistivity fitting below T_{MI}. Data have been fitted to the equation $\rho = \rho_0 + \rho_2 T^2$.

Parameters / Samples	ρ_0(Ωcm)			ρ_2 ($\times 10^{-4}$Ωcm)			rmsd (%)		
	0kOe	10kOe	50kOe	0kOe	10kOe	50kOe	0kOe	10kOe	50kOe
x = 0.20	20.427 ±0.018	15.625 ±0.021	12.389 ±0.027	9.211 ±0.015	9.198 ±0.019	6.327 ±0.014	0.85	1.03	1.32
x = 0.25	5.478 ±0.004	4.390 ±0.004	3.479 ±0.014	2.093 ±0.003	2.149 ±0.004	1.596 ±0.008	1.9	2.3	0.7
x = 0.30	1.049 ±0.002	0.785 ±0.001	0.651 ±0.001	0.358 ±0.001	0.3679 ±0.0001	0.2897 ±0.0007	1.6	0.4	0.8
x = 0.40	0.4895 ±0.0004	0.3725 ±0.0002	0.3088 ±0.0003	0.1227 ±0.0002	0.1268 ±0.0002	0.0835 ±0.0002	2.3	1.6	1.3
x = 0.50	---	---	---	---	---	---	---	---	---
x = 0.60	0.0850 ±0.0001	---	---	0.0324 ±0.00014	---	---	1.5		
x = 0.70	0.0397 ±0.0001	---	---	0.0143 ±0.0004	---	---	1.1		
x = 0.80	0.3925 ±0.0001	---	---	0.0366 ±0.0001	---	---	1.2		

3.2. $Sr_{1-x}La_xMnO_3$ (x = 0 to 0.82) Compounds

In this section the preparation and characterization of electron doped $Sr_{1-x}La_xMnO_3$ compounds and their electrical transport and magnetic properties are reported. A few hole doped materials in this series are also discussed for comparison.

3.2.1. Preparation

$Sr_{1-x}La_xMnO_3$ compounds were prepared for x = 0, 0.10, 0.15, 0.20, 0.25, 0.30, 0.40, 0.50, 0.70 and 0.82 by following conventional solid state route. Stoichiometric ratio of starting compounds such as La_2O_3 (99.9%), $SrCO_3$ (99%) and $C_4H_6MnO_4.4H_2O$ (99.5%) were weighed and mixed thoroughly under acetone with the help of agate mortar & pestle. The mixture was presintered at 800^0C for 30 hours with an intermediate grinding at room temperature. The presintered powder was pressed into cylindrical pellets of 13mm diameter and 2 to 5mm thickness by using a hand operated hydraulic press with a maximum load capacity of 6 Ton/cm^2. The sintering in pellet form was carried out at 1000^0C for 8 hours. The pellets were crushed into fine powder and repelletized for better homogeneity. These pellets were again annealed at 1050^0C for 10 hours and then at 1100^0C for 6 hours with an intermediate grinding and repelletizing at room temperature. The final sintering was carried out at 1250^0C for over 72 hours with intermediate grindings and repelletizing at the interval of 24 hours. All the above annealing processes were carried out in air and the samples were furnace cooled after final sintering.

3.2.2. Characterization

X-ray diffraction (XRD) patterns were recorded at room temperature for all the above materials. XRD patterns of parent compound $SrMnO_3$ (x = 0) and electron doped materials in the composition range x = 0.10 to 0.20 are shown in Fig. 3.31. XRD patterns of x = 0 and x = 0.10 samples are found to be essentially in single phase form. They could be indexed to $P6_3$ space group with hexagonal symmetry. For x = 0.15 & 0.20 minor extra peaks at 2θ = 40.5 and 47.1^0 are observed. XRD patterns for x = 0.25 to 0.50 are shown in Fig. 3.32 and for x = 0.70 and 0.82 are shown in Fig. 3.33. The materials exhibit structural transition from hexagonal symmetry with $P6_3$ space group to rhombohedral symmetry with $R\bar{3}c$ space group. The XRD patterns for x = 0.40 to 0.82 could be indexed to $R\bar{3}c$

space group. The two extra peaks appearing at 40.5 and 47.1^0 for x = 0.15 to 0.30 are basically due to the presence of minor $R\bar{3}c$ structure, which can be seen by comparing the patterns of higher doped materials. For x = 0.40, the pattern could be mostly indexed to $R\bar{3}c$ space group. However traces of minor peaks corresponding to $P6_3$ space group also appear as marked by hollow circles. Thus the material is undergoing structural transition in the composition range x = 0.30 & 0.40 and there is a presence of minor peaks due to alternate structure. Such secondary peaks are observed even in two stage prepared samples [217].

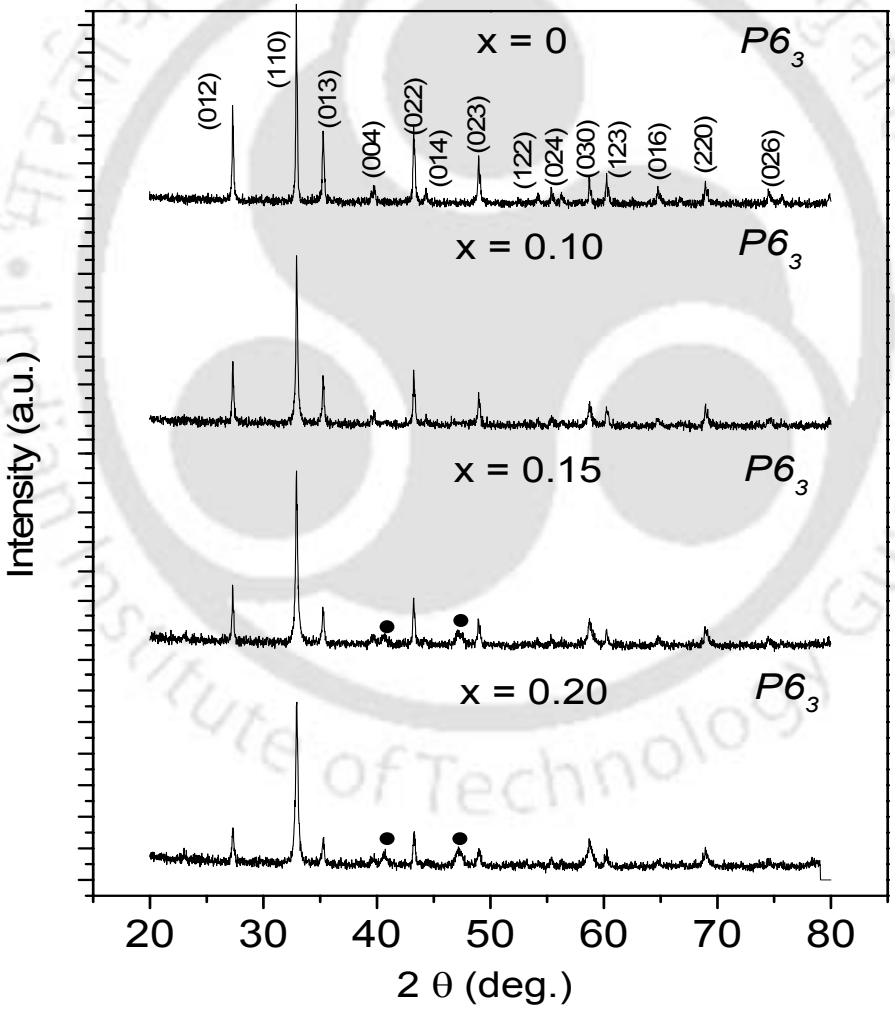

Fig. 3.31: XRD patterns of $Sr_{1-x}La_xMnO_3$ for x = 0, 0.10, 0.15 and 0.20. Solid circles represent the peaks due to minor secondary crystal structure, i.e. $R\bar{3}c$ space group.

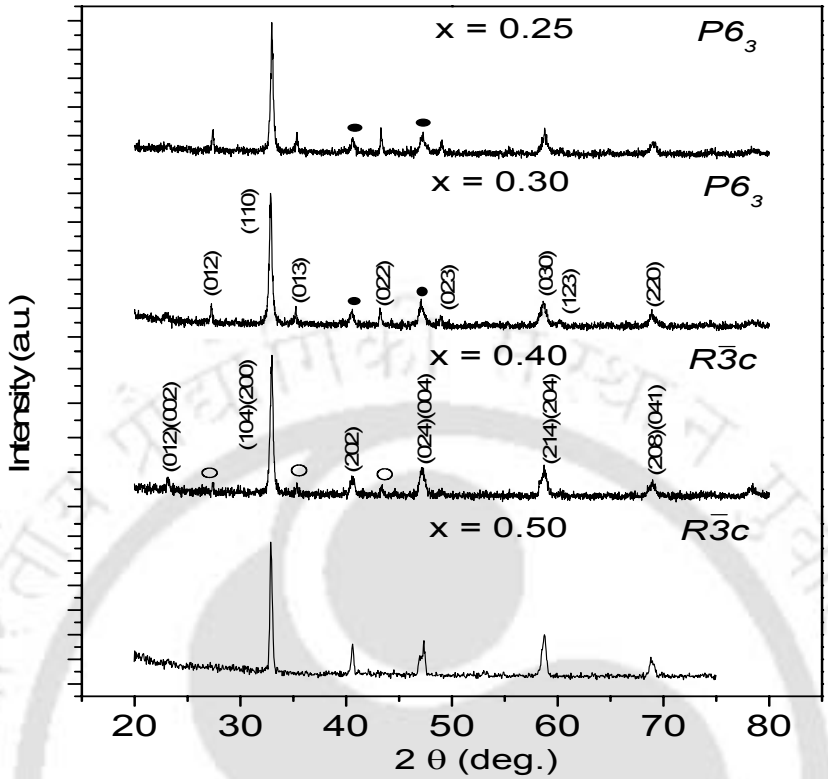

Fig. 3.32: XRD patterns of $Sr_{1-x}La_xMnO_3$ for x = 0.25, 0.30, 0.40 and 0.50. Solid and hollow circles represent the peaks due to minor secondary crystal structure, i.e. $R\bar{3}c$ and $P6_3$ space groups respectively.

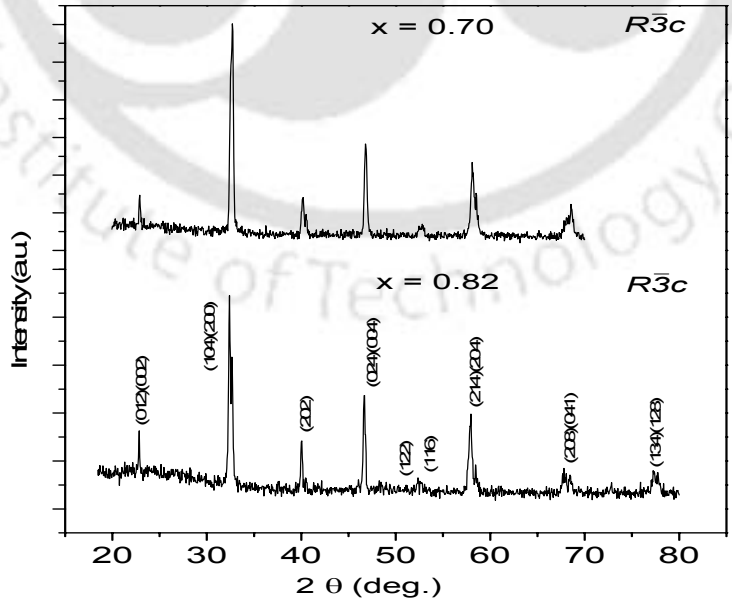

Fig. 3.33: XRD patterns of $Sr_{1-x}La_xMnO_3$ for x = 0.70 and 0.82 (hole doped materials).

The lattice parameters were obtained by carrying out Rietveld refinement with the help of Fullprof program [191]. Typical XRD patterns along with Rietveld refinements are shown in the Figs. 3.34 - 3.37 for the samples x = 0.10, 0.30, 0.50 and 0.70. Here the experimental data are shown as crosses (+) and calculated intensities are shown as solid lines. The dotted lines represent the difference between measured and calculated intensities. The typical values of refined parameters such as atomic position, isotropic displacement (temperature) parameter and occupancy values are given in Table 3.9 for x = 0.10 sample and Table 3.10 for x = 0.70 sample. The reliability factors R_p, $R_{\omega p}$, R_{exp}, R_{Bragg}, R_F and χ^2 for all the above samples are tabulated in Table 3.11.

The space groups, unit cell volume and lattice parameters for all the samples are listed in Table 3.11. The lattice parameters for electron doped materials are comparable with the reported value [217]. The lattice parameter 'a' and unit cell volume are found to mostly increase with decrease of 'Sr' concentration. The above result is comparable to that observed in $Ba_{1-x}La_xMnO_3$ series as given in the previous section (section 3.1.2).

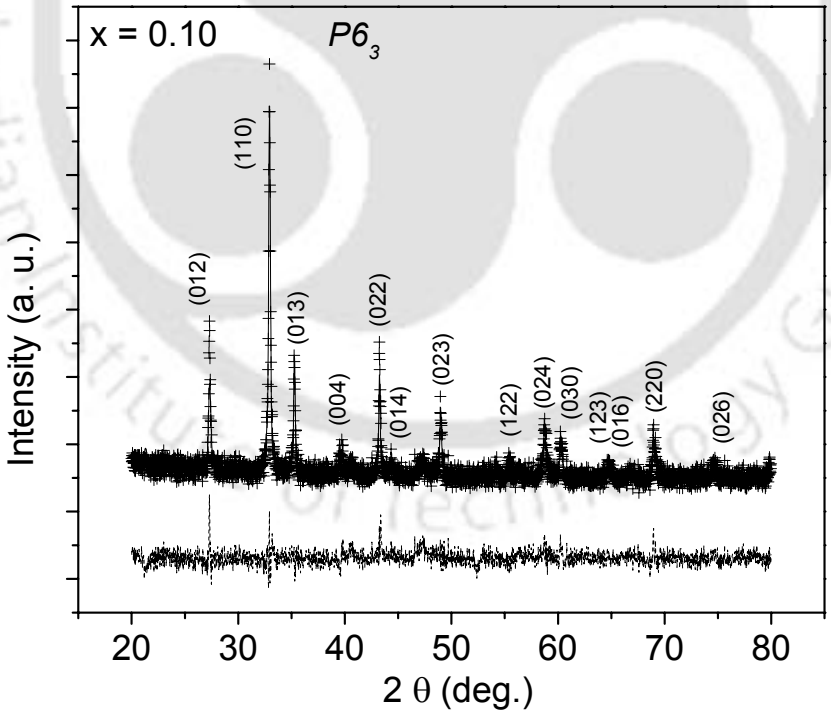

Fig. 3.34: XRD patterns with Rietveld refinement for $Sr_{0.9}La_{0.1}MnO_3$ (x = 0.10). The recorded data, refined data and the difference between them are shown as crosses, solid line and dashed lines respectively.

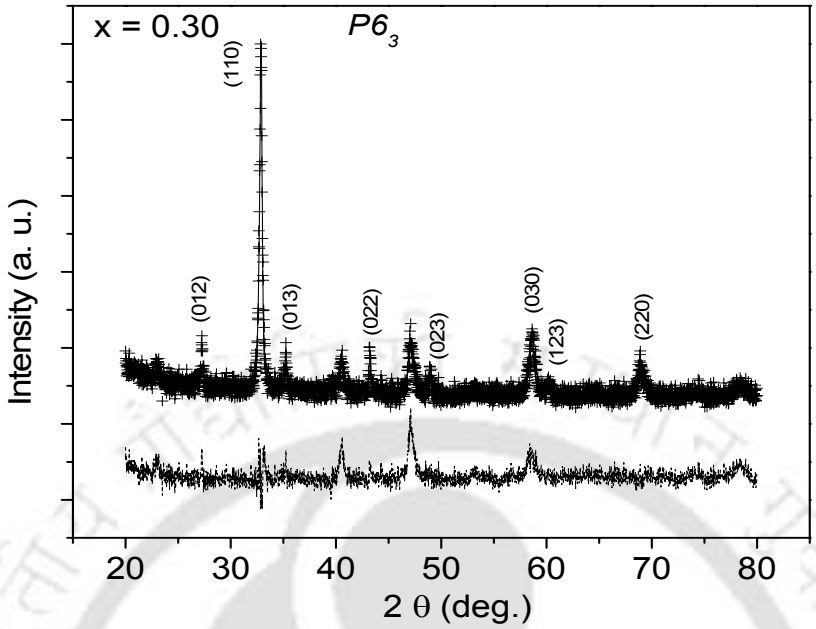

Fig. 3.35: XRD patterns with Rietveld refinement for $Sr_{0.7}La_{0.3}MnO_3$ (x = 0.30). The recorded data, refined data and the difference between them are shown as crosses, solid line and dashed lines respectively.

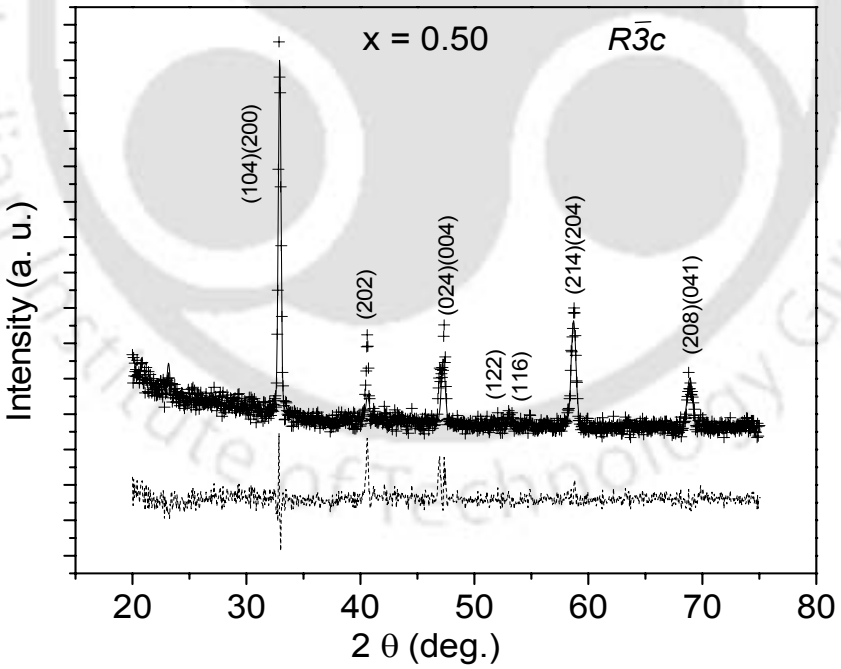

Fig. 3.36: XRD patterns with Rietveld refinement for $Sr_{0.5}La_{0.5}MnO_3$ (x = 0.50). The recorded data, refined data and the difference between them are shown as crosses, solid line and dashed lines respectively.

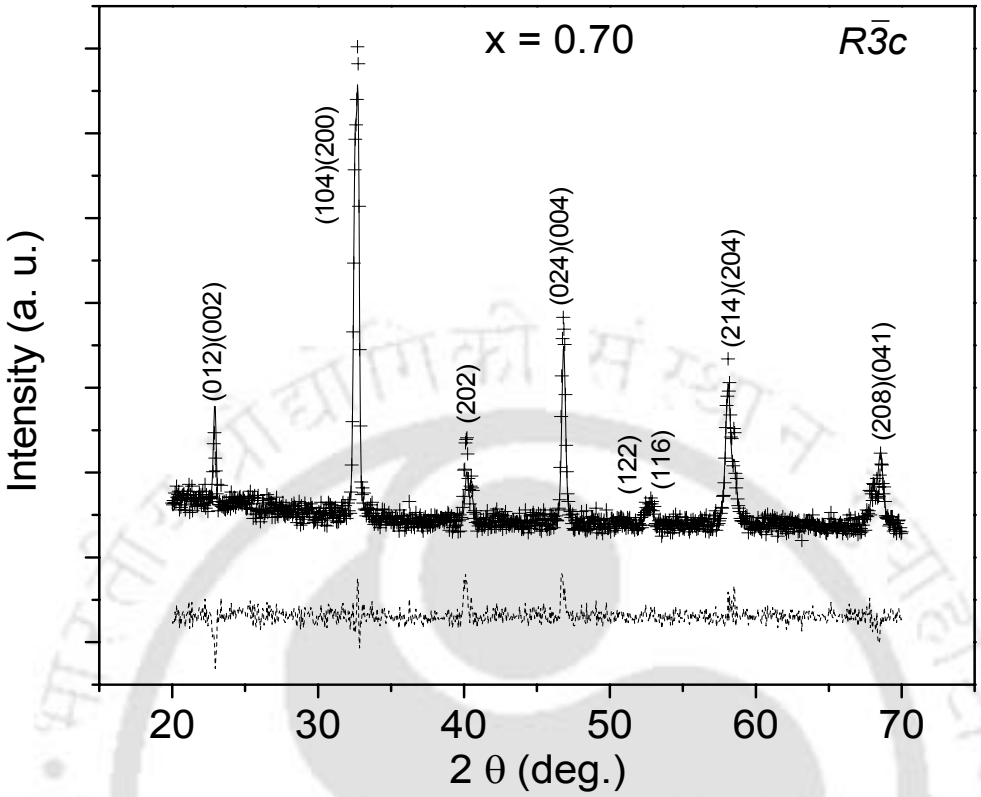

Fig. 3.37: XRD patterns with Rietveld refinement for $Sr_{0.3}La_{0.7}MnO_3$ (x = 0.70, hole doped sample). The recorded, refined and the difference in intensity are shown as crosses, solid line and dashed lines respectively.

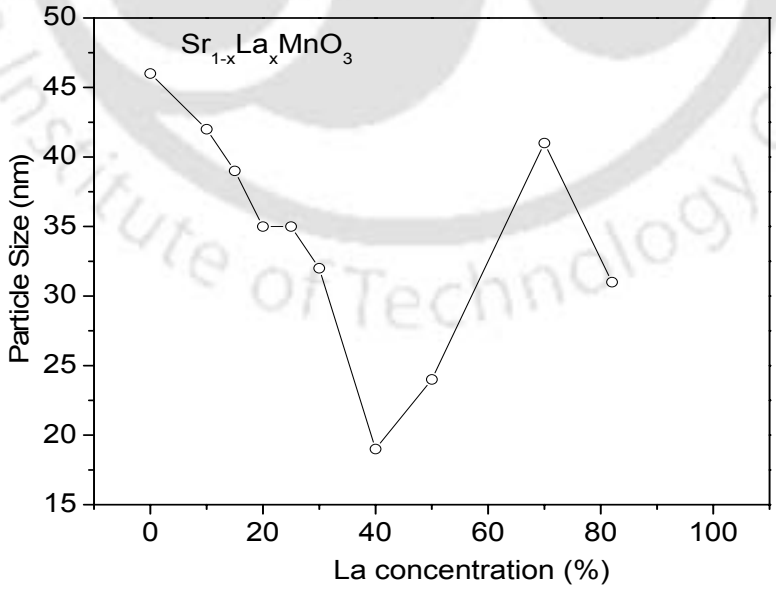

Fig. 3.38: Plots of particle size versus the percentage of 'La' concentration.

The particle size (S_G) is estimated from the width of the XRD peak and using the eqn. 2.11. These values are listed in Table 3.11. It is found that the particle size decreases with 'La' doping up to x = 0.40 and then start increasing. The values are found to be in nanometer range. These values are comparable with other manganites [213]. For the sake of clarity the concentration versus particle size is shown in Fig. 3.38.

The average valency of 'Mn' ions determined from the chemical titration for the above compounds are listed in Table 3.12. The measured values suggest that, for x < 0.50 the materials are rich in Mn^{4+} concentration as expected and x = 0.70 and 0.82 (hole doped) materials are rich in Mn^{3+} concentration. The marginal difference between expected and actual 'Mn' valency could be mainly due to oxygen off-stoichiometry. Such oxygen off-stoichiometry has been reported by other groups [208, 210] in the manganite perovskites.

Typical optical microscopes recorded for x = 0.30 and 0.50 samples with a magnification of 40 is shown in Fig. 3.39 and 3.40 respectively. We can see almost uniform morphology throughout the material.

The SEM photograph has been taken for the sample x = 0.30 and is shown in Fig. 3.41 for a magnification of 5,000. The composition of the sample from EDAX measurement is found to be $(Sr_{0.653}La_{0.318})Mn_{1.029}O_3$ and it is comparable to the starting composition $Sr_{0.7}La_{0.3}MnO_3$. The 'Mn' valency from the above compositional analysis is found to be 3.62 and it is comparable to that obtained from chemical titration (i.e. 3.68).

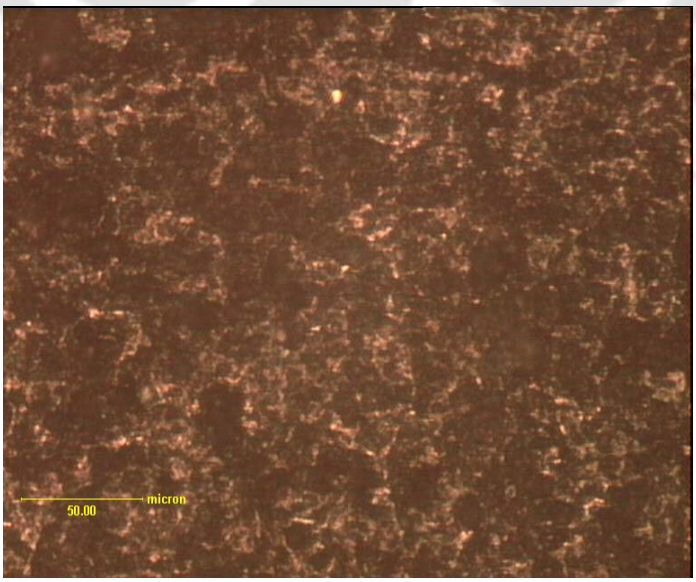

Fig. 3.39. Optical micrograph (magnification-40) of the $Sr_{0.7}La_{0.3}MnO_3$ sample.

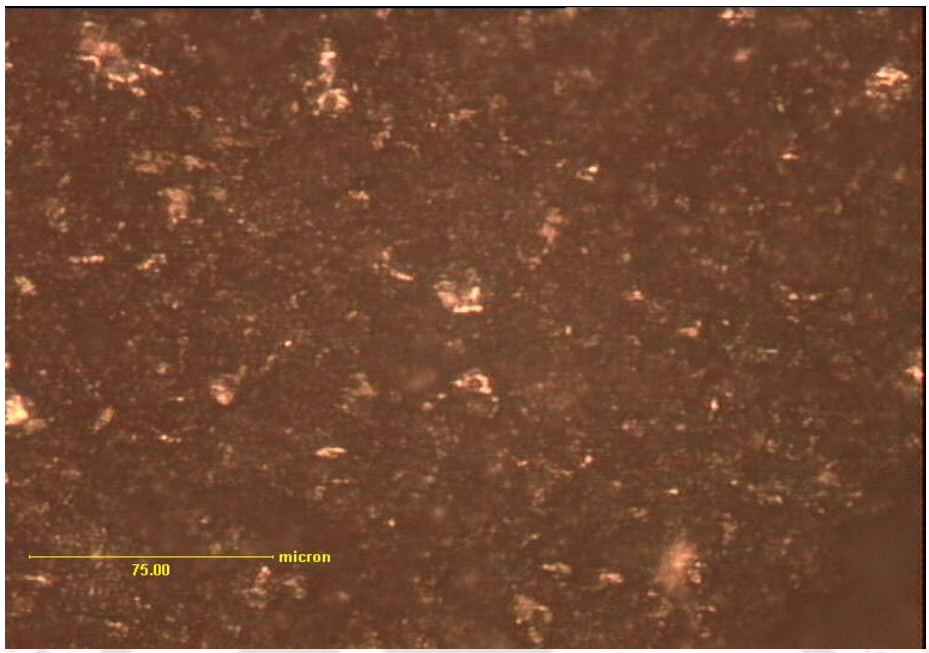

Fig. 3.40: Optical micrograph (magnification-40) of the sample $Sr_{0.5}La_{0.5}MnO_3$.

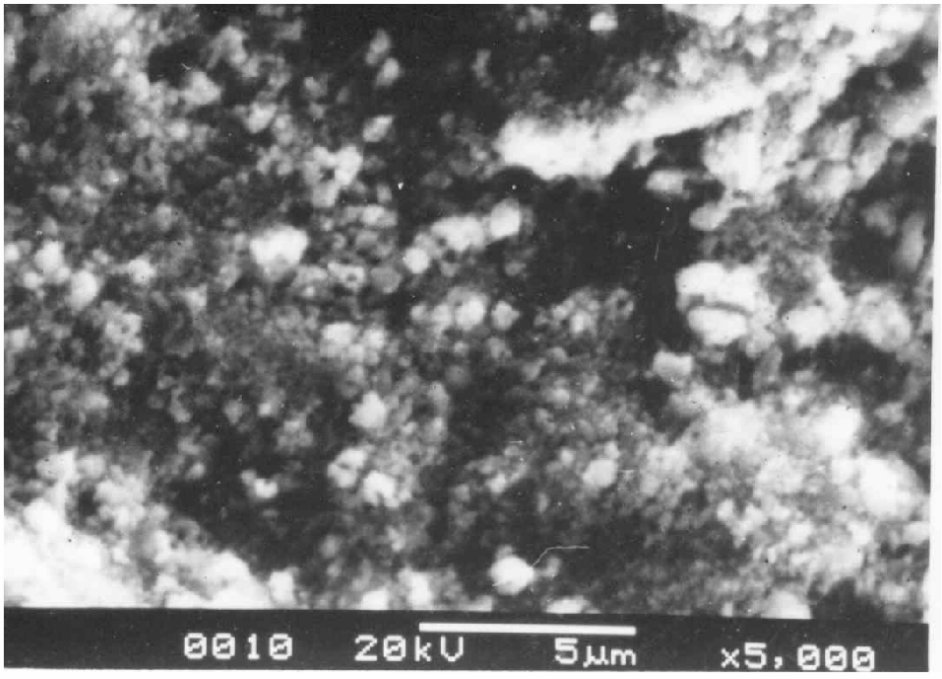

Fig. 3.41: SEM photograph (magnification-5,000) for the sample $Sr_{0.7}La_{0.3}MnO_3$.

Table 3.9: Parameters obtained from the Rietveld analysis of XRD pattern of the sample $Sr_{0.9}La_{0.1}MnO_3$ (x = 0.10). The XRD pattern has been refined using *P6₃* space group. The lattice parameters are a = b = 5.438Å and c = 9.068Å. Biso is the isotropic displacement (temperature) parameter and Occ is the occupancy number.

Parameters	Fractional coordinates			Biso	Occ
Atoms	x	y	z	Å^2	
Sr1	0.0000	0.0000	0.0000	1.13	0.887
Sr1	0.3333	0.6666	0.2500	1.82	0.887
La1	0.0000	0.0000	0.0000	1.13	0.096
La2	0.3333	0.6666	0.2500	1.82	0.096
Mn1	0.3333	0.6666	0.5857	0.57	0.998
Mn2	0.3333	0.6666	0.8677	0.51	0.998
O1	0.57981	0.02937	0.01965	0.35	1.000
O2	-0.2200	-0.3666	0.2700	0.35	1.000

Table 3.10: Parameters obtained from the Rietveld analysis of XRD pattern of the sample $Sr_{0.30}La_{0.70}MnO_3$ (x = 0.70). The XRD pattern has been fitted to $R\bar{3}c$ space group. The lattice parameters are a = b = 5.516Å and c = 13.384Å. Biso is the isotropic displacement (temperature) parameter and Occ is the occupancy number.

Parameters	Fractional coordinates			Biso	Occ
Atoms	x	y	z	(Å^2)	
Ba	0.0000	0.0000	0.2500	0.92	0.690
La	0.0000	0.0000	0.2500	0.92	0.296
Mn	0.0000	0.0000	0.0000	0.38	0.988
O	0.5641	0.0000	0.2500	0.74	1.000

Table 3.11: Parameters obtained from the XRD analysis of the samples $Sr_{1-x}La_xMnO_3$ (x = 0.0, 0.10, 0.15, 0.20, 0.25, 0.30, 0.40, 0.50, 0.70 and 0.82). R_p, $R_{\omega p}$, R_{exp}, R_{Bragg}, R_F and χ^2 are the reliability factors. 'G' is the occupancy of different materials. 'S_G' is the average particle size calculated from the line broadening of the XRD pattern.

Samples Parameters	x = 0.0	x = 0.10	x = 0.15	x = 0.20	x = 0.25	x = 0.30	x = 0.40	x = 0.50	x = 0.70	x = 0.82
Space Group	$P6_3$	$P6_3$	$P6_3$	$P6_3$	$P6_3$	$P6_3$	$R\bar{3}c$	$R\bar{3}c$	$R\bar{3}c$	$R\bar{3}c$
a (Å)	5.429	5.438	5.441	5.442	5.446	5.448	5.458	5.476	5.516	5.525
c (Å)	9.047	9.068	9.071	9.074	9.079	9.072	13.389	13.389	13.384	13.363
G_{Sr}	0.993	0.887	0.836	0.804	0.724	0.716	0.603	0.469	0.296	0.172
G_{La}	---	0.096	0.144	0.199	0.223	0.250	0.375	0.455	0.690	0.823
G_{Mn}	0.992	0.998	0.998	0.978	0.979	0.983	0.981	0.960	0.988	0.980
R_p	11.6	11.8	11.9	14.3	13.9	14.7	13.4	15.8	11.2	13.5
$R_{\omega p}$	15.2	14.9	15.1	16.2	17.9	18.8	17.5	20.6	15.0	17.5
R_{exp}	10.3	12.5	12.6	13.4	14.5	14.2	15.4	13.83	11.8	13.7
R_{Bragg}	16.0	15.3	17.6	17.8	19.5	22.6	8.9	16.4	9.5	15.0
R_F	13.6	13.4	18.2	14.2	13.8	21.9	12.3	13.2	5.8	14.2
χ^2	1.83	1.42	1.42	1.45	1.53	1.75	1.29	1.74	1.61	1.63
Volume ($Å^3$)	231.7	232.2	232.5	232.7	233.2	233.2	345.3	347.8	352.7	353.2
S_G (nm)	46	42	39	35	35	32	19	24	41	37

3.2.3. AC Susceptibility Study

Temperature variations of ac susceptibility have been measured for all the above samples in the temperature range 420 to 30 K.. Plots of temperature variation of in-phase ac susceptibility (χ') for the electron doped samples $Sr_{1-x}La_xMnO_3$ for x = 0.10, 0.15, 0.20, 0.25, 0.30, 0.40 and 0.50 are shown in Figs. 3.42 - 3.44. For $x \leq 0.30$, the materials exhibit PM to FM transition with a weak FM saturation signal. A secondary rise in susceptibility followed by a broad peak has been observed below 300K. Further reduction in temperature results sharp fall in susceptibility. The secondary rise in χ' can be attributed to the onset of competing antiferromagnetic interaction (T_{aon}). Parent compound, $SrMnO_3$ is found to exhibit AFM transition at 280K, which is relatively higher than the value reported in literature [62] and this could be mainly due to oxygen off-stoichiometry. All the electron doped materials, $x \leq 0.50$ exhibit such a transition from FM phase to AFM.

For a comparison, the χ' versus T plots for two hole doped materials, x = 0.70 and 0.82 are given in Fig. 3.45. They exhibit PM to FM transition without any trace of AFM ordering. The linear decrease in susceptibility below the saturation values are mainly due to magnetic anisotropy and domain structure. The transition temperature and saturation susceptibility of x = 0.82 sample is found to be smaller compared to x = 0.70 sample. Similar trend has been observed in $Ba_{1-x}La_xMnO_3$ compounds. Thus, the optimum doping for high FM T_c is $x \approx 0.70$ in hole doped region. The T_{on} value for x = 0.70 sample is found to be 404K and it is comparable to that reported by Urushibara et al. [26].

For the entire electron doped materials, no appreciable change in FM onset temperature is observed. The T_{on} values vary from 389K for x= 0.10 to 402K for x = 0.50. On the other hand, the maximum susceptibility values continuously increase with increase in 'La' concentration. The saturation susceptibility values, χ'_s at the end of FM transition are tabulated in Table 3.12. The increase in χ'_s values with 'La' concentration can be understood as a result of enhanced intensity of double exchange interaction due to increase in concentration of Mn^{3+} ions. For clarity the χ'_s values are plotted as a function of doping concentration and they are shown in Fig. 3.47 as squares. The observed variation is comparable to that observed in 'Ba' based electron doped materials ($Ba_{1-x}La_xMnO_3$). However, the magnitude of χ'_s in (Sr,La)-Mn-O series is found to be quite small compared to the (Ba,La)-Mn-O series. This can be explained on the basis of large 'e_g' band width of 'Mn' ions in (Ba,La)-Mn-O series due to large ionic size of 'Ba' compared to 'Sr'.

The mid-point of ferromagnetic transition temperature, T_c was determined from the temperature corresponding to peak in $|d\chi'/dT|$ versus T plot and these values are listed in Table 3.12. For the sake of clarity the variation of χ'_s with 'La' concentration is shown in Figure 3.47 (circles). The T_c value of x = 0.82 sample is found to be 340 K and it is not shown in the figure.

The AFM Neel temperature, T_N was taken as the temperature corresponding peak observed below FM transition. The T_N values along with FM transition temperature T_c are tabulated in Table 3.12.

The temperature variations of out of phase susceptibility for all the above samples are shown in Fig. 3.46. These values increase with decrease in temperature from the onset of FM transition. Below Neel temperature, the loss components mostly decrease with decrease in temperature.

Table 3.12: Parameters obtained from the chemical titration and ac susceptibility measurements. The T_{on}(K) and T_c(K) are the ferromagnetic transition onset and mid point temperatures respectively. χ'_s(emu/gmOe) is the saturation susceptibility. The error in T_{on}, T_N and T_{DL} is ±2K and, for T_c is ±1K.

Parameters / Samples	'Mn' Valency	T_{on}(K)	T_c(K)	T_N (K)	χ'_s(emu/gmOe)	T_{DL}(K)
x = 0.0	4.01	---	---	---	---	---
x = 0.10	3.88	389	375	260	0.008	270
x = 0.15	3.85	389	375	251	0.009	270
x = 0.20	3.83	393	375	221	0.011	295
x = 0.25	3.77	396	381	235	0.014	280
x = 0.30	3.68	402	386	238	0.018	290
x = 0.40	3.54	402	388	241	0.022	312
x = 0.50	3.5	402	393	241	0.024	320
x = 0.70	3.27	404	393	---	0.084	---
x = 0.82	3.19	348	340	---	0.070	---

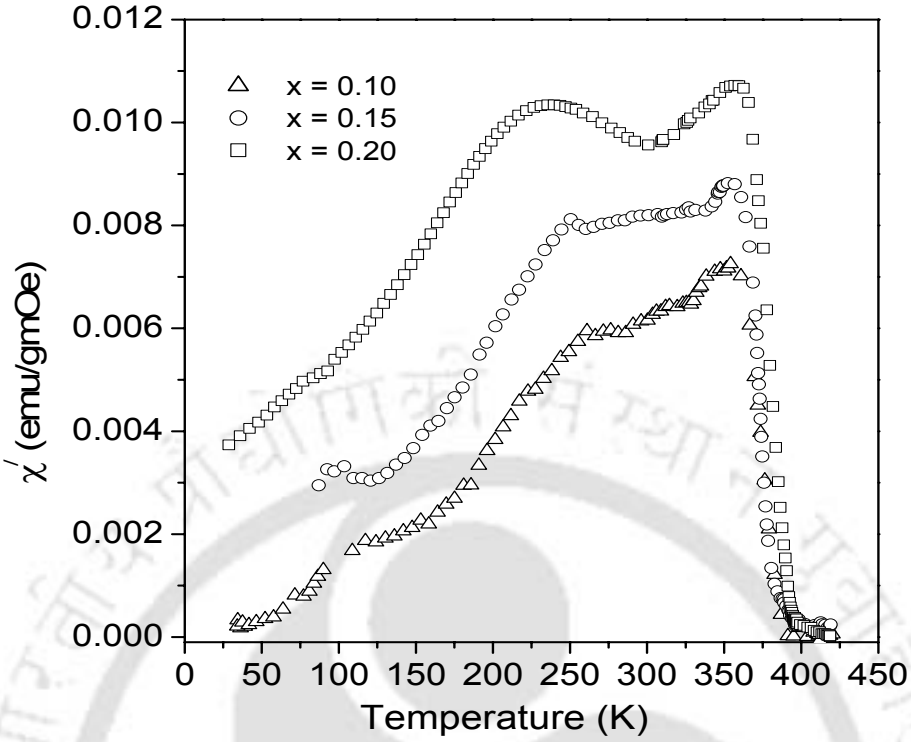

Fig. 3.42: Temperature variation of in-phase ac susceptibility (χ') for the samples $Sr_{1-x}La_xMnO_3$ for x = 0.10 (triangles), 0.15 (circles) and 0.20 (squares).

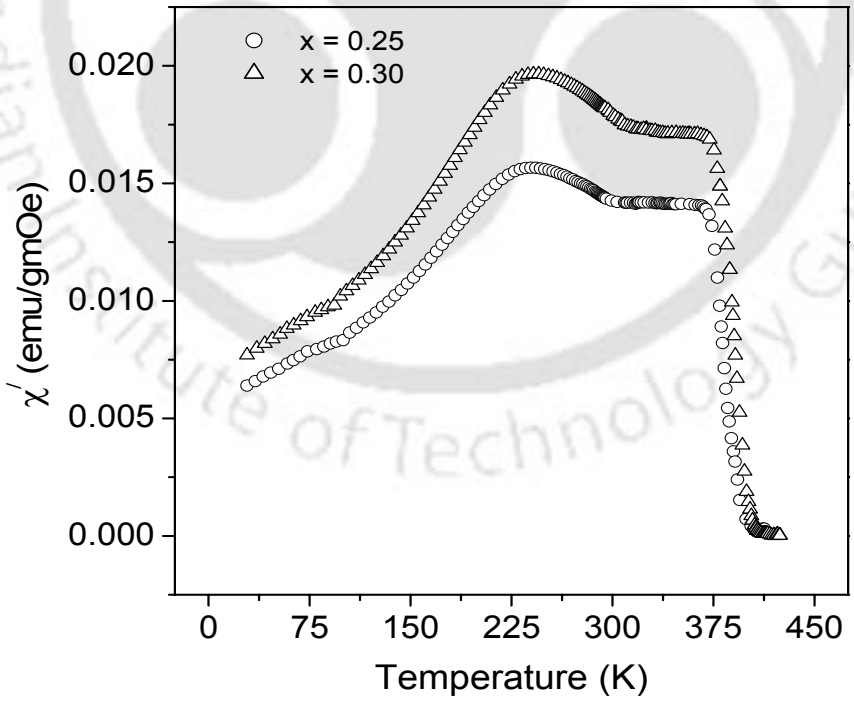

Fig. 3.43: Temperature variation of in-phase ac susceptibility (χ') of samples $Sr_{1-x}La_xMnO_3$ for x = 0.25 (circles) and 0.30 (triangles).

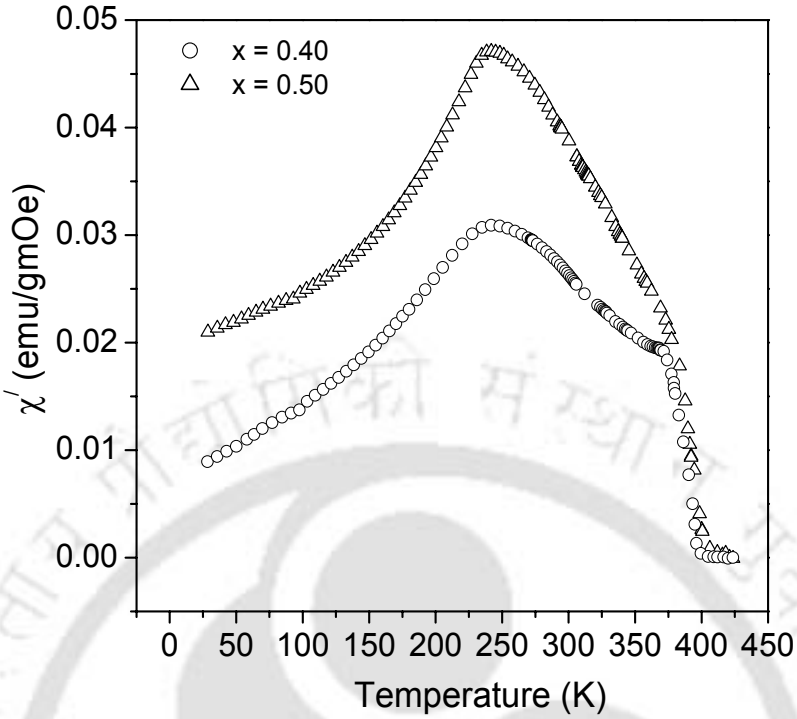

Fig. 3.44: Temperature variation of in-phase ac susceptibility (χ') of samples $Sr_{1-x}La_xMnO_3$ for x = 0.40 (circles) and 0.50 (triangles).

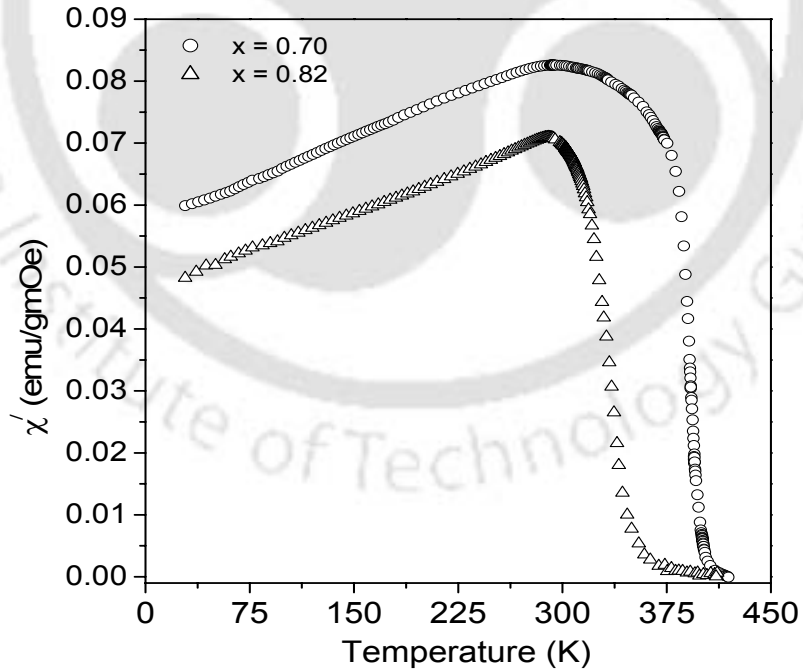

Fig. 3.45: Temperature variation of in-phase ac susceptibility (χ') of hole doped samples $Sr_{1-x}La_xMnO_3$ for x = 0.70 (circles) and 0.82 (triangles). These are hole doped materials.

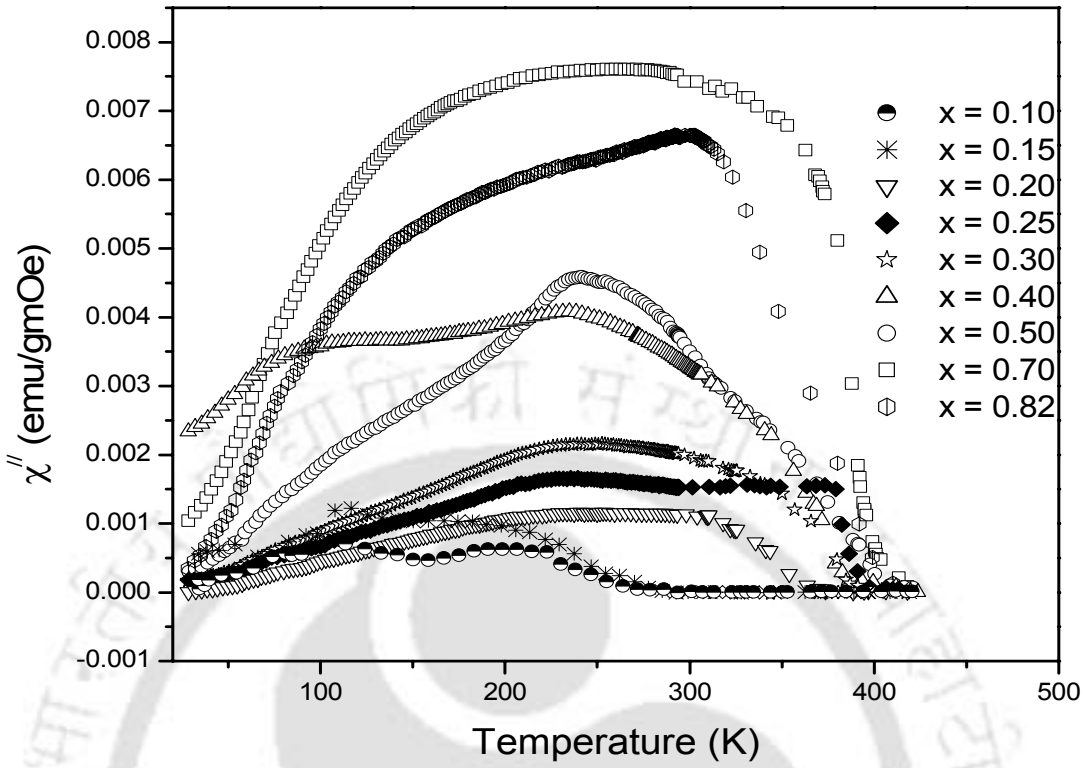

Fig. 3.46: Temperature variation of out of phase ac susceptibility ($\chi^{//}$) of samples $Sr_{1-x}La_xMnO_3$.

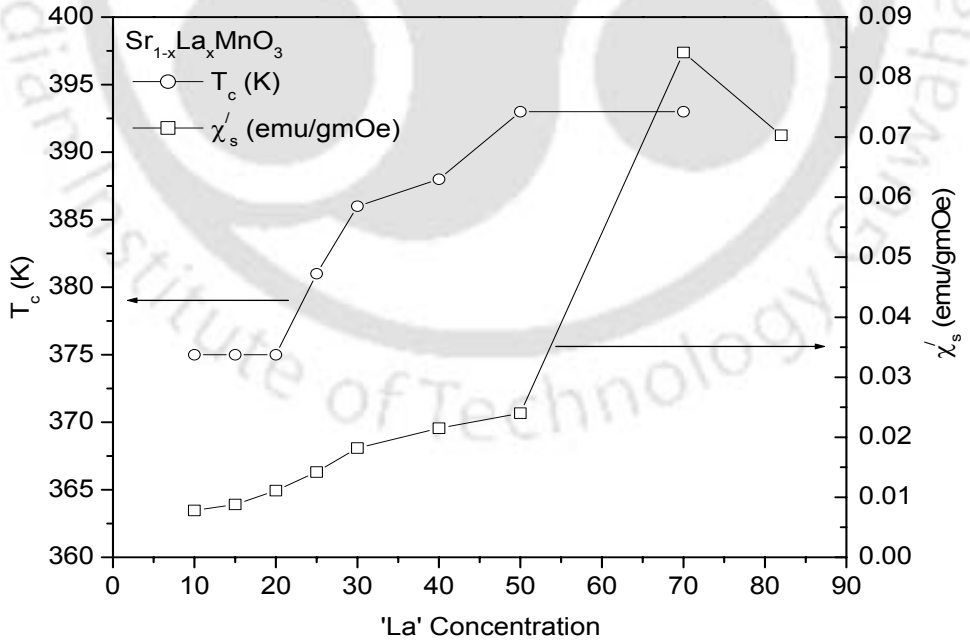

Fig. 3.47: Plots of T_c(circles) and χ'_s (squares) versus the percentage of doped 'La' concentration.

For the sake of comparison, typical DC magnetization as a function of temperature for x = 0.30 sample from 80K to 300K are shown in Fig. 3.48 for both ZFC and FC cases. It is observed that, the T_{aon} is close to the value observed from ac susceptibility measurement. The T_c value is above the room temperature. There is a large difference between the ZFC (circles) and FC (squares) curves and it is similar to that observed in $Ba_{1-x}La_xMnO_3$ series and is discussed in section 3.1.3.

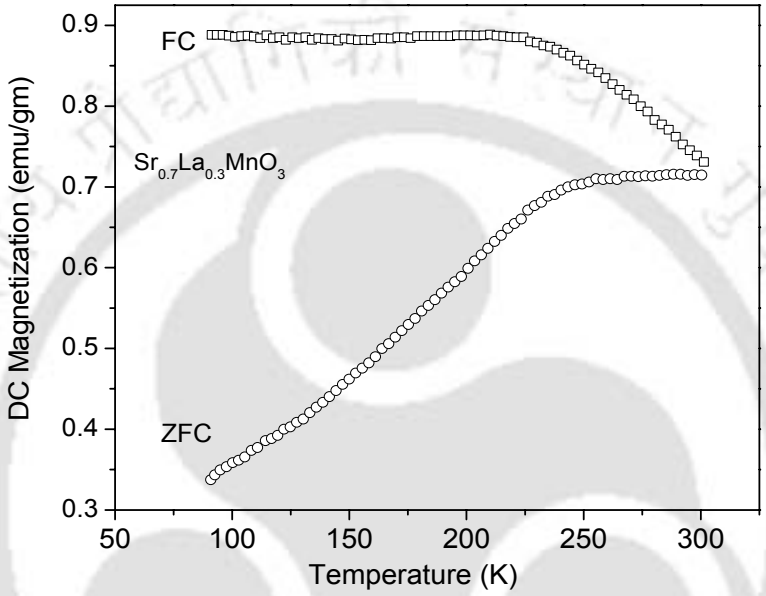

Fig. 3.48: Plot of temperature variation of DC magnetization of the sample $Sr_{1-x}La_xMnO_3$ (x = 0.30) in ZFC (circles) and FC (squares) conditions.

3.2.4. Electrical Resistivity Study

Temperature variation of electrical resistivity (ρ) was measured from 30 to 420K for all the above samples. For the sake of clarity and comparison of ρ versus T of different samples, plots of $\log_{10}[\rho]$ versus T are shown in Fig. 3.49 for the samples x = 0.10 - 0.50. All the electron doped materials are found to exhibit semiconducting behaviour. Change of slope in resistivity curves in logarithmic scale has been observed as marked by arrows in the vicinity of AFM transition temperature. However, we have not observed any sharp rise in resistivity with decrease in temperature and this suggests that the AFM transitions observed in the above samples are unlikely due to charge ordering. One can find that the resistivity systematically decreases with 'La' doping and it is in correlation with increase in concentration of Mn^{3+} ions. Even though electron doped materials exhibit FM

transitions, no M-I transition has been observed. The absence of M-I transition could be due to the lack of percolation threshold of FM phase.

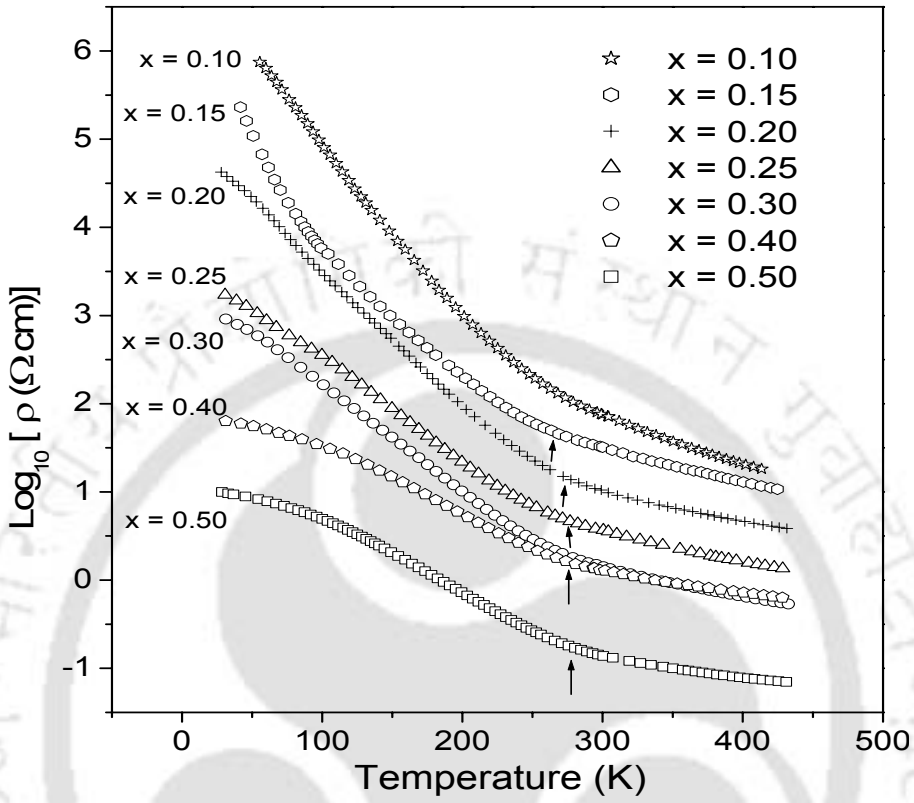

Fig. 3.49: Temperature variation of electrical resistivity for x = 0.10, 0.15, 0.20, 0.25, 0.30, 0.40 and 0.50 samples. For clarity resistivity data have been shown in logarithmic scale.

We have analyzed the resistivity data by following Mott-VRH model [139] as discussed in section 1.3.3 and for easy reference the equation (eqn. 1.20) is reproduced below, i.e.

$$\rho = \rho_{0m} \exp\left(\frac{T_{0m}}{T}\right)^{1/4} \text{----------} \quad (3.7)$$

Here ρ_{0m} is the Mott residual resistivity and T_{0m} is the Mott characteristic temperature. Typical plots of ln(ρ) versus $T^{-1/4}$ are shown in Figs. 3.50 and 3.51 for x = 0.20 and 0.30 samples respectively. One can find that ln(ρ) versus $T^{-1/4}$ exhibits linear plot in the temperature range 290 to 420K. The fitted data in the linear region are shown as solid lines in Figs. 3.50 and 3.51. There is a clear deviation from linearity below certain temperature, T_{DL} and these values are tabulated in Table 3.12. The T_{DL} values are found to be

comparable with the onset temperature of antiferromagnetic transition. Thus there is a change in electrical conduction mechanism below the onset of AFM.

The density of states in the vicinity of the Fermi level ($N(E_F)$), hopping distance, $R_{hop}(T)$ and hoping energy $E_{hop}(T)$ have been estimated from the fitted parameters and using the relations given in section 1.3.3 and for easy reference it (eqns. 1.21-1.23) has been reproduced here,

$$T_{0m} = \frac{18}{k_B N(E_F) a^3} \quad \text{----------} \quad (3.8)$$

$$R_{hop}(T) = \frac{3}{8} a \left(\frac{T_{0m}}{T} \right)^{1/4} \quad \text{----------} \quad (3.9)$$

$$E_{hop}(T) = \frac{1}{4} k_B T^{3/4} T_{0m}^{1/4} \quad \text{----------} \quad (3.10)$$

Here 'a' is the localization length and k_B is the Boltzmann constant. By following Viret *et al.* [140], I have taken a = 4.5Å in the above calculations. The fitted and estimated parameters from the resistivity analysis are tabulated in Table 3.13. The R_{hop} (400K) and E_{hop}(400K) values decrease with the 'La' concentration while the $N(E_f)$ values increase with doping. Such variations result in enhanced frequency of hopping of charge carriers and improved conductivity and are in correlation with experimental results.

The samples in hole doped region exhibit M-I transition and the typical plot of ρ versus T is shown in Fig. 3.52 for x = 0.70 (hole doped). The M-I transition temperature (T_{MI}) is found to be 375K and it is comparable with the reported value [26]. The resistivity data have been analyzed in the metallic region using the relation for itinerant–carrier resistivity explained in section 1.3.2 and the eqn. 1.16 is reproduced here,

$$\rho = \rho_o + \rho_2 T^2 + \rho_{4.5} T^{4.5} \quad \text{----------} \quad (3.11)$$

Here, ρ_0 is the temperature-independent residual resistivity due to scattering by impurities, defects, grain boundaries, domain walls, etc. The second term with the coefficient ρ_2 is ascribed to the electron-electron scattering and the third term with the coefficient $\rho_{4.5}$ is to the electron magnon scattering [123]. The fitted data are shown as dashed lines in Fig. 3.52 for x = 0.70. The resistivity data above T_{MI} could be fitted by following Mott-VRH model and is shown as solid line in the Fig. 3.52.

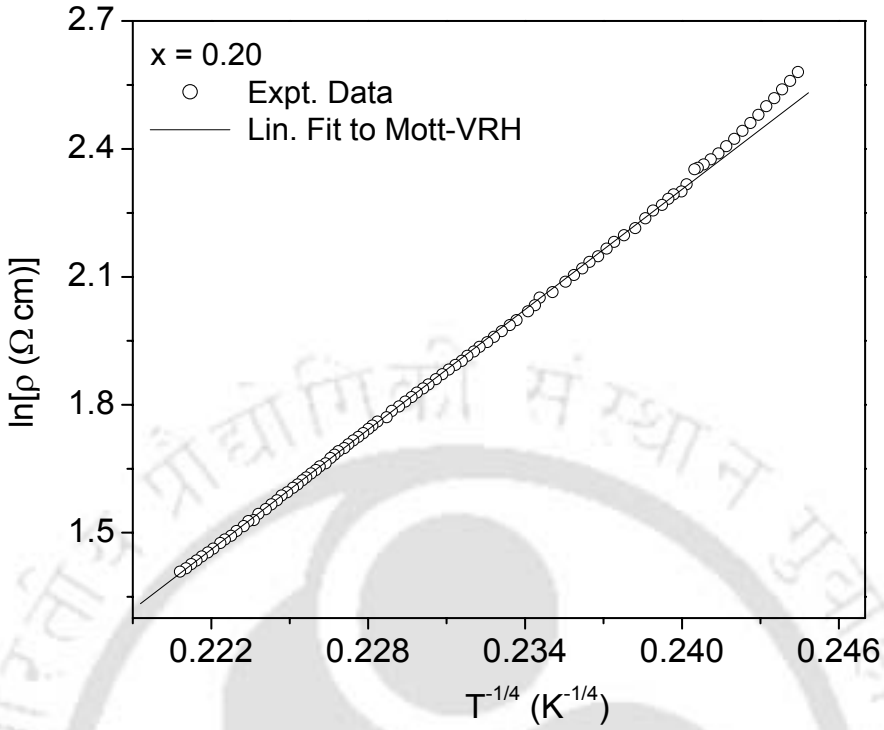

Fig. 3.50: Resistivity versus $T^{-1/4}$ for the sample $Sr_{0.8}La_{0.2}MnO_3$ (x = 0.20). The solid line shows the fit to Mott-VRH model.

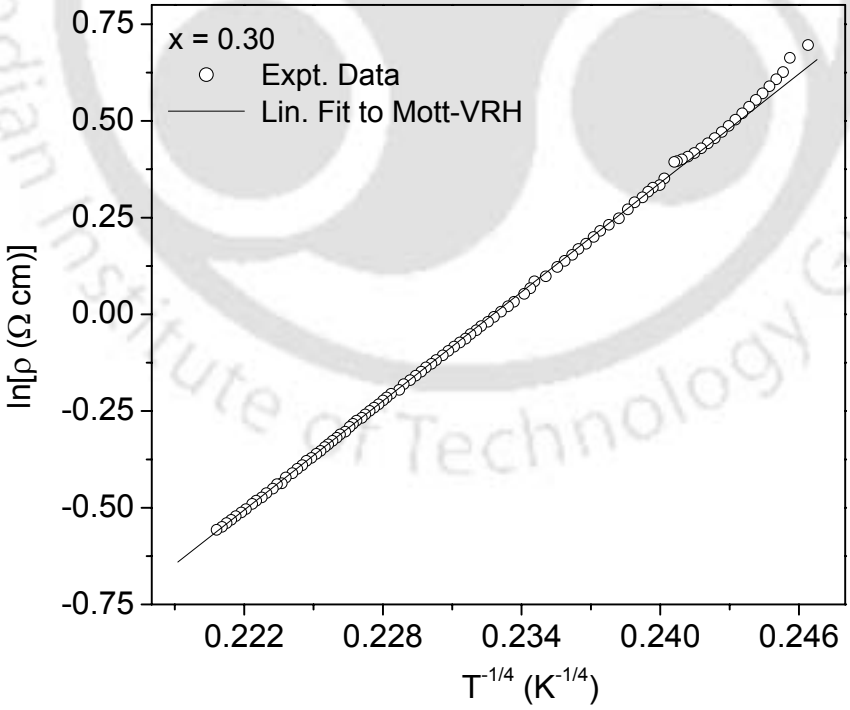

Fig. 3.51: Resistivity versus $T^{-1/4}$ for the sample $Sr_{0.7}La_{0.3}MnO_3$ (x = 0.30). The solid line shows the fit to Mott-VRH model.

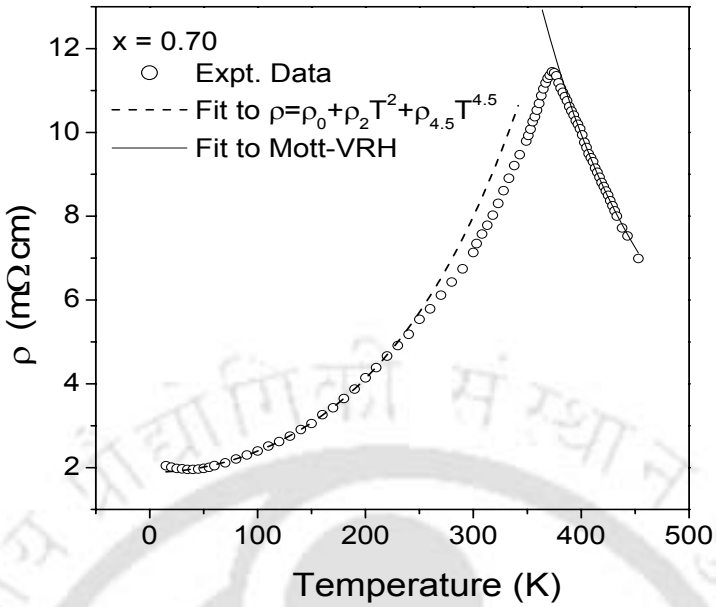

Fig. 3.52. Resistivity versus temperature for the sample $Sr_{0.3}La_{0.7}MnO_3$ (x = 0.70, hole doped). The solid line represents the fit to Mott-VRH model and dashed lines represent the fit to equation $\rho = \rho_o + \rho_2 T^2 + \rho_{4.5} T^{4.5}$.

Table 3.13: Parameters obtained from electrical resistivity measurements and analysis. ρ_{0m} and T_{0m} are the Mott residual resistivity and Mott characteristic temperature respectively. R_{hop}(400K) and E_{hop}(400K) are estimated hopping length and hopping energy at 400K. $N(E_F)$ is the density of states in the vicinity of Fermi level.

Parameters → / Samples ↓	ρ_{0m} ($\times 10^{-5}$ Ωcm)	T_{0m} ($\times 10^{7}$ K)	R_{hop}(400K) (Å)	E_{hop}(400K) (meV)	$N(E_f)$ ($\times 10^{26}$ $eV^{-1}m^{-3}$)
x = 0.10	0.06±0.011	3.604±0.0013	29.2	149.2	0.64
x = 0.15	8.26±0.014	0.822±0.0011	20.2	103.1	2.79
x = 0.25	2.64±0.012	0.591±0.0012	18.6	94.9	3.89
x = 0.30	1.79±0.011	0.486±0.0011	17.7	90.4	4.72
x = 0.40	38.33±0.012	0.129±0.0014	12.7	64.9	17.70
x = 0.50	10.09±0.013	0.079±0.0013	11.2	57.3	29.20

3.3: Summary and Conclusions:

In brief, the electron doped materials $A_{1-x}La_xMnO_3$ (A = Ba and Sr) have been prepared and characterized using XRD, etc. Their electrical transport and magnetic

properties have been studied. Both series exhibit structural transition from hexagonal to orthorhombic/rhombohedral depending upon the 'La' concentration. The $Ba_{1-x}La_xMnO_3$ series exhibits a structural transition from *P6₃/mmc* to *Pbnm* followed by transition into $R\bar{3}c$ space group. Where as, $Sr_{1-x}La_xMnO_3$ series exhibit a structural transition from *P6₃* to $R\bar{3}c$. For $Ba_{1-x}La_xMnO_3$, the structural transition takes place at $0.10 \leq x \leq 0.20$ and for $Sr_{1-x}La_xMnO_3$, the structural transition takes place at $0.15 \leq x \leq 0.30$. The lattice parameters in both the series are found to increase with the 'La' concentration. It is due to the increase of Mn^{3+} concentration at the expense of smaller size Mn^{4+} ions.

The electron doped $Ba_{1-x}La_xMnO_3$ compounds exhibit ferromagnetic transition for $x \geq 0.20$, where as $Sr_{1-x}La_xMnO_3$ compounds exhibit FM transition for $x \geq 0.10$. The charge ordering has been observed in $Ba_{1-x}La_xMnO_3$ series for $x \leq 0.50$ i.e in the electron doped region. To my knowledge, probably for the first time charge ordering has been observed in this series for composition close to $x \leq 0.50$. In addition, the earlier reports were mostly multiphase material in the electron doped regime of $Ba_{1-x}La_xMnO_3$. It is found that, the charge ordering is intrinsic property for $x = 0.50$, where as, it is due to the grain boundary effect for $x = 0.30$. It reveals that, even though the electron doped materials are in single phase form for $x \geq 0.20$, the materials exhibit a complex magnetic behaviour at low temperature, such as, charge ordering and reentrant spin glass behaviour.

The electron doped $Ba_{1-x}La_xMnO_3$ compounds exhibit metal-insulator (M-I) transition for $x \geq 0.20$. However, in electron doped $Sr_{1-x}La_xMnO_3$ series no M-I was observed and it is mainly due to the fact that, the FM interaction is below the threshold value. The increase in saturation susceptibility and decrease in resistivity at 300K are observed with increase in 'La' concentration. It is mainly due to increase in number of Mn^{3+}-Mn^{4+} pairs and hence the enhanced intensity of the double exchange interaction.

The resistivity data in the metallic region for $Ba_{1-x}La_xMnO_3$ series could be fitted to the equation $\rho = \rho_0 + \rho_2 T^2$. So, the mechanism of electrical resistivity is due to electron-electron scattering and it is generally the intrinsic property of perovskite manganites. The colossal magneto-resistivity with a maximum value of 61% at 243K has been observed for $Ba_{0.5}La_{0.5}MnO_3$ sample.

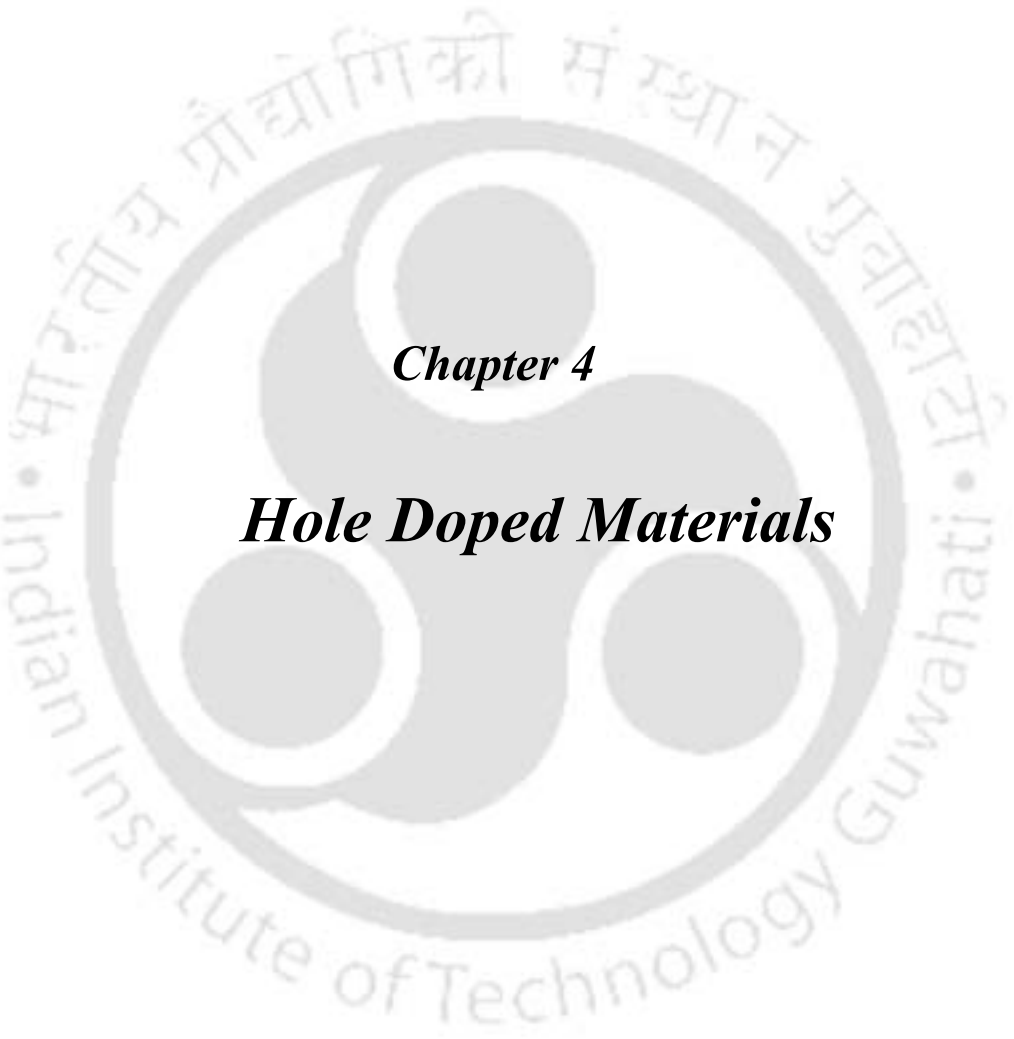

Chapter 4

Hole Doped Materials

HOLE DOPED MATERIALS

The compound $LaMnO_3$ is an electrical insulator and it exhibits antiferromagnetic transition with Neel temperature (T_N) at around 141K [12]. As discussed in introduction (section 1.1.1**),** the substitution of divalent elements in place of 'La' with the general chemical formula $La_{1-x}A_xMnO_3$ (Where A = Ca, Sr, Ba, Pb etc.) is the subject of interest because, these materials exhibit interesting magnetic and electronic properties, including the colossal magneto-resistivity (CMR) effect. It has been established that, $x \approx 0.33$ is the optimum doping for divalent substitutions, where the ratio of Mn^{3+}/Mn^{4+} is 67/33. One can also generate mixed valency of 'Mn' ions by doping monovalent atoms in place of 'La'. Here each doped monovalent atom can oxidize two 'Mn' ions from Mn^{3+} to Mn^{4+} state. Thus, the optimum ratio of Mn^{3+} and Mn^{4+} ions can be obtained by doping relatively small fraction of monovalent atoms. In the latter case, the distortion due to ionic size mismatch would be minimized due to small concentration of doping but with optimum ratio of Mn^{3+}/Mn^{4+} ions. There are a few reports on monovalent substitutions (Na, K, Li etc.) in place of trivalent rare earth atom 'La' [43, 46, 48]. Recently couple of groups reported 'Ag' doping in 'La' site ($La_{1-x}Ag_xMnO_3$) mainly to study the magneto-caloric effect [52, 53, 56]. I have prepared $(La_{1-x}Ag_x)MnO_3$ and $(La_{1-x}Cu_x)MnO_3$ i.e. by substituting 'Ag' & 'Cu' in place of 'La'. So, far no one has reported 'Cu' doping in place of 'La' to the best of my knowledge. The above two series have been characterized by XRD, micrographs, etc. The temperature variation of electrical resistivity, magneto-resistivity and ac susceptibility measurements have been carried out and the details of analysis and results are presented in this chapter.

4.1. $La_{1-x}Ag_xMnO_3$ (x = 0 to 0.35) Compounds

4.1.1. Preparation

The $La_{1-x}Ag_xMnO_3$ compounds were prepared for x = 0, 0.05, 0.10, 0.15, 0.20, 0.25, and 0.35 by solid state route. Stoichiometric ratio of La_2O_3, $AgNO_3$, and $C_4H_6MnO_4.4H_2O$ were weighed and mixed thoroughly under acetone. The mixture was presintered at 800^0C for 36 hours with intermediate grindings at room temperature at the end of every 12 hours. The sintering in pellet form was carried out at 1000^0C to 1100^0C

for over 24 hours with intermediate grindings. The above sintering was done in a step by step process at a few intermediate temperatures. The final sintering in pellet form was carried out at 1200^0C for over 40 hours. At the end of approximately every 12 hours of annealing, the pellet was crushed into fine powder and was repelletized. All the above heat treatments were carried out in air and finally the samples were furnace cooled.

4.1.2. Characterization

The XRD patterns recorded for $La_{1-x}Ag_xMnO_3$ compounds for x = 0, 0.05, 0.10 & 0.15 are shown in Fig. 4.1 and for 0.20, 0.25 & 0.35, they are shown in Fig. 4.2. It can be seen from the figures the samples are in single phase form up to x = 0.15 and it is in agreement with ref. [56]. All the observed peaks in XRD patterns could be indexed to *Pbnm* space group for x = 0 and 0.05. For $0.10 \leq x \leq 0.15$, the splitting of some of the peaks have been observed and the patterns could be indexed to $R\bar{3}c$ space group. The XRD patterns of samples with $x \geq 0.20$ could also be indexed to $R\bar{3}c$ space group, however two minor impurity peaks are observed at 36.25^0 and 38.41^0. These two peaks are shown as solid circles in Fig. 4.2. They are comparable with the report of Tang *et al*. [52]. The intensity of both the peaks increases gradually with 'Ag' concentration. The careful analysis shows that the peaks observed at 36.25^0 and 38.41^0 correspond to Mn_3O_4 impurity [218].

The XRD patterns were analyzed with the help of Fullprof program by employing Rietveld refinement technique [191]. The patterns for x = 0 and 0.05 could be refined using *Pbnm* space group. The typical lattice parameters for x = 0 is found to be a = 5.524Å, b = 5.550Å, and c = 7.815Å. They are comparable with the reported values [56]. The patterns for $x \geq 0.10$ could be refined using space group $R\bar{3}c$. The typical values of atomic position, occupancy, isotropic temperature parameters and lattice parameters are given in Table 4.1 for the sample $La_{0.85}Ag_{0.15}MnO_3$ (x = 0.15). Lattice parameters are comparable with those reported by Pi *et al*. [56]. The occupancy value of oxygen (O) is taken as '1' and it was not varied during the fit. The Mn-Mn & Mn-O bond lengths and, Mn-O-Mn bond angles have been calculated from the fitted values of atomic positions. The lattice parameters, reliability factors, unit cell volume, bond length and bond angles are given in Table 4.2.

It has been observed that cell volume and the lattice parameters gradually decrease with the increase of 'Ag' concentration up to $x \leq 0.15$ and then start increasing. The partial replacement of La^{3+} by Ag^{1+} ions produces Mn^{4+} ions. The Mn^{4+} ionic radius is smaller than that of Mn^{3+}. Thus the decrease in lattice parameter is due to the oxidation of Mn^{3+} ions into Mn^{4+} ions, since every Ag^{1+} ion is expected to generate two Mn^{4+} ions. However, for $x > 0.15$, the unit cell volume and lattice parameters are found to increase with 'Ag' doping. Beyond the optimum doping, the rate of generation of Mn^{4+} ions is reduced due to the segregation of Mn_3O_4 impurity and as a result the ionic size of doped Ag^{1+} ion plays a major role compared to that of 'Mn' ions.

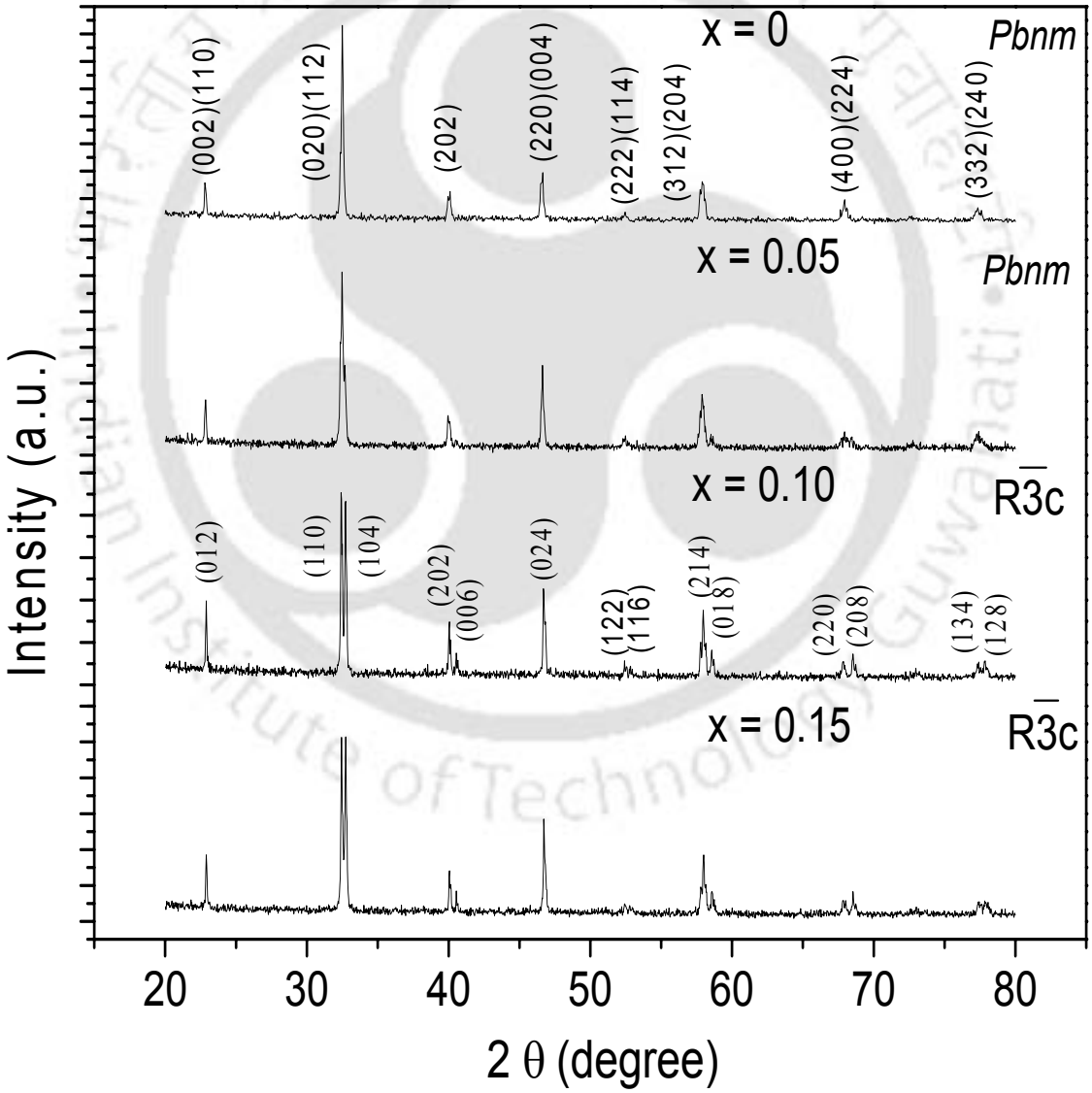

Fig. 4.1: XRD patterns of $La_{1-x}Ag_xMnO_3$ for x = 0, 0.05, 0.10 and 0.15.

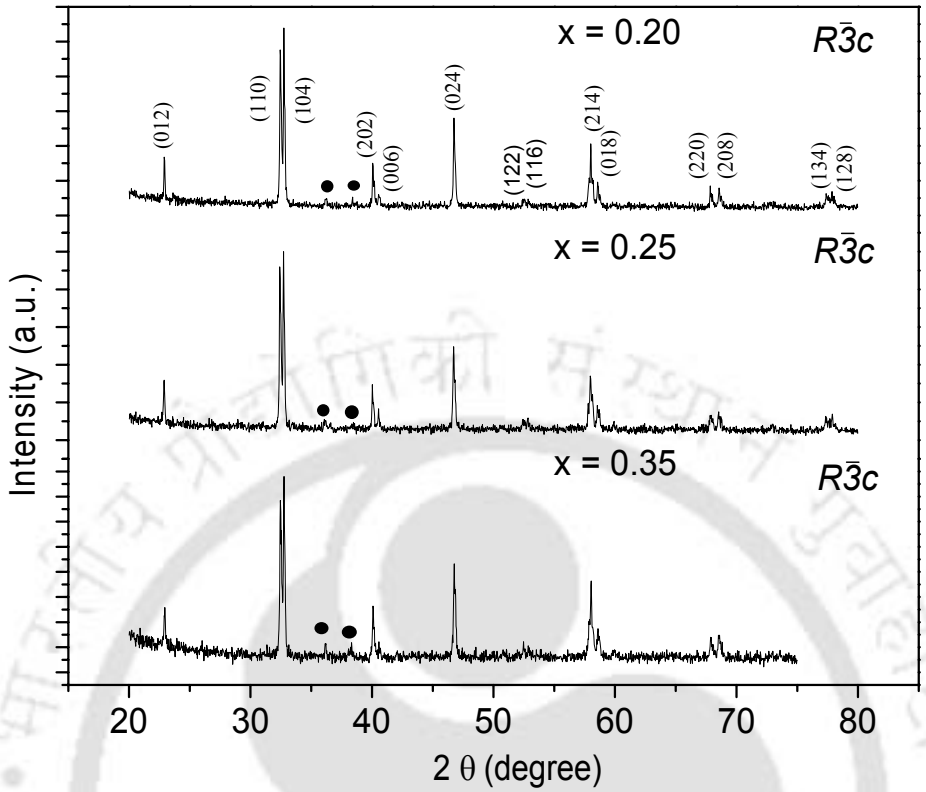

Fig. 4.2: XRD patterns of $La_{1-x}Ag_xMnO_3$ for x = 0.20, 0.25 and 0.35. Solid circles represent the peaks due to minor Mn_3O_4 impurity.

Typical XRD patterns along with Rietveld refinement are shown in Figs. 4.3 and 4.4 respectively for x = 0.05 & 0.25 samples. Here, the experimental data are shown as crosses (+) and calculated intensities are shown as solid lines. The dotted lines represent the difference between measured and calculated intensities. The expanded view of (020) & (112) peaks and the splitting of (110) & (104) peaks are shown in the inset of respective figures.

The average particle size has been calculated using the Scherrer's formula (eqn. 2.11) [192] by following the method discussed in section 3.1.2. The values are listed in Table 4.2 and they are comparable with those reported in literature [52]**.** One can find that particle size increases with 'Ag' concentration up to x ≈ 0.20 and then decreases. The initial increase of particle size could be due to the tendency of formation of stable perovskite structure with low level 'Ag' doping. The decrease of particle size for x > 0.20 could be due to the presence of secondary impurity phase at high level of 'Ag' doping. So,

the optimum doping for the stable perovskite formation in this series could be in between 0.15 to 0.20.

The average valency of 'Mn' ion in the above compounds determined from the chemical titration is listed in Table 4.3. The measured value suggests that, the materials are rich in Mn^{3+} concentration compared to Mn^{4+} ion as expected. The marginal difference between expected and actual 'Mn' valency could be mainly due to oxygen off-stoichiometry. Such oxygen off-stoichiometry is generally observed in manganite perovskites.

'Mn' valency is found to be close to the expected value for $x \leq 0.20$. For $x > 0.20$, there is a some discrepancy between expected and measured values. The measured value is less than the expected value. It suggests that, some of the 'Mn' is contributing to form Mn_3O_4 phase as seen from the XRD (Fig. 4.2) rather than going from Mn^{3+} to Mn^{4+}.

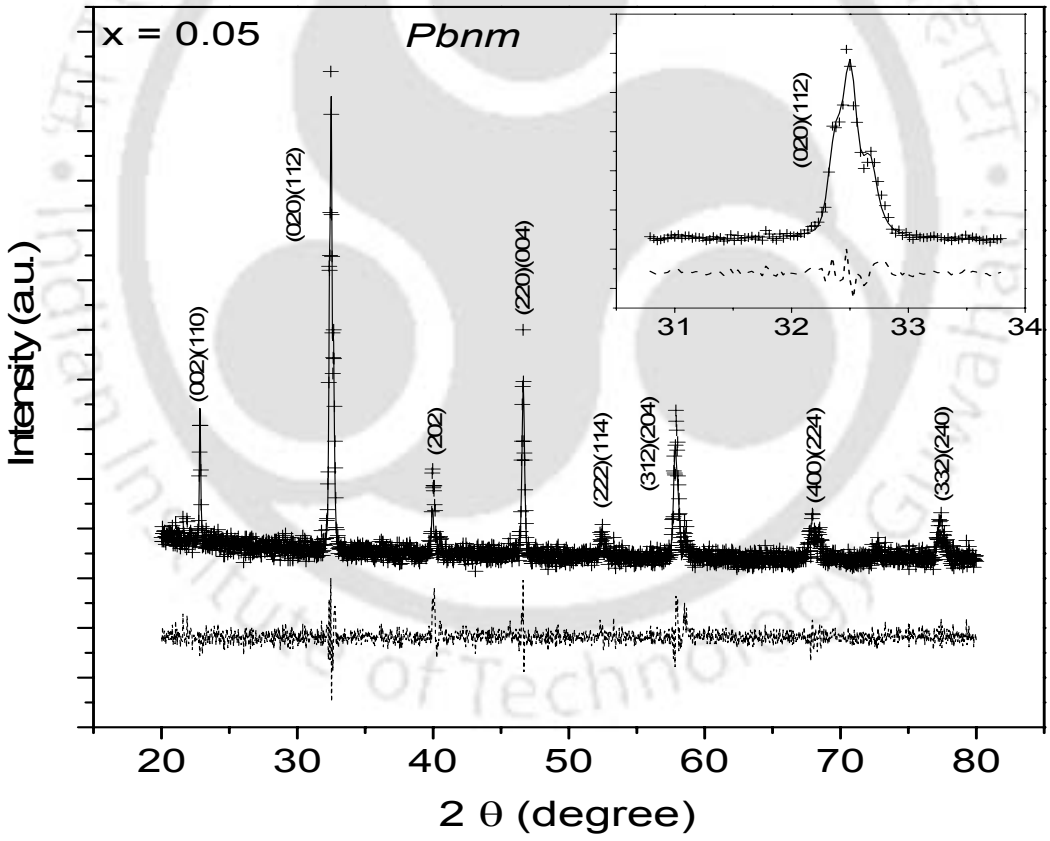

Fig. 4.3: XRD pattern along with Rietveld refinement for the sample $La_{0.95}Ag_{0.05}MnO_3$ (x = 0.05). The '+' signs represent experimental data points and solid line represents Rietveld refined data. The dotted lines show the difference between experimental & refined data. The inset shows expanded view of (020) & (112) peaks.

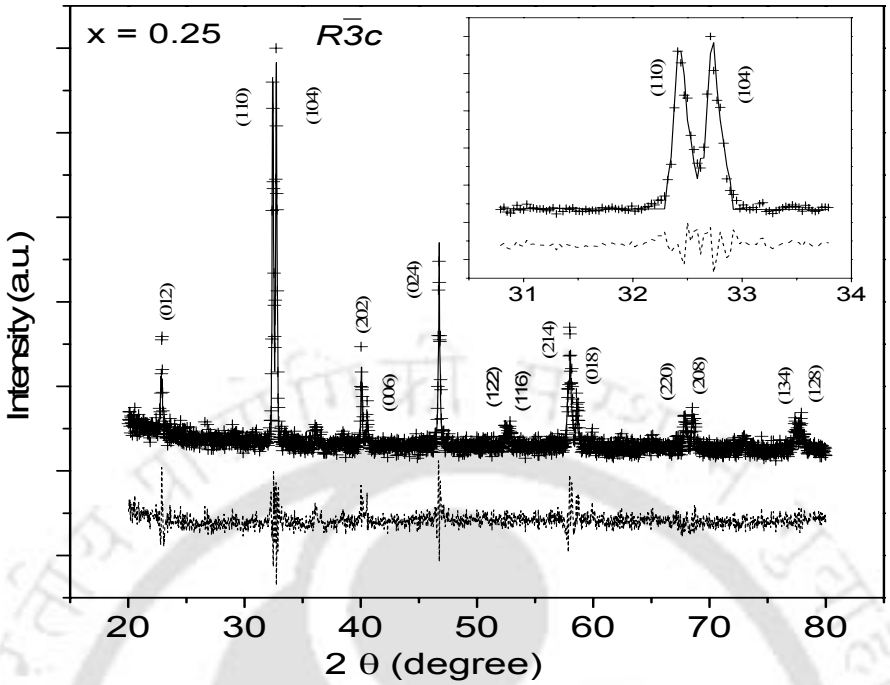

Fig. 4.4: XRD pattern along with Rietveld refinement for the sample $La_{0.75}Ag_{0.25}MnO_3$ (x = 0.25). The '+' signs represent experimental data points and solid line represents Rietveld refined data. The dotted lines show the difference between experimental & refined data. The inset shows expanded view of splitting of (110) & (104) peaks.

Table 4.1: Parameters obtained from the Rietveld analysis of XRD pattern of the sample $La_{0.85}Ag_{0.15}MnO_3$ (x = 0.15). The XRD pattern has been fitted to $R\bar{3}c$ space group. The lattice parameters are a = b = 5.524Å and c = 13.355Å. Biso is the isotropic displacement (temperature) parameter and Occ is the occupancy number.

Parameters →	Fractional coordinates			Biso	Occ
Atoms ↓	x	y	z	Å^2	
La	0.0000	0.0000	0.2500	0.85	0.849
Ag	0.0000	0.0000	0.2500	0.15	0.151
Mn	0.0000	0.0000	0.0000	0.96	0.962
O1	0.5504	0.0000	0.2500	0.68	1.000

Table 4.2: Parameters obtained from the XRD analysis of the samples $La_{1-x}Ag_xMnO_3$ (x = 0, 0.05, 0.10, 0.15, 0.20, 0.25 and 0.35). G_{La}, G_{Ag} and G_{Mn} are the occupancy of La, Ag and Mn respectively. R_p, $R_{\omega p}$, R_{exp}, R_{Bragg}, R_F and χ^2 are the reliability factors. 'S_G' is the average particle size obtained from the line broadening of the XRD pattern.

Samples → / Parameters ↓	x = 0	x = 0.05	x = 0.10	x = 0.15	x = 0.20	x = 0.25	x = 0.35
Space Group	*Pbnm*	*Pbnm*	$R\bar{3}c$	$R\bar{3}c$	$R\bar{3}c$	$R\bar{3}c$	$R\bar{3}c$
a (Å)	5.524	5.493	5.527	5.524	5.526	5.531	5.530
b (Å)	5.550	5.543	---	---	---	---	---
c (Å)	7.815	7.814	13.356	13.355	13.360	13.370	13.370
G_{La}	1	0.918	0.914	0.849	0.786	0.731	0.625
G_{Ag}	---	0.069	0.085	0.151	0.195	0.253	0.355
G_{Mn}	1	0.987	0.996	0.962	0.981	0.984	0.980
R_p	15.2	16.5	17.9	17.5	16.6	16.2	15.3
$R_{\omega p}$	19.4	21.4	23.1	22.1	20.9	20.3	19.4
R_{exp}	17.31	18.0	16.4	17.5	16.7	16.3	15.9
R_{Bragg}	9.0	12.0	12.9	11.0	12.8	11.1	13.2
R_F	9.4	10.3	12.5	7.6	12.8	9.4	11.1
χ^2	1.43	1.41	1.74	1.59	1.57	1.56	1.48
Volume ($Å^3$)	239.8	237.9	353.3	352.9	353.4	354.3	354.4
Mn-Mn (Å)	3.915	3.902	3.891	3.889	3.891	3.894	3.893
Mn-O_1 (Å)	1.977	1.959	1.969	1.965	1.966	1.969	1.967
Mn-O_2 (Å)	2.013	2.087	---	---	---	---	---
$\angle Mn-O_1-$	164.14	169.7	162.0	163.6	163.4	162.8	163.3
$\angle Mn-O_2-$	153.07	158.4	---	---	---	---	---
S_G (nm)	41	43	46	50	53	46	36

To study the morphology of the materials optical microscope photograph has been taken for all the materials. The magnification is used 100. Typical microscope photograph for the sample x = 0.15 is shown in the Fig. 4.5. The morphology is found to be uniform through out the material.

The typical SEM micrographs for x = 0.15 is shown in the Fig. 4.6. The average grain size is found to be 2.4μm for x = 0.15 sample. The composition of the sample from EDAX is found to be $La_{0.85}Ag_{0.07}Mn_{1.035}O_3$. It has been normalized to 3 oxygen atoms per formula unit. The 'Mn' valency from above compositional analysis is found to be 3.15.

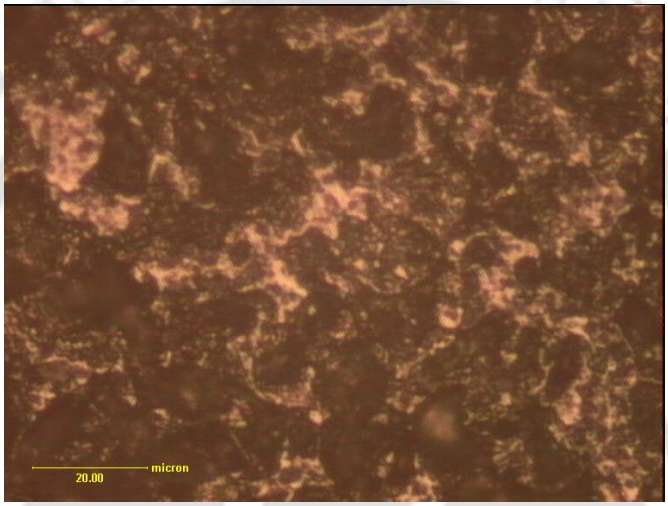

Fig. 4.5: Microscope photograph (magnification-100) of the sample $La_{0.85}Ag_{0.15}MnO_3$ (x = 0.15).

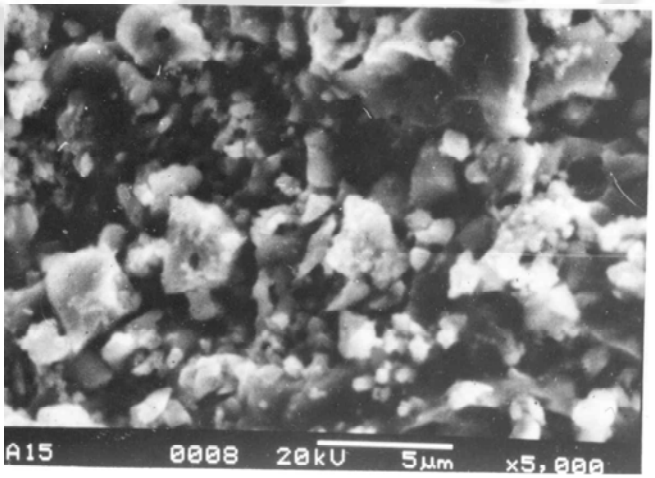

Fig. 4.6: SEM photograph of $La_{0.85}Ag_{0.15}MnO_3$ (x = 0.15) with magnification-5,000.

4.1.3. AC Susceptibility Study

Fig. 4.7 shows the plots of in phase susceptibility, χ' versus temperature (T) for the samples x = 0.05, 0.10 and 0.15. These plots for x = 0.20, 0.25 & 0.30 are shown in the Fig. 4.8. The magnitude of applied ac field was 5.3Oe at a frequency of 233Hz. One can see that all the 'Ag' doped samples exhibit paramagnetic to ferromagnetic transition when they are cooled. In addition to FM transition a small step like behaviour at around 210K and sharp fall in susceptibility below the FM saturation has been observed for x = 0.05 sample. There are two onset temperatures observed for x = 0.05 sample at 251 and 208K and, it could be due to anisotropy and surface effect of the materials [83]. The onset of ferromagnetic transition temperature (T_{on}) is tabulated in Table 4.3. The error in T_{on} is found to be ±2K, which is mainly due to the uncertainty as a result of broad transition. The variation of T_{on} with the 'Ag' concentration is shown in Fig. 4.9(a). It is observed that the T_{on} value increases rather sharply with the 'Ag' concentration up to x = 0.15 and then it increases gradually. The T_c value increases sharply up to x = 0.15 and beyond that no appreciable variation is noticed. As expected, the T_c increases up to the optimum doping, i.e. near about 30% of Mn^{4+} ions in the sample.

The saturation susceptibility (χ'_s) is determined at the end of FM transition and these values are tabulated in Table 4.3. The χ'_s versus 'Ag' concentration is shown in the Fig. 4.10. The saturation susceptibility increases with the 'Ag' concentration up to x = 0.20 and then it is decreasing. Similar behaviour has been observed in divalent substituted (hole doped) samples such as $La_{1-x}Ca_xMnO_3$, $La_{1-x}Sr_xMnO_3$, etc. [87]. Such variation is not surprising, because as Mn^{4+} concentration increases beyond the optimum value and approach towards 50%, the intensity of double exchange interaction is reduced.

The out of phase of ac susceptibility, χ'' versus temperature (T) is shown in the Fig. 4.11 for x = 0.05 - 0.15 and in Fig. 4.12 for x = 0.20-0.35. It is observed that the ac loss is more in the transition region. After getting a saturation value, the ac loss reduces. The ac loss is close to zero at low temperature.

Fig. 4.13 shows the expanded view of χ' vs. T plot in the low temperature range (30 to 140K). It is observed that there is a minor slope change at around 100K. A low temperature peak at around 44K is observed. The peak is gradually getting prominent with the increase in 'Ag' concentration. This low temperature peak has been observed by S. Krupička *et al*. [219] in other manganites, especially in low field magnetization

measurements [219]. It could be due to the presence of Mn_3O_4 impurity [219, 220], which is seen from the XRD patterns especially for $x \geq 0.20$.

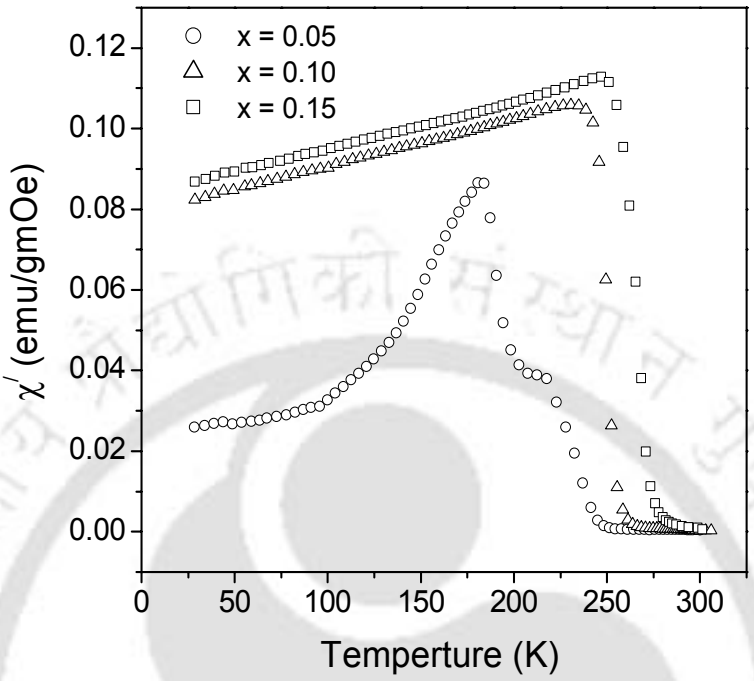

Fig. 4.7: Temperature variation of in phase ac susceptibility (χ') of samples $La_{1-x}Ag_xMnO_3$ for x = 0.05, 0.10 and 0.15.

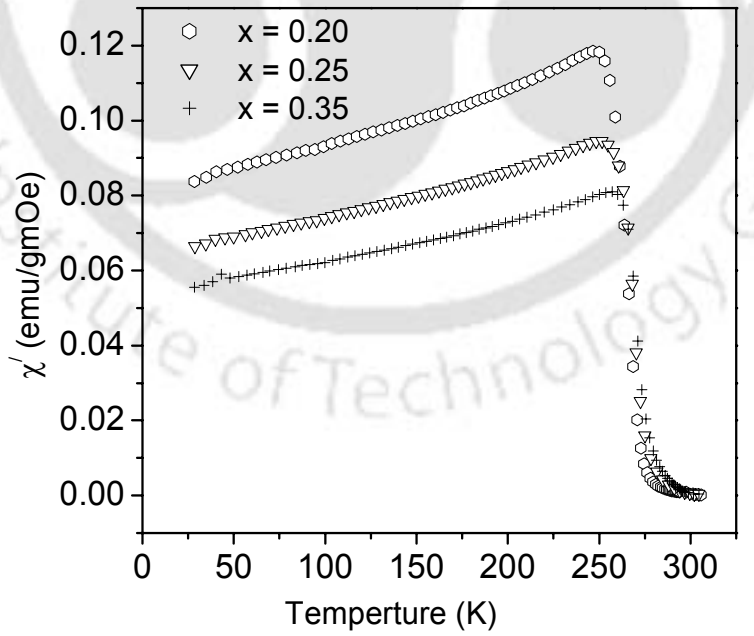

Fig. 4.8: Temperature variation of in phase ac susceptibility (χ') of samples $La_{1-x}Ag_xMnO_3$ for x = 0.20, 0.25 and 0.35.

Table 4.3: Parameters obtained from the chemical titration and ac susceptibility measurement. The error in T_{on} and T_c are ±2K and ±1K respectively.

Samples → / Parameters ↓	x = 0	x = 0.05	x = 0.10	x = 0.15	x = 0.20	x = 0.25	x = 0.35
'Mn' Valency	2.99	3.09	3.22	3.31	3.39	3.43	3.48
T_{on}(K)	---	251	263	282	284	289	294
T_c(K)	---	234	250	269	269	270	270
χ'_s(emu/gmOe)	---	0.087	0.106	0.113	0.119	0.095	0.081

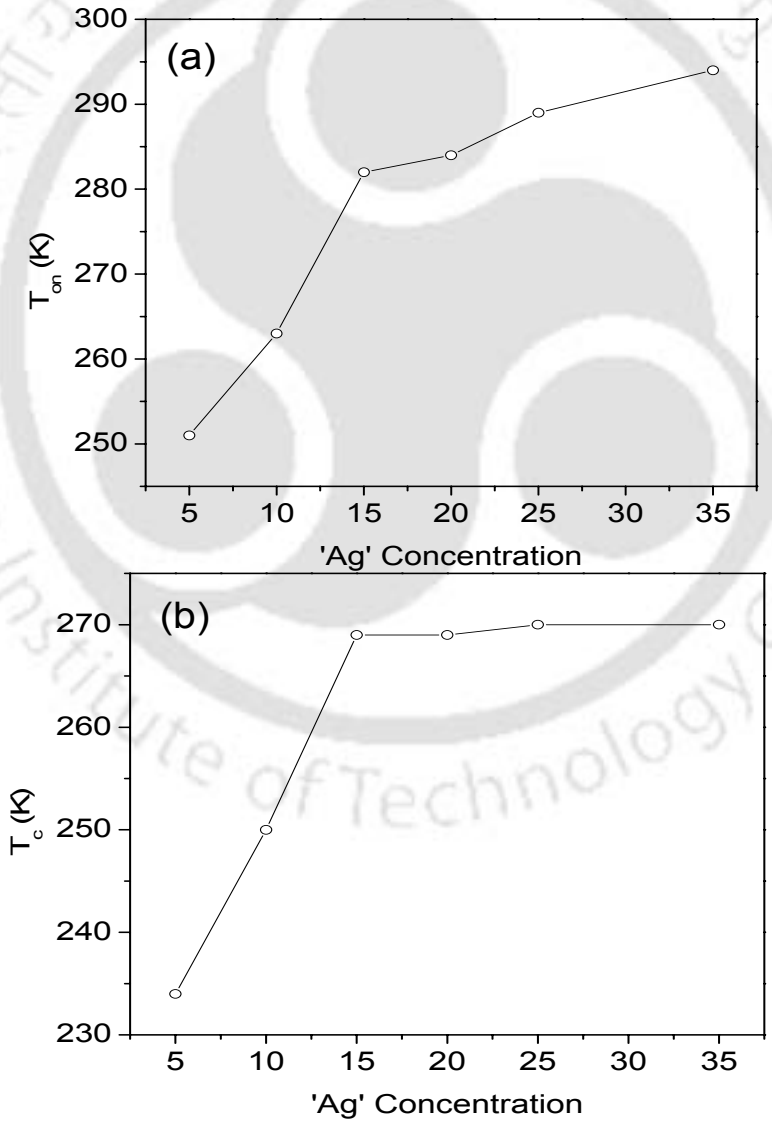

Fig. 4.9: Plot of variation of (a) T_{on} and (b) T_c as a function of 'Ag' concentration.

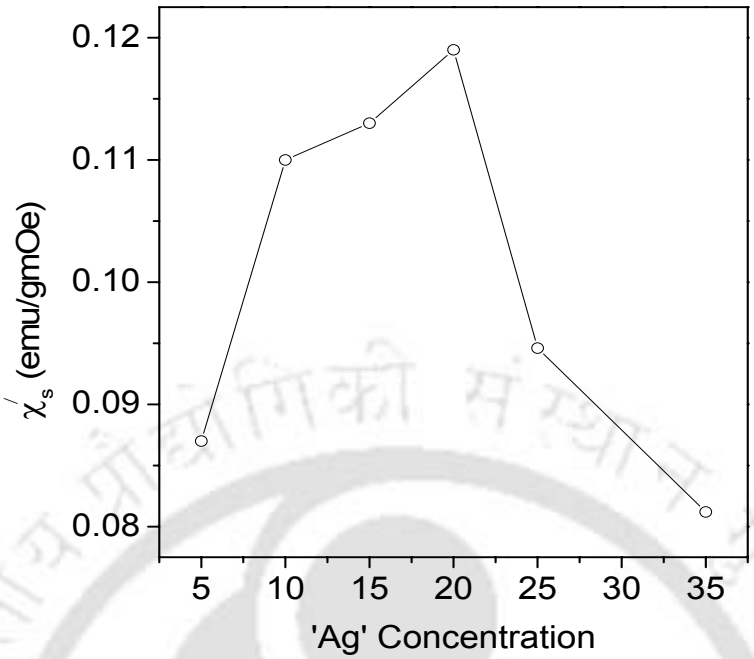

Fig. 4.10: Plot of χ'_s versus 'Ag' concentration.

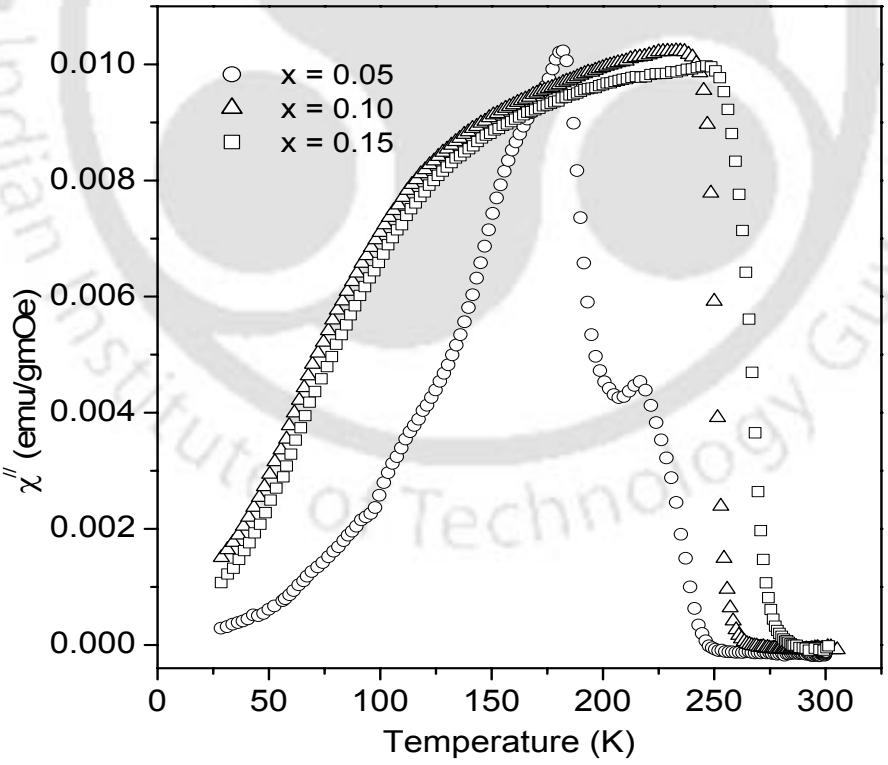

Fig. 4.11: Temperature variation of out of phase ac susceptibility (χ'') of samples $La_{1-x}Ag_xMnO_3$ for x = 0.05, 0.10 and 0.15.

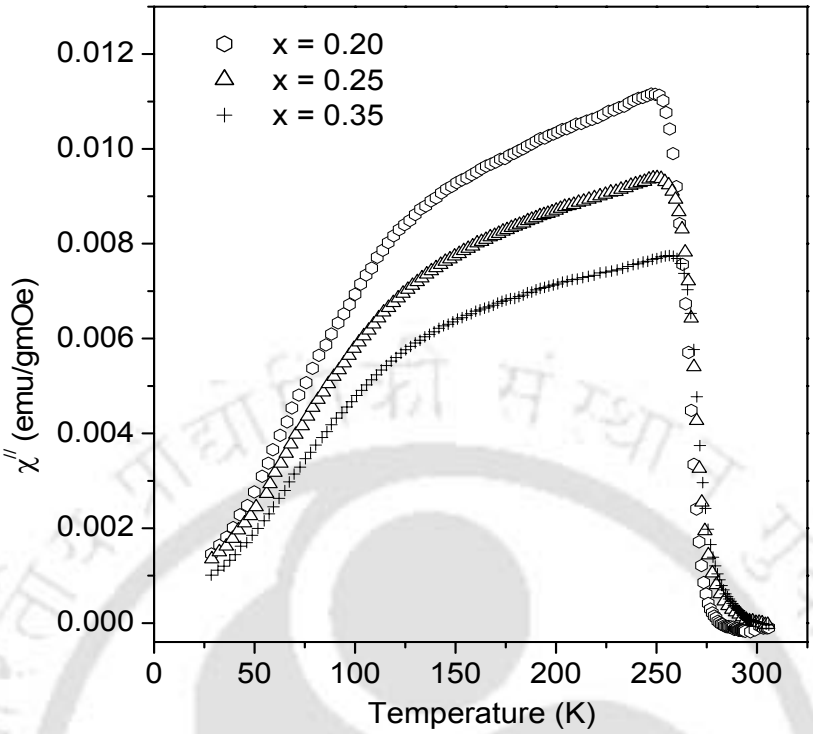

Fig. 4.12: Temperature variation of out of phase ac susceptibility (χ'') of samples $La_{1-x}Ag_xMnO_3$ for x = 0.20, 0.25 and 0.35.

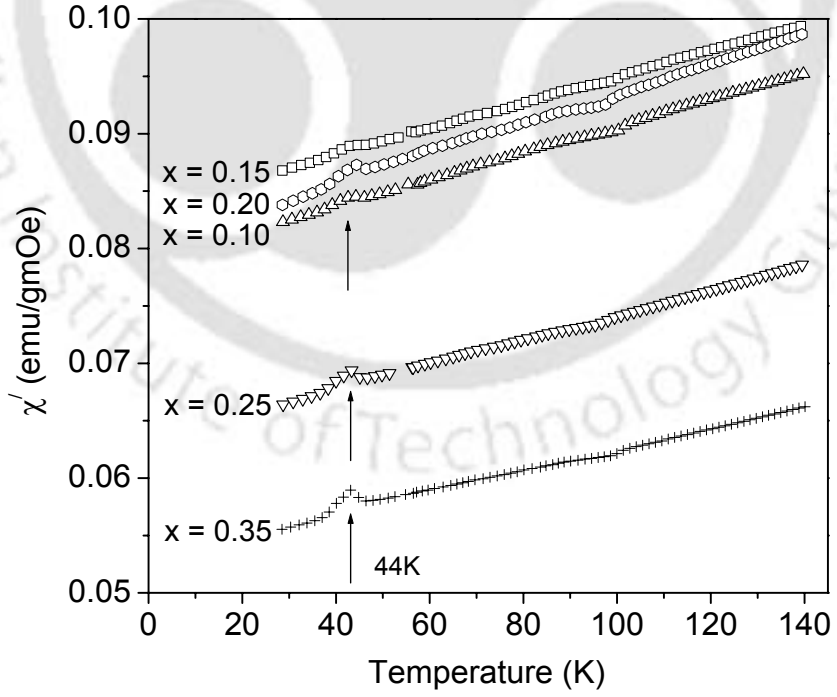

Fig. 4.13: Temperature variation of in phase ac susceptibility (χ') of the samples x = 0.10, 0.15, 0.20, 0.25 and 0.35 in the temperature range 30 to 140K.

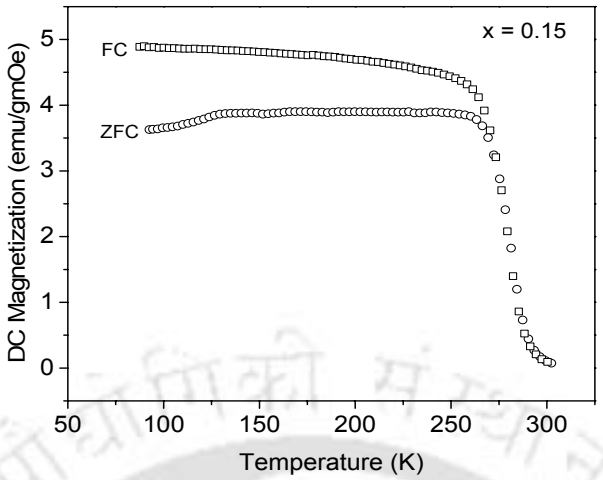

Fig. 4.14: Plots of temperature variation of DC magnetization of the sample $La_{0.85}Ag_{0.15}MnO_3$ (x = 0.15) for ZFC (circles) and FC (squares) cases.

For the sake of comparison the DC magnetization of the sample $La_{0.85}Ag_{0.15}MnO_3$ has been measured at Inter-University Consortium for Department of Atomic Energy Facilities, Indore, India. The applied field was 50Oe. The measurements were carried out for both zero field cooled (ZFC) and field cooled (FC) conditions. These plots are shown in Fig. 4.14 as circles (ZFC) and squares (FC). The T_{on} and T_c values are found to be respectively 290 and 281K, which are higher than that observed from ac susceptibility measurements. The shifting of T_c could be due to higher applied field. There is an appreciable difference between ZFC and FC curves. This trend is similar to that observed in electron doped materials discussed in sections 3.1.3 and 3.2.3.

4.1.4. Electrical Resistivity and Magneto-Resistivity Studies

The temperature variation of dc electrical resistivity (ρ) was measured on the above samples. Electrical resistivity in the presence of magnetic field, i.e. magneto-resistivity has also been measured on a few selected samples. These results are discussed in detail. DC electrical resistivity (ρ) as a function of temperature (T) are shown in Fig. 4.15 for samples x = 0.05 - 0.35. It is observed that all the 'Ag' doped samples exhibit metal-insulator transitions. The temperature corresponding to peak in ρ versus T is taken as M-I transition temperature T_{MI}. The T_{MI} values vary from 242 for x = 0.05 to 289K for x = 0.35, and these values are tabulated in Table 4.4. For clarity T_{MI} versus 'Ag' concentration is plotted and it is shown Fig. 4.16(a). One can find that the T_{MI} values

rapidly increases with 'Ag' concentration up to x = 0.15 and then it increases slowly. Secondary peaks have been observed especially for x = 0.05 and 0.10 samples at around 190 and 214K respectively. Such secondary peaks have been reported in 'Ag' and other monovalent doped materials [55, 56]. It could be mainly due to inhomogenity and intergranular tunneling effects. Such a secondary transition has been observed from the susceptibility measurement of x = 0.05 sample. The T_{MI} values are found to be marginally lower then the T_{on} values. Thus the FM phase exceeds the percolation threshold to exhibit M-I transition at a temperature of a few Kelvin below T_{on}. The variation of resistivity at 300K (ρ_{300K}) as a function of 'Ag' concentration is shown in Fig. 4.16 (b) and these values are found to decrease systematically with 'Ag' doping up to x = 0.25. Thus the hole doping results in enhanced mobility of charge carriers or delocalization. Unlike the electron doped materials such as $Ba_{1-x}La_xMnO_3$ which is discussed in chapter 3 (section 3.1.4), these materials do not show any upturn in electrical resistivity at low temperature. This is as a result of absence of reentrant spin glass behaviour in the present samples. Thus the 'Ag' doped materials show stable FM phase without any competing antiferromagnetic interaction.

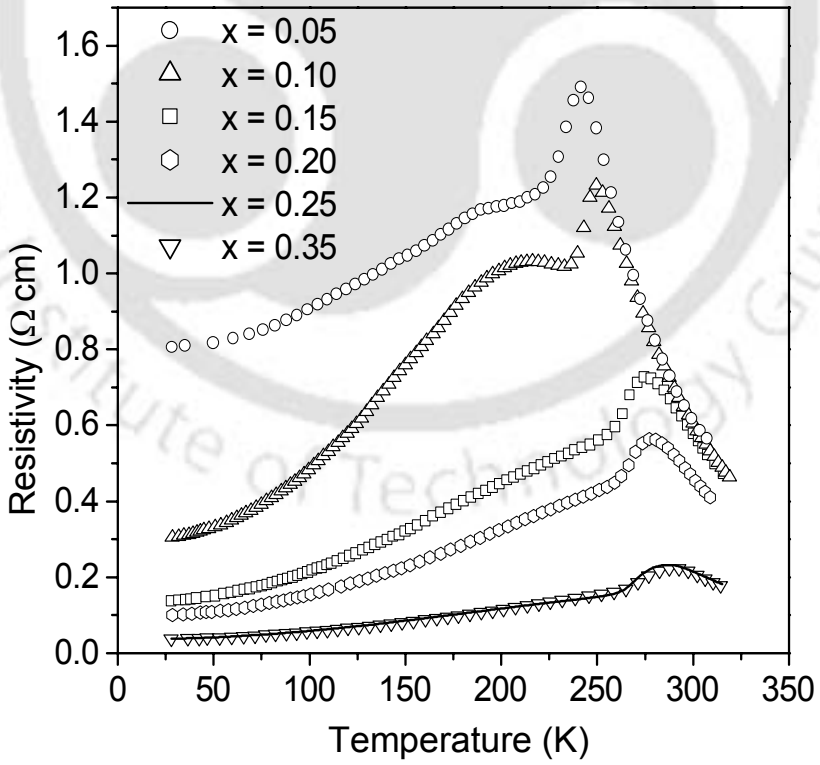

Fig. 4.15: Temperature variation of dc electrical resistivity of $La_{1-x}Ag_xMnO_3$ for x = 0.05, 0.10, 0.15, 0.20, 0.25 and 0.35 samples.

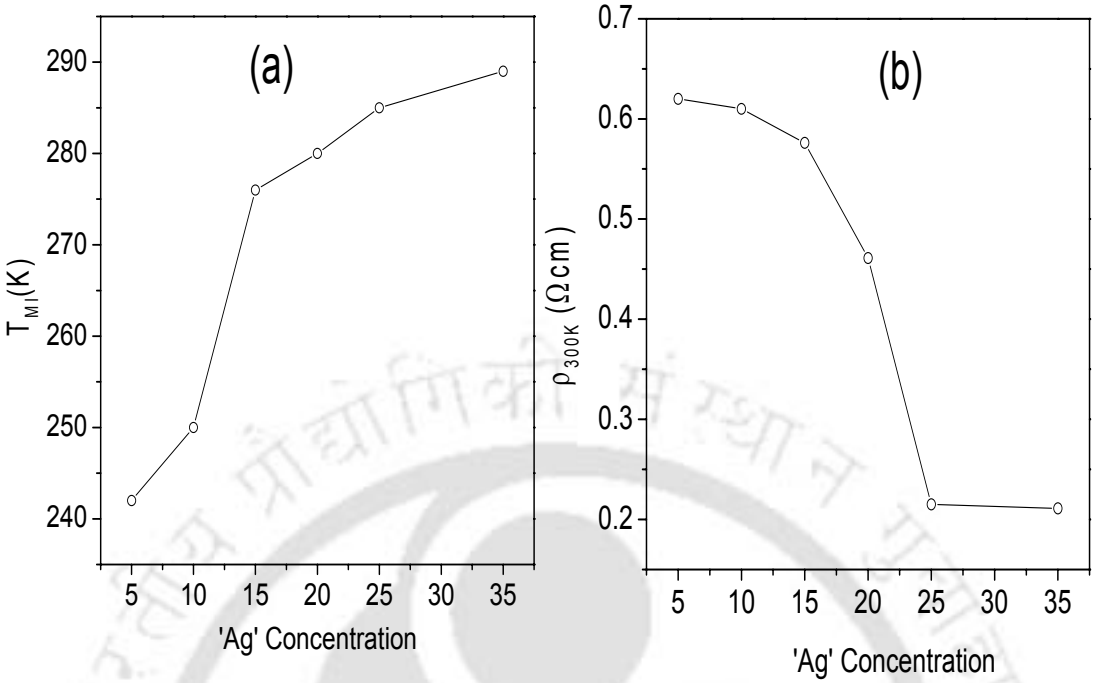

Fig. 4.16: Variation of (a) T_{MI} (K) and (b) ρ_{300K}(K) with 'Ag' concentration.

Table 4.4: Parameters obtained from the resistivity measurement and its analysis in the metallic region ($T < T_{MI}$) of $La_{1-x}Ag_xMnO_3$ (x = 0.05-0.35) . The error of T_{MI} is found to be approximately ±2K.

Samples → / Parameters ↓	x = 0.05	x = 0.10	x = 0.15	x = 0.20	x = 0.25	x = 0.35
T_{MI}	242	250	276	280	285	289
ρ(300K)(Ωcm)	0.620	0.610	0.580	0.461	0.215	0.211
ρ_0 (Ωcm)	0.793 ±0.001	0.2835 ±0.0003	0.1303 ±0.0001	0.0953 ±0.0001	0.0362 ±0.0002	0.03644 ±0.00006
ρ_2 (10^{-6} ΩcmK^{-2})	9.79 ±0.29	19.087 ±0.007	8.39 ±0.01	5.83 ±0.02	2.271 ±0.007	2.07 ±0.01
$\rho_{4.5}$ (10^{-12}ΩcmK$^{-4.5}$)	13.6 ±1.6	9.6 ±0.3	1.59 ±0.07	0.9 ±0.1	0.0012 ±0.0009	0.11 ±0.08
rmsd(%)	0.15	0.14	0.3	0.4	0.15	0.24

Table 4.5: Parameters obtained from the analysis of resistivity in the semiconducting region ($T > T_{MI}$) of $La_{1-x}Ag_xMnO_3$ for the samples x = 0.05 and 0.10.

Parameters → / Samples ↓	ρ_{0m} ($10^{-8}\Omega$cm)	T_{0m} (10^7K)	$N(E_F)$ (10^{25} $eV^{-1}m^{-3}$)	R_{hop} (300K) (Å)	E_{hop} (300K) (meV)	rmsd(%)
X = 0.05	1.78 ±0.09	2.719 ±0.006	8.44 ± 0.01	29.30	112.1	0.66
X = 0.10	2.39 ±0.09	2.532 ±0.008	9.06 ±0.01	28.76	110.1	0.35

The resistivity data, in the metallic region could be analyzed using the empirical relation as discussed in introduction (section 1.3.2) and the eqn. 1.16 is reproduced here,

$$\rho = \rho_o + \rho_2 T^2 + \rho_{4.5} T^{4.5} \quad \text{----------} \quad (4.1)$$

where, ρ_0 is the temperature independent residual resistivity due to scattering by impurities, defects, grain boundaries and domain walls. The second term with the coefficient ρ_2 is ascribed to the electron-electron [136] or single magnon [123] scattering and the third term with the coefficient $\rho_{4.5}$ corresponds to the electron magnon scattering [127]. The fitted data are shown as solid lines in Fig. 4.17 for the samples x = 0.10 (a) and 0.25 (b). The fitted parameters ρ_0, ρ_2, and $\rho_{4.5}$ are tabulated in Table 4.4. These values are comparable to those reported for $La_{0.7}Ca_{0.3}MnO_3$ [154].

The resistivity data above T_{MI} (semiconducting region) for the samples x = 0.05 and 0.10 were analyzed by following Mott Variable Range Hopping (Mott-VRH), Efros-Shklovskii VRH (ES-VRH), and Small Polaron Hopping (SPH) models as discussed in introduction (section 1.3.3). The experimental data could be fitted well to Mott-VRH (eqn. 1.20) model, i.e.

$$\rho = \rho_{0m} \exp\left(\frac{T_{0m}}{T}\right)^{1/4} \quad \text{----------} \quad (4.2)$$

compared to other models. The ρ_{0m} and T_{0m} are listed in Table 4.5. The plots of $\ln(\rho)$ versus $T^{-1/4}$ are shown in Fig. 4.18 for the samples x = 0.05 and 0.10 and, the fitted data are shown as solid lines. So, the resistivity data above T_{MI} could be explained by using Mott-VRH model. The T_{MI} values for samples with $x \geq 0.15$ are quite close to room

temperature, and as a result there are only few data in the semiconducting region. So, I could not carry out the fit in the semiconducting region of those samples.

($N(E_F)$), $R_{hop}(T)$ and $E_{hop}(T)$ have been estimated from the fitted parameters and by following section 3.2.4 (eqn. 3.8-3.10). The fitted and estimated parameters from the resistivity analysis are tabulated in Table 4.5.

The temperature variation of resistivity in zero field and in the presence of 10kOe magnetic fields are shown in Fig. 4.19 for samples x = 0.15 and 0.20. We can see the reduction of magnitude of resistivity and shifting of T_{MI} towards higher temperature in the presence of magnetic field. Thus the applied magnetic field enhances the FM interaction. The resistivity in the metallic region in the presence of magnetic field could also be fitted to eqn. 4.1. The values of parameters ρ_0, ρ_2 & $\rho_{4.5}$ for x = 0.15 & 0.20 samples in the presence of magnetic field are found to be ($0.092\Omega cm$, $5.44\times10^{-6}\Omega cmK^{-2}$, $2.72\times10^{-12}\Omega cmK^{-4.5}$) and ($0.067\Omega cm$, $4.10\times10^{-6}\Omega cmK^{-2}$, $1.73\times10^{-12}\Omega cmK^{-4.5}$) respectively. The values of ρ_0 are found to be small compared to the case of zero field resistivity (Table 4.4) and this is mainly due to growth of domain size in the presence of magnetic field. The temperature variation of percentage of negative magneto-resistivity (-MR%) is shown in Fig. 4.20 for (a) x = 0.15 and (b) x = 0.20. A sharp peak in the vicinity of T_c has been observed. These values are found to be 23% and 20% for x = 0.15 and 0.20 respectively. Increase in magnitude of MR has been observed with decrease in temperature below T_{MI}. Such behaviour has been observed by other group in this system [56].

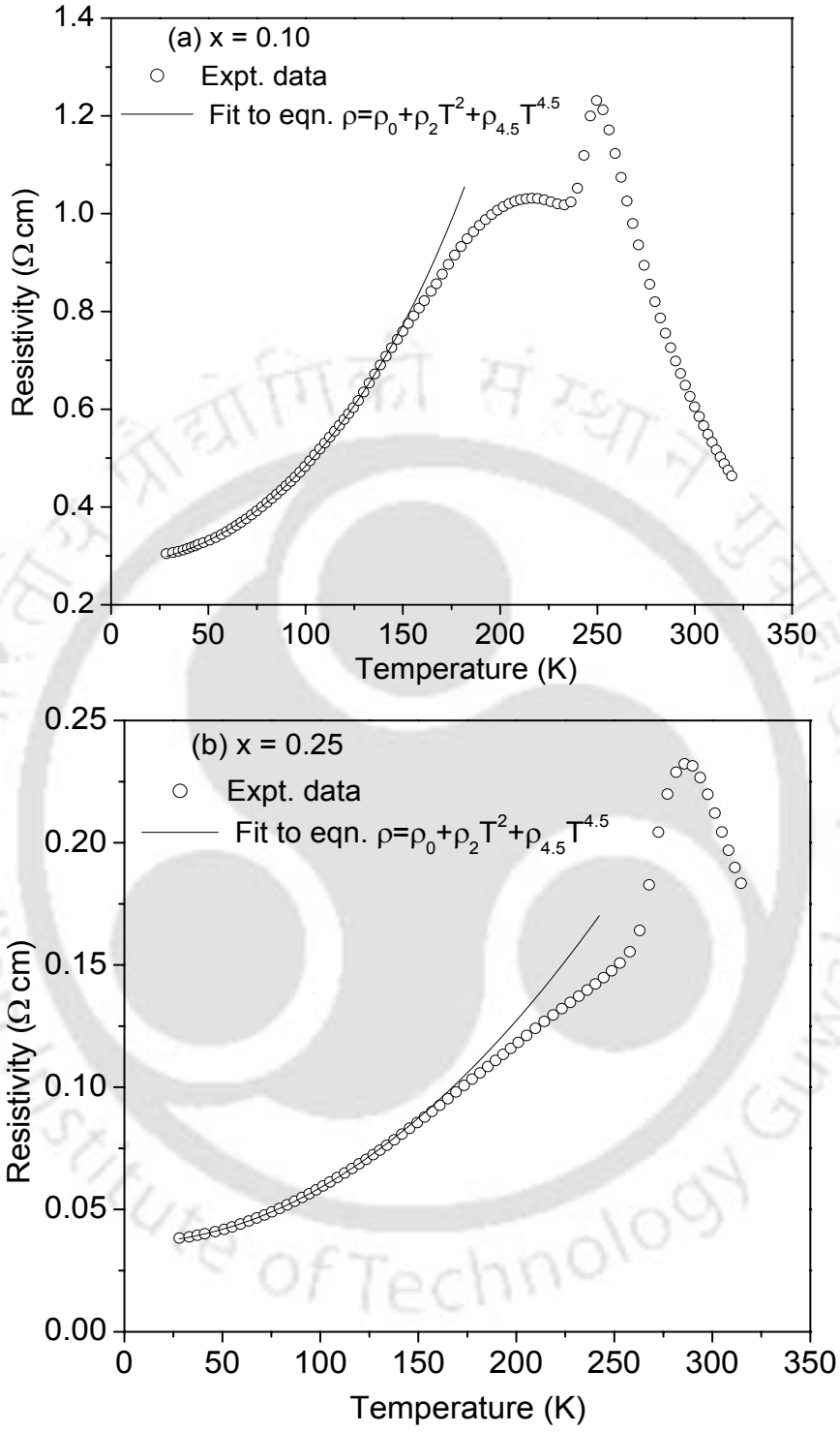

Fig. 4.17: Temperature variation of resistivity of $La_{1-x}Ag_xMnO_3$ for (a) x = 0.10 and (b) x = 0.25 samples. Solid lines are the fit to eqn. $\rho = \rho_o + \rho_2 T^2 + \rho_{4.5} T^{4.5}$.

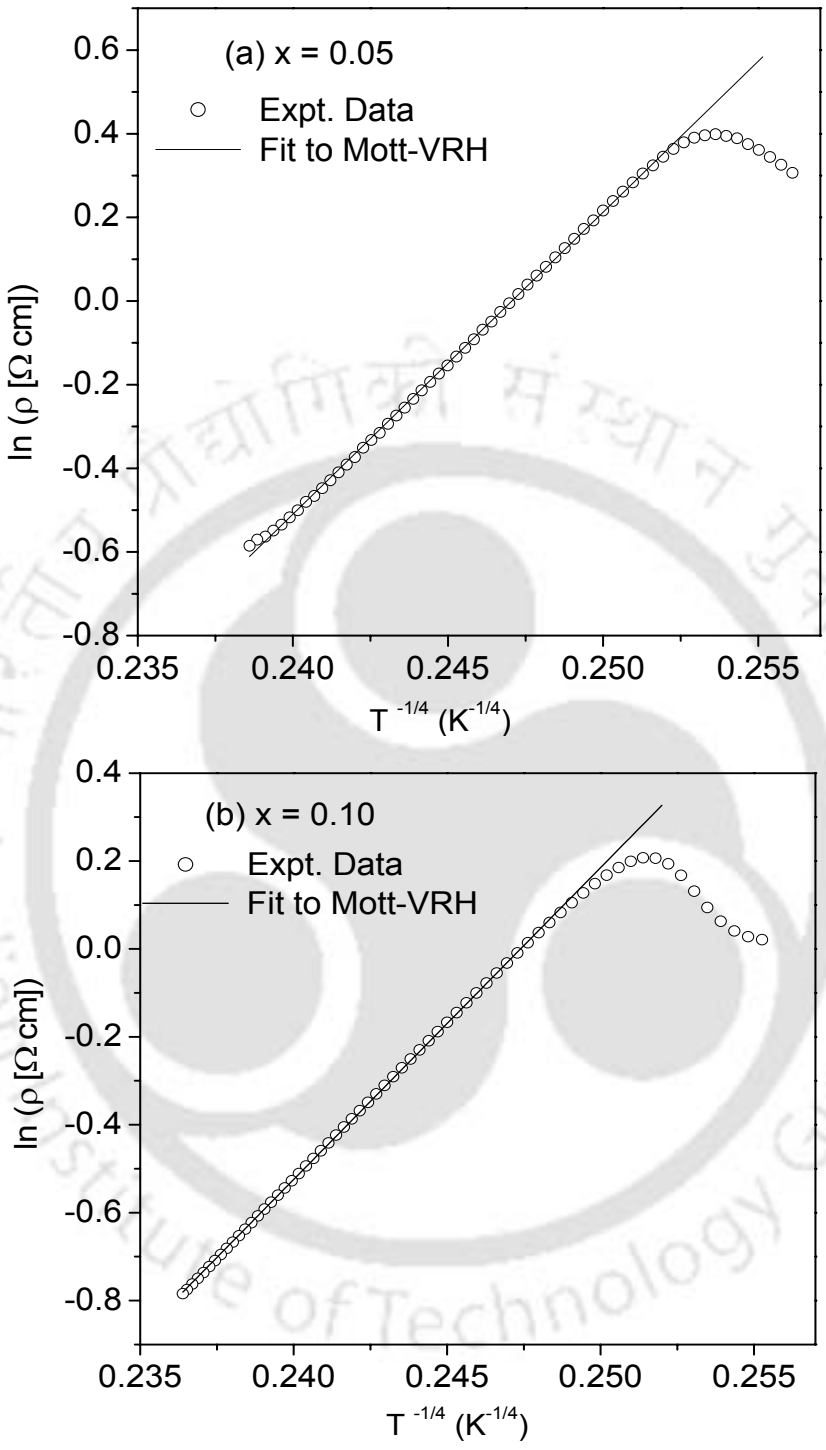

Fig. 4.18: ln(ρ) versus $(1/T)^{1/4}$ plots of $La_{1-x}Ag_xMnO_3$ for (a) x = 0.05 and (b) x = 0.10. Solid lines are the fit to eqn. $\rho = \rho_{0m} \exp\left(\frac{T_{0m}}{T}\right)^{1/4}$.

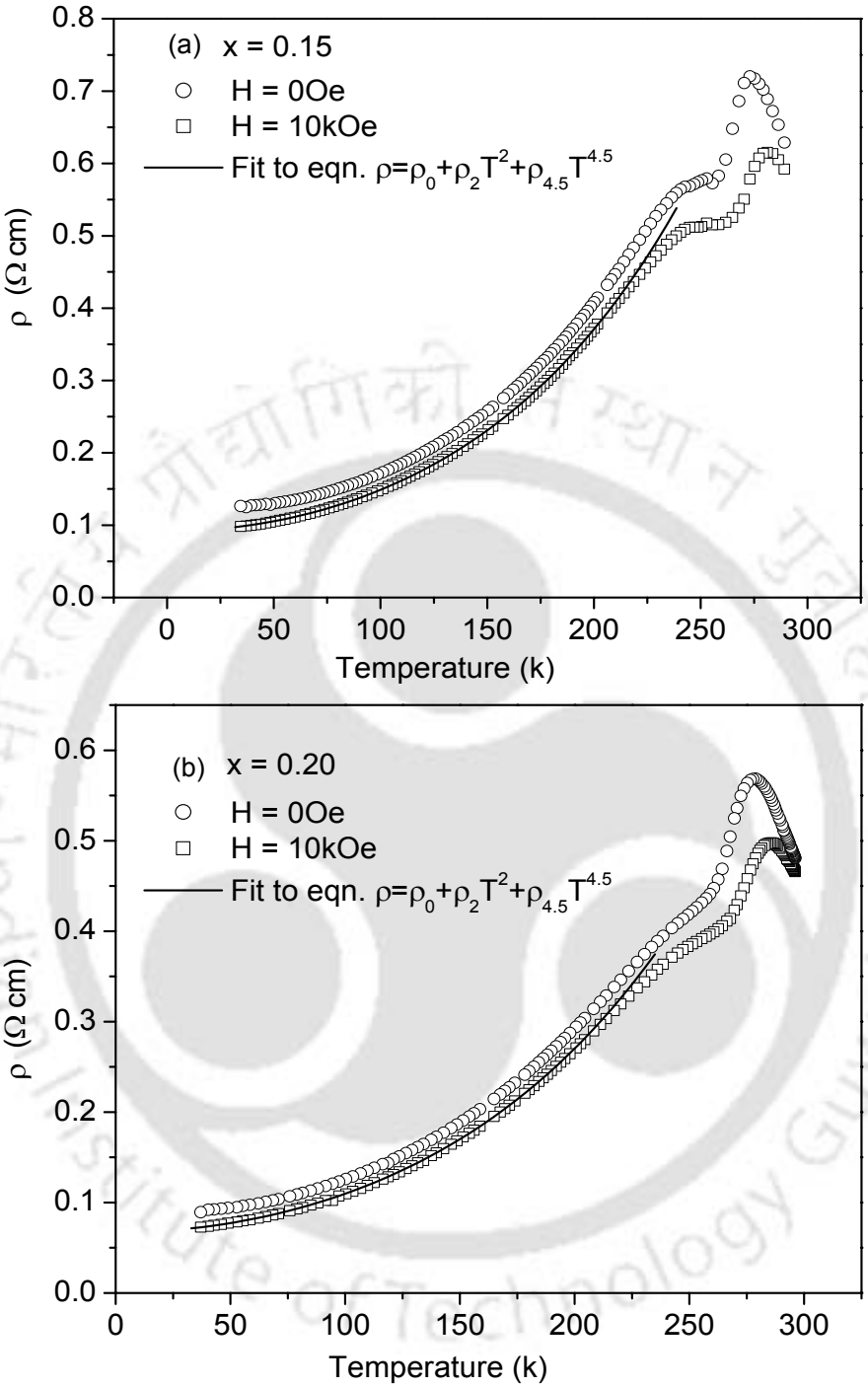

Fig. 4.19: Electrical resistivity as a function of temperature for (a) $La_{0.85}Ag_{0.15}MnO_3$ (x = 0.15) and (b) $La_{0.8}Ag_{0.2}MnO_3$ (x = 0.20) samples. The experimental data corresponding to 0 and 10kOe magnetic fields are shown as circles and squares respectively. Solid lines represent the fit to eqn. $\rho = \rho_0 + \rho_2 T^2 + \rho_{4.5} T^{4.5}$.

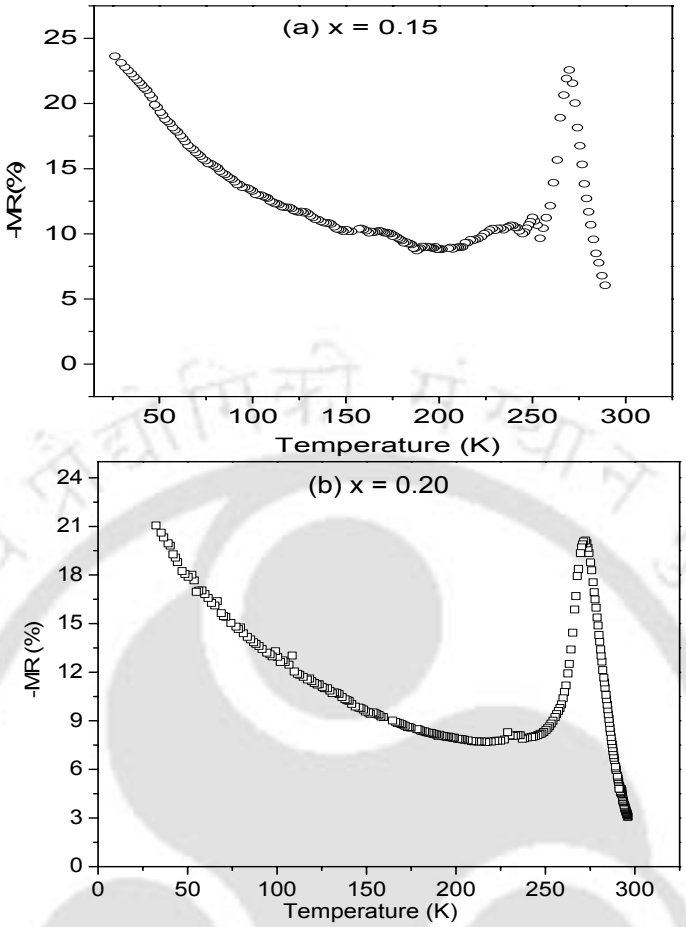

Fig. 4.20: Temperature variation of negative magneto-resistivity measured at 10kOe fields for (a) $La_{0.85}Ag_{0.15}MnO_3$ (x = 0.15) and (b) $La_{0.8}Ag_{0.2}MnO_3$ (x = 0.20) samples.

4.1.5. Effect of Low Temperature Annealing

To study the effect of low temperature annealing, one set of $La_{1-x}Ag_xMnO_3$ compounds were prepared for x = 0.05, 0.10, 0.15, 0.20 and 0.30 by annealing at 1050^0C for over 40 hours. The XRD patterns for all the samples are shown in Fig. 4.21. The patterns are mostly comparable to those obtained from high temperature annealing method. The patterns are essentially in single phase form for x ≤ 0.20 and they could be refined using $R\bar{3}c$ space group. Minor extra peaks corresponding to Mn_3O_4 impurity is observed for x = 0.30 sample and it is marked as solid circle. The lattice parameters are given in Table 4.6.

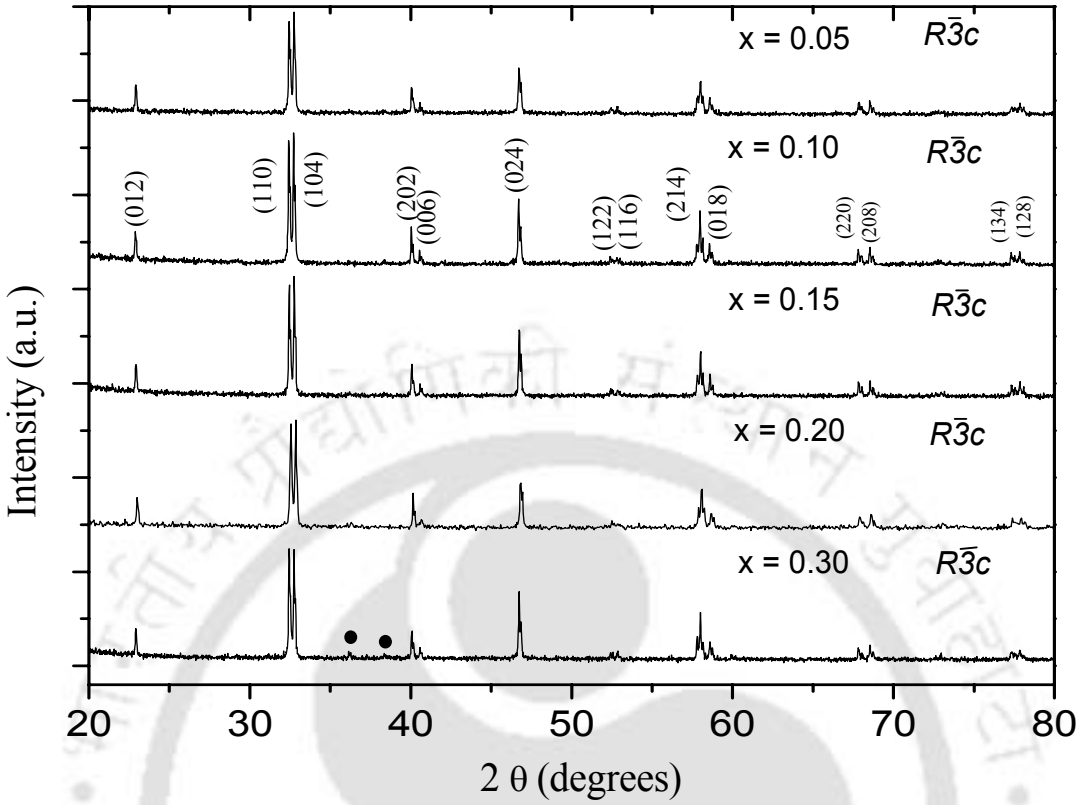

Fig. 4.21: XRD patterns of $La_{1-x}Ag_xMnO_3$ compounds prepared at low temperature for x = 0.05, 0.10, 0.15, 0.20 and 0.30. Solid circles represent the peak due to the presence of minor Mn_3O_4.

AC susceptibility measurements show that all samples exhibit ferromagnetic transition with T_{on} values in the range of 253 to 262K. The typical plots of χ' versus T are shown in the Fig. 4.22 for x = 0.15 & 0.30 samples. The FM transition temperature is quite low compared to the materials prepared at high temperature (section 4.1.3), in other words, the FM interaction is relatively weak. In addition to that a change of slope with minor fall in susceptibility has been observed at around 100K. This could be either due to freezing of cluster glass state or reentrant spin glass behaviour.

Electrical resistivity data show that these materials exhibit metal-insulator transitions with T_{MI} values ranging from 254 to 259K. The T_{MI} values are listed in Table 4.6. The T_{MI} values are comparable to the onset of ferromagnetic transition temperature T_{on}. Typical plots of temperature variation of electrical resistivity at 0, 10 and 50kOe magnetic fields are shown in Fig. 4.23 for x = 0.30 sample. The reduction in resistivity magnitude and shift in T_{MI} towards higher temperature can be observed. A small upturn in

resistivity with decrease in temperature has been observed below around 100K for zero field resistivity data. It is found to be in the vicinity of sharp fall in susceptibility observed at around 100K. The resistivity data in the metallic region could be fitted to the empirical relation $\rho = \rho_0 + \rho_n T^n$ with n ranges from 3 to 2. The zero field data could be fitted with n = 3. The above exponent suggests that the electrical conduction in zero field is controlled by scattering of charge carriers by spin fluctuations [129]. The value of n for 10 and 50kOe fields are found to be 2.5 and 2 respectively. Thus in the presence of magnetic field the spin fluctuation scattering is suppressed and the conductivity mechanism is mainly due to electron-electron scattering. The resistivity data in the semiconducting region could be fitted to variable range hopping model. The typical plot of negative magneto resistivity versus temperature is shown in Fig. 4.24 for x = 0.15 sample. All samples show CMR behaviour. The maximum magneto-resistivity of 73% was observed for x=0.15 sample at 50kOe field in the vicinity of T_c. The maximum MR values obtained for different samples are tabulated in Table 4.6.

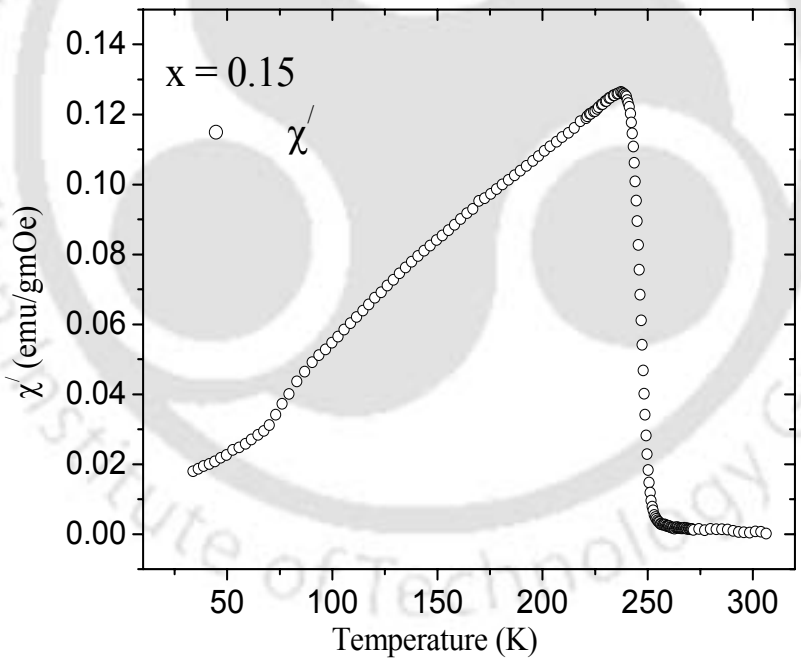

Fig. 4.22: Temperature variation of in phase (χ') component of ac susceptibility of $La_{1-x}Ag_xMnO_3$ for x = 0.15 sample (low temperature annealed sample).

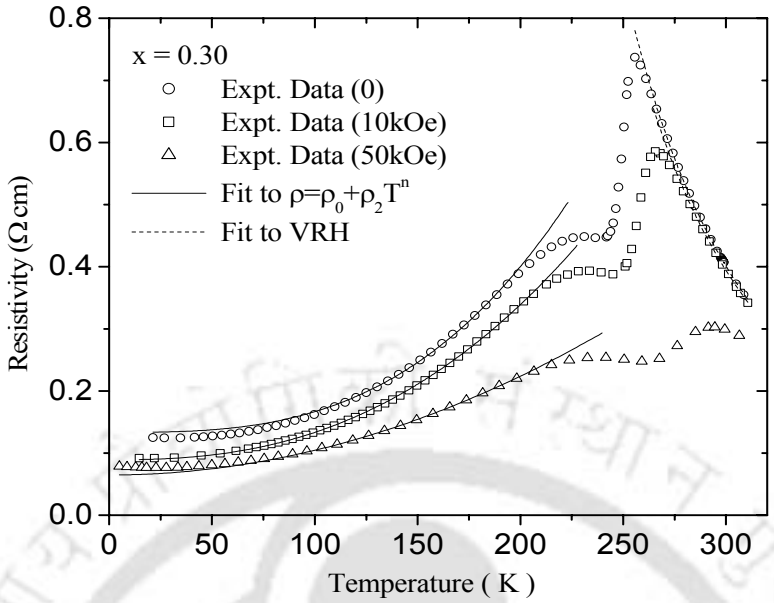

Fig. 4.23: Electrical resistivity as a function of temperature for x = 0.30, low temperature annealed sample. The experimental data corresponding to zero, 10kOe and 50kOe magnetic fields are shown as circles, squares and triangles respectively. Solid lines and dashed lines represent fit to eqn. $\rho = \rho_0 + \rho_2 T^n$ and Mott-VRH model respectively.

Table 4.6: Parameters obtained from XRD pattern refinement and, electrical resistivity, magneto-resistivity and ac susceptibility measurements of low temperature annealed sample. a and c are the lattice parameters. T_{on} and T_c are the ferromagnetic transition temperatures corresponding to onset and mid-point respectively. T_{MI} is the metal-insulator transition temperature. $-MR_{max}(\%)$ is the maximum magneto-resistivity for 10 kOe and 50 kOe magnetic field.

Sample → / Parameters ↓	x = 0.05	x = 0.10	x = 0.15	x = 0.20	x = 0.30
Space group	$R\bar{3}c$	$R\bar{3}c$	$R\bar{3}c$	$R\bar{3}c$	$R\bar{3}c$
a (Å)	5.524	5.531	5.532	5.525	5.522
c (Å)	13.349	13.365	13.366	13.353	13.345
T_{on}(K)	262	256	253	255	257
T_c(K)	258	256	247	246	252
T_{MI}(K)	259	256	254	255	254
$-MR_{max}(\%)$ (10kOe)	33	43	51	26	41
$-MR_{max}(\%)$ (50kOe)	61	70	73	53	66

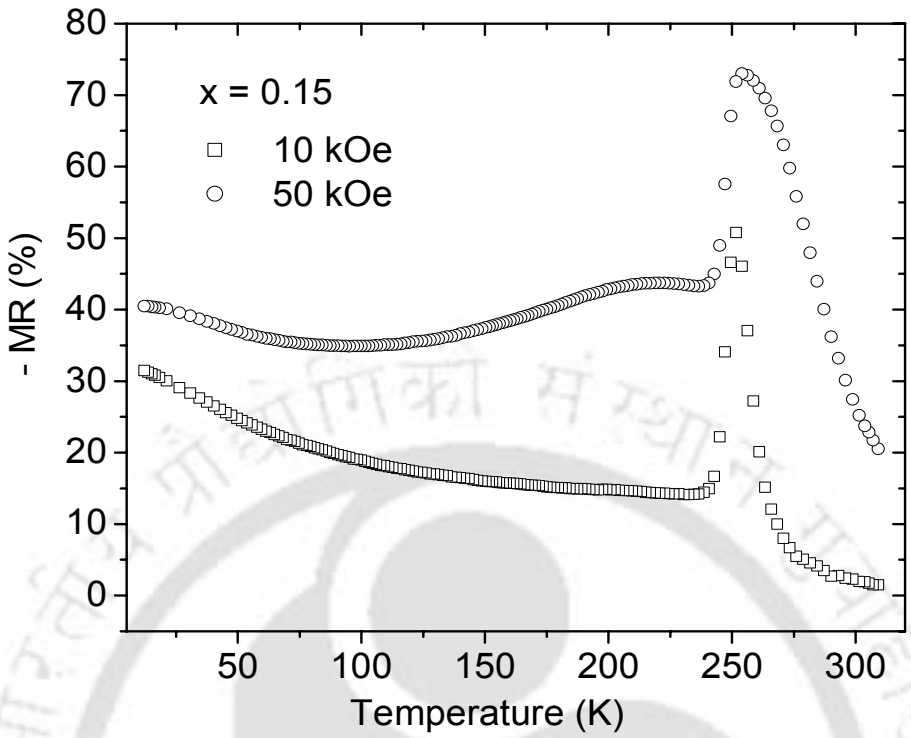

Fig. 4.24: Temperature variation of negative magneto-resistivity measured at 10kOe (squares) and 50kOe (circles) fields of $La_{1-x}Ag_xMnO_3$ for x = 0.15 sample (low temperature annealed sample).

4.2. $La_{1-x}Cu_xMnO_3$ (x = 0.05 to 0.40) Compounds

The preparation of $La_{1-x}Cu_xMnO_3$ compounds, its characterization and results obtained from X-ray diffraction, electrical resistivity, magneto-resistivity and ac susceptibility are discussed in this section.

4.2.1. Preparation

The $La_{1-x}Cu_xMnO_3$ compounds were prepared for x = 0.05, 0.10, 0.15, 0.20, 0.30 and 0.40 by nitrate route to have better homogeneous mixture of starting materials. Stoichiometric ratio of La_2O_3, 'Cu' metal and 'Mn' metal with 99.9% purity were weighed and dissolved in nitric acid. The metal nitrate solutions were mixed together and heated slowly using a hot plate. The mixture was presintered at 800^0C for 30 hours with intermediate grindings at an interval of 10 hours. The sintering in pellet form was carried out at 950^0C to 1050^0C for over 20 hours. At the end of every 10 hours, the pellets were crushed into the powder and repelletized. The above type of sintering was repeated at 1200^0C for over 50 hours. All the above heat treatments were carried out in air and finally the samples were furnace cooled.

4.2.2. Characterization

XRD patterns recorded for $(La_{1-x}Cu_x)MnO_3$ compounds are shown in Figs. 4.25 (for x = 0.05, 0.10 and 0.15) and 4.26 (for x = 0.20, 0.30 and 0.40). It is observed that the samples are in single phase form for $x \leq 0.20$ and they could be indexed to $R\bar{3}c$ space group. Two extra peaks appearing at 36.25^0 and 38.41^0 for the samples x = 0.30 and 0.40 are marked as solid circles. The careful analysis shows that these two peaks are due to the presence of minor Mn_3O_4 impurity [218].

The XRD patterns were analyzed with the help of Fullprof program by employing Rietveld refinement technique [191]. Typical XRD patterns along with Rietveld refinement are shown in Figs. 4.27 and 4.28 for x = 0.10 and 0.20 respectively. Here, the experimental data are shown as crosses (+) and the calculated intensities are shown as solid lines. The dotted lines represent the difference between measured and calculated intensities. The expanded view of splitting of (110) & (104) peaks are shown in the inset of the respective figures. The refined values of lattice parameters, occupancy values and reliability factors are given in Table 4.7. The lattice parameters are comparable to those of

'Ag' doped, $La_{1-x}Ag_xMnO_3$ compounds as discussed in the previous section (4.1.2). However, no systematic variation of lattice parameters is observed. The occupancy values are mostly comparable to the starting composition. For a few samples, vacancy in 'Mn' site can be observed. I could not unequivocally determine the occupancy value of oxygen, because X-ray scattering power of oxygen is quite low. The occupancy value of oxygen is assumed to be one in the above refinement. Typical values of refined isotropic displacement (temperature) parameter for La/Cu, Mn and O are respectively 0.75, 0.12 and 0.15Å^2 for x = 0.15 sample.

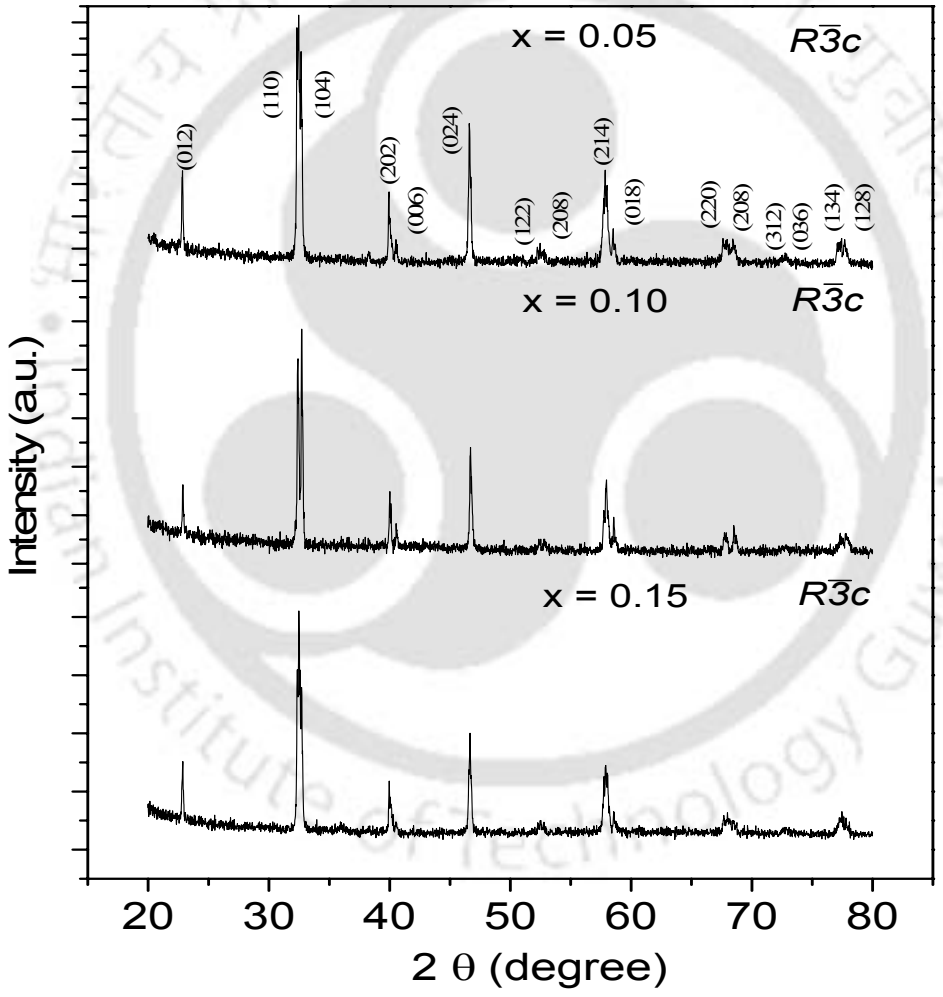

Fig. 4.25: XRD patterns of $La_{1-x}Cu_xMnO_3$ for x = 0.05, 0.10 and 0.15.

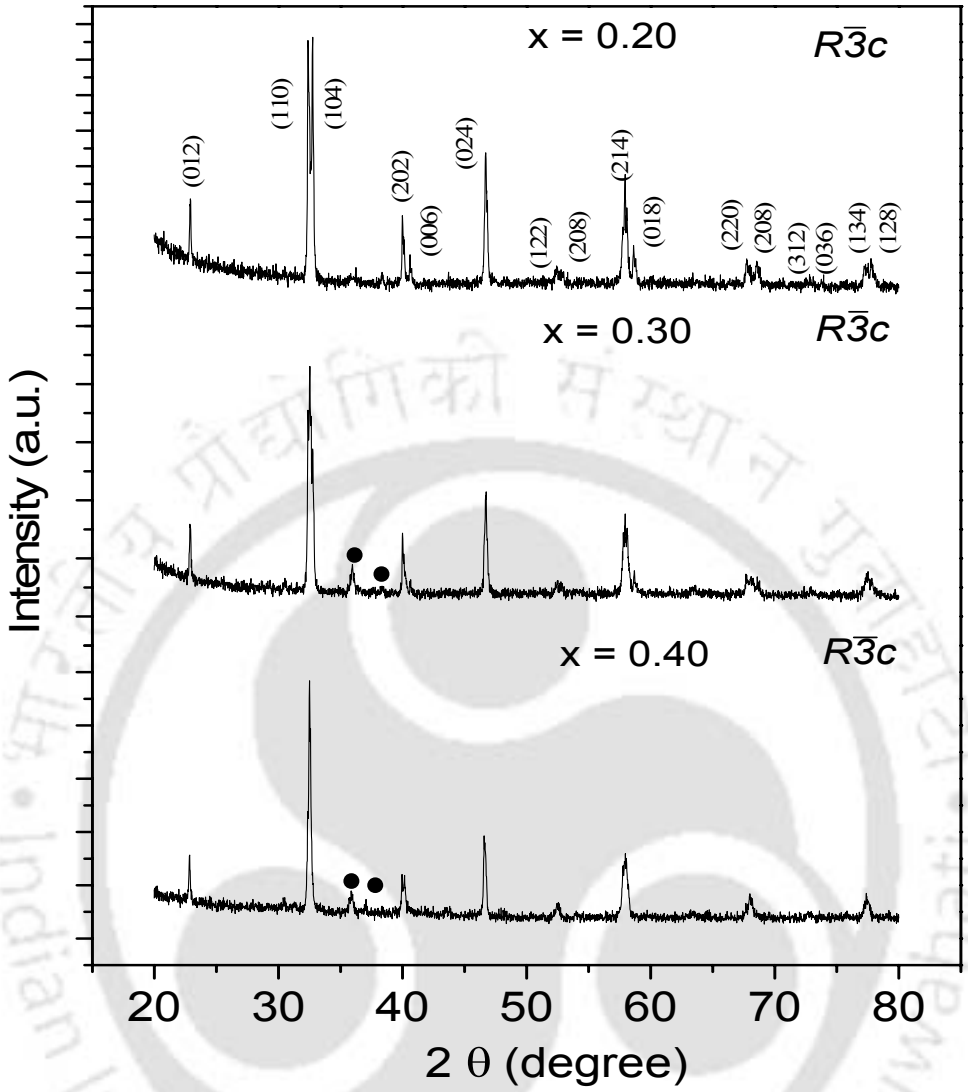

Fig. 4.26: XRD patterns of $La_{1-x}Cu_xMnO_3$, for x = 0.20, 0.30 and 0.40. Solid circles represent the peaks due to the presence of minor Mn_3O_4 impurity in the materials.

It is found that particle size decreases with increase in 'Cu' concentration. This suggests that the instability of crystal structure increases with the increase of 'Cu' due to ionic size mismatch. The Mn-O & Mn-Mn bond lengths and, $\angle Mn-O-Mn$ bond angles were calculated using the parameters obtained from the Rietveld refinement and these values are listed in Table 4.7.

The average valency of 'Mn' ions was determined by the chemical titration and these values are tabulated in Table 4.8. It is observed that the mixture of Mn^{3+} and Mn^{4+} ions are present in this compound. The Mn^{4+} concentration increases with the doping as

expected. The values of valency are mostly in agreement with the expected result by supposing 'Cu' is in Cu^{1+} state. However for x = 0.30 and x = 0.40 samples, the average 'Mn' valency is found to be quite different from the expected results and it is mainly due to the segregation of Mn_3O_4 impurity.

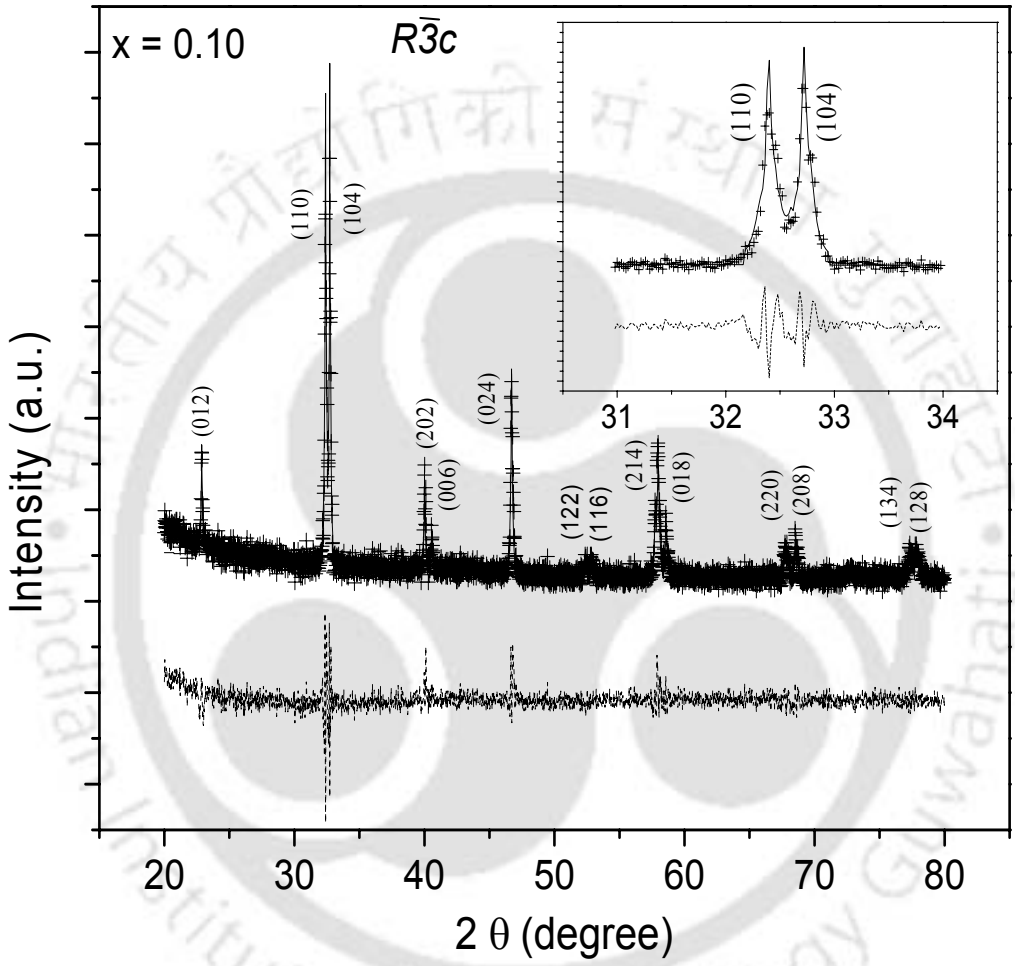

Fig. 4.27: XRD pattern along with Rietveld refinement for the sample $La_{0.9}Cu_{0.1}MnO_3$ (x = 0.10). The '+' signs represent experimental data points and solid line represents Rietveld refined data. The dotted lines show the difference between experimental & refined data. The inset shows the expanded view of (110) & (104) peaks.

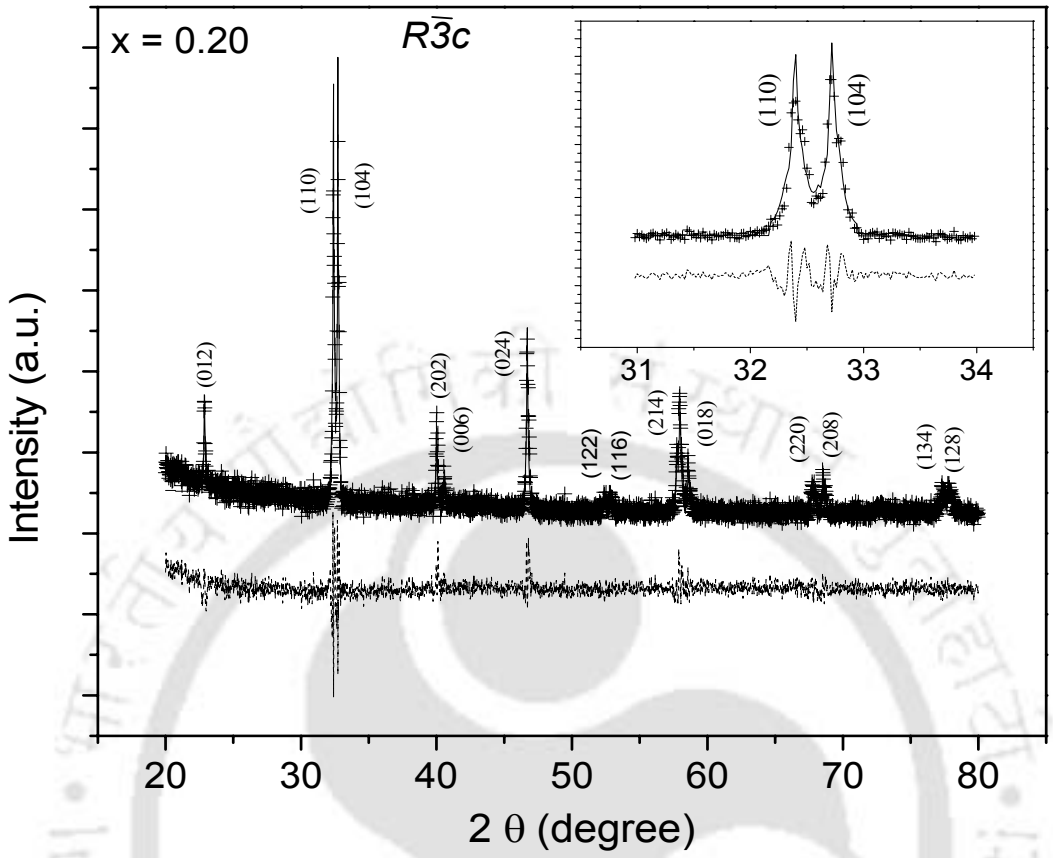

Fig. 4.28: XRD pattern along with Rietveld refinement for the sample $La_{0.8}Cu_{0.2}MnO_3$ (x = 0.20). The '+' signs represent experimental data points and solid line represents Rietveld refined data. The dotted lines show the difference between experimental & refined data. The inset shows expanded view of (110) & (104) peaks.

Typical optical microscope photograph for the sample x = 0.10 with a magnification of 100 is shown in Fig. 4.29. The morphology is found to be uniform throughout the material.

The typical SEM micrograph for x = 0.10 sample is shown in the Fig. 4.30. The composition of the sample from EDAX is found to be $La_{0.92}Cu_{0.12}Mn_{0.96}O_3$. It has been normalized to 3 oxygen atom per formula unit. The 'Mn' valency from above compositional analysis is found to be 3.25 and it is comparable to the value obtained from chemical titration.

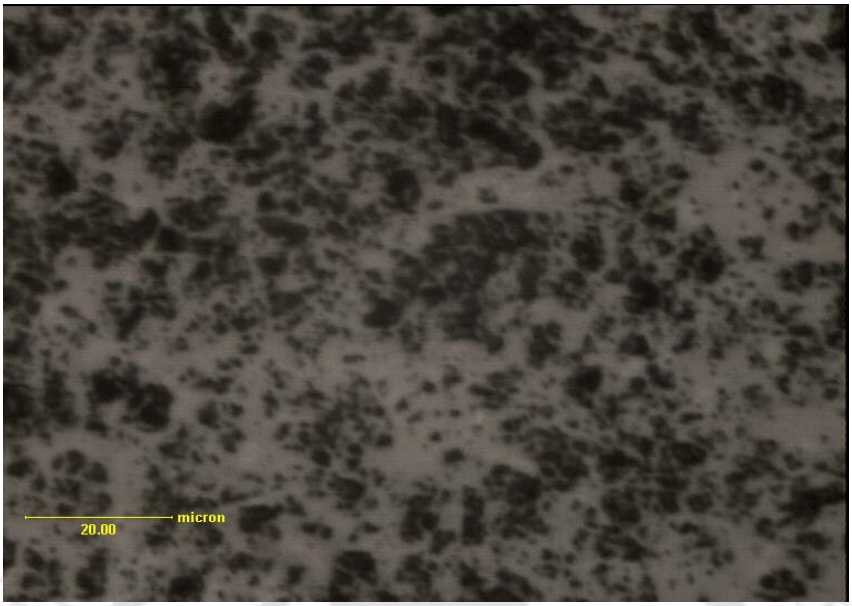

Fig. 4.29: Optical micrograph (magnification-100) of the sample $La_{0.9}Cu_{0.1}MnO_3$ (x = 0.10).

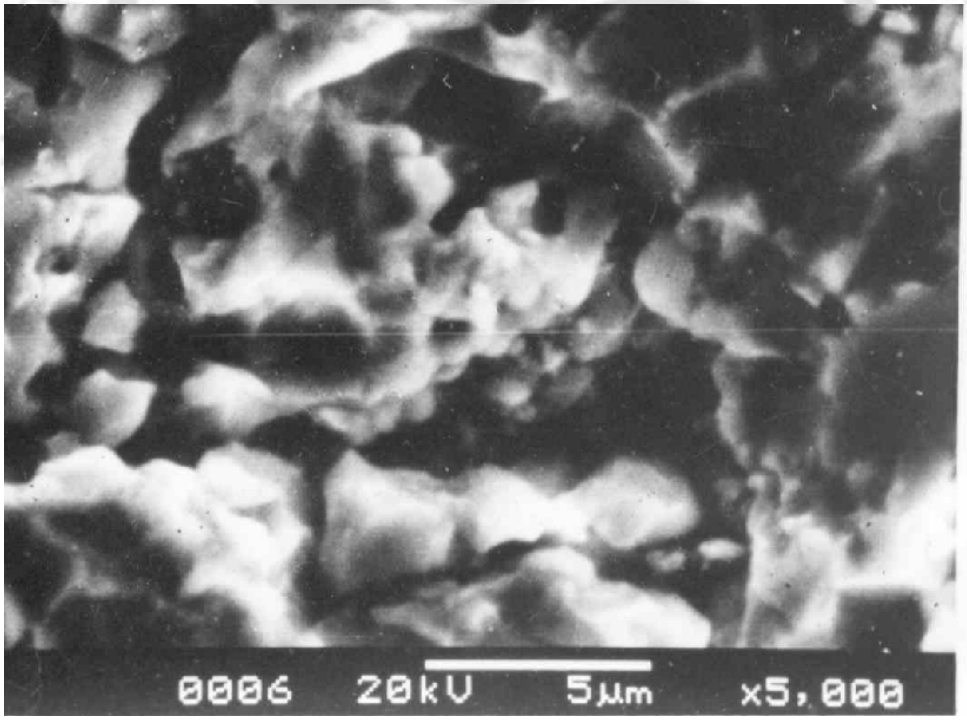

Fig. 4.30: SEM-micrograph (magnification-5,000) of the sample $La_{0.9}Cu_{0.1}MnO_3$ (x = 0.10).

Table 4.7: Parameters obtained from the XRD analysis of the samples $La_{1-x}Cu_xMnO_3$ (x = 0.05, 0.10, 0.15, 0.20, 0.30 and 0.40). R_p, $R_{\omega p}$, R_{exp}, R_{Bragg}, R_F and χ^2 are the reliability factors obtained from the Rietveld refinement. 'S_G' is the average particle size obtained from the line broadening of the XRD pattern.

Samples → / Parameters ↓	x = 0.05	x = 0.10	x = 0.15	x = 0.20	x = 0.30	x = 0.40
Space Group	$R\bar{3}c$	$R\bar{3}c$	$R\bar{3}c$	$R\bar{3}c$	$R\bar{3}c$	$R\bar{3}c$
a (Å)	5.535	5.531	5.528	5.534	5.512	5.526
c (Å)	13.373	13.352	13.370	13.352	13.373	13.469
G_{La}	0.873	0.919	0.847	0.845	0.745	0.559
G_{Cu}	0.029	0.081	0.153	0.155	0.254	0.441
G_{Mn}	0.958	0.995	0.947	0.982	0.999	0.977
R_p	17.4	16.1	18.6	13.9	16.6	12.8
$R_{\omega p}$	22.0	19.6	24.1	17.7	20.9	16.0
R_{exp}	13.9	14.3	14.4	13.5	18.0	12.7
R_{Bragg}	12.8	9.7	19.4	13.8	23.1	13.4
R_F	7.0	7.2	11.5	8.5	12.8	10.1
χ^2	1.6	1.6	1.7	1.7	2.3	1.1
Volume ($Å^3$)	354.7	353.7	353.8	354.1	351.9	356.2
Mn-Mn (Å)	3.910	3.892	3.892	3.894	3.885	3.901
Mn-O (Å)	1.973	1.971	1.967	1.973	1.963	1.973
$\angle Mn-O-Mn$	164.5	161.6	163.2	161.1	163.4	167.1
S_G(nm)	67	58	50	43	38	35

4.2.3. AC Susceptibility Study

Ac susceptibility as a function of temperature was measured for the above samples at an ac field amplitude of 5.3Oe and a frequency of 233Hz. χ' and χ'' as a function of temperature are shown in Fig. 4.31 for x = 0.05 (a), 0.10(b) and 0.15(c). We can see that all the above materials exhibit ferromagnetic transition with onset temperature ranging from 203 to 164K. Let us first take the χ' versus T plot of x = 0.10 sample for discussion (Fig. 4.31(b)), here below the FM transition, the susceptibility decreases with decrease in temperature and such a trend has been observed in other perovskite manganites [50, 83, 144, 216]. This is mainly due to magnetic anisotropy, or in other words, loss of long range FM ordering. In addition to that, a minor fall in susceptibility is observed at around 100K.

The χ' versus T plots of x = 0.05 and x = 0.15 samples show that in addition to FM transition and loss of long range FM ordering, a sharp fall in susceptibility is observed at around 116 and 107K respectively. They can be attributed to reentrant spin glass (RSG) behaviour. χ'' versus T plots of respective samples show peak in the vicinity of reentrant spin glass behaviour and the peak temperature is taken as freezing temperature of RSG state and, these values are listed in Table 4.8. As discussed in the section 3.1.3, the RSG state is mainly due to the presence of competing antiferromagnetic interaction. However, the χ'' versus T plot of x = 0.10 sample doest not show any appreciable peak and this suggests that the RSG state may be almost absent in the sample. Thus the composition x = 0.10 sample is found to be optimum doping in the present series with relatively strong FM interaction. The minor fall in χ' versus T plot at around 101K can be attributed to the presence of weak AFM phase in isolated regions. For x = 0.05 and 0.15 samples in addition to peaks corresponding to RSG state, higher temperature peaks at 176 & 150K respectively are observed in χ'' versus T plots. This can be attributed to Neel temperature of AFM transition, where loss is expected to be maximum due to the presence of FM phase. Such peak can not be seen in the plot of x = 0.10 sample. The composition x = 0.05 is very close to the parent compound (x = 0) and the appearance of AFM could be mainly due to inhomogeneous distribution of Mn^{3+} and Mn^{4+} ions.

Similarly, the χ' and χ'' plots as a function of temperature for higher doped materials (x = 0.20, 0.30 & 0.40) are shown in Fig. 4.32. These materials also exhibit FM and AFM transitions. However, the FM contribution is quite weak, which result in sharp fall in susceptibility at the end of FM transition and it can be attributed to the presence of

dominant AFM interaction. The $\chi^{//}$ versus T plots of x = 0.20 & 0.40 samples show sharp peak at around 110K, which is the Neel temperature. As a result of low FM transition with weak signal, I have not observed any strong RSG in these materials.

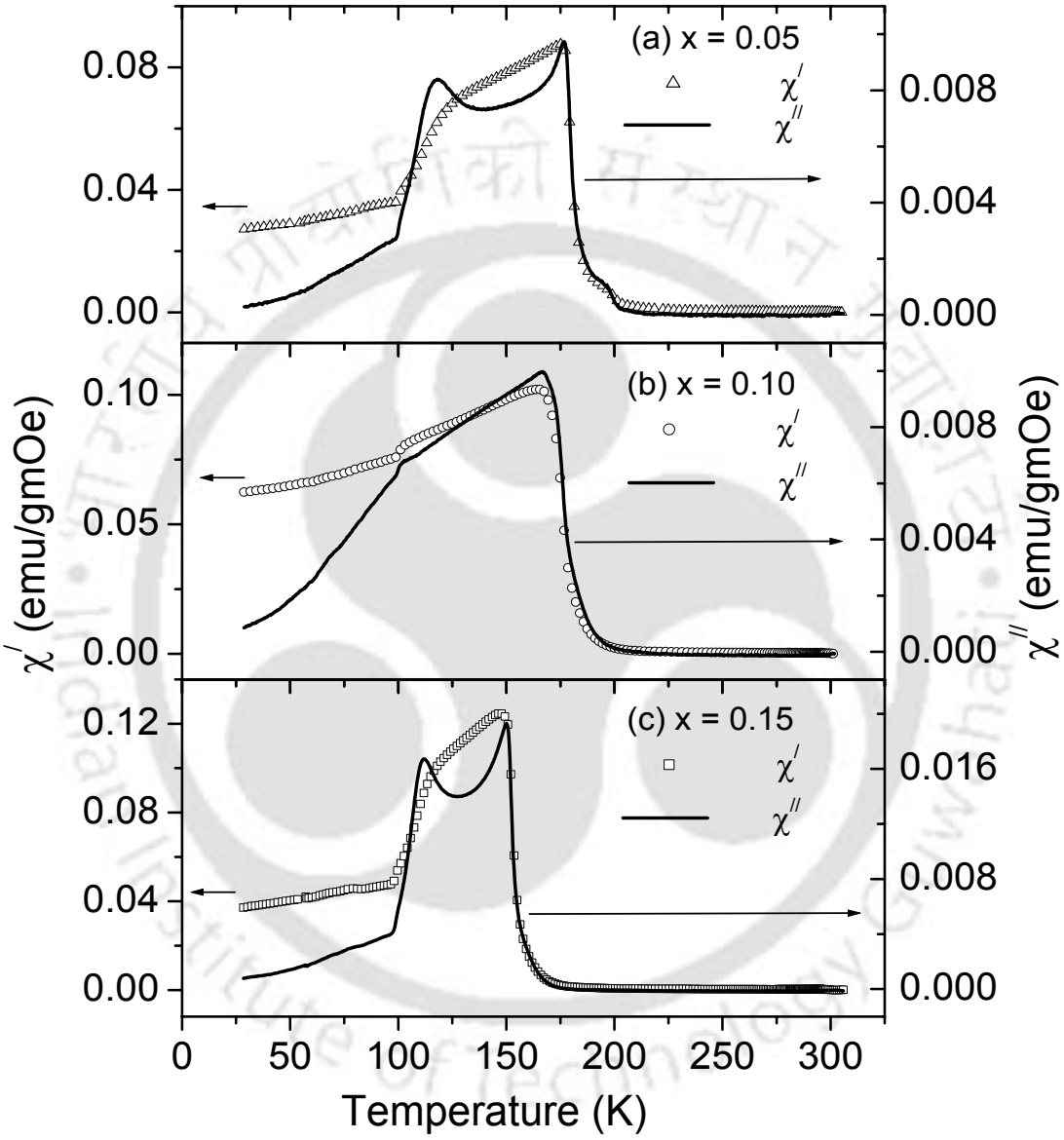

Fig. 4.31: Temperature variation of in phase ($\chi^{/}$) and out of phase ($\chi^{//}$) ac susceptibility of samples, $La_{1-x}Cu_xMnO_3$ for (a) x = 0.05, (b) x = 0.10 and (c) x = 0.15.

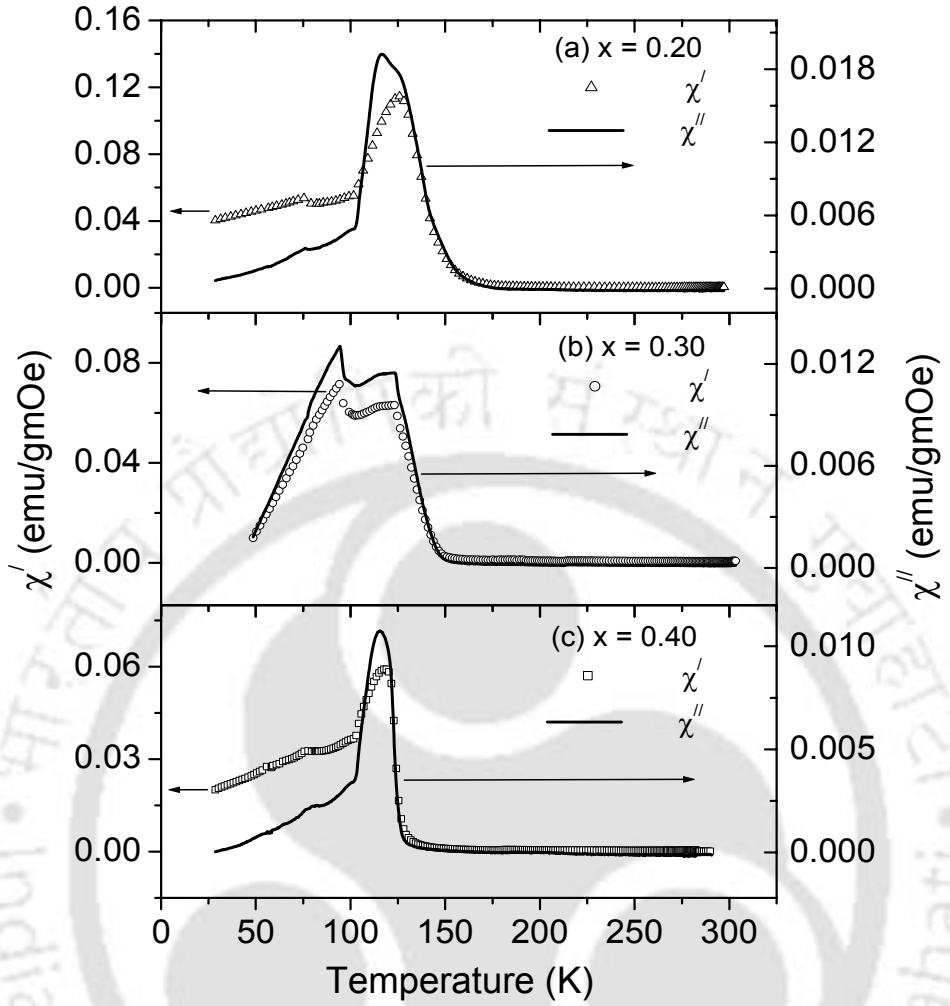

Fig. 4.32: Temperature variation of in phase ($\chi^{/}$) and out of phase ($\chi^{//}$) ac susceptibility of samples, $La_{1-x}Cu_xMnO_3$ for (a) x = 0.20, (b) x = 0.30 and (c) x = 0.40.

The mid-point of FM transition temperature, T_c was determined from the temperature corresponding to peak in $|d\chi/dT|$ versus temperature (T) plot. The ferromagnetic onset temperature, T_{on} was determined from $\chi^{/}$ vs. T plots and these values are listed in Table 4.8. Saturation susceptibility ($\chi^{/}_s$) values are taken at the end of PM to FM transitions and these values are listed in Table 4.8. The $\chi^{/}_s$ value increases with the 'Cu' concentration up to x = 0.15 and then decreases. This suggests that the concentration of Mn^{3+} and Mn^{4+} pairs increases with 'Cu' doping and reaches the optimum value for x = 0.15. At the same time, the ferromagnetic transition temperature is found to decrease with 'Cu' doping and this could be as a result of some of the 'Cu' entering into the 'Mn' site and weakening the DE interaction. Such a decrease in ferromagnetic transition

temperature is reported in 'Cu' doped samples, i.e. 'Cu' doping in 'Mn' site in mixed valent hole doped CMR manganites [30, 166, 221, 222]. Unlike the case of 'Cu' doping [166] in place of 'Mn', where ferromagnetism is completely destroyed for about 20% 'Cu', the present set of samples exhibit ferromagnetic behaviour even up to 40% of 'Cu' doping in place of 'La'.

Table 4.8: Parameters obtained from the chemical titration and ac susceptibility measurements. The T_{on}(K), T_c(K) and χ'_s(emu/gmOe) are FM onset, mid point temperature and saturation susceptibility respectively. The uncertainty in T_{on} and T_c are ±2K and ±1K respectively. T_f is the reentrant spin glass transition temperature.

Samples ⟶ / Parameters ↓	x = 0.05	x = 0.10	x = 0.15	x = 0.20	x = 0.30	x = 0.40
'Mn' Valency	3.18	3.19	3.25	3.38	3.42	3.63
T_{on}(K)	203	190	164	154	148	131
T_c(K)	180	176	154	136	130	123
T_f(K)	116	101	107	117	102	112
χ'_s(emu/gmOe)	0.088	0.102	0.127	0.115	0.064	0.059

To ascertain the origin of low temperature peaks observed in some of the χ'' versus T plots, I have carried out the susceptibility measurements on two samples x = 0.15 and 0.40 for three different frequencies, viz. 233, 1133 and 3333Hz. They are shown in Figs. 3.33 and 3.34 respectively. We can see that (Fig. 3.33) the low temperature peak observed in χ'' versus T plots of x = 0.15 sample shifts towards higher temperature, i.e. from 107K for 233Hz to 111K for 3333Hz and it is a manifestation of RSG state. On the other hand, the position of peak observed at higher temperature is almost independent of frequency, so, the high temperature peak could be mostly due to loss associated with AFM transition.

In the case of x = 0.40 sample (Fig.3.34), no low temperature peak is observed and the high temperature peak is independent of frequency. So, it supports the earlier argument of absence of RSG state in higher doped materials.

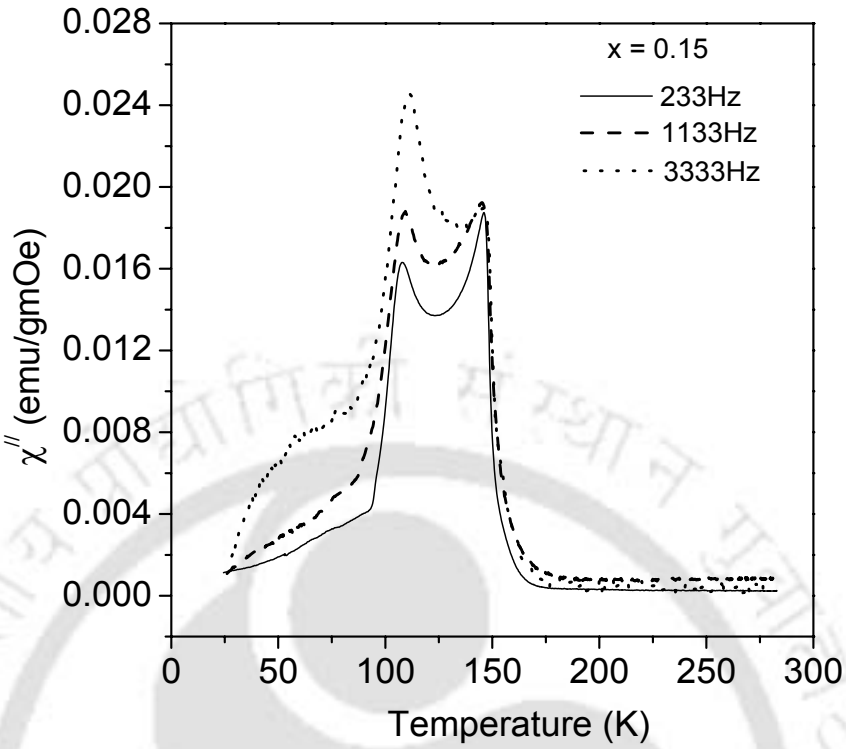

Fig. 4.33: Temperature variation of out of phase ac susceptibility ($\chi^{//}$) of samples $La_{0.85}Cu_{0.15}MnO_3$ (x = 0.15) for the frequencies 233, 1133 and 3333Hz.

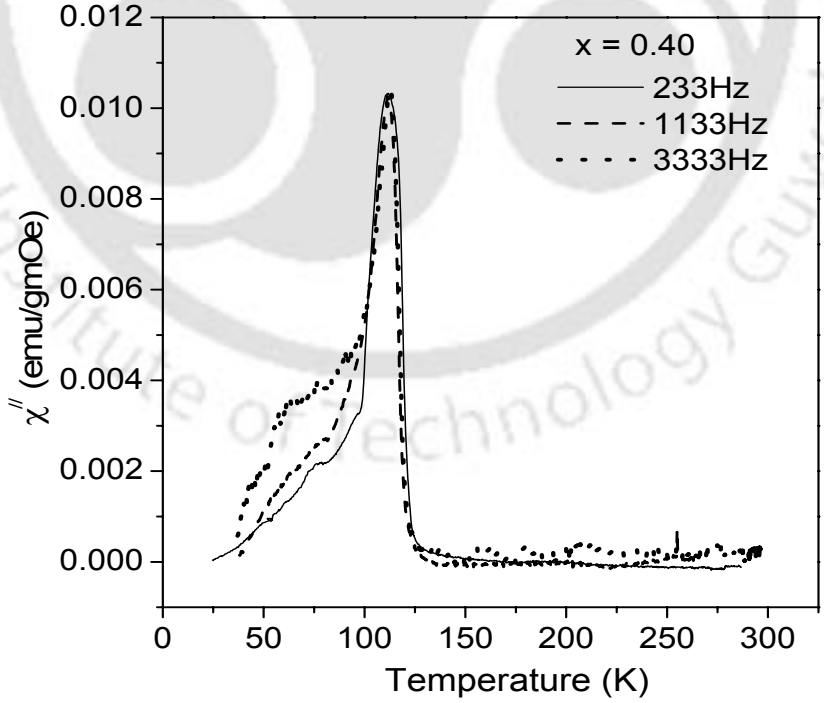

Fig. 4.34: Temperature variation of out of phase ac susceptibility ($\chi^{//}$) of samples $La_{0.6}Cu_{0.4}MnO_3$ (x = 0.40) for the frequencies 233, 1133 and 3333Hz.

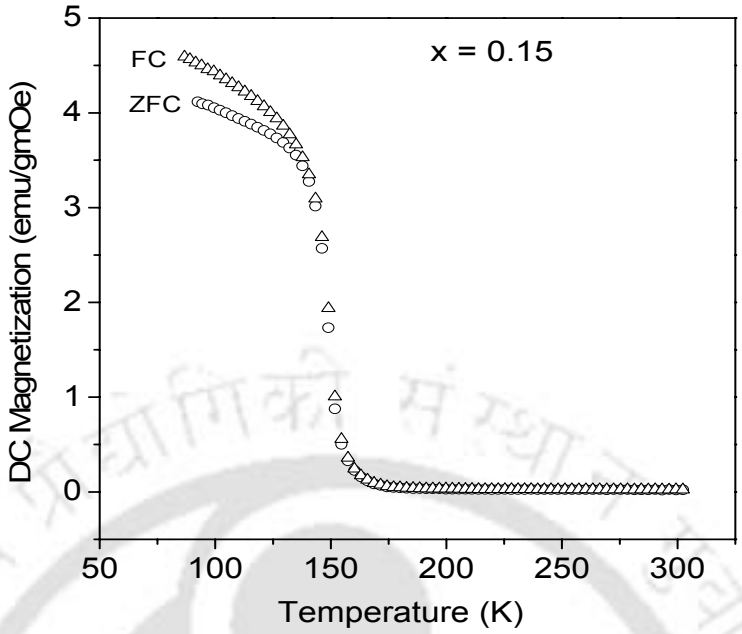

Fig. 4.35: Plot of temperature variation of DC magnetization for ZFC (circles) and FC (triangles) cases of the sample $La_{0.85}Cu_{0.15}MnO_3$ (x = 0.15).

For the sake of comparison, the dc magnetization as a function of temperature has been measured down to 80K for the sample x = 0.15 with an applied field of 50Oe. The temperature variation of zero field cooled (Circles) and field cooled (Triangles) curves are shown in Fig. 4.35. The T_{on} and T_c values are found to be 165 and 153K respectively, which are close to the values obtained from ac susceptibility measurement. There is an appreciable difference between ZFC and FC curve.

4.2.4. Electrical Resistivity and Magneto-Resistivity Studies

Temperature variation of electrical resistivity (ρ) was measured for all the above samples. Plots of ρ versus T are shown in Figs. 4.36 and 4.37 for x = 0.05 and 0.10 respectively. These two samples exhibit metal-insulator transitions at T_{MI} = 43 and 92K respectively. The T_{MI} values are found to be quite small compared to the onset of FM transition. The large difference between T_{MI} & T_{on} could be mainly due to intergranular weak links with relatively low FM transition. Such behaviour has been observed in other manganites [222].

All other samples for x > 0.10 show semiconducting behaviour. For the sake of clarity the resistivity plot is shown in logarithmic scale in Fig. 4.38 for the samples (a) x =

0.15, (b) 0.20, (c) 0.30 and (d) 0.40. The semiconducting behaviour observed for $x \geq 0.15$ samples can be explained in the basis of some of the 'Cu' entering into the 'Mn' site. The resistivity values at 290K, ρ(290K) are tabulated in Table 4.9. It has been observed that the value of ρ(290K) decreases with the increase of 'Cu' concentration up to x = 0.10 and then it is increasing. Initial decrease could be due to the generation of Mn^{4+} ions (holes) which enhances the mobility of charge carriers. The increase of ρ(290K) for $x \geq 0.15$ could be due to extrinsic parameters such as large concentration of grain boundaries due to reduced particle size and segregation of secondary phase etc.

The resistivity data in the metallic region, i.e. below T_{MI} could be fitted to eqn. 4.1 for x = 0.10 sample. The fitted data are shown as solid line in the Fig. 4.37. The fitted parameters are $\rho_0 = 103.6\Omega cm$, $\rho_2 = 2.44\times10^{-3}\Omega cmK^{-2}$, and $\rho_{4.5} = 1.8\times10^{-8}\Omega cmK^{-4.5}$. Thus the metallic resistivity of x =0.10 sample is controlled by the combination of electron-electron and electron-magnon scattering.

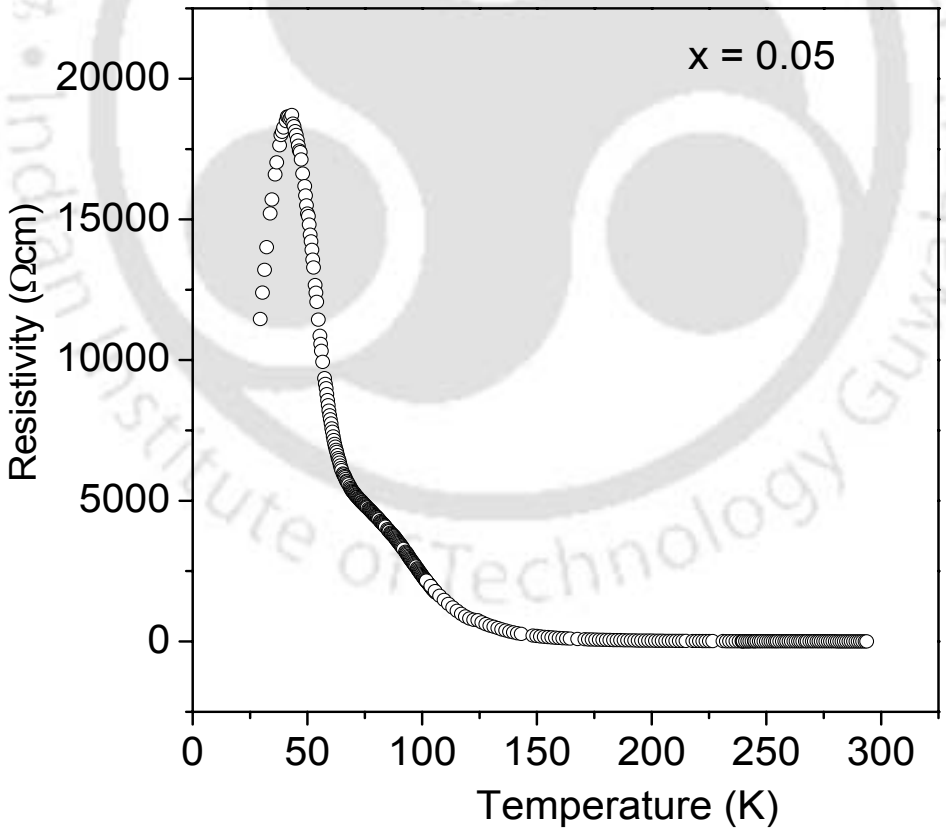

Fig. 4.36: Electrical resistivity as a function of temperature for $La_{0.95}Cu_{0.05}MnO_3$ (x = 0.05) sample.

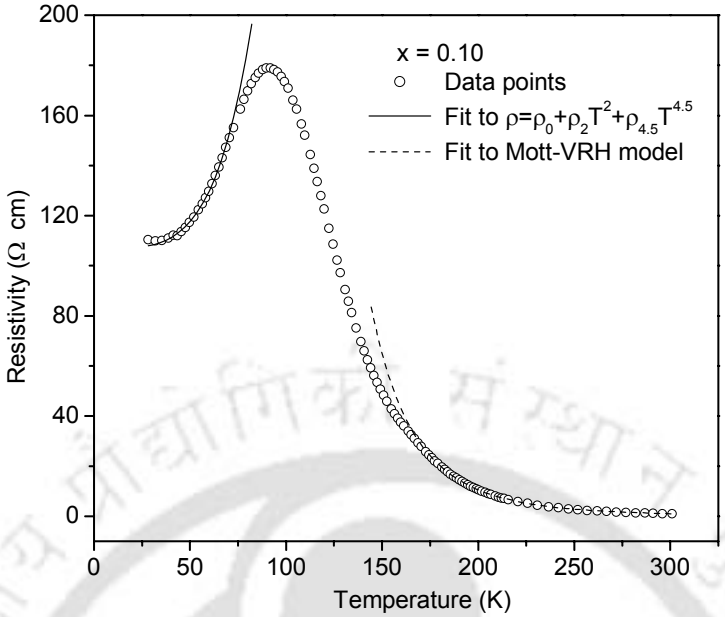

Fig. 4.37: Electrical resistivity as a function of temperature for $La_{0.9}Cu_{0.1}MnO_3$ (x = 0.10) sample. Solid line represents the fit to eqn. $\rho = \rho_0 + \rho_2 T^2 + \rho_{4.5} T^{4.5}$ and dashed lines represent the fit to Mott-VRH model.

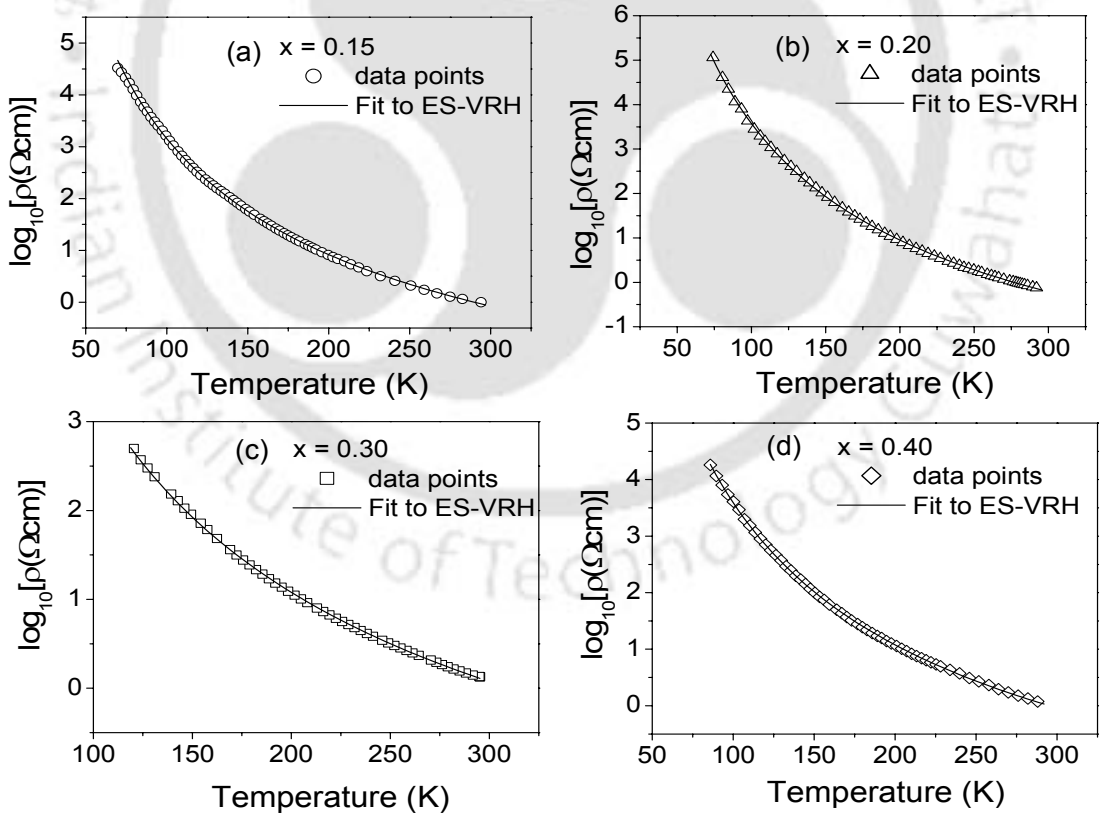

Fig. 4.38: Plots of $\log_{10}[\rho(\Omega cm)]$ versus T for (a) $La_{0.85}Cu_{0.15}MnO_3$ (x = 0.15), (b) $La_{0.8}Cu_{0.2}MnO_3$ (x = 0.20), (c) $La_{0.7}Cu_{0.3}MnO_3$ (x = 0.30) and (d)$La_{0.6}Cu_{0.4}MnO_3$ (x = 0.40). Solid lines represent the fit to ES-VRH model.

The resistivity data in the semiconducting region have been analyzed mostly using Mott variable range hopping (Mott-VRH), Efros-Shklovskii VRH (ES-VRH), and small polaron hopping (SPH) models (section 1.3.3).

Both Mott-VRH and ES-VRH models are found to fit the experimental data of x = 0.05 and 0.10 samples. However Mott-VRH model gives a better fit compared to the ES-VRH model with a low root mean square deviation (rmsd) value. The parameters such as, average hopping distance $R_{hop}(T)$ and average hopping energy $E_{hop}(T)$ at 300K and, density of states in the vicinity of Fermi level have been calculated from the fitted parameters and following section 3.2.4 (eqns. 3.8-3.10). These values are listed in Table 4.9. The typical plot of $\ln(\rho)$ vs. $T^{-1/4}$ is shown in Fig. 4.39 for x = 0.10 sample, we can observe the linear curve and it confirms the applicability of Mott-VRH model. The solid line represents the fit to Mott-VRH model.

The resistivity data for samples with $x \geq 0.15$ could be fitted to ES-VRH model. The typical $\ln(\rho)$ versus $(1/T)^{1/2}$ plot is shown in Fig. 4.40. The above plot exhibits linear behaviour in the temperature range 60-300K and the solid line represents the fit to ES-VRH model. It reveals that the resistivity data of higher doped materials ($x \geq 0.15$) could be explained based on ES-VRH model. Therefore the electrical transport properties for $x \geq 0.15$ could be understood mostly by variable range hopping with coulomb interaction. The dielectric constants are calculated using the eqn. (1.25), i.e. $T_{0s} = \beta_1 e^2 / (k_B a 4\pi\varepsilon_o\varepsilon_r)$ by taking '*a*' as 4.5 Å by following Viret *et al*. [140] and those values are listed in Table 4.9.

The resistivity as a function of temperature for x = 0.10 sample in the presence of 10kOe magnetic field is shown in Fig. 4.41 for the temperature range 30 to 184K. For a comparison the zero field resistivity is also reproduced. We can see the reduction in resistivity. The T_{MI} value shifts towards higher temperature in the presence of magnetic field i.e. 92K for absence of magnetic field to 95K in presence of magnetic field. The temperature variation of magneto-resistivity for the above sample is shown in Fig. 4.42. There are two peaks, one is in the vicinity of ferromagnetic transition mid point, T_c and the other one is in the vicinity of the metal-insulator transition temperature, T_{MI}. The maximum value of negative MR is found to be 20% in the vicinity of T_c. The low temperature peak is found to be quite broad and it could be mainly due to the intergranular weak link with weak FM transition.

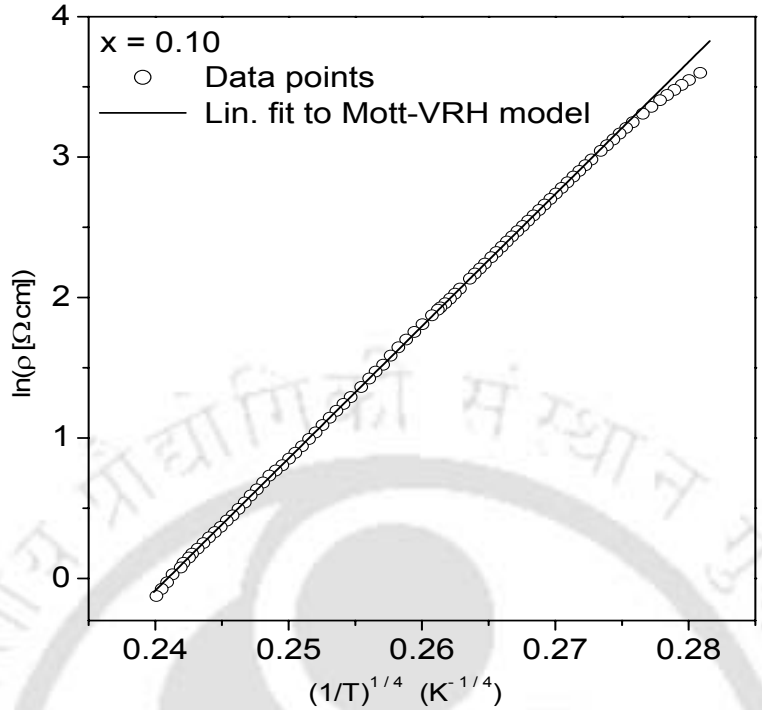

Fig. 4.39: ln(ρ) vs. $(1/T)^{1/4}$ plots for $La_{0.9}Cu_{0.1}MnO_3$ (x = 0.10). Solid line is the fit to Mott- VRH model.

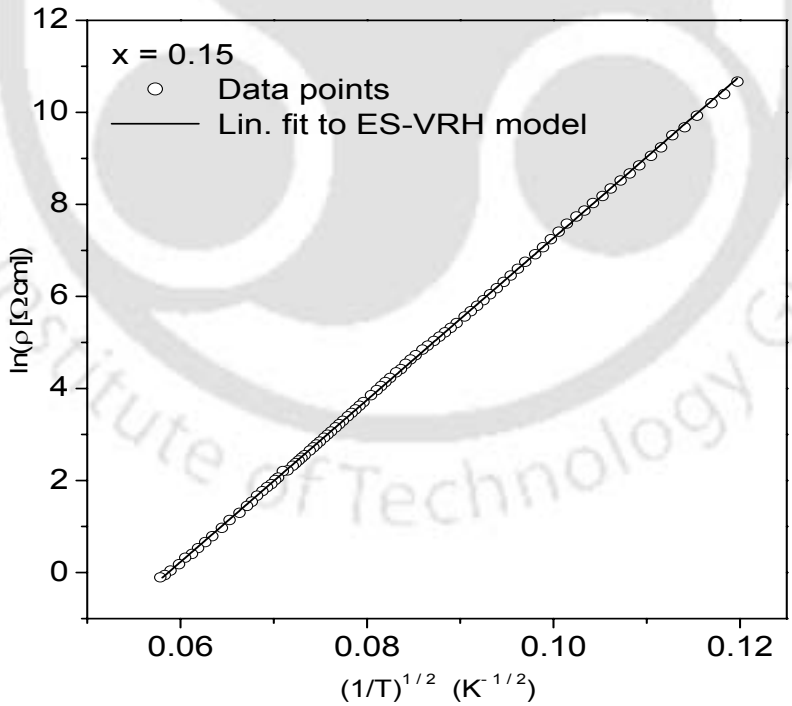

Fig. 4.40: ln(ρ) vs. $(1/T)^{1/2}$ plots for $La_{0.85}Cu_{0.15}MnO_3$ (x = 0.15). Solid line is the fit to ES- VRH model.

Table 4.9: Parameters obtained from the fit of Mott-VRH and ES-VRH models. ρ_{0m} and T_{0m} are Mott residual resistivity and characteristic temperature respectively. $N(E_F)$ is the density of states in the vicinity of Fermi level. $R_{hop}(300K)$ and $E_{hop}(300K)$ are mean hopping distance and hopping energy respectively at 300K. ρ_{0s} and T_{0s} are ES residual resistivity and characteristic temperature respectively. ε_r is the dielectric constant.

Sample → / Parameters ↓	x = 0.05	x = 0.10	x = 0.15	x = 0.20	x = 0.30	x = 0.40
T_{MI}(K)	43	92	---	---	---	---
ρ(290K)(Ωcm)	2.39	0.85	1.06	1.17	1.44	1.46
rmsd (Mott-VRH)(%)	0.57	0.36	2.89	0.89	1.58	0.49
$T_{0m}(10^8K)$	1.050 ±0.040	0.784 ± 0.005	---	---	---	---
ρ_{om} $(10^{-11}\Omega cm)$	5.5 ±0.1	14.3 ±0.1	---	---	---	---
R_h(300K) (Å)	41.01	38.16	---	---	---	---
E_{hm} (300K)(meV)	156.9	146.0	---	---	---	---
$N(E_F)$ $(10^{25}$ $eV^{-1}m^{-1})$	2.19	2.93	---	---	---	---
rmsd (ES – VRH)(%)	2.34	0.85	0.75	0.89	0.73	0.35
T_{0s} (10^4K)	---	---	3.14 ±0.01	4.26 ±0.01	3.33 ±0.01	3.34 ±0.01
ρ_{0s} $(10^{-5}\Omega cm)$	---	---	2.980 ±0.060	0.416 ±0.002	3.054 ±0.004	2.790 ±0.030
ε_r	---	---	3.3	2.4	3.11	3.11

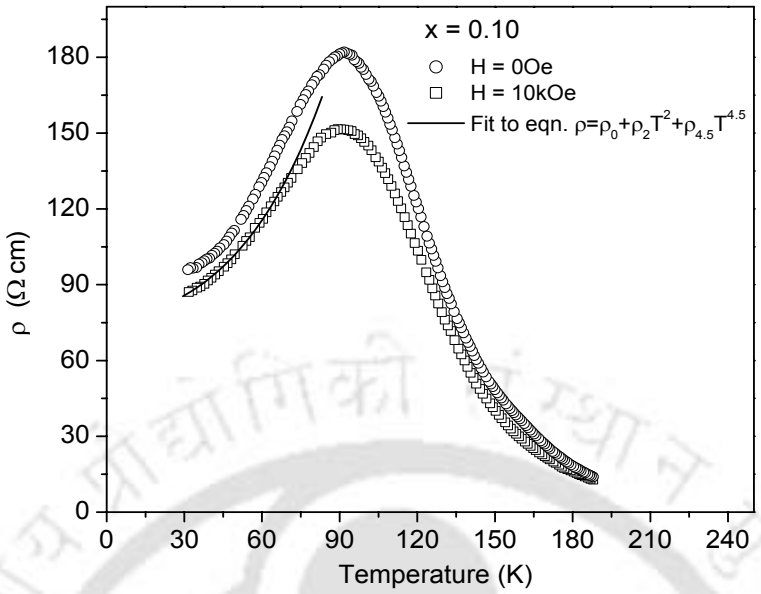

Fig. 4.41: Electrical resistivity as a function of temperature for x = 0.10 sample. The experimental data corresponding to 0 and 10kOe magnetic fields are shown as circles and squares respectively. Solid line represents the fit to eqn. $\rho = \rho_0 + \rho_2 T^2 + \rho_{4.5} T^{4.5}$.

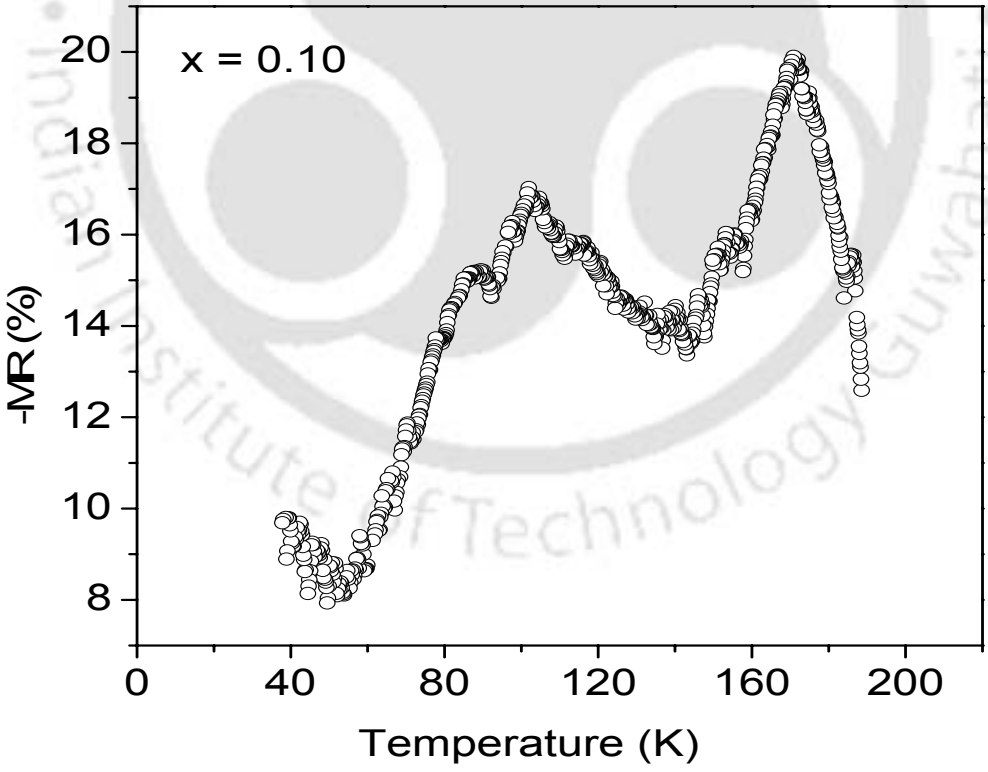

Fig. 4.42: Temperature variation of negative magneto-resistivity measured at 10kOe field for $La_{0.9}Cu_{0.1}MnO_3$ (x = 0.10).

4.3. Summary and Conclusions

The properties of $La_{1-x}M_xMnO_3$ compounds, where M = 'Ag' and 'Cu', have been described in this chapter. The maximum diffusibility of 'M' into the crystal site is found to be $x \approx 0.20$ for both the series. For $x > 0.20$, the minor Mn_3O_4 impurity is found to present in the compounds. Structural transition has been observed from orthorhombic to rhombohedral for 'Ag' substitution.

Both the series show ferromagnetic transition for $x \geq 0.05$. For the 'Ag' doping in place of 'La', the ferromagnetic transition temperature T_c is found to increase with the 'Ag' concentration up to the optimum doping close to 0.15 and then it is almost constant. It is explained on the basis of increase in Mn^{3+}-Mn^{4+} pairs to the optimum ratio of 70/30%. For 'Cu' doping, the T_c value is found to decrease with the 'Cu' concentration and it is explain on the basis of some of the 'Cu' entering the 'Mn' site and weakening the DE interaction. The saturation susceptibility for both the series increases up to $x = 0.15$ and then decreases with the 'M' concentration. It could be due to the segregation of minor Mn_3O_4 phase in the material which reduces the concentration of Mn^{3+}/Mn^{4+} pairs in the material.

Metal-insulator transitions have been observed for both the series. For M = Ag, all the materials ($0.05 \leq x \leq 0.35$) show M-I transitions. The M-I transition temperature, T_{MI} increases up to 0.15 and then it is almost constant with the 'Ag' concentration. The low temperature resistivity in the metallic region could be fitted to $\rho = \rho_0 + \rho_2 T^2 + \rho_{4.5} T^{4.5}$. So the mechanism of metallic resistivity is mainly due to the electron-electron and electron-magnon scattering. The materials with M = Cu, exhibit M-I transition for $0.05 \leq x \leq 0.10$. The resistivity data above T_{MI} could be explained using Mott-VRH model. The materials for $x \geq 0.15$ show semiconducting behaviour and the resistivity could be explained using ES-VRH model. So there is a cross over of conduction mechanism from Mott-VRH to ES-VRH depending upon the 'Cu' concentration in the material.

Chapter 5

MANGANESE SITE DOPED MATERIALS

MANGANESE SITE DOPED MATERIALS

$CaCuO_2$ and La_2CuO_4 are the parent compounds of high temperature superconductors (HTSC). $CaMnO_3$ and $LaMnO_3$ are the parent compounds of CMR materials. Both HTSC and CMR materials have similarity in their physical properties in a great extent. The above parent compounds are electrical insulators with antiferromagnetic (AFM) ordering. By increasing the hole carrier concentration, the cuprate parent compounds undergo transition from AFM insulator to diamagnetic HTSC and the manganite parent compounds undergo transition from AFM insulator to FM metallic state with CMR effect. The Cu-O planes play a vital role on HTSC and Mn-O in CMR materials. Both 'Cu' and 'Mn' ions are in the form of mixed valency in HTSC and CMR materials respectively. It would be interesting to study the effect of 'Mn' doping in place of 'Cu' for HTSC and vice versa for CMR materials. There are several reports on the study of 'Mn' doping in place of 'Cu' in HTSC [223-227]. It is found that, superconductivity is destroyed in the above doping. There are also a few reports on 'Cu' doping in 'Mn' site in CMR materials [158,221,222,228]. It has been found that 'Cu' doping enhances the antiferromagnetic interaction by reducing the ferromagnetic Curie temperature and increases the electrical resistivity by localizing the charge carriers. In this chapter, the result of 'Cu' doping in place of 'Mn' in CMR parent compounds, (Ca-Mn-O and La-Mn-O) have been studied. It would be interesting to study these two series as substitution of 'Cu' in place of 'Mn' is expected to introduce the mixed valence of 'Mn' ions and double exchange interaction. Simultaneously, one can study the magnetic interaction between 'Mn' and 'Cu' ions.

5.1. $LaMn_{1-x}Cu_xO_3$ (x = 0.05 to 0.40) Compounds

The preparation details, characterization and results of electrical resistivity and ac susceptibility measurements and analysis on $LaMn_{1-x}Cu_xO_3$ compounds are given in this section.

5.1.1. Preparation

The $LaMn_{1-x}Cu_xO_3$ compounds were prepared for x = 0.05, 0.10, 0.15, 0.20, 0.30 and 0.40 by solid state route. Stoichiometric ratio of La_2O_3, $(CH_3COO)_2Cu.H_2O$ and $C_4H_6MnO_4.4H_2O$ were weighed and mixed thoroughly under acetone. The mixture was presintered at 800^0C for 24hours with intermediate grindings at an interval of 12 hours. The sintering in pellet form was carried out at 900^0C, 1000^0C, 1050^0C, 1100^0C, 1150^0C and 1200^0C for 12 hours duration in each temperature. The pellets were crushed into fine homogeneous powder and repelletized after each annealing. The final sintering has been carried out at 1200^0C for over 50 hours. All the above heat treatments were carried out in air and finally the samples were furnace cooled.

5.1.2. Characterization

XRD patterns recorded on $LaMn_{1-x}Cu_xO_3$ compounds with x = 0.05, 0.10, 0.15, 0.20, 0.30 and 0.40 are shown in Fig. 5.1. It is observed that the samples are in single phase form for $x \leq 0.30$. The XRD pattern of x = 0.05 sample could be indexed to $R\bar{3}c$ space group, where as the XRD patterns of samples with $0.10 \leq x \leq 0.40$ could be indexed to *Pbnm* space group. For x = 0.40, one can see that a minor extra peak due to Mn_3O_4 impurity is present at $2\theta = 36.41^0$ [218].

Typical XRD patterns along with Rietveld refinement using Fullprof program are shown in Figs. 5.2 and 5.3 for x = 0.05 and 0.15 samples respectively. The inset shows the expanded view of prominent peak observed at around 32.5^0. One can see the splitting of that peak in $R\bar{3}c$ space group and absence of splitting in *Pbnm* space group.

The typical values of atomic position, isotropic displacement (temperature) parameters and occupancy are given in Tables 5.1 and 5.2 for the samples $LaMn_{0.95}Cu_{0.05}O_3$(x = 0.05) and $LaMn_{0.85}Cu_{0.15}O_3$(x = 0.15) respectively. The lattice parameters, occupancy values, reliability factors and unit cell volumes are tabulated in Table 5.3. No appreciable variation in lattice parameters and unit cell volume has been observed. It is not surprising because the ionic size of 'Cu' is comparable to that of 'Mn'. The particle size has been calculated using the Scherrer's formula using eqn. (2.11) and these values are listed in Table 5.3. The particle size of x = 0.05 and x = 0.30 samples are found to be relatively large compared to other samples. No appreciable change in particle

size is observed even for higher level of doping and this suggests that the crystal is quite stable for wide doping range due to comparable ionic size of 'Cu' & 'Mn'. The bond length and bond angles are calculated using the atomic positions and lattice parameters obtained from Rietveld analysis. These values are tabulated in Table 5.3 and they are comparable to those reported in literature [26].

The average valency of 'Mn' ions determined from chemical titration is tabulated in Table 5.4. We can see that 'Mn' valency increases with doping, thereby confirming the generation of Mn^{3+}/Mn^{4+} pairs.

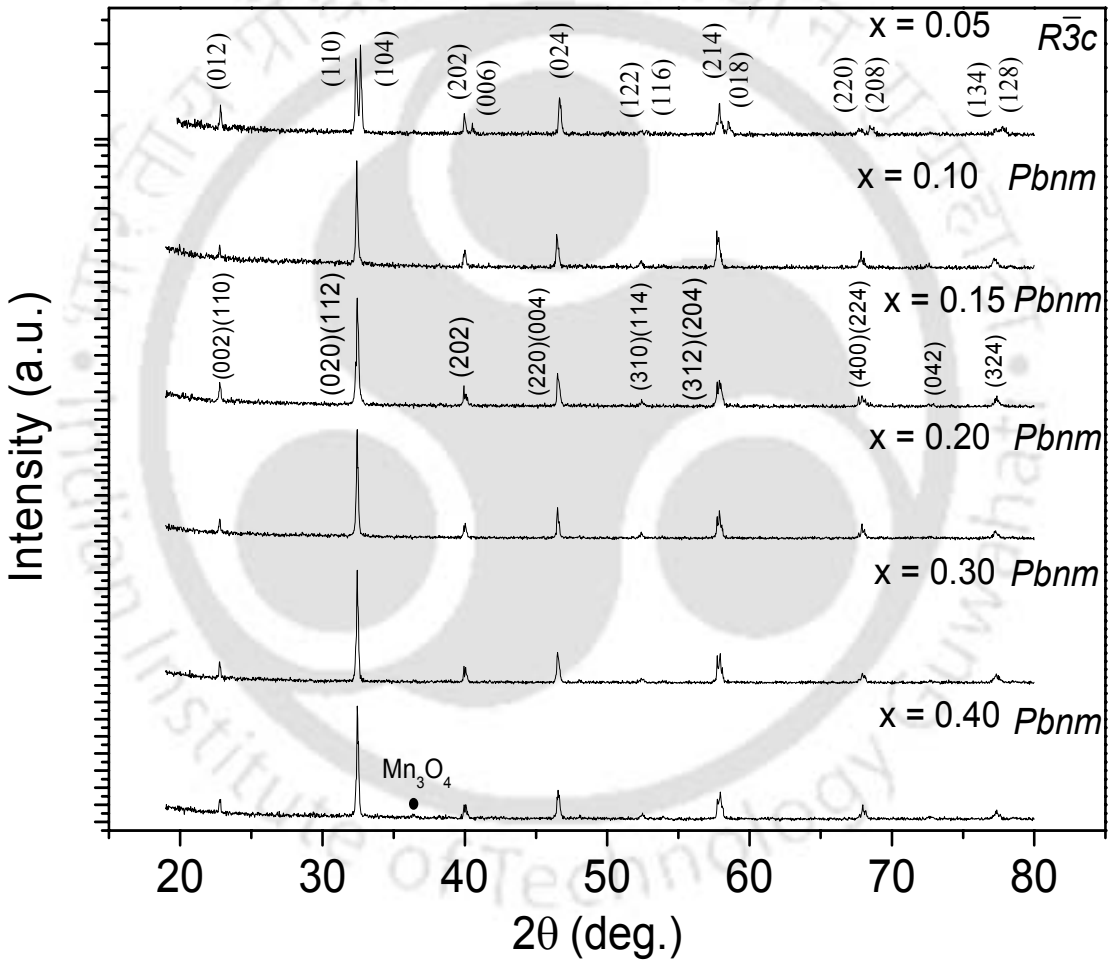

Fig. 5.1: XRD patterns of $LaMn_{1-x}Cu_xO_3$ for x = 0.05, 0.10, 0.15, 0.20, 0.30 and 0.40 samples.

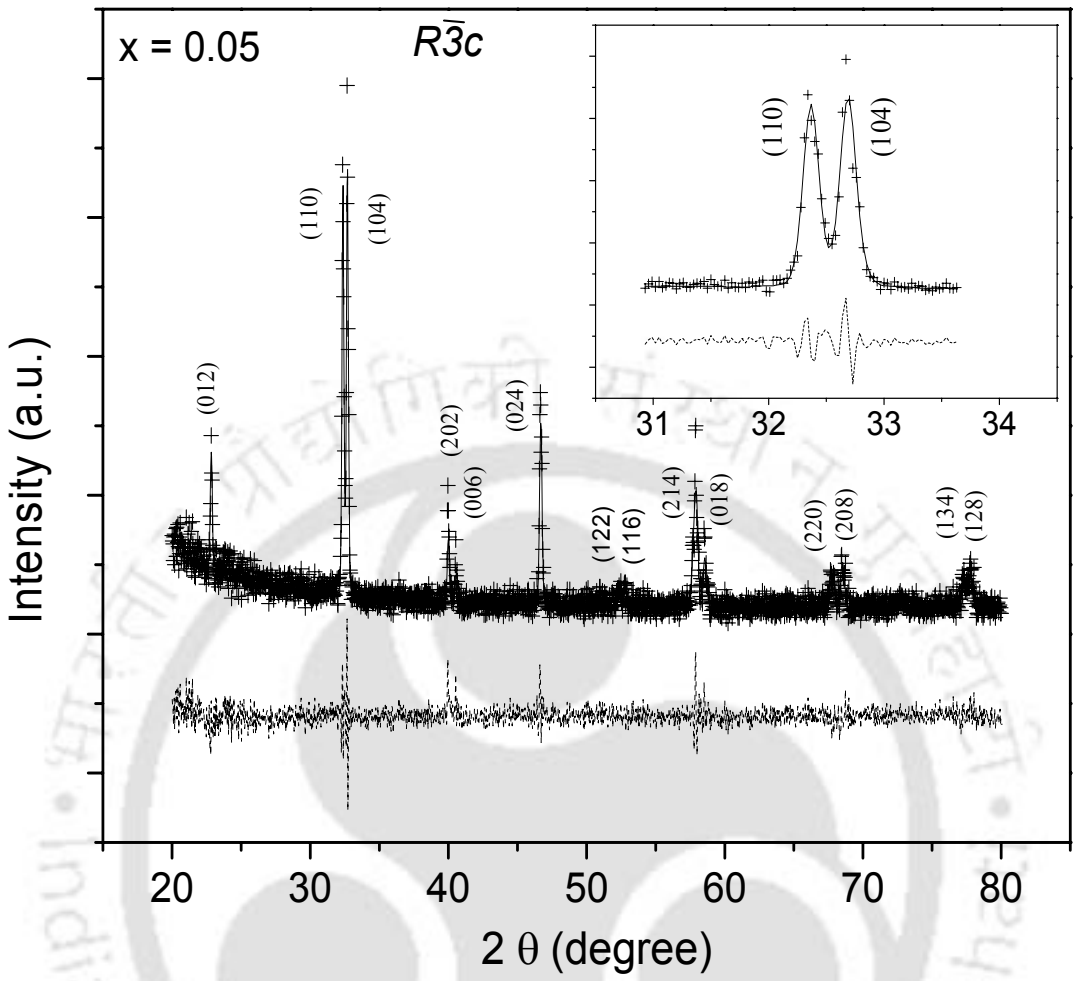

Fig. 5.2: XRD pattern along with Rietveld refinement for $LaMn_{0.95}Cu_{0.05}O_3$ (x = 0.05) sample. The experimental data, refined data and the difference between them are shown as crosses, solid line and dashed lines respectively. The inset shows expanded view of (110) & (104) peaks.

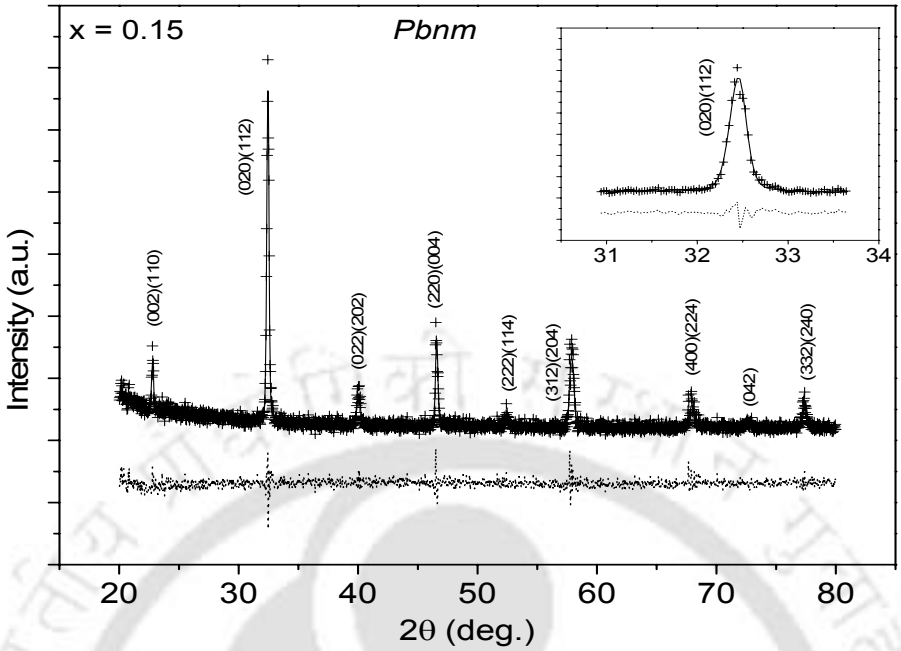

Fig. 5.3: XRD pattern along with Rietveld refinement for $LaMn_{0.85}Cu_{0.15}O_3$ (x = 0.15) sample. The experimental data, refined data and the difference between them are shown as crosses, solid line and dashed lines respectively. The inset shows expanded view of (020) & (112) peaks.

To study the morphology of the materials optical microscope photograph has been taken for all the materials. The magnification used was 40. Typical microscope photograph for the sample x = 0.20 is shown in Fig. 5.4. The morphology is found to be uniform through out the material.

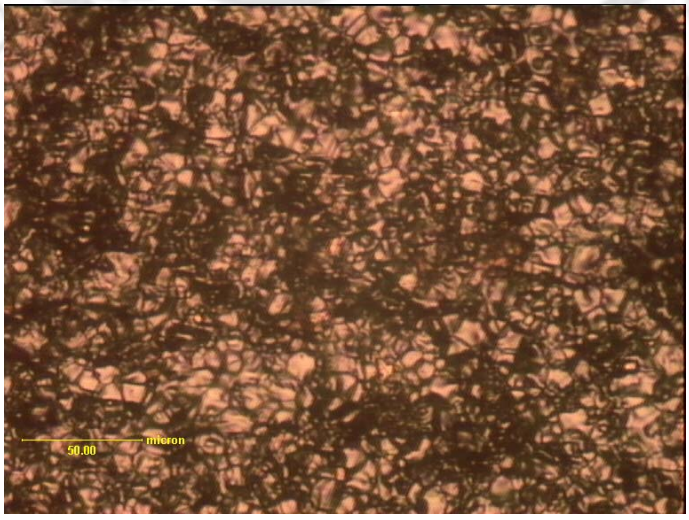

Fig. 5.4: Microscope photograph (magnification-40) of the sample $LaMn_{0.8}Cu_{0.2}O_3$.

Table 5.1: Parameters obtained from the Rietveld analysis of XRD pattern of the sample $LaMn_{0.95}Cu_{0.05}O_3$ (x = 0.05). The XRD pattern has been fitted to $R\bar{3}c$ space group. The lattice parameters are a = b = 5.537Å and c = 13.370Å. Biso is the isotropic displacement (temperature) parameter and Occ is the occupancy number.

Parameters → / Atoms ↓	Fractional coordinates			Biso Å^2	Occ
	x	y	z		
La	0.0000	0.0000	0.2500	0.20	0.978
Mn	0.0000	0.0000	0.0000	0.47	0.936
Cu	0.0000	0.0000	0.0000	0.47	0.049
O1	0.5505	0.0000	0.2500	0.16	1.000

Table 5.2: Parameters obtained from the Rietveld analysis of XRD pattern of the sample $LaMn_{0.85}Cu_{0.15}O_3$ (x = 0.15). The XRD pattern has been fitted to *Pbnm* space group. The lattice parameters are a = 5.543Å, b = 5.512Å and c = 7.815Å. Biso is the isotropic displacement (temperature) parameter and Occ is the occupancy number.

Parameters → / Atoms ↓	Fractional coordinates			Biso Å^2	Occ
	x	y	z		
La	0.9927	0.0103	0.2500	0.70	0.990
Mn	0.5000	0.0000	0.0000	0.26	0.848
Cu	0.5000	0.0000	0.0000	0.26	0.148
O1	0.02074	0.6047	0.2500	0.79	1.000
O2	0.7718	0.23031	-0.0522	0.16	1.000

Table 5.3: Parameters obtained from the XRD analysis of the samples $LaMn_{1-x}Cu_xO_3$ (x = 0.05, 0.10, 0.15, 0.20, 0.30 and 0.40). R_p, $R_{\omega p}$, R_{exp}, R_{Bragg}, R_F and χ^2 are the reliability factors. 'S_G' is the average particle size obtained from the line broadening of the XRD pattern. 'M' is Mn/Cu.

Samples ⟶ / Parameters ↓	x = 0.05	x = 0.10	x = 0.15	x = 0.20	x = 0.30	x = 0.40
Space Group	$R\bar{3}c$	*Pbnm*	*Pbnm*	*Pbnm*	*Pbnm*	*Pbnm*
a (Å)	5.537	5.543	5.543	5.542	5.545	5.540
b (Å)	5.537	5.519	5.512	5.518	5.517	5.519
c (Å)	13.370	7.835	7.815	7.812	7.810	7.820
G_{La}	0.978	0.999	0.990	0.999	0.993	0.944
G_{Mn}	0.936	0.905	0.848	0.798	0.699	0.599
G_{Cu}	0.049	0.098	0.148	0.189	0.303	0.322
R_p	16.1	19.4	19.5	20.2	22.5	22.3
$R_{\omega p}$	20.0	18.0	17.8	18.1	18.7	18.4
R_{exp}	17.28	14.28	14.43	13.54	18.0	12.74
R_{Bragg}	11.7	10.3	11.0	10.1	9.53	15.6
R_F	10.7	8.90	10.1	9.66	10.6	13.9
χ^2	1.58	1.63	1.73	1.71	2.28	1.15
Volume ($Å^3$)	355.0	239.7	238.7	238.9	238.9	239.1
M-M (Å)	3.897	3.911	3.909	3.911	3.912	3.910
M-O_1 (Å)	1.968	1.963	1.994	1.974	1.958	1.957
M-O_2 (Å)	---	2.048	2.041	2.076	2.015	2.013
$\angle M - O_1 - M$	163.6	169.9	157.5	164.0	174.6	174.3
$\angle M - O_2 - M$	---	145.2	146.9	140.8	152.3	152.4
S_G(nm)	44	38	37	37	41	38

5.1.3. AC Susceptibility Study

AC susceptibility as a function of temperature was measured for the above samples at an ac field amplitude of 5.3Oe with a frequency of 233Hz. The temperature variation of χ' and χ'' for x = 0.05 sample is shown in Fig. 5.5. We can see that the material exhibits sharp PM to FM transition with a small step like behaviour at low temperature. Below the FM transition the χ' value decreases slowly with decrease in temperature. This is the general behaviour of FM sample measured at low field, which is mainly due to the formation of FM domains and increase in magnetic anisotropy. A small additional step like behaviour is observed at around 90K, which could mostly due to weak AFM phase present in the material as a result of inhomogeneous distribution of Mn^{3+} and Mn^{4+} ions. The χ'' plot shows sharp increase in loss at the onset of FM transition and then it falls monotonously with decrease in temperature with a change of slope at around 90K. The FM transition mid-point is taken from the temperature corresponding to peak in $\left|\frac{d\chi'}{dT}\right|$ versus T plot and it is found to be 203K.

Similar χ' versus T plots for x = 0.10, 0.15 and 0.20 samples are shown in Fig. 5.6 as (a) squares, (b) circles and (c) triangles respectively. We can see that these materials also exhibit PM to FM transition. However the FM transition temperature decreases with increase in 'Cu' doping. Unlike x = 0.05 sample, χ' versus T of these samples exhibit sharp fall in susceptibility below the FM transition. Such sharp falls cannot be explained using conventional magnetic anisotropy or the loss of long range FM ordering. They are mainly due to the presence of competing AFM interaction at low temperature, i.e. below the T_c. The sharpness of the fall increases with increase in 'Cu' doping. The χ'' versus T plots of these samples are shown as solid lines in Fig. 5.6. They show very interesting features. Each sample shows two peaks just below FM saturation (completion of FM transition). They are in the vicinity of sharp falls observed in χ' versus T plots. For x = 0.20 sample, even though it appears that it is a single peak, the careful observation reveals that it is a overlap of two peaks. The low temperature peaks can be attributed to freezing temperature, T_f of reentrant spin glass (RSG) state. According to Jonason *et al.* [215], the sharp fall in χ' versus T plots below the FM transition and the corresponding peak in χ'' versus T plots is a signature of presence of RSG state. The competition between FM ordering and competing random AFM interaction results in freezing of spins in random

direction and it is called as RSG state. Similar behaviour also has been observed in $La_{1-x}Cu_xMnO_3$ compounds, which is explained in section 4.2.3.

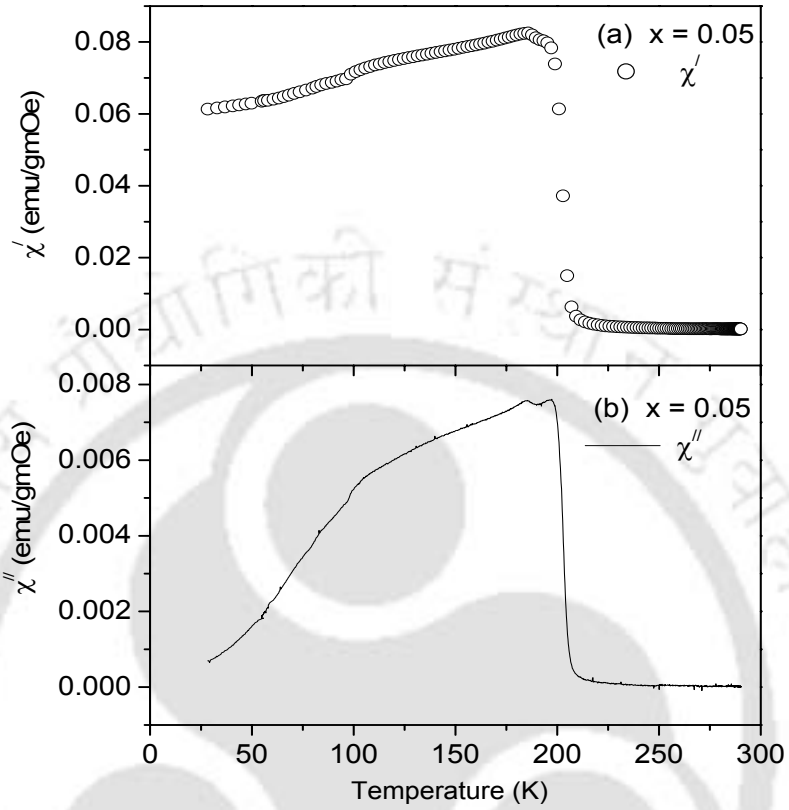

Fig. 5.5: χ' and χ'' versus temperature for $LaMn_{0.95}Cu_{0.05}O_3$ sample (x = 0.05).

The χ' versus T plots of x = 0.30 and x = 0.40 samples are shown in Fig. 5.7 (a) & (b) respectively. The x = 0.30 sample exhibits FM transition followed by strong AFM interaction. The magnitude of susceptibility is quite small compared to other samples, and it is mainly due to weak FM signal for higher doped materials. The x = 0.40 sample does not show any FM transition. Thus, when 'Cu' doping reaches 40%, the FM is completely destroyed. Small anomaly observed at around 100K is mainly due to some stray FM phase at isolated region.

Thus the parent compound with 'Cu' substitution $LaMn_{1-x}Cu_xO_3$ for x = 0.05 to 0.30 exhibit PM-FM transitions when they are cooled. It reveals that, 'Cu' doping oxidizes some of Mn^{3+} ions into Mn^{4+} ions, thereby generating the Mn^{3+}/Mn^{4+} mixture, which in turn contribute FM double exchange interaction. The ferromagnetic interaction is not observed for x = 0.40 sample and it could be due to presence of high concentration of 'Cu' in 'Mn' site, which causes the magnetic disordered.

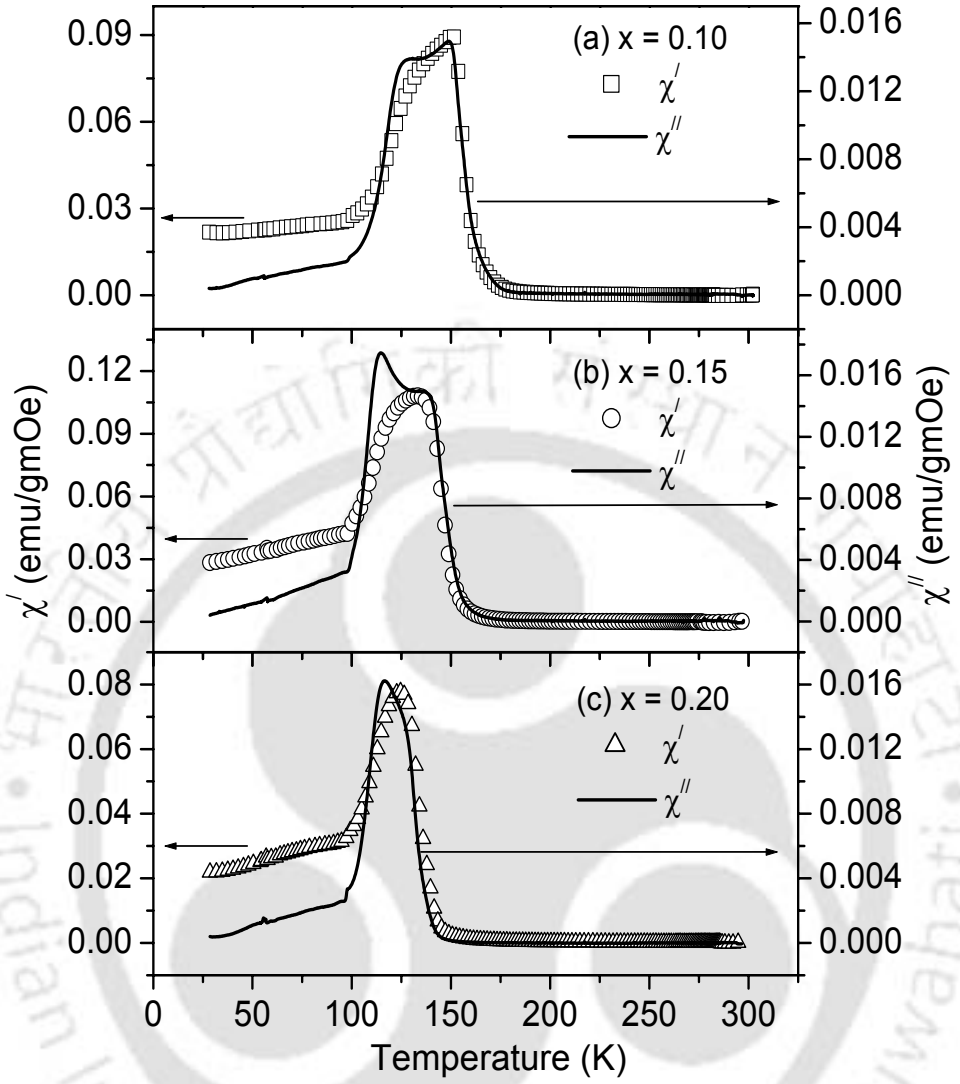

Fig. 5.6: Temperature variation of in phase ($\chi^{/}$) and out of phase ($\chi^{//}$) ac susceptibility of samples $La_{1-x}Cu_xMnO_3$ for (a) x = 0.10, (b) x = 0.15 and (c) x = 0.20.

The mid-point transition temperature T_c, ferromagnetic onset temperature T_{on}, FM saturation susceptibility, $\chi_s^{/}$ and freezing temperature of RSG state, T_f are given in Table 5.4. The T_{on} value decreases with the 'Cu' doping. It is found that the saturation susceptibility increases up to x = 0.15 and then decreases with the 'Cu' concentration. The decrease of T_{on} and increase of saturation susceptibility up to x = 0.15 reveals that, even though 'Cu' doping creates the Mn^{3+}/Mn^{4+} mixture, which contribute the enhanced concentration of DE interaction, simultaneously the antiferromagnetic interaction sets in due to the occupation of 'Cu' ions in 'Mn' site. The maximum $\chi_s^{/}$ value observed for x =

0.15 sample could be as a result of optimum concentration of Mn^{3+}/Mn^{4+} pairs. Unlike the case of 'Cu' doping [166] in place of 'Mn' for the CMR materials ($La_{1-x}A_xMnO_3$, A is an alkaline earth element), where ferromagnetism is completely destroyed for about 20% 'Cu', in the present set of samples, FM is observed even up to 30% doping. It is because, the 'Cu' doping in 'Mn' site of $LaMnO_3$ compound produces the mixture of Mn^{3+}/Mn^{4+} which tends to optimum value for certain level of doping. However, the doping of 'Cu' in optimum doped CMR material results in generation of Mn^{3+}/Mn^{4+} ions which go beyond the optimum value. So, in the present samples the 'Cu' doping plays a dual role.

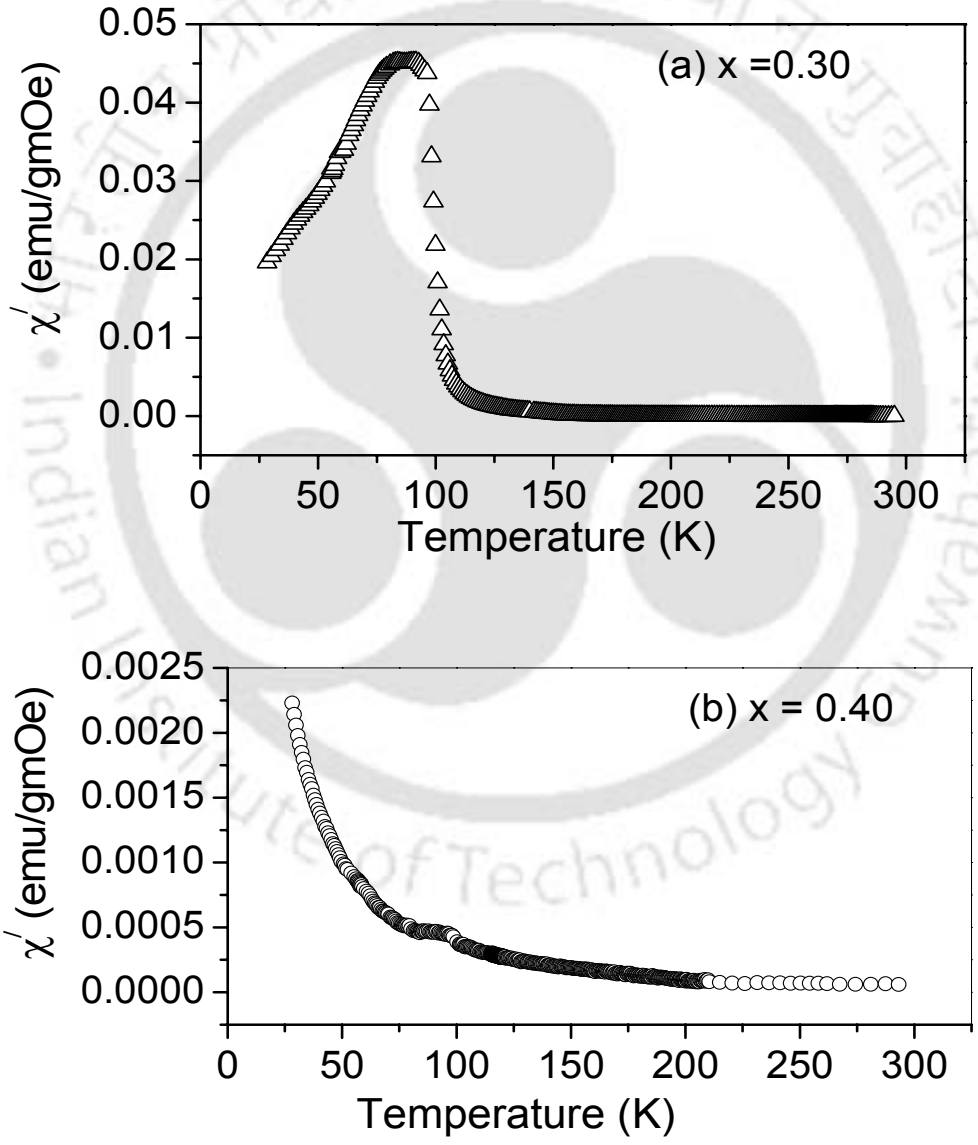

Fig. 5.7: Temperature variation of in phase ac susceptibility (χ') of samples $LaMn_{1-x}Cu_xO_3$ for (a) x = 0.30 and (b) x = 0.40.

Table 5.4: Parameters obtained from the chemical titration and ac susceptibility measurement. The uncertainty in T_{on}, T_f and T_c values are ±2K, ±1K & ±1K respectively.

Samples → / Parameters ↓	x = 0.05	x = 0.10	x = 0.15	x = 0.20	x = 0.30	x = 0.40
'Mn' Valency	3.12	3.14	3.18	3.29	3.34	3.48
T_{on}(K)	210	182	159	147	110	---
T_c(K)	203	154	144	133	98	---
T_f (K)	100	125	116	114	93	---
χ'_s(emu/gmOe)	0.083	0.090	0.108	0.078	0.045	---

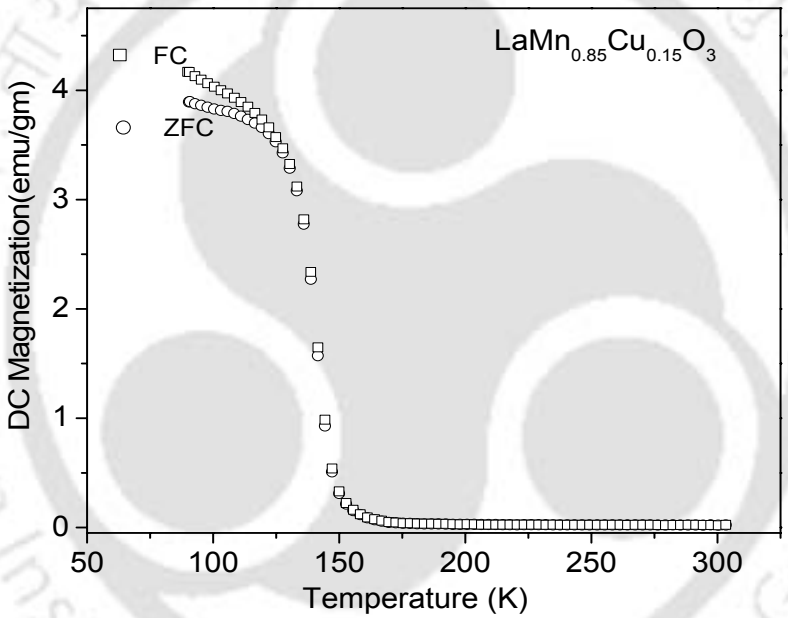

Fig. 5.8: Plot of temperature variation of DC magnetization of $LaMn_{0.85}Cu_{0.15}O_3$ (x = 0.15) sample in ZFC (circles) and FC (squares) conditions.

For the sake of comparison, the dc magnetization down to 80K has been measured for the sample x = 0.15 for both zero field cooled (ZFC) and field cooled (FC) conditions. The applied field was 50Oe. The temperature variation of ZFC (Circles) and FC (squares) curves are shown in the Fig. 5.8. The T_{on} and T_c values are found to be respectively 158 and 143K and they are close to the values found from ac susceptibility measurement (Table 5.4). There is difference between ZFC and FC curve for a narrow temperature region i.e. 80 to 100K. Since the T_c of the sample is quite low, the complete saturation magnetization is not achieved.

5.1.4. Electrical Resistivity Study

Temperature variation of electrical resistivity (ρ) was measured for all the above samples. Fig. 5.9 shows the plot of ρ versus T for x = 0.05, where one can see the metal-insulator transitions. Two M-I transitions, one corresponding to sharp peak at 201K and other one corresponding to broad peak at 153K. The observation of double peaks could be mainly due to the presence of large intergranular weak links, with T_c distribution. The sharp peak at higher temperature can be attributed to the intrinsic property of the material, since it is close to FM T_c. On the other hand, the broad peak at 153K can be attributed to intergranular weak links. Such double M-I transitions have been reported by other groups in manganites [26, 50, 152].

The samples for x ≥ 0.10 show semiconducting behaviour. The temperature variation of resistivity of x = 0.10 & x = 0.15 samples are shown in Fig. 5.10 and that of x = 0.20, 0.30 & 0.40 samples are shown in Fig. 5.11. For the ease of comparison, the resistivity data are shown in logarithmic scale. A minor anomaly is observed at around 160K for x = 0.10 sample as marked by an arrow and it is close to the FM transition temperature T_c. Even though the materials for 0.10 ≤ x ≤ 0.30 show ferromagnetic transition but no M-I transition is observed. It reveals that the ferromagnetism is below the threshold value and AFM is dominating as discussed in the previous section (section 5.1.3).

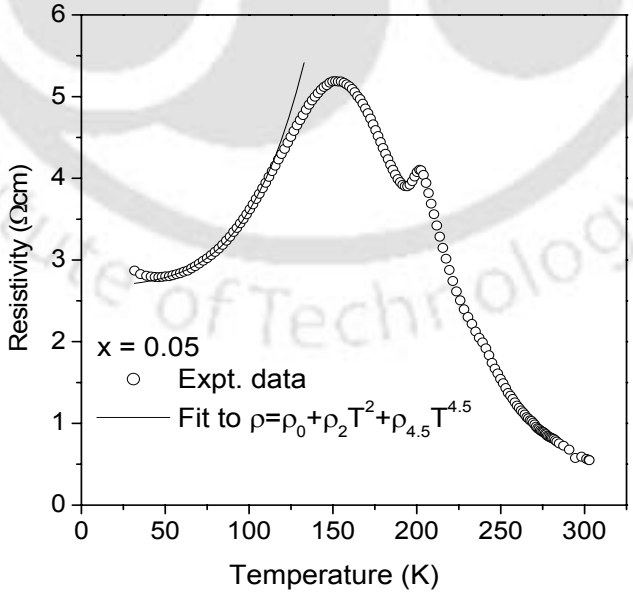

Fig. 5.9: Plot of resistivity versus T for $LaMn_{0.95}Cu_{0.05}O_3$ (x = 0.05). Solid line represents the fit to the equation $\rho = \rho_o + \rho_2 T^2 + \rho_{4.5} T^{4.5}$.

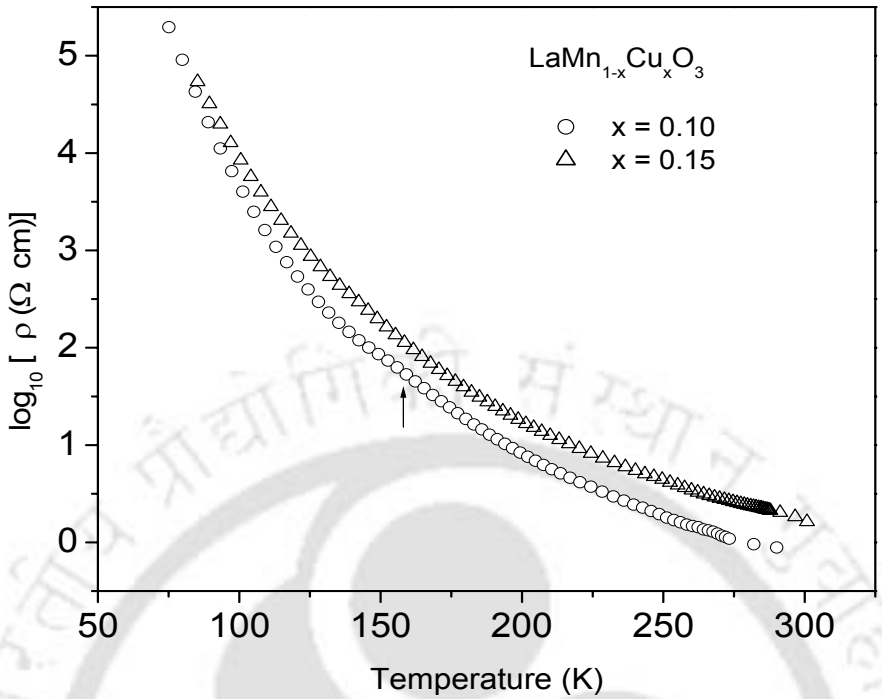

Fig. 5.10: Plots of $\log_{10}[\rho(\Omega cm)]$ versus T for $LaMn_{0.9}Cu_{0.1}O_3$ (x = 0.10, circles) and $LaMn_{0.85}Cu_{0.15}O_3$ (x = 0.15, triangles).

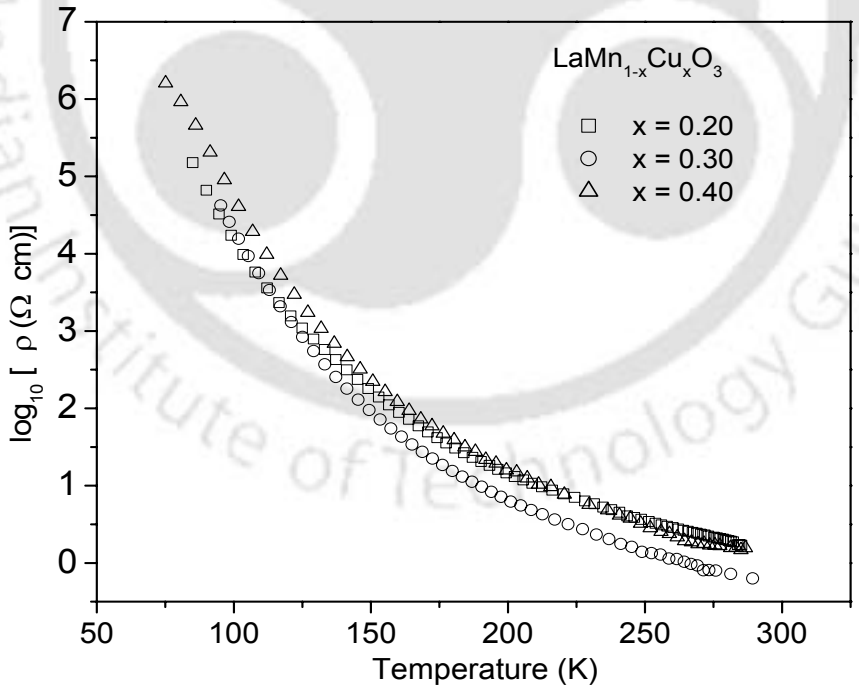

Fig. 5.11: Plots of $\log_{10}[\rho(\Omega cm)]$ versus T for $LaMn_{0.8}Cu_{0.2}O_3$ (x = 0.20), $LaMn_{0.7}Cu_{0.3}O_3$ (x = 0.30) and $LaMn_{0.6}Cu_{0.4}O_3$ (x = 0.40) samples. They are represented by squares, circles and triangles respectively.

The resistivity data, in the metallic region for x = 0.05 is analyzed using the empirical relation as discussed in section 1.3.2 and the eqn. 1.16 is reproduced below, i.e.

$$\rho = \rho_o + \rho_2 T^2 + \rho_{4.5} T^{4.5} \qquad \text{----------} \qquad (5.1)$$

The fitted data are shown as solid line in Fig. 5.9. The fitted parameters are found to be ρ_0 = 2.679±0.003Ωcm, ρ_2 = (3.0±0.1)×10^{-5} ΩcmK^{-2}, and $\rho_{4.5}$ = (6.05±0.06)×10^{-10}ΩcmK$^{-4.5}$). These values are comparable to those reported for $La_{0.7}Ca_{0.3}MnO_3$ [154].

The resistivity data for x ≥ 0.10 have been analyzed mostly using Mott variable range hopping (Mott-VRH), Efros-Shklovskii VRH (ES-VRH), and small polaron hopping (SPH) models as discussed in section 1.3.3.

The expression for small polaron hopping model is given in the eqn. (1.19) and for easy reference it is reproduced here,

$$\rho = \rho_{sp} T^n \exp\left(\frac{E_{sp}}{\kappa_B T}\right) \qquad \text{----------} \qquad (5.2)$$

The resistivity data of x = 0.05 sample in the semiconducting region could be fitted to ES-VRH model with relatively low root mean square deviation value (0.5%). The ln(ρ) versus $(1/T)^{1/2}$ plot in Fig. 5.12 shows linear behaviour and the fitted data are shown as solid line.

The typical plot of ln(ρ/T) versus (1/T) for the sample x = 0.15 is shown in entire temperature range in Fig. 5.13. We can see a change of slope at around 204K. However, in both high temperature & low temperature region, linear curves are obtained. This confirms the applicability of adiabatic small polaron hoping model, i.e. n =1 in eqn. (5.2). The downward deviation at low temperature region supports the idea of delocalization of charge carriers due to FM interaction. However, the FM interaction is not dominant enough to impose M-I transition. The resistivity data have been fitted in two different regions, one is in low temperature ferromagnetic region (LTR) and the other one is in high temperature region (HTR). It is found that the adiabatic small polaron model fits well in both low and high temperature regions. The fitted data are shown as solid and dashed lines for HTR & LTR respectively. For the sample x = 0.30 and 0.40, the resistivity data could be fitted to ASPH model only in single temperature region, i.e. above T_c because, T_c values are quite low and only limited data are available below T_c.

Table 5.5: Parameters obtained from the resistivity fitting. ρ_{sp} is the residual resistivity and E_{sp} is the polaron hopping energy. LTR and HTR represent the fitting in the low temperature and high temperature regions respectively.

Sample → / Parameters ↓	x = 0.10		x = 0.15		x = 0.20		x = 0.30	x = 0.40
Temperature Range	LTR 90 to 132K	HTR 158 to 290K	LTR 90 to 138K	HTR 150 to 290K	LTR 90 to 130K	HTR 139 to 290K	100 to 290K	100 to 290K
Model	ASPH	ASPH	ASPH	ASPH	ASPH	ASPH	ASPH	ASPH
rmsd(%)	0.91	0.53	0.57	0.40	0.24	1.28	1.61	0.99
ρ_{sp} ($10^{-6}\Omega$cm)	6.8 ± 0.12	8.8 ±0.13	29.9 ±0.13	26.7 ±0.13	9.8 ±0.16	19.9 ±0.15	5.1 ±0.14	10.0 ±0.11
E_{sp} (meV)	115.2 ±0.12	145.1 ±0.18	108.5 ±0.12	139.3 ±0.13	123.1 ±0.15	141.5 ±0.11	151.0 ±0.13	154.0 ±0.15

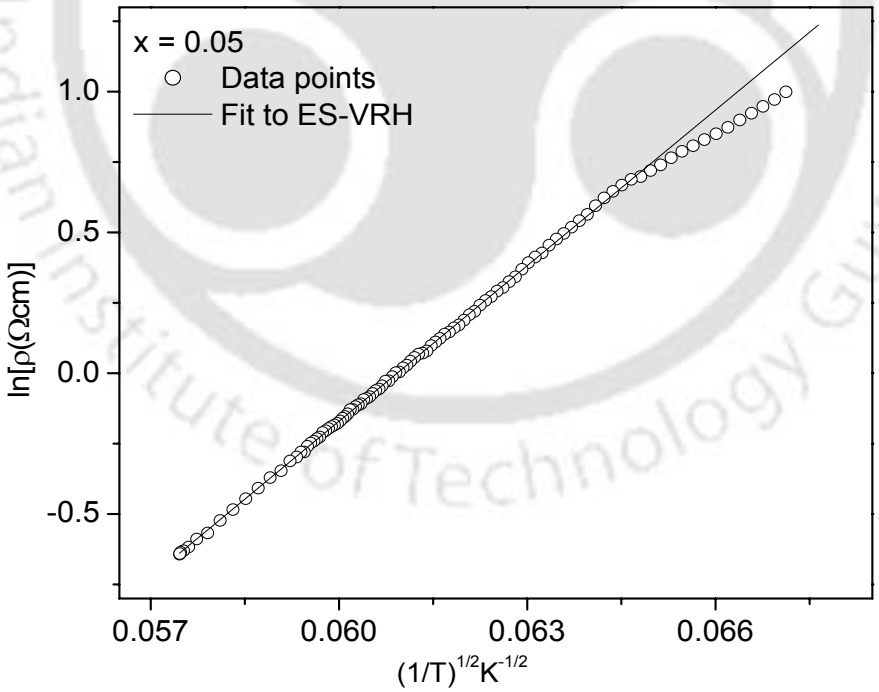

Fig. 5.12: Plot of ln[ρ(Ωcm)] versus (1/T) for $LaMn_{0.95}Cu_{0.05}O_3$ (x = 0.05). The solid line represents the fit to ES-VRH model.

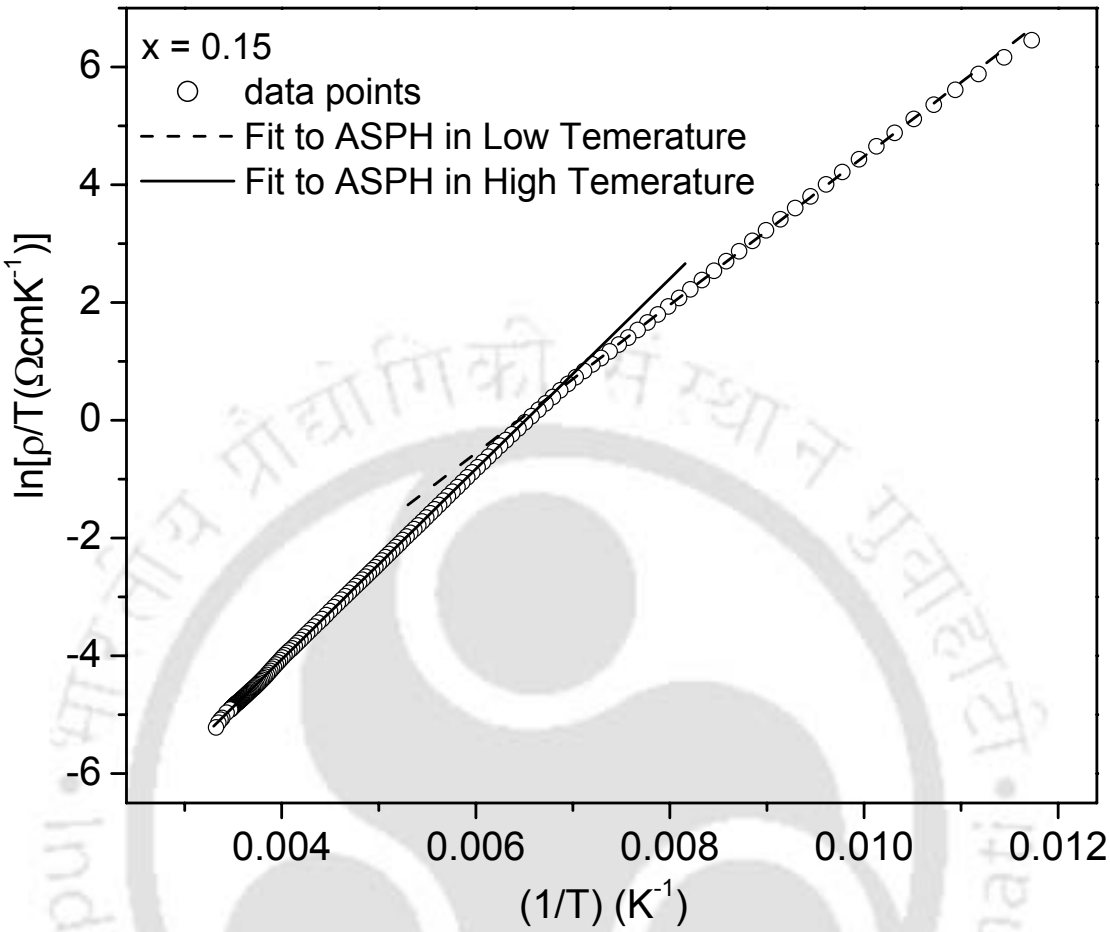

Fig. 5.13: Plot of $\ln[\rho/T(\Omega cmK^{-1})]$ versus (1/T) for $LaMn_{0.85}Cu_{0.15}O_3$ (x = 0.15). Fit to ASPH model is shown as solid line for high temperature region and dashed lines in the low temperature region.

5.2. $CaMn_{1-x}Cu_xO_3$ (x = 0 to 0.40) Compounds

5.2.1. Preparation

$CaMn_{1-x}Cu_xO_3$ compounds for x = 0, 0.10, 0.20, 0.30 and 0.40 have been prepared by solid state route. Stoichiometric ratio of $CaCO_3$, $MnCl_2.4H_2O$ and $(CH_3COO)_2Cu.H_2O$ were weighed and ground under acetone. The mixture of the above compounds were presintered in the temperature range 850 to 950ºC for over 50 hours with several intermediate grindings. The presintered powder was pressed into cylindrical pellet form and was annealed in the temperature range 1000 to 1100ºC for 50 hours with intermediate grindings and repelletising. All the above heat treatments were carried out in air. Finally the samples were furnace cooled.

5.2.2. Characterization

The XRD patterns recorded for $CaMn_{1-x}Cu_xO_3$ compounds with x = 0, 0.10, 0.20, 0.30 and 0.40 are shown in Fig. 5.14. The samples are essentially in single phase form with orthorhombic symmetry up to x = 0.20. The XRD patterns were analyzed using Fullprof program by employing Rietveld refinement technique up to x = 0.20. The patterns could be refined by using *Pbnm* space group in orthorhombic symmetry. Typical XRD patterns along with Rietveld refinement are shown in Fig. 5.15 for 0.20. The experimental data are shown as crosses (+) and the calculated intensities (solid line) closely follow the experimental data. The dotted lines represent the difference between experimental and calculated intensities. The values of reliability factors R_p, $R_{\omega p}$, R_{exp}, R_{Brag}, R_F and χ^2 are tabulated in Table 5.6. The occupancy values obtained from Rietveld analysis are listed in Table 5.6. These values are close to the expected atomic ratio.

The lattice parameters are tabulated in table 5.6 and these values are comparable to those reported by Zeng *et al.*[194] for $CaMnO_3$. The lattice parameters marginally increase with doping and this could be mainly due to larger ionic size of Cu^{2+} or Cu^{3+} compared to Mn^{4+}. The values of average Mn-O bond length and $\angle Mn-O-Mn$ bond angles are calculated using the lattice parameters and fractional coordinates obtained from the Rietveld analysis of the XRD patterns. These values are tabulated in Table 5.6 and are comparable to those reported by Jorge *et al.* [229] for $CaMnO_3$. The Mn-O bond length values increase with doping and it is in correlation with larger ionic size of 'Cu'. The particle size has been calculated from the line broadening of XRD and these values are

also listed in the Table 5.6. The Mn-O length is found to be around 1.900Å and these values are small compared to $LaMnO_3$ type of materials (≈ 1.960Å). This is a result of dominant Mn^{4+} concentration in this series.

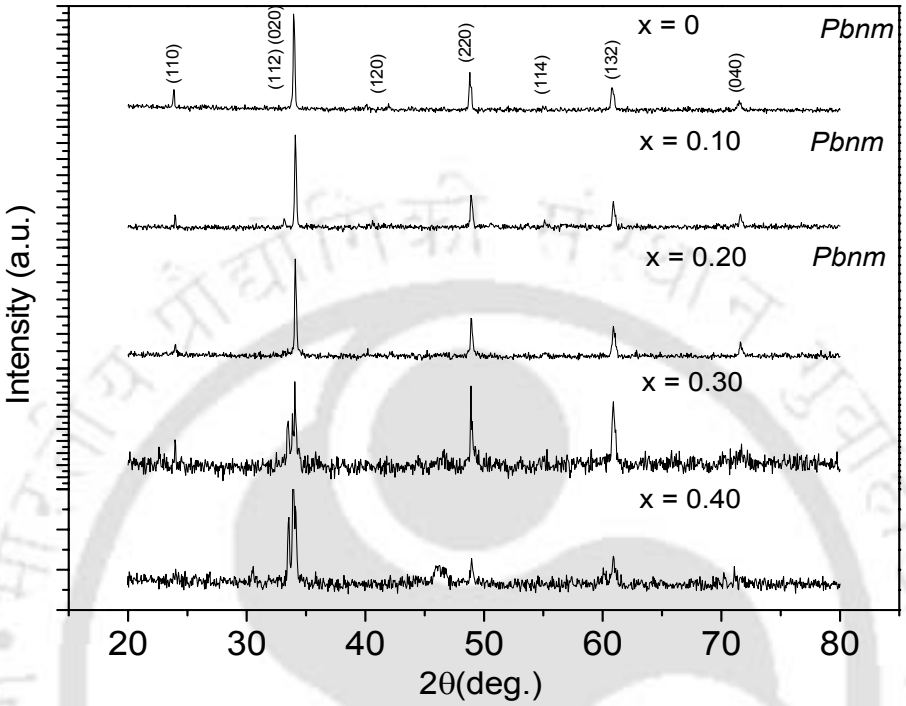

Fig. 5.14: XRD patterns of $CaMn_{1-x}Cu_xO_3$ for x = 0, 0.10, 0.20, 0.30 and 0.40.

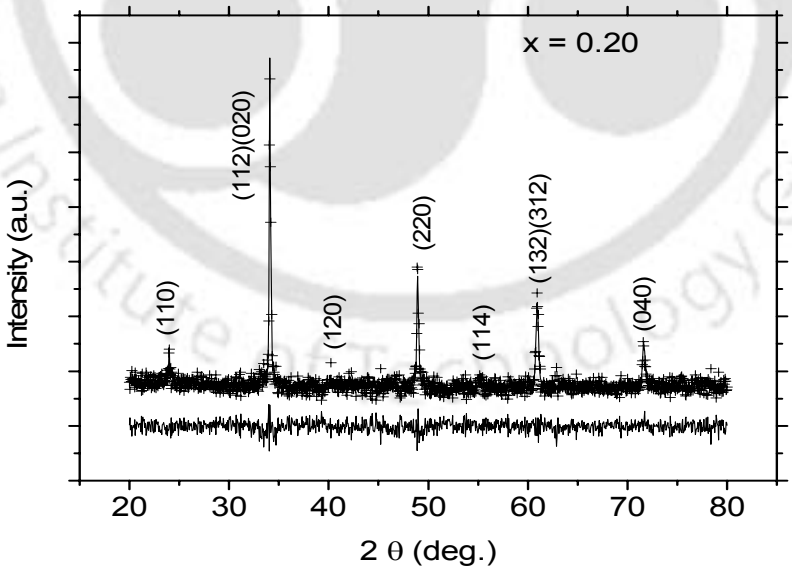

Fig. 5.15: XRD pattern for $CaMn_{0.8}Cu_{0.2}O_3$ (x = 0.20) sample. The '+' signs represent experimental data points and solid line represents Rietveld refined data. The dotted lines show the difference between experimental and refined data.

Table 5.6: Parameters obtained from the XRD analysis of the samples $CaMn_{1-x}Cu_xO_3$ (x = 0, 0.10 and 0.20). R_p, $R_{\omega p}$, R_{exp}, R_{Bragg}, R_F and χ^2 are the reliability factors. 'S_G' is the average particle size obtained from the line broadening of the XRD pattern. 'M' is Mn/Cu.

Samples → / Parameters ↓	x = 0.10	x = 0.15	x = 0.20
Space Group	*Pbnm*	*Pbnm*	*Pbnm*
a (Å)	5.276	5.278	5.278
b (Å)	5.259	5.261	5.260
c (Å)	7.459	7.464	7.462
G_{Ca}	0.906	0.993	0.990
G_{Mn}	0.922	0.859	0.765
G_{Cu}	---	0.092	0.197
R_p	9.76	8.99	9.38
$R_{\omega p}$	12.4	11.4	11.9
R_{exp}	11.2	10.7	11.06
R_{Bragg}	13.5	12.6	12.6
R_F	15.1	16.7	16.6
χ^2	1.63	1.13	1.16
Volume (Å^3)	206.9	207.3	207.2
M-M (Å)	3.724	3.726	3.726
M-O_1 (Å)	1.874	1.868	1.884
M-O_2 (Å)	1.901	1.914	1.908
$\angle M - O_1 - M$	167.4	172.2	162.9
$\angle M - O_2 - M$	156.9	153.7	155.2
S_G(nm)	42	37	36

The average valency of 'Mn' ion in the above compounds determined from the chemical titration is listed in table 5.7. The valency is found to be close to 4.0 for x = 0 and it increases with 'Cu' doping as expected.

To study the morphology of the materials optical microscope photograph has been taken for all the materials. The magnification used was 40. Typical microscope

photograph for the sample x = 0.10 is shown in Fig. 5.16. The morphology is found to be uniform throughout the material.

The typical SEM micrograph for x = 0.20 is shown in Fig. 5.17. The average grain size is found to be 4.2μm for x = 0.20 sample. The value is much higher than that calculated from the line broadening of XRD patterns. Such discrepancy has been found on particle size calculation from XRD patterns [213]. It could be due to the assumption of circular shape of the particle.

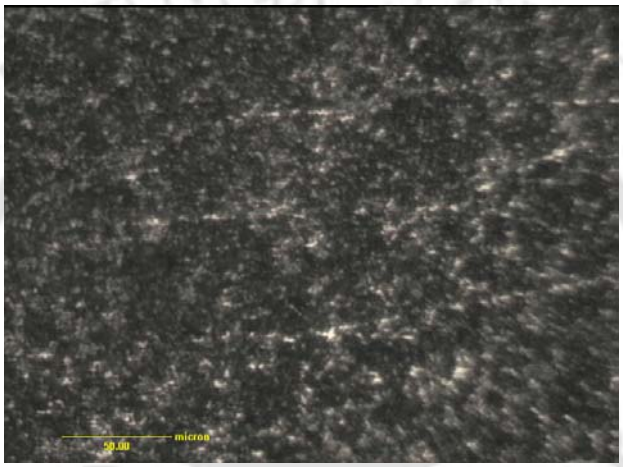

Fig. 5.16: Optical micrograph (magnification-40) of the sample $CaMn_{0.80}Cu_{0.20}O_3$ (x = 0.20).

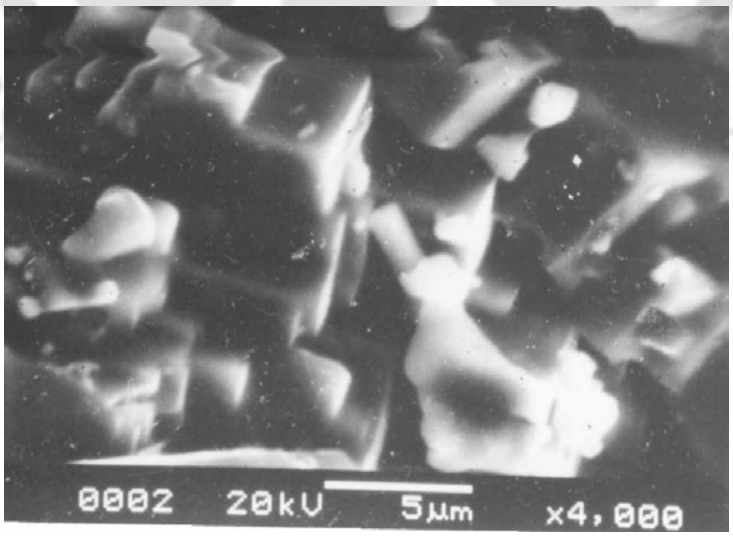

Fig. 5.17: SEM photograph of $CaMn_{0.8}Cu_{0.2}O_3$ (x = 0.20) with 4,000 magnification.

5.2.3. AC Susceptibility Study

The temperature variations of ac susceptibility are measured for the sample x = 0, 0.10 and 0.20. Typical plots of temperature variations of ac susceptibility (χ') for x = 0 & 0.20 are shown in Fig. 5.18. Antiferromagnetic transition has been observed and the values of Neel temperature, T_N and $\chi'(T_N)$ for different samples are tabulated in Table-5.7. These values are comparable to those reported in literature for $CaMnO_3$ based compounds [71]. For x = 0, the parent compound, a weak ferromagnetic signal of magnitude $\chi' \cong 3x10^{-4}$emu/gmOe is observed below the antiferromagnetic transition temperature and this could be mainly due to some defect concentrations and such weak ferromagnetic signal at low temperature has been observed by other groups in this system [64, 71,230]. The $\chi'(T_N)$ values are found to increase with 'Cu' doping. The weak ferromagnetic signal observed at low temperature for x = 0 sample disappears in the presence of 'Cu' doping. Thus the 'Cu' atoms take part in antiferromagnetic (AFM) interaction with 'Mn' atoms and AFM interaction increases with 'Cu' doping. The width of the magnetic transition mostly increases with 'Cu' doping and this may be basically a smearing of magnetic transition as a result of occupation of 'Cu' atoms at random 'Mn' sites.

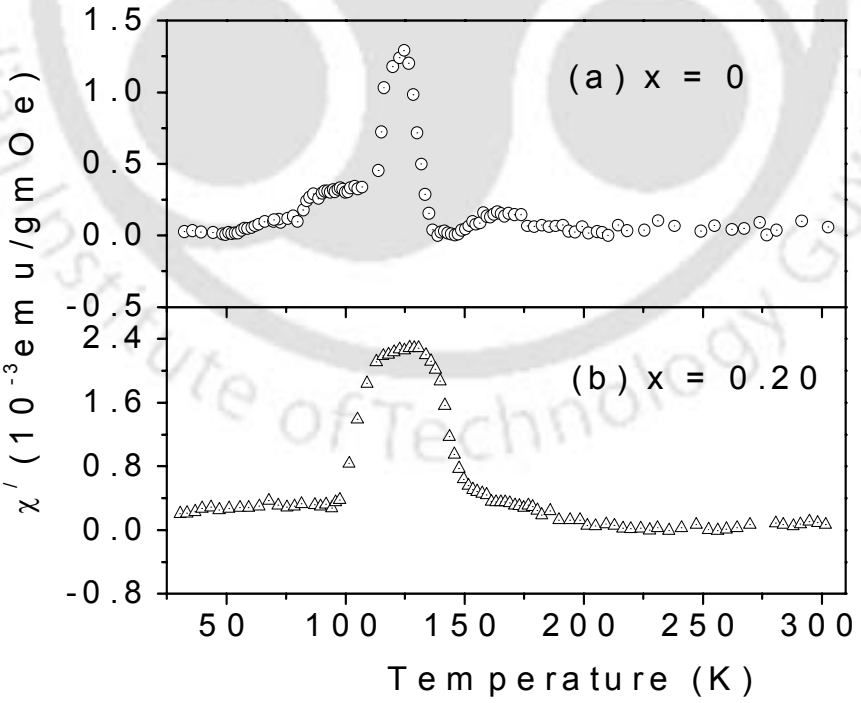

Fig. 5.18: Temperature variations of ac susceptibility of $CaMn_{1-x}Cu_xO_3$ for (a) x = 0 and (b) x = 0.20 samples.

Table 5.7: Parameters obtained from ac susceptibility measurement and chemical titration for the sample $CaMn_{1-x}Cu_xO_3$.

Samples → / Parameters ↓	x = 0	x = 0.10	x = 0.20
'Mn' valency	4.07	4.10	4.19
T_N(K)	124.2	124.6	125.0
$\chi'(T_N)$ (10^{-3} emu/gmOe)	1.27	1.27	2.30

5.2.4. Electrical Resistivity Study

The plots of temperature variations of electrical resistivity for x = 0.10 and 0.20 are shown in Fig. 5.19. For the sake of clarity, the resistivity axis is shown in logarithmic scale. All samples exhibit semiconducting behaviour. To understand the mechanism of electrical conduction, the resistivity data were analyzed in terms of small polaron hopping and variable range hopping models. It is not observed any linear behaviour of ln(ρ/T) versus (1/T) plots in the above samples. Thus the electrical conduction in the present samples is not controlled by small polaron hopping mechanism.

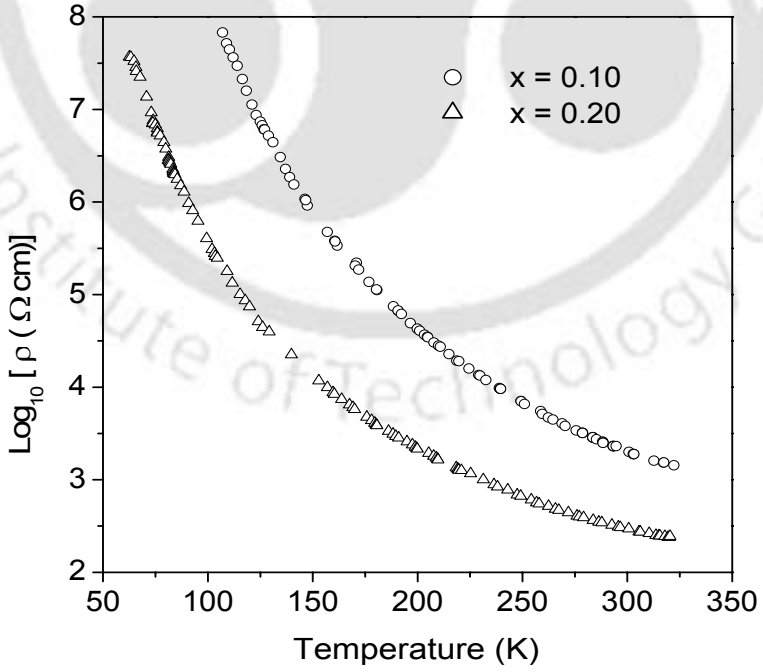

Fig. 5.19: Temperature variation of electrical resistivity of $CaMn_{1-x}Cu_xO_3$ for x = 0.10 & 0.20 samples. For clarity the resistivity axis is shown in logarithmic scale.

Typical plots of ln(ρ) versus $T^{-1/4}$ are shown in Figs. 5.20 and 5.21 for x = 0 and 0.20 samples respectively. The experimental data are found to follow linear curve and they could be fitted to Mott-VRH model (eqn. 1.20). The fitted data are shown as solid lines. The fitted data closely follow the experimental data. The curve deviates from linearity at higher temperature. The parameters T_{0m} and ρ_{0m} obtained from the fit are given in Table 5.8 for different samples. The density of states in the vicinity of Fermi level, $N(E_F) = 18/(k_B T_{0m} a^3)$, hopping distance $R_{hop}(T) = (3/8)a(T_{0m}/T)^{1/4}$ and hopping energy, $E_{hop}(T) = (1/4)k_B T^{3/4} T_{0m}^{1/4}$ were determined from the fitted values of T_{0m} and by taking T = 300K. Here '*a*' is the localization length and it is taken as 4.5 Å by following Viret *et al.* [140]. The estimated values of $N(E_F)$, R_{hop}(300 K) and E_{hop}(300 K) are given in Table 5.8. The $N(E_F)$ values are found to be in the same order of magnitude as reported by Banerjee *et al.* [231] in $La_{0.5}Pb_{0.5}Mn_{1-x}Cr_xO_3$ sample. From Table 5.8, it can be seen that $N(E_F)$ values are marginally smaller in 'Cu' doped materials compared to undoped, x = 0 sample and this suggests that 'Cu' doping enhances the charge carrier localization as observed by other groups in La-Mn-O based materials [158,166]. However, no systematic variation of above parameters with different 'Cu' concentrations is observed. The root mean square deviation (*rmsd*) values for different fittings are also given in Table 5.8.

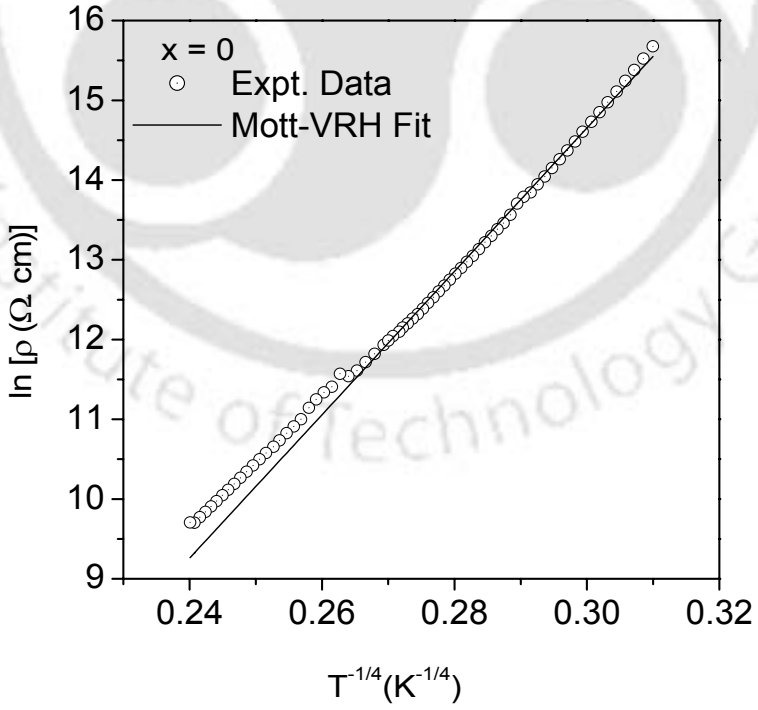

Fig. 5.20: Plot of ln(ρ) as a function of $T^{(-1/4)}$ for $CaMnO_3$ (x = 0) sample. Solid line is the fit to Mott-VRH model.

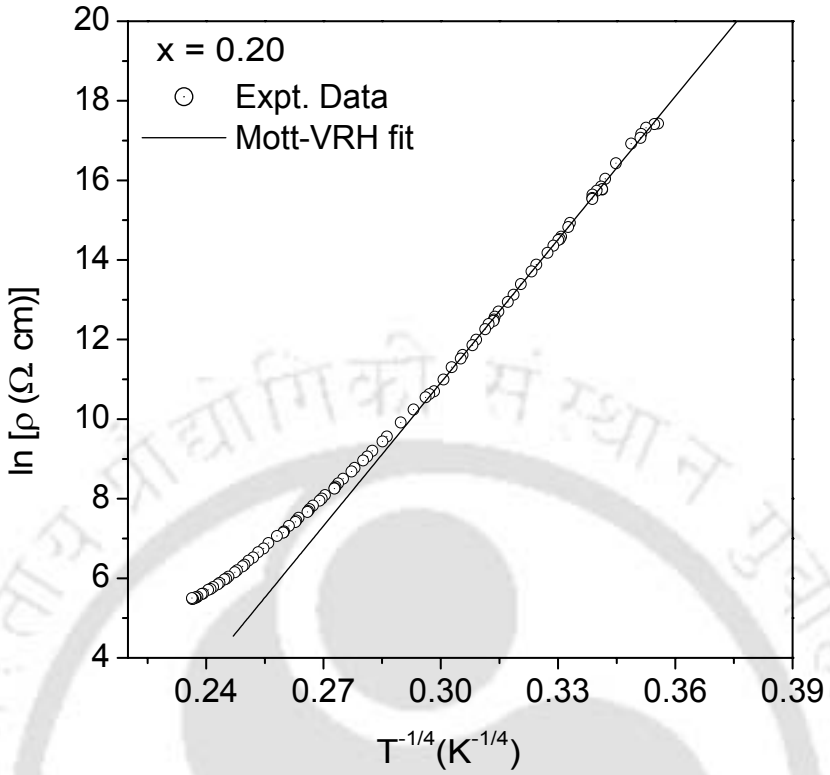

Fig. 5.21: Plot of ln(ρ) as a function of $T^{(-1/4)}$ for $CaMn_{0.8}Cu_{0.2}O_3$ (x = 0.20) sample. Solid line is the fit to Mott-VRH model.

Table 5.8: Parameters obtained from the fit of Mott VRH model. ρ_{0m} and T_{0m} are Mott residual resistivity and characteristic temperature respectively. $N(E_F)$ is the density of states in the vicinity of Fermi level. R_{hop}(300K) and E_{hop}(300K) are mean hopping distance and hopping energy respectively at 300K.

Samples → / Parameters ↓	x = 0	x = 0.10	x = 0.20
ρ_{0m}(Ω cm)	4.46 ±0.018 × 10^{-6}	2.51 ±0.024 × 10^{-15}	1.30±0.011 × 10^{-11}
T_{0m} (10^7 K)	6.53±0.021	74.80±0.031	20.70±0.015
$N(E_F)$ (10^{19} $eV^{-1}cm^{-3}$)	3.50	0.31	1.10
R_{hop}(300 K)(Å)	36.5	67.1	48.7
E_{hop}(300 K) (eV)	0.140	0.257	0.186
rmsd %	0.37	0.51	0.36

Typical plots of ln(ρ) versus $T^{-1/2}$ are shown in Figs. 5.22 and 5.23 for x = 0 and 0.20 samples respectively. The experimental data exhibit linear plot. They have been fitted to equation 1.24 by varying the parameters ρ_{0s} and T_{0s}. The fitted data are shown as solid lines. The experimental data closely follow the theoretical fit. The *rmsd* values are tabulated in Table 5.9. It is observed that for x = 0 and 0.10, the rmsd values for ES-VRH fit are relatively small compared to those of Mott-VRH fit. Thus the present samples for x ≤ 0.10 mostly follow the VRH model with Coulomb interaction. For x =0.20, the *rmsd* value for Mott-VRH fit is relatively small compared to that of ES-VRH fit. However, one can find from Figs. 5.22 and 5.23 that ES-VRH model fits for wider temperature range with minor deviation at high temperature compared to Mott-VRH model. So, the x = 0.20 sample also follows the ES-VRH model. The present results are in agreement with Bratico *et al.* [230], who have also found the evidence for Mott & ES -VRH mechanism in $CaMnO_{3-\delta}$. From the ES-VRH fitted values of T_{0s}, dielectric constant ε_r, hopping distance $R_{hs}(T) = (1/4)a(T_{0s}/T)^{1/2}$ and hopping energy $E_{hs}(T) = (1/2)k_BT(T_{0s}/T)^{1/2}$ were estimated and they are tabulated in Table 5.9. The values of T_{0s} are found to be in the same order of magnitude as reported by Laiho *et al.* [167] in 'Fe' doped $La_{0.7}Ca_{0.3}Mn_{1-y}Fe_yO_3$.

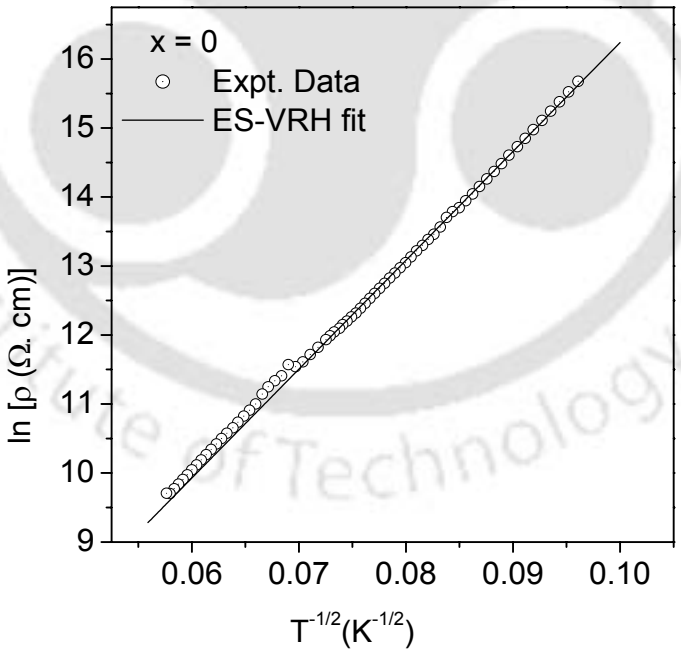

Fig. 5.22: Plot of ln(ρ) as a function of $T^{(-1/2)}$ for $CaMnO_3$ (x = 0) sample. Solid line is the fit to ES-VRH model.

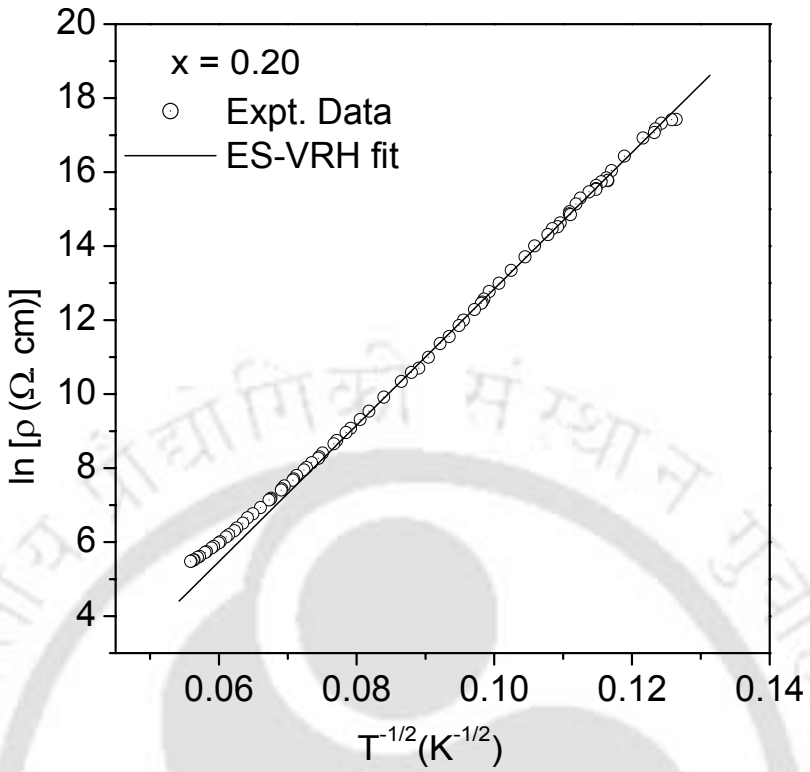

Fig. 5.23: Plot of ln(ρ) as a function of $T^{(-1/2)}$ for $CaMn_{0.8}Cu_{0.2}O_3$ (x = 0.20) sample. Solid line is the fit to ES-VRH model.

Table 5.9: Parameters obtained from ES-VRH model fitting. ρ_{0s} is the residual resistivity and T_{0s} is the characteristic temperature. R_{hs}(300K) and E_{hs}(300K) are mean hopping distance and hopping energy at 300K. ε_r is the dielectric constant.

Samples → / Parameters ↓	x=0	X=0.10	X=0.20
ρ_{0s} (mΩcm)	1584 ±0.52	0.06±0.011	3.74±0.013
$T_{0s}(10^4K)$	2.49±0.012	8.21±0.011	3.34±0.014
R_{hs}(300 K) (Å)	10.3	18.6	12.0
E_{hs}(300 K) (eV)	0.118	0.214	0.138
ε_r	4.01	1.27	3.11
rmsd %	0.20	0.42	0.43

5.3. Summary and Conclusions

The $LaMn_{1-x}Cu_xO_3$ and $CaMn_{1-x}Cu_xO_3$ compounds have been studied in this chapter. The former compounds could be prepared in single phase form up to x = 0.30 and in the latter series single phase is obtained up to x = 0.20.

The materials for $0.05 \leq x \leq 0.30$, in the series $LaMn_{1-x}Cu_xO_3$ exhibit ferromagnetism. The ferromagnetic transition temperature decreases with the 'Cu' concentration, where as, the saturation susceptibility value increases up to x = 0.15 and then decreases. It reveals that, even though 'Cu' doping increases the Mn^{4+} concentration, thereby increasing the Mn^{3+}- Mn^{4+} pairs, the 'Cu' atoms exhibit a strong antiferromagnetic interactions with 'Mn' ions. So the DE ferromagnetic interaction is weakened and the ferromagnetic T_c is reduced with doping. In $CaMn_{1-x}Cu_xO_3$ materials, 'Mn' ions are transformed from 4+ state to higher valency state which does not contribute any DE interactions and hence no ferromagnetic transition is observed. But, the increase of 'Cu' concentration results in smearing of antiferromagnetic transition.

$LaMn_{1-x}Cu_xO_3$ compound with x = 0.05 exhibits metal-insulator transition. For $x \geq 0.10$, even though FM transition is observed, no M-I transition is seen. It is mainly due to the domination of AFM interaction and the FM phase is below the percolation threshold. The electrical resistivity behaviour could be understood by the adiabatic small polaron hopping model.

Chapter 6

CONCLUSIONS

CONCLUSIONS

The important conclusions drawn in the thesis work are compiled as below.

To my knowledge, for the first time single phase samples of electron doped $Ba_{1-x}La_xMnO_3$ compounds ($x \leq 0.05$) have been prepared. These compounds are found to be free from impurity due to parent compound, i.e. $BaMnO_3$, which is generally reported in literature. These materials exhibit structural transition from orthorhombic cell to rhombohedral cell with increase in 'La' concentration. The typical values of lattice parameters for $Ba_{0.7}La_{0.3}MnO_3$ compound are found to be a = 5.470, b = 5.521 and c = 7.763Å and that of hole doped $Ba_{0.3}La_{0.7}MnO_3$ sample are found to be a = b = 5.543 and c = 13.458Å. Even in electron doped materials metal-insulator transition as high as 280K was observed for x = 0.30 and they also exhibit paramagnetic to ferromagnetic transition close to room temperature. All the electron doped materials exhibit colossal magneto-resistivity. The maximum value of colossal magneto-resistivity was observed for x = 0.50 sample and its value is 61% for 50kOe field at 243K.

The above electron doped materials show complex magnetic behavior. The paramagnetic to ferromagnetic transition is followed by loss of long range FM ordering due to magnetic anisotropy. Susceptibility contribution from intergranular weak links and reentrant spin glass behaviour due to competition between random antiferromagnetic interaction and ferromagnetic ordering have been observed. The presence of reentrant spin glass behaviour is confirmed from the susceptibility measurements at different frequencies. The freezing temperature of reentrant spin glass state, T_f is found to shift towards higher temperature with increase in frequency. The T_f value is taken as the temperature corresponding to peak in $\chi^{//}$ versus temperature plot.

For the first time charge ordering type transition is observed in $Ba_{0.5}La_{0.5}MnO_3$ compound from ac susceptibility measurements. The reentrant semiconducting behaviour has been observed in the vicinity of charge ordering temperature. The presence of dominant intergranular weak link networks have been demonstrated by performing susceptibility measurements in solid and powdered samples. The zero field cooled and field cooled ac susceptibility measurements carried out as a function of temperature on electron doped samples show that the FC susceptibility is enhanced below the spin glass freezing. This is explained in the light of stabilization of ferromagnetic phase rather than

the antiferromagnetism. The electrical resistivity data in the metallic region could be explained on the basis of electron-electron scattering mechanism.

In electron doped $Sr_{1-x}La_xMnO_3$ samples, structural transition from hexagonal symmetry to rhombohedral symmetry with increase in 'La' doping has been observed. When the materials undergo structural transition with doping minor peaks due to alternate structure have been found in a few intermediate compositions. Typical values of lattice parameters for x = 0.10 sample are found to be a = b = 5.438 and c = 9.068Å and those of x = 0.40 sample are a = b = 5.458 and c = 13.389Å. The refined occupancy values are found to be close to the expected values. The above materials show paramagnetic to ferromagnetic transition followed by low temperature antiferromagnetic transition. However, no trace of charge ordering and reentrant spin glass like behaviour is observed in the present series. The lack of reentrant spin glass behaviour in electron doped $Sr_{1-x}La_xMnO_3$ compounds could be mainly due to weak ferromagnetic interaction compared to $Ba_{1-x}La_xMnO_3$ series. It can be seen that in both electron doped series, the saturation susceptibility mostly increase with increase in Mn^{3+} concentrations and it leads to the conclusion that even in electron doped region, the ferromagnetic interaction is mainly due to Zener double exchange mechanism.

In electron doped $Sr_{1-x}La_xMnO_3$ series no metal-insulator transition is observed, it is mainly due to lack of percolation threshold of ferromagnetic phase. Change of slope with small upturn has been observed, in the plots of resistivity in logarithmic scale versus temperature in the vicinity of Neel temperature. The resistivity data in the semiconducting region could be mostly fitted to Mott-variable range hopping model.

Single phase samples of hole doped materials, i. e. by doping 'Ag' and 'Cu' in place of 'La', with the compositions $La_{1-x}Ag_xMnO_3$ and $La_{1-x}Cu_xMnO_3$ have been prepared. To my knowledge, hole doped materials using 'Cu' have been prepared for the first time.

Single phase samples of $La_{1-x}Ag_xMnO_3$ were obtained for the doping concentration up to x = 0.15, where as in 'Cu' doping, single phase materials were obtained up to x = 0.20. These materials are found to be mostly with orthorhombic or rhombohedral symmetries with *Pbnm* and $R\bar{3}c$ space group respectively. EDAX compositional analysis has been performed on a few selected representative samples from each series and they are found to be close to the starting stoichiometric ratio.

All the 'Ag' doped materials show paramagnetic to ferromagnetic and metal-insulator transitions with colossal magneto-resistivity behaviour. The maximum metal-insulator transition and ferromagnetic onset temperatures are found to be 289K and 294K respectively for x = 0.35 sample. The ferromagnetic T_c rises sharply from 5 to 15% of 'Ag' doping and then it almost remains constant. The 'Ag' doped materials are mostly free from any antiferromagnetic interaction. Maximum magneto-resistivity of about 25% has been observed in the vicinity of metal-insulator transition temperature for 10kOe applied field. The electrical resistivity data in the metallic region could be mostly explained on the basis of combination of electron-electron and electron-magnon scattering. The electrical resistivity data in the semiconducting region could be mostly explained on the basis of Mott-VRH model.

The 'Cu' doping in place of 'La' plays a dual role. It generates more Mn^{3+}-Mn^{4+} pairs, such that the population of 'Mn' ion pairs taking part in double exchange interaction is enhanced. On the other hand it weakens the double exchange interaction due to antiferromagnetic interaction between 'Cu' and 'Mn' ions. As a result, the saturation susceptibility is found to increase with doping while the ferromagnetic transition temperature is reduced. The susceptibility plots (both χ' & χ'') show the signature of reentrant spin glass like behaviour at low temperature, which is further confirmed from frequency variation measurements. One can observe the peaks due to antiferromagnetic transition and reentrant spin glass behaviour in χ'' versus T plots.

Metal-insulator transitions were observed in $La_{1-x}Cu_xMnO_3$ series for x = 0.05 and 0.10 samples with a maximum transition temperature of 92K. Large difference between M-I & FM-PM transition temperature has been observed and it is explained on the basis of weak link networks. The electrical resistivity in the metallic region could be analyzed in the light of combination of electron-electron and electron-magnon scattering. The maximum magneto-resistivity value is found to be around 20% for 10kOe field at around 180K.

To study the magnetic interaction between 'Cu' and 'Mn' atoms, $LaMn_{1-x}Cu_xO_3$ and $CaMn_{1-x}Cu_xO_3$ compounds have been investigated. 'Cu' doping results in generation of mixed valency of 'Mn' ions. However, it undergoes antiferromagnetic interaction with 'Mn' ions. In $LaMn_{1-x}Cu_xO_3$ compound, paramagnetic to ferromagnetic transition were observed for x up to 0.30. However no metal-insulator transition was observed for $x \geq 0.10$. The metal-insulator transition temperature for x = 0.05 sample is found to be around

201K. The susceptibility behaviour is mostly similar to that of $La_{1-x}Cu_xMnO_3$ compounds. The electrical conduction mechanism is mostly controlled by ES-VRH and adiabatic small polaron hopping model.

In $CaMn_{1-x}Cu_xO_3$, series materials exhibit only AFM interaction with semiconducting behaviour.

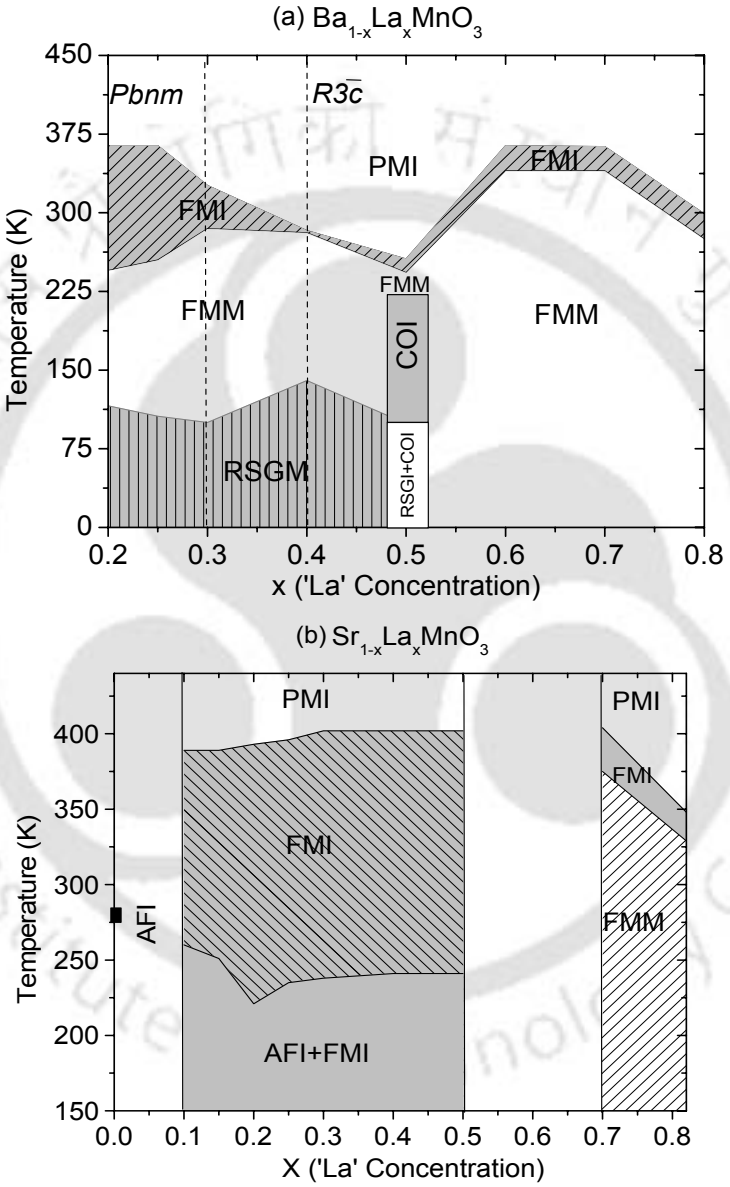

Fig. 6.1. Phase diagrams of (a)$Ba_{1-x}La_xMnO_3$ and (b)$Sr_{1-x}La_xMnO_3$. The different regions are abbreviated as follows, PMI = Paramagnetic Insulator, FMI = Ferromagnetic Insulator, FMM = Ferromagnetic Metal, AFI = Antiferromagnetic Insulator, COI = Charge Ordered Insulator, RSGI = Reentrant Spin Glass Insulator, RSGM = Reentrant Spin Glass Metal.

The phase diagrams of electron doped materials are shown in Figure 6.1(a) and 6.1(b) for $Ba_{1-x}La_xMnO_3$ and $Sr_{1-x}La_xMnO_3$ respectively. One can see the phase diagrams of electron doped materials are complicated. The $Ba_{1-x}La_xMnO_3$ materials exhibit transition from reentrant spin glass metallic (RSGM) to ferromagnetic metallic (FMM) and then to ferromagnetic insulator (FMI) with the increase of temperature and, finally it shows paramagnetic insulator (PMI) behaviour. For $x \approx 0.50$, charge ordering state has been observed. In electron doped $Sr_{1-x}La_xMnO_3$ materials, ferromagnetism with competing antiferromagnetic interaction has been observed in the low temperature region with insulating behaviour (FMI+AFI). As the temperature increases FM-insulating region appear followed by PMI. On the otherhand in hole doped regime the material is found to be predominately in FMM state below $\approx$ 350K.

The phase diagrams of hole doped materials are shown in Figure 6.2(a) and 6.2(b) for $La_{1-x}Ag_xMnO_3$ and $La_{1-x}Cu_xMnO_3$ respectively. In contrast to electron doped materials, one can see a smooth phase transition from PMI to FMM state as the temperature is lowered in $La_{1-x}Ag_xMnO_3$. In $La_{1-x}Cu_xMnO_3$ material, FMM state is observed in a narrow composition range. Mostly the low temperature region is dominated by reentrant spin glass insulator (RSGI) state.

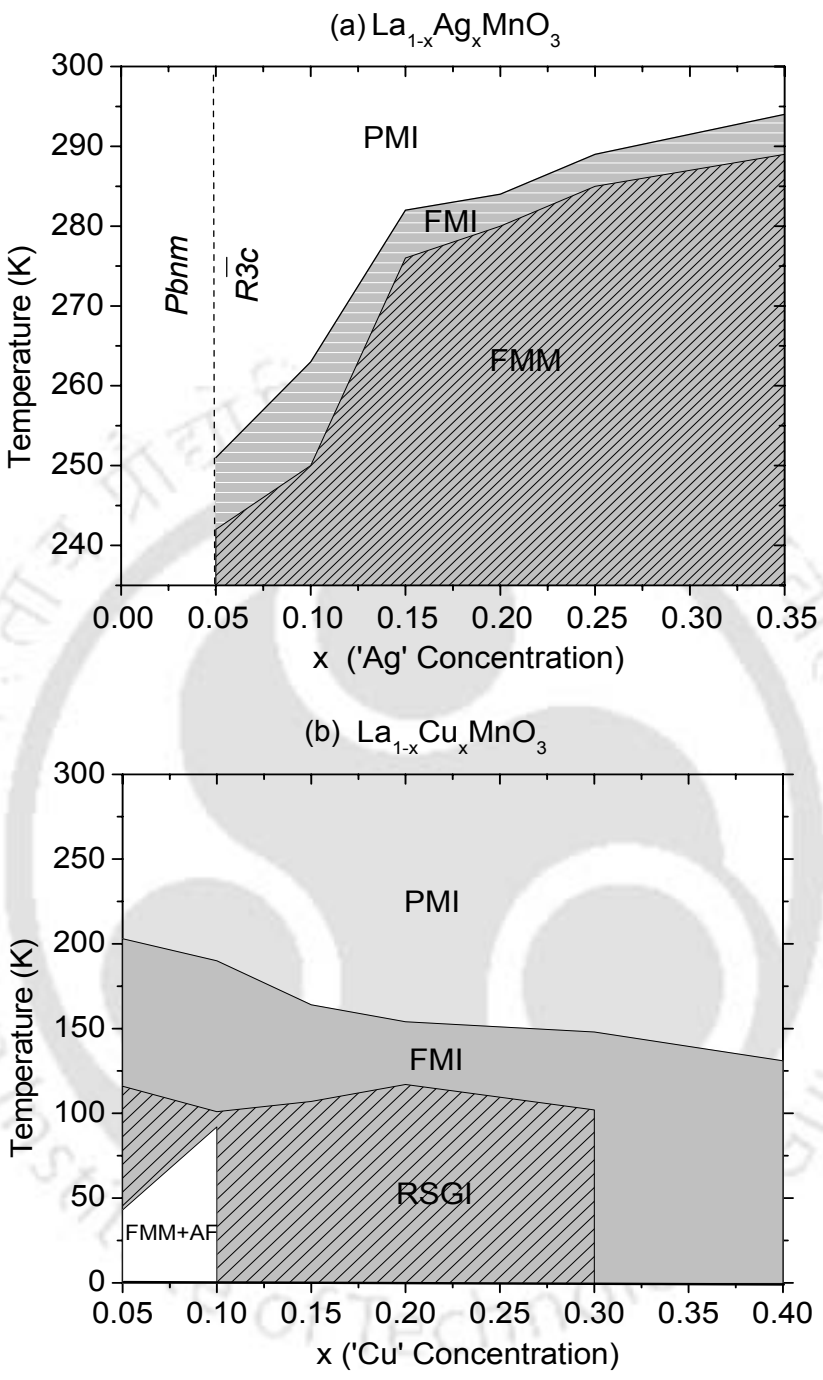

Fig. 6.2. Phase diagrams of (a)$La_{1-x}Ag_xMnO_3$ and (b)$La_{1-x}Cu_xMnO_3$. The different regions are abbreviated as follows, PMI = Paramagnetic Insulator, FMI = Ferromagnetic Insulator, FMM = Ferromagnetic Metal, RSGI = Reentrant Spin Glass Insulator.

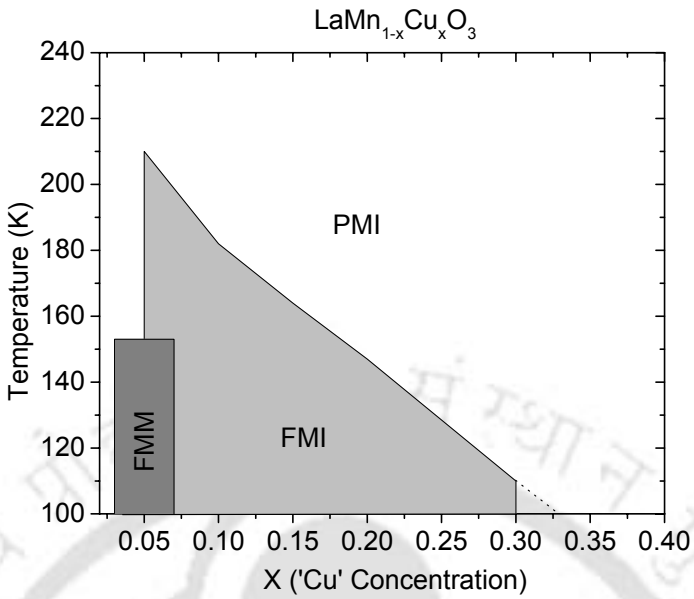

Fig. 6.3. Phase diagram of $LaMn_{1-x}Cu_xO_3$. The different regions are abbreviated as follows, PMI = Paramagnetic Insulator, FMI = Ferromagnetic Insulator, FMM = Ferromagnetic Metal.

The phase diagram of manganese site doped ($LaMn_{1-x}Cu_xO_3$) materials is shown in Fig. 6.3. The materials exhibit transition from FMI to PMI with the increase of temperature. FMM state is observed for $x \approx 0.05$ at low temperature region.

---------XXX-------

REFERENCES

1. G. H. Jonker and J. H. van Santen, *Physica,* **16** (377) 1950.
2. J. H. van Santen and G. H. Jonker, *Physica*, **16** (599) 1950.
3. J. Volger, *Physica*, **20** (49)1954.
4. C. W. Searle and S. T. Wang, *Can. J. Phys.* **47** (2703) 1969.
5. C. W. Searle and S. T. Wang, *Can. J. Phys.* **48** (2023) 1970.
6. A. H. Morrish, B. J. Evans, J. A. Eaton and L. K. Leung, *Can. J. Phys.*, **47** (2691) 1969.
7. L. K. Leung, A. H. Morrish and C. W. Searle, *Can. J. Phys.* **47** (2697) 1969.
8. R. M. Kusters, J. Singleton, D. A. Keen, R. McGreevy and W. Hayes, *Physica B*, **155** (362) 1989.
9. R. von Helmolt, J. Wecker, B. Holzapfel, L. Schulz and K. Samwer, *Phys. Rev. Lett.* **71** (2331) 1993.
10. K. Chahara, T. Ohno, M. Kasai and Y. Kozono, *Appl. Phys. Lett.* **63** (1990) 1993.
11. S. Jin, T. H. Tiefel, M. McCormack, R. A. Fastnacht, R. Ramesh and L. H. Chen, *Science*, **264** (413) 1994.
12. E. O. Wollan and W. C. Koehler, *Phys. Rev.* **100** (545) 1955.
13. G. H. Jonker, *Physica,* **22** (707) 1956.
14. C. Zener , *Phys. Rev.* **81** (440) 1951.
15. C. Zener , *Phys. Rev.* **82** (403) 1951.
16. P. W. Anderson and H. Hasegawa, *Phys. Rev.* **100** (675) 1955.
17. P. W. Anderson, *Phys. Rev.* **109** (1492) 1958.
18. J. B. Goodenough, *Phys. Rev. B*, **100** (564) 1995.
19. P. -G. de Gennes, *Phys. Rev.* **118** (141) 1960.
20. A. J. Millis, P. B. Littlewood and B. I. Shraiman, *Phys. Rev. Lett.* **74** (5144) 1995.
21. P. Schiffer, A. P. Ramirez, W. Bao and S. –W Cheong, *Phys. Rev. Lett.* **75** (3336) 1995.
22. G. Q. Gong, C. Canedy, G. Xiao, J. Z. Sun, A. Gupta and W. J. Gallagher, *Appl. Phys. Lett.* **67** (1783) 1995.
23. G. Q. Gong, A. Gupta, G. Xiao, P. Lecoeur and T. R. McGuire, *Phys. Rev. B*, **54** (R3742) 1996.

24. R. Mahesh, R Mahendiran, A. K. Raychaudhuri and C. N. R. Rao, *Appl. Phys. Lett.* **68** (2291) 1996.
25. Y. G. Zhao, W. Cai, J. Zhao, X. P. Zhang, B. S. Cao, M. H. Zhu, L. W. Zhang, S. B. Ogale, T. Wu, T. Venkatesan, Li Lu, T. K. Mandal and J. Gopalakrishnan, *Phys. Rev. B*, **65** (144406) 2002.
26. A. Urushibara, Y. Moritomo, T. Arima, A. Asamitsu, G. Kido and Y. Tokura, *Phys. Rev. B*, **51** (14103) 1995.
27. J.-S Zhou, J. B. Goodenough, A. Asamitsu and Y. Tokura, *Phys. Rev. Lett.* **79** (3234) 1997.
28. S. Uhlenbruck, R. Teipen, R. Klingeler, B. Büchner, O. Friedt, M. Hücker, H. Kierspel, T. Niemöller, L. Pinsard, A. Revcolevschi and R. Gross, *Phys. Rev. Lett.* **82** (185) 1998.
29. A. Asamitsu, Y. Moritomo, Y. Tomioka, T. Arima and Y. Tokura, *Nature* **373** (407) 1995.
30. R. von Helmolt, L. Haupt, K. Bärner and U Sondermann, *Solid State Comm.* **82** (641) 1992.
31. H. L. Ju and H. Sohn, *Solid State Comm.* **102** (463) 1997.
32. H. L. Ju, J. Gopalakrishnan, J. L. Peng, Q. Li, G. C. Xiong, T. Venkatesan and R. L. Greene, *Phys. Rev. B*, **51** (6143) 1995.
33. P. Mandal and B. Ghosh, *Phys. Rev. B*, **68** (14422) 2003.
34. S. S. Manoharan, N. Y. Vasanthacharya, M. S. Hegde, K. M. Satyalakshmi, V. Prasad and S. V. Subramanyam, J. Appl. Phys. **76** (3923) 1994.
35. R. Mahendiran, R. Mahesh, A. K. Raychaudhuri and C. N. R. Rao, J. Phys. D: Appl. Phys. **28** (1743) 1995.
36. G. Ji, X. J. Fan, J. H. Zhang, C. S. Xiong and X.-G. Li, *J. Phys. D: Appl. Phys.* **31** (3036) 1998.
37. Y. X. Jia, Li Lu, K. Khazeni, V. H. Crespi, A. Zettl and M. L. Cohen, *Phys. Rev. B*, **52** (9147) 1995.
38. A. Banerjee, S. Pal, E. Rozenberg and B. K. Chaudhuri, *J. Phys: Conden. Matt.* **13** (9489) 2001.
39. R. Kajimoto, H. Yoshizawa, H. Kawano, H. Kuwahara, Y. Tokura, K. Ohoyama and M. Ohashi, *Phys. Rev. B*, **60** (9506) 1999.

40. M. Pattabiraman, P. Murugaraj, G. Rangarajan, V. Prasad, S. V. Subramanyam, V. S. Satry, Sang-Mo-Koo and K. V. Rao, *Pramana-J. of Phys.* **55** (455) 2000.
41. Y. Tomioka, A. Asamitsu, H. Kuwahara, Y. Moritomo and Y. Tokura, *Phys. Rev. B,* **53** (R1689) 1996.
42. Y. Moritomo, H. Kuwahara, Y. Tomioka and Y. Tokura, *Phys. Rev. B* **55** (7549) 1997.
43. M. Itoh, T. Shimura, J. D. Yu, T. Hayashi and Y. Inaguma, *Phys. Rev. B,* **52** (12522) 1995.
44. R. J. H. Voorhoeve, J. P. Remeika, L. E. Trimble, A. S. Cooper, F. J. Disalvo and D. K. Gallagher, *J. Solid State Chem.* **14** (395) 1975.
45. T. Shimura, T. Hayashi, Y. Inaguma and M. Itoh, *J. Solid State Chem.* **124** (250) 1996.
46. T. Diehl, P. Chaudouët, J. C. Joubert and J. Pierre, *J. App. Phys.* **81** (4970 1997.
47. X. L. Wang, S. J. Kennedy, P. Gehringer, W. Lang, H. K. Liu and S. X. Dou, *J. Appl. Phys.* **83** (7177) 1998.
48. C. Boudaya, L. Laroussi, E. Dhahri, J. C. Joubert and A. Cheikh-Rouhou, *J. Phys. Cond. Matt.* **10** (7485) 1998.
49. G. H. Rao, J. R. Sun, K. Bärner and N. Hamad, *J. Phys. Cond. Matt.* **11** (1523) 1999.
50. S. L. Ye, W. H. Song, J. M. Dai, S. G. Wang, K. Y. Wang, C. L. Yuan and Y. P. Sun, *J. App. Phys.* **88** (5915) 2000.
51. S. Roy, Y. Q. Guo, S. Venkatesh and N. Ali, *J. Phys. Condens. Matt.* **13** (9547) 2001.
52. T. Tang, K. M. Gu, Q. Q. Cao, D. H. Wang, S. Y. Zhang and Y. W. Du, *J. Magn. Magn. Mater,* **222** (110) 2000.
53. N. T. Hien and N. P. Thuy, *Physica B*, **319** (168) 2002.
54. T. Tang, Q. Q. Cao, K. M. Gu, H. Y. Xu, S. Y. Zhang, and Y. W. Du, *Appl. Phys. Lett.* **77** (723) 2000.
55. S. L. Ye, W. H. Song, J. M. Dai, K. Y. Wang, S. G. Wang, C. L. Zhang, J. J. Du, Y. P. Sun and J. Fang, *J. Magn. Magn. Mater.* **248** (26) 2002.
56. L. Pi, M. Hervieu, A. Maignan, C. Martin and B. Raveau, *Solid State Comm.* **126** (229) 2003.

57. M. Hervieu, R. Mahesh, N. Rangavittal and C. N. R. Rao, *Eur. J. Solid. State. Inorg. Chem.* **32** (79) 1995.
58. A. Gupta, T. R. McGuire, P. R. Duncombe, M. Rupp, J. Z. Sun, W. J. Gallagher and G. Xiao, *Appl. Phys. Lett.* **67** (3494) 1995.
59. L Ranno, M. Viret, A. Mari, R. M. Thomas and J. M. D. Coey, *J. Phys. Cond. Matt.* **8** (L33) 1996.
60. Q. Huang, A. Santoro, J. W. Lynn, R. W. Erwin, J. A. Borchers, J. L. Peng and R. L. Greene, *Phys. Rev. B*, **55** (14987) 1997.
61. J. B. Macchesney, H. J. Williams, J. F. Potter and R. C. Sherwood, *Phys. Rev.* **164** (779) 1967.
62. K. Kikuchi, H. Chiba, M. Kikichi and Y. Syono, *J. Solid State Chem.* **146** (1) 1996.
63. C. H. Chen and S. –W. Cheong, *Phys. Rev. Lett.* **76** (4042) 1996.
64. J. J. Neumeier and J. L. Cohn, *Phys. Rev. B,* **61** (14319) 2000.
65. Cz. Kapusta, P. C. Riedi, M. Sikora and M. R. Ibarra, *Phys. Rev. Lett.* **84** (4216) 2000.
66. H. Chiba, M. Kikuchi, K. Kusaba, Y. Muraoka and Y. Syono, *Solid State Comm.* **99** (499) 1996.
67. W. Bao, J. D. Axe, C. H. Chen and S. –W. Cheong, *Phys. Rev. Lett.* **78** (543) 1997.
68. H. Aliaga, M. T. Causa, B. Alascio, H. Salva, M. Tovar, D. Vega, G. Polla, G. Leyva and P. Konig, *J. Magn. Magn. Mater.* **226-230** (791) 2001.
69. D. Vega, G. Polla, A. G. Leyva, P. Konig, H. Lanza, A. Esteban, H. Aliaga, M. T. Causa, M. Tovar and B. Alascio, *J. Solid State Chem.* **156** (458) 2001.
70. C. Martin, A. Maignan, F. Damay, M. Hervieu and B. Raveau, *J. Solid State Chem.* **134** (198) 1997.
71. A. Maignan, C. Martin, F. Damay, B. Raveau and J. Hejtmanek, *Phys. Rev. B*, **58** (2758) 1998.
72. C. Martin, A. Maignan, M. Hervieu, B. Raveau, Z. Jirák, A. Kurbakov, V. Trounov, G. André and F. Bourée, *J. Magn. Magn. Mater,* **205** (184) 1999.
73. L. M. Belova, N. A. Babushkina, A. N. Taldenkov, A. Maignan, C. Martin and B. Raveau, *J. Phys. Condens. Matt*. **13** (1103) 2001.
74. M. Respaud, J. M. Broto, H. Rakoto, J. Vanacken, P. Wagner, C. Martin, A. Maignan and B. Raveau, *Phys. Rev. B* **63** (144426) 2001.

75. I. O. Troyanchuk, N. V. Samsonenku, H. Szymczak and A. Nabialok, *J. Solid State Chem.* **131** (144) 1997.
76. Y. Murakami, D. Shindo, H. Chiba, M. Kikuchi and Y. Syono, *Phys. Rev. B,* **59** (6395) 1999.
77. S. L. Yuan, Y. Jiang, X. Y. Zeng, W. Y. Zhao, Y. P. Yang, J. P. Qian, G. Q. Zhang, F. Tu and C. Q. Tang, *Phys. Rev. B*, **62** (11347) 2000.
78. B. Raveau, C. Martin, A. Maignan and M. Hervieu, *J. Phys. Condes. Matt.* **14** (1297) 2002.
79. Y. Moritomo, T. Akimoto, A. Nakamura, K. Ohoyama and M. Ohashi, *Phys. Rev. B,* **58** (5544) 1998.
80. S. I. Patil, S. M. Bhagat, Q. Q. Shu, S. E. Lofland, S. B. Ogale, V. N. Smolyaninova, X. Zhang, B. S. Palmer, R. S. Decca, F. A. Brown, H. D. Drew and R. L. Greene, *Phys. Rev. B,* **62** (9548) 2000.
81. A. Sundaresan, P. L. Paulose, R. Mallik and E. V. Sampathkumaran, *Phys. Rev. B,* **57** (2690) 1998.
82. H. Wakai, F. Munakata and E. Iguchi, *Mat. Sci. & Eng. B*, **103** (26) 2003.
83. J. H. Zhao, H. P. Kunkel, X. Z. Zhou and G. Williams, *Phys. Rev. B*, **66** (184428) 2002.
84. Y. Moritomo, Y. Tomioka, A. Asamitsu, Y. Tokura and Y. Matsui, *Phys. Rev. B*, **51** (3297) 1995.
85. Y. Moritomo, A. Asamitsu, H. Kuwahara and Y. Tokura, *Nature*, **380** (141) 1996.
86. R. Mahesh, R. Mahendiran, A.K. Raychaudhuri and C. N. R. Rao, *J. Solid State Chem.* **122** (448) 1996.
87. A. P. Ramirez, *J. Phys. Cond. Matt.* **9** (8171) 1997.
88. J. M. D. Coey, M. Viret and S. von Molnar, *Advances In Phys*. **48** (167) 1999.
89. E. Dagotto, T. Hotta and A. Moreo, *Phys. Reports*, **344** (1) 2001.
90. W. Prellier, Ph Lecoeur and B. Mercey, *J. Phys. Cond. Matt.* **13** (R915) 2001.
91. E. L. Nagaev, *Phys. Reports*, **346** (387) 2001.
92. C. N. R. Rao and B. Raveau, Colossal Magnetoresistance, Charge Ordering and Related Properties of Manganese Oxides, World Scientific, Singapore, 1998.
93. Y. Tokura, Colossal magneto-resistive Oxides, Gordon and Breach Science Publishers, 2000.

94. Eduard L Nagaev, Colossal Magnetoresistance and Phase Separation in Magnetic Semiconductors, Imperical College Press, 2002.
95. Y. Shimakawa, Y. Kubo and T. Manako, *Nature*, **379** (53) 1996.
96. S. –W. Cheong, H. Y. Hwang, B. Batlogg and L. W. jr Rupp, *Solid State Comm.* **98** (163) 1996.
97. M. A. Subramanian, B. H. Toby, A. P. Ramirez, W. J. Marshall, A. W. Sleight and G. H. Kwei, *Science*, **273** (81) 1996.
98. D. –K. Seo, M. –H. Whangbo and M. A. Subramanian, *Solid State Comm.* **101** (417) 1997.
99. D. J. Singh, *Phys. Rev. B*, **55** (313) 1997.
100. A. P. Ramirez, R. J. Cava and J. Krajewski, Nature, **387** (268) 1997.
101. A.M. Glazer, *Acta Cryst.* **B28** (3384) 1972.
102. A.M. Glazer, *Acta Cryst.* **A31** (756) 1975.
103. V. M. Goldsmith, Geochemische Verteilungsgesetze der Elemente, **VII-VIII** (1928) 1927.
104. C. Rao and B. Raveau, Transition metal Oxides (2nd ed.), New York, Wiley-VCH.
105. S. Blundell, "Magnetism in Condensed Matter", Oxford University Press, 2003, Page 45.
106. H. Jahn and E. Teller, *Proc. Roy. Soc. London*, **A161** (220) 1937.
107. J. B. Goodenough, Magnetism and the chemical bond (New York; Wiley Interscince) 1996.
108. J. Brink, G. Khaliullin and D. Khomskii, *Phys. Rev. Lett.* **83** (5118) 1999.
109. Z. –H. Wang, H. Kronmüller, O. I. Lebedev, G. M. Gross, F. S. Razavi, H. –U. Habermeier and B. G. Shen, *Phys. Rev. B*, **65** (054411) 2002.
110. Y. Yamada, O. Hino, S. Nohdo, R. Kanao, T. Inami and S. Katano, *Phys. Rev. Lett.* **77** (904) 1996.
111. W. Thomson, *Proc. Roy. Soc. London*, **8** (546) 1857.
112. M. Baibich, J. Broto, A. Fert, F. Nguyen Van Dau, F. Petroff, P. Eitenne, G. Creuzet, A. Friedrich, and J. Chazelas, *Phys. Rev. Lett.* **61** (2472) 1988.
113. H. Y. Hwang, S. -W. Cheong, P. G. Radaelli, M. Marezio and B. Batlogg, *Phys. Rev. Lett.* **75** (914) 1995.
114. R. Mahendiran, R. Mahesh, N. Rangavittal, S. Tewari, A. K. Raychaudhuri, T. Ramakrishnan and C. N. R. Rao, *Phys. Rev. B*, **53** (3348) 1996.

115. C. L. Canedy, K. B. Ibsen, G. Xiao, J. Z. Sun, A. Gupta and W. J. Gallagher, *J. Appl. Phys.* **79** (4546) 1996.
116. N. Sharma, A. K. Nigam, R. Pinto, N. Venkataramani, S. Prasad, G. Chandra and S. P. Pai, *J. Magn. Magn. Mater*, **154** (296) 1996.
117. J. Fontcuberta, B. Martinez, A. Seffar, S. Piñol, J. L. Gracia-Muñoz and X. Obradors, *Phys. Rev. Lett.* **76** (1122) 1996.
118. G. C. Xiong, S. Bhagat, Q. Li, M. Dominguez, H Ju, R. Greene and T. Venkatesan, *Solid State Comm.* **97** (599)1996.
119. B. Martinez, J. Fontcuberta, A. Seffar, J. L. Gracia-Muñoz, S. Piñol and X. Obradors, *Phys. Rev. B*, **54** (10001)1996.
120. G. J. Snyder, M. R. Beasley, T. H. Geballe, R. Hiskes and S. DiCarolis, *Appl. Phys. Lett.* **69** (4254) 1996.
121. H. Y. Hwang, S. -W. Cheong, N. P Ong and B. Batlogg, *Phys. Rev. Lett.* **77** (2041) 1996.
122. J. Y. Gu, C. Kwon, M. C. Robson, Z. Trajanovic, K. Ghosh, R. P. Sharma, R. Shreekala, M. Rajeswari, T. Venkatesan, R. Ramesh and T. W. Noh, *App. Phys. Lett.* **70** (1763) 1997.
123. M. Jaime, P. Lin, M. B. Salamon and P. D. Han, *Phys. Rev. B*, **58** (R5901) 1998.
124. S. Angappane, K. Sethupathi and G. Rangarajan, *Pramana-J. of Phys.* **58** (1079) 2002.
125. I. Mannari, *Prog. of Theo. Phys.* **22** (335) 1959.
126. G. J. Snyder, R. Hiskes, S. DiCarolis, M. R. Beasley and T. H. Geballe, *Phys. Rev. B*, **53** (14434) 1996.
127. K. Kubo and N. Ohata, *J. Phys. Soc. Japan*, **33** (21) 1972.
128. X. Wang and X. –G. Zhang, *Phys. Rev. Lett.* **82** (4276) 1999.
129. N. Furukawa, *J. Phys. Soc. Japan*, **69** (1954) 2000.
130. J. F. Lawler, J. G. Lunney and J. M. D. Coey, *Appl. Phys. Lett.* **65** (3017) 1994.
131. M. Ohtaki, H. Koga, T. Tokunaga, K. Eguchi and H. Arai, *J. Solid State Chem.* **120** (105) 1995.
132. J. de Teressa, M. Ibarra, P. Algarabel, C. Ritter, C. Marquina, J. Blasco, J. Garcia, A. del Moral and Z. Arnold, *Nature*, **386** (256) 1997.
133. T. M. Palstra, A. P. Ramirez, S. –W. Cheong, B. Zegarski, P. Schiffer and J. Zaanen, *Phys. Rev. B*, **56** (5104) 1997.

134. M. Jaime, H. T. Hardner, M. B. Salamon, M. Rubinstein, P. Dorsey and D. Emin, *Phys. Rev. Lett.* **78** (951) 1997.
135. J. M. D. Coey, M. Viret, L. Ranno and K. Ounadjela, *Phys. Rev. Lett.* **75** (3910) 1995.
136. M. Ziese and C. Srinitiwarawong, *Phys. Rev. B*, **58** (11519) 1998.
137. G. Jakob, W. Westerburg, F. Martin and H. Adrian, *Phys. Rev. B*, **58** (14966) 1998.
138. N. F. Mott, Conduction in non-crystalline materials (2nd ed.) Oxford: Oxford University Press (1993).
139. N. F. Mott "Metal – Insulator Transitions" 1990 2nd edition (London, Taylor & Francis).
140. M. Viret, L. Ranno and J. M. D. Coey, *Phys. Rev. B*, **55** (8067) 1997.
141. M. F. Hundley, M. Hawley, R. H. Heffner, Q. X. Jia, J. J. Neumeier, J. Tesmer, J. B. Thompson and X. D. Wu, *Appl. Phys. Lett.* **67** (860) 1995.
142. J. O'Donnell, M. Onellion, M. S. Rzchowski, J. N. Eckstein and I. Bozovic, *Phys. Rev. B.* **54** (R6841) 1996.
143. N. Furukawa, *J. Phys. Soc. Japan*, **63** (3214) 1994.
144. Y. Tokura and Y. Tomioka, *J. Magn. Magn. Mater,* **200** (1) 1999.
145. S. Kirkpatrick, *Phys. Rev. Lett.* **27** (1722) 1971.
146. B. J. Last and D. J. Thouless, *Phys. Rev. Lett.* **27** (1719) 1971.
147. T. P. Eggarter and M. H. Cohen, *Phys. Rev. Lett.* **25** (807) 1970.
148. V. Ambegaokar, B. I. Halperin and J. S. Langer, *Phys. Rev. B*, **4** (2612) 1971.
149. H. L. Frisch, J. M. Hammersley and D. J. A. Welsh, *Phys. Rev.* **126** (949) 1962.
150. V. K. S. Sante and S. Kirkpatrick, *Adv. Phys.* **20** (325) 1971.
151. G. H. Rao, J. R. Sun, Y. Z. Sun, Y. L. Zhang and J. K. Liang, *J. Phys. Cond. Matt.* **8** (5393) 1996.
152. R. V. Krishnan and A. Banerjee, *J. Phys. Cond. Matt.* **12** (7887) 2000.
153. M. Rubinstein, *J. App. Phys.* **87** (5019) 2000.
154. H. Huhtinen, R. Laiho, K. G. Lisunov, V. N. Stamov and V. S. Zakhvalinskii, *J. Magn. Magn. Mater.* **238** (160) 2002.
155. G. Matsumoto, *J. Phys. Soc. Japan* **29** (606) 1970.
156. J. B. Elimans, B. Van Laar, K. R. Van Der Keen and B. Loopstra, *J. Solid State Chem.* **3** (238) 1971.

157. J. M. De Teresa, M. R. Ibarra, J. García, J. Blasco, C. Ritter, P. A. Algarabel, C. Marquina and A. del Moral, *Phys. Rev. Lett.* **76** (3392) 1996.
158. R. von Helmholt, L. Haupat, K. Bärner and Sondermann, *Solid State Comm.,* **82** (693) 1992.
159. C. Martin, A, Maignan and B. Raveau, *J. Matt. Chem*. **6** (1245) 1996.
160. S. K. Hasanain, W.S. Shah, A. Mumtaz, M. Nadeem and M. J. Akhtar, *J. Magn. Magn. Mater.* (in press, 2004).
161. J. L. Gracia-Muñoz, J. Fontcuberta, M. Suaaidi and X. Obradors, *J. Phys. Cond. Matt.* **8** (L787) 1996.
162. R. Mahendiran, R. Mahesh, A. K. Raychaudhuri and C. N. R. Rao, *Phys. Rev. B*, **53** (12160) 1996.
163. R. Mahesh, R. Mahendiran, A. K. Raychaudhuri and C. N. R. Rao, *J. Solid state Chem*. **120** (204) 1996.
164. A. Maignan, C. Simon, V. Caignaert and B. Raveau, *Z. Phys. B*, **99** (305) 1996.
165. J. Blasco, J. García, J. M. de Teresa, M. R. Ibarra, J. Perez, P. A. Algarabel, C Marquina and C. Ritter*, Phys. Rev. B*, **55** (8905) 1997.
166. Li Pi, Lei Zheng and Y. Zhang, *Phys. Rev. B*, **61** (8917) 2000.
167. R. Laiho, K. G. Lisunov, E. Lähderanta, P. A. Petrenko, J. Salminen, M. A. Shakhov, M. O. Safontchik, V. S. Stamov, M. V. Shubnikov and V. S. Zakhvalinskii, *J. Phys. Cond. Matt.* **14** (8043) 2002.
168. B. Singh, R. K. Sahu, S. S. Manoharan, K. Dörr and K. –H. Müller, *J. Magn. Magn. Mater.* **270** (358) 2004.
169. A. J. Millis, B. I. Shraiman and R. Mueller, *Phys. Rev. Lett.* **77** (175) 1996.
170. A. J. Millis, R. Mueller and B. I. Shraiman, *Phys. Rev. B*, **54** (5389) 1996.
171. A. J. Millis, R. Mueller and B. I. Shraiman, *Phys. Rev. B*, **54** (5405) 1996.
172. A. J. Millis, T. Darling, and A. Migliori, *J. App. Phys.*, **83** (1588) 1998.
173. A. J. Millis, *Nature*, **392** (147) 1998.
174. J. R. Cullen and E. Callan, *Phys. Rev.* **7** (397) 1973.
175. J. Kanamori, *J. Phys. Chem. Solids*, **10** (87) 1959.
176. Y. Tokura, H. Kuwahara, Y. Moritomo, Y. Tomioka and A. Asamitsu, *Phys. Rev. Lett.* **76** (3184) 1996.
177. H. Kuwahara, Y. Tomioka, A. Asamitsu, Y. Moritomo and Y. Tokura, *Science*, **270** (961) 1995.

178. J. –S. Zhou, W. Archibald and J. B. Goodenough, *Nature*, **381** (770) 1996.
179. M. F. Hundley and J. J. Neumeier, *Phys. Rev. B*, **55** (11511) 1997.
180. A. Asamitsu, Y. Moritomo and Y. Tokura, *Phys. Rev. B*, **53** (R2952) 1996.
181. M. Jaime, M. B. Salamon, K. Pettit, M. Rubinstein, R. E. Treece, J. S. Horwitz and D. B. Chrisey, *Appl. Phys. Lett.* **68** (1576) 1996.
182. T. Kasuya, *Prog.Theo. Phys.* **22** (227) 1959.
183. L. Campbell and A. Fert, Ferromagnetic materials, Vol. 3, edited by E. P. Walford (Amsterdam: North Holand), 1982.
184. S. Zhang, *J. App. Phys*., **79** (45426) 1996.
185. G. S. Rao, C. Rao and J. Ferraro, *Appl. Spetro*. **24** (436) 1970.
186. J. H. Jung, K. H. Kim, D. J. Eom, T. W. Noh, E. J. Choi, J. Yu, Y. S. Kwon and Y. Chung, *Phys. Rev. B*, **55** (15489) 1997.
187. T. Arima and Y. Tokura, *J. Phys. Soc. Japan*, **64** (2488) 1995.
188. P. Fumagalli, C. Spaeth, G. Guntherodt and R. von Helmolt, *IEEE Trans. Magn*. **31** (3277) 1995.
189. B. F. Woodfield, M. L. Wilson and J. M. Byers, *Phys. Rev. Lett.* **78** (3201)1997.
190. D. W. Visser, A. P. Ramirez and M. A. Subramanian, *Phys. Rev. Lett.* **78** (3947) 1992.
191. R. A. Young, "The Rietveld Method" International Union of Crystallography, (New York, Oxford University Press 1996).
192. A. Taylor, X – ray Metallography (Wiley, New York, 1961).
193. G. H. Jeffery, J. Bassette, J. Mendham and R. C. Denney, Vogal's Textbook of quantitative Chemical Analysis, 5th ed., Addison Wesley Longman Limited, 1989.
194. Z. Zeng, M. Greenblatt and M. Croft, *Phys. Rev. B,* **59** (8784) 1999.
195. A. J. Van Duynevelt, *J. App. Phys.* **53** (11) 1982.
196. J. R. Owers-Bradley, Wen-Sheng Zhou and W. P. Halperin, *Rev. Sci. Instr.* **52** (1106) 1981.
197. M. Ishizuka and Y. Tohi, *Jap. J. Appl. Phys.* **19** (639) 1980.
198. M. Ocio and J. Hamman, *Rev. Sci. Instr.* **56** (1367) 1985.
199. A. F. Deutz, R. Hulstman and F. J. Kranenburg, *Rev. Sci. Instr.* **60** (113) 1989.
200. "Ballistic and Bridge Methods of Magnetic Measurements of Materials", D. –X. Chen, China Metorology, Beijing (1990), PP-526-572.

201. "Magnetic Susceptibility of superconductors and Other Spin Systems", Edited by R. A. Hein, Plenum Press, New York, 1991, PP-71.
202. R. B. Goldfarb and J. V. Minervini, *Rev. Sci. Instr.* **55** (761) 1984.
203. A. Earnshaw "Introduction of Magnetochemistry", Academic Press, London, 1968.
204. "Introduction to Solid State Physics", Charles Kittel, John-Wiley Sons, 7th Edition, 2000.
205. B. N. Figgis and J. Levis, "In Progress in inorganic Chemistry" (ed. F. P. Cotton) Vol. **6**, PP 37-240, Interscince, New York, 1964.
206. J. H. Zhao, H. P. Kunkel, X. Z. Zhou and G. Williams, J. Phys. Conden. Matt. **13** (5785) 2001.
207. A. Hardy, *Acta Crystallogr.* **15** (179) 1962.
208. C. Roy and R. C. Budhani, *J. Appl. Phys.* **85** (3124) 1999.
209. B. Dabrowski, K. Rogacki, X. Xiong, P. W. Klamut, R. Dybzinski, J. Shaffer and J. D. Jorgensen, *Phys. Rev. B*, **58** (2716) 1998.
210. S. V. Trukhanov, L. S. Lobanovski, M. V. Bushinsky, I. O. Troyanchuk and H. Szymczak, *J. Phys. Condens. Matt.*, **15** (1783) 2003.
211. Y. Mukovskii, V. Arkhipov, A. Arsenov, N. Bebenin, V. Dyakina, V. Gaviko, A. Korolev, S. Karabashev, V. Mashkautsan, E. Neifeld, D. Shulyatev and R. Zainullina, *J. Alloys & Compounds*, **326** (108) 2001.
212. A. Maignan, C. Michel, M. Hervieu and B. Raveau, *Solid State comm.* **101** (277) 1997.
213. P. N. Lisboa-Filho, A. W. Mombrú, H. Pardo, E. R. Leite and W. A. Ortiz, Solid State Comm. (in press, 2004).
214. H. Wakai, *J. Phys. Condens. Matt.* **13** (1627) 2001.
215. K. Jonason, J. Mattsson and P. Nordblad, *Phys. Rev. Lett.* **77** (2562) 1996.
216. Y. Tomioka, A. Asamitsu, Y. Moritomo, H. Kuwahara and Y. Tokura, *Phys. Rev. Lett.* ***74*** (5108) 1995.
217. T. Mori and N. Kamegashira, *J. of Alloys and Compounds*, **313** (L1) 2000.
218. D. Jarosch, *Mineralogy & Petrology*, **37** (15) 1987.
219. S. Krupička, M. Maryško, Z. Jirák and J. Hejtmánek, *J. Mag. Mag. Mater.* **206** (45) 1999.
220. R. Ganguly, I. K. Gopalkrishnan and J. V. Yakhmi, *Physica B*, **275** (308) 2000.

221. J. B. Goodenough, A. Wold, A. J. Arnott and N. Menyuk, *Phys. Rev*. **124** (373) 1961.

222. V. B. Podopedov, A. Weber, D. B. Romero, J. P. Rice and H. D. Drew, *Phys. Rev. B*, **58** (43) 1998.

223. G. Xiao, F. H. Streitz, A. Gavrin, Y. W. Du and C. L. Chien, *Phys. Rev. B*, **35** (35) 1987.

224. H. Hasegawa, K. Kisho, M. Aoki, N. Ooba, K. Kitazaw and S. Tanaka, *J. Appl. Phys.* **26** (L337) 1987.

225. B. I. Kochelaev, L. Kan, B. Elschner and S. Elschner, *Phys. Rev. B***, 49** (3106) 1994.

226. I. Dhingra, S. C. Kashyap and B. K. Das, *J. Mater Res.* **9** (2771) 1994.

227. N. L. Saini, P. Srivastava, B. R. Sekhar and K. B. Garg, *Int. J. Mod. Phys. B,* **6** (3515) 1992.

228. M. N. Iliev, H. –G Lee, V. N. Popov, Y. Y. Sun, C. Thomsen, R. L. Meng and C. W. Chu, *Phys. Rev. B,* **57** (2872) 1998.

229. M. E. Melo Jorge, A. Correia dos Santos and M. R. Nunes, *Int. J. of Inorg. Mat.* **3** (915) 2001.

230. J. Briatico, B. Alascio, R. Allub, A. Butera, A. Caneiro, M. T. Causa and M. Tovar, *Phys. Rev. B,* **53** (14020) 1996.

231. A. Banerjee, S. Pal and B. K. Chaudhuri, *J. Chem. Phys.* **115** (1550) 2001.

-------XXX------

APPENDIX – A

A.1. PCR file (input file to program Fullprof-2000) of $SrMnO_3$

```
          SrMnO3
! Current global Chi2 (Bragg contrib.) =      1.835
NPATT      1
W_PAT   1.000
!Nph Dum Ias Nre Cry Opt Aut
  1   0   0   0   0   0   0
!Job Npr Nba Nex Nsc Nor Iwg Ilo Res Ste Uni Cor
  0   5   0   0   0   0   0   0   0   0   0   0
!File names of data(patterns) files
f50a63
!
!Mat Pcr NLI Rpa Sym Sho
  0   2   0   0   0   0
!Ipr Ppl Ioc Ls1 Ls2 Ls3 Prf Ins Hkl Fou Ana
  1   0   1   0   0   0   1   0   0   0   0
!
! lambda1 Lambda2    Ratio    Bkpos    Wdt    Cthm     muR   AsyLim   Rpolarz ->Patt# 1
 1.541800 1.541800  1.0000    1.000  5.0000  0.8000  0.0000   40.00    0.0000
!
!NCY  Eps  R_at  R_an  R_pr  R_gl
  5  0.30  0.80  0.80  0.80  0.80
!    Thmin      Step      Thmax    PSD    Sent0  -> Patt#: 1
   20.0000    0.0200    80.0000   0.000   0.000
!
!
    11    !Number of refined parameters
!
! Zero    Code    Sycos    Code   Sysin    Code  Lambda     Code MORE ->Patt# 1
 -0.05449  21.00  0.00000   0.00  0.00000   0.00 0.000000    0.00   0
!   Background coefficients/codes  for Pattern#  1
  105.74     -2.4079     0.38849E-01-0.98435E-04-0.42479E-05 0.34610E-07
     31.000      41.000       0.000       0.000       0.000       0.000
!-------------------------------------------------------------------------------
!  Data for PHASE number:   1  ==> Current R_Bragg for Pattern#  1:    16.03
!-------------------------------------------------------------------------------
CMR
!
!Nat Dis Ang Jbt Isy Str Furth     ATZ   Nvk More
  6   0   0   0   0   0   0  2571.0112   0   0
!Contributions (0/1) of this phase to the  1 patterns
 1
!Irf Npr Jtyp  Nsp_Ref for Pattern#  1
  0   5   0   0
```

```
! Pr1    Pr2    Pr3   Brind.   Rmua   Rmub   Rmuc     for Pattern#  1
  0.000  0.000  1.000  1.000  0.000  0.000  0.000
!
P 63                  <--Space group symbol
!Atom Typ       X       Y       Z     Biso      Occ     In Fin N_t Spc /Codes
!    beta11   beta22   beta33   beta12   beta13   beta23  /Codes
SR1  SR      0.00000  0.00000  0.00000  0.44201  0.99293   0   0   2    0
             0.00     0.00     0.00   0.00     0.00
   0.00000  0.00000  0.00000  0.00000  0.00000  0.00000
      0.00     0.00     0.00     0.00     0.00     0.00
SR2  SR      0.33333  0.66666  0.25000  0.77845  0.99293   0   0   2    0
             0.00     0.00     0.00   0.00     0.00
   0.00000  0.00000  0.00000  0.00000  0.00000  0.00000
      0.00     0.00     0.00     0.00     0.00     0.00
MN1  MN      0.33333  0.66666  0.58566  0.02766  0.99274   0   0   2    0
             0.00     0.00     0.00   0.00    0.00
   0.00000  0.00000  0.00000  0.00000  0.00000  0.00000
      0.00     0.00     0.00     0.00     0.00     0.00
MN2  MN      0.33333  0.66666  0.86768  0.41101  0.99274   0   0   2    0
             0.00     0.00     0.00   0.00   0.00
   0.00000  0.00000  0.00000  0.00000  0.00000  0.00000
      0.00     0.00     0.00     0.00     0.00     0.00
O1   O       0.57981  0.02937  0.01965  0.09254  1.00000   0   0   2    0
             0.00     0.00     0.00     0.00     0.00
   0.00000  0.00000  0.00000  0.00000  0.00000  0.00000
      0.00     0.00     0.00     0.00     0.00     0.00
O2   O      -0.22000 -0.36664  0.27000  0.01799  1.00000   0   0   2    0
             0.00     0.00     0.00     0.00     0.00
   0.00000  0.00000  0.00000  0.00000  0.00000  0.00000
      0.00     0.00     0.00     0.00     0.00     0.00
!-------> Profile Parameters for Pattern #  1
!  Scale       Shape1      Bov      Str1      Str2      Str3    Strain-Model
 0.66494E-05   0.56662  -7.74508   0.00000   0.00000   0.00000       0
    11.00000   101.000   111.000     0.000     0.000     0.000
!      U         V         W         X         Y       GauSiz   LorSiz Size-Model
   1.474094  -1.033564   0.211746   0.000830   0.000000   0.000230   0.000000    0
     71.000     81.000     91.000      0.000      0.000      0.000      0.000
!    a         b         c        alpha      beta       gamma
   5.429182   5.429182   9.047327  90.000000  90.000000 120.000000
   51.00000   51.00000   61.00000    0.00000    0.00000   51.00000
!  Pref1    Pref2      Asy1      Asy2      Asy3      Asy4
  0.07478  0.00000  0.38432  0.00000  0.00000  0.00000
   0.00     0.00   0.00   0.00   0.00     0.00
```

A.2. PCR file (input file to program Fullprof-2000) of $LaMnO_3$

```
          LaMnO3
! Current global Chi2 (Bragg contrib.) =      1.431
NPATT      1
W_PAT   1.000
!Nph Dum Ias Nre Cry Opt Aut
  1   0   0   0   0   0   0
!Job Npr Nba Nex Nsc Nor Iwg Ilo Res Ste Uni Cor
  0   5   0   0   0   0   0   0   0   0   0   0
!File names of data(patterns) files
g2ag0p
!
!Mat Pcr NLI Rpa Sym Sho
  0   2   0   0   0   0
!Ipr Ppl Ioc Ls1 Ls2 Ls3 Prf Ins Hkl Fou Ana
  1   0   1   0   0   0   1   0   0   0   0
!
! lambda1 Lambda2    Ratio    Bkpos    Wdt    Cthm     muR   AsyLim   Rpolarz ->Patt# 1
 1.541800 1.541800  1.0000    1.000  5.0000  0.8000  0.0000   40.00    0.0000
!
!NCY  Eps  R_at  R_an  R_pr  R_gl
 5  0.30  0.80  0.80  0.80  0.80
!    Thmin       Step       Thmax    PSD    Sent0  -> Patt#: 1
   20.0000     0.0200    80.0000   0.000   0.000
!
!
    30    !Number of refined parameters
!
!  Zero    Code    Sycos    Code   Sysin    Code  Lambda     Code MORE ->Patt# 1
  0.15032  81.00  0.00000   0.00  0.00000   0.00 0.000000    0.00   0
!   Background coefficients/codes  for Pattern#  1
  84.468     -3.1096     0.58726E-01-0.50943E-03 0.17732E-05-0.14870E-08
     21.000      31.000      41.000       0.000       0.000       0.000
!------------------------------------------------------------------------------
!  Data for PHASE number:   1  ==> Current R_Bragg for Pattern#  1:     9.02
!------------------------------------------------------------------------------
CMR
!
!Nat Dis Ang Jbt Isy Str Furth     ATZ   Nvk More
  4   0   0   0   0   0   0  3613.4768   0   0
!Contributions (0/1) of this phase to the  1 patterns
 1
!Irf Npr Jtyp  Nsp_Ref for Pattern#  1
  0   5   0   0
! Pr1    Pr2    Pr3   Brind.   Rmua   Rmub   Rmuc     for Pattern#  1
  0.000  0.000  1.000  1.000  0.000  0.000  0.000
!
P B N M                 <--Space group symbol
```

```
!Atom Typ       X       Y       Z     Biso      Occ     In Fin N_t Spc /Codes
!   beta11   beta22   beta33   beta12   beta13   beta23  /Codes
LA   LA      0.98680  0.01845  0.25000  0.51335  0.99988   0   0   2    0
           121.00   131.00     0.00     0.00     0.00
   0.09233  0.00345  0.00790 -0.00122  0.00000  0.00000
    191.00   221.00   231.00   241.00     0.00     0.00
MN   MN      0.50000  0.00000  0.00000  0.60381  0.99965   0   0   2    0
             0.00     0.00     0.00     0.00     0.00
   0.00000  0.00000  0.00000  0.00000  0.00000  0.00000
      0.00     0.00     0.00     0.00     0.00     0.00
O1   O      -0.03899  0.50072  0.25000  0.36797  1.00000   0   0   2    0
           141.00   151.00     0.00     0.00     0.00
  -0.00332 -0.09125 -0.04090  0.01118  0.00000  0.00000
    201.00   251.00   261.00   271.00     0.00     0.00
O2   O       0.71280  0.38958 -0.00204  0.26797  1.00000   0   0   2    0
           161.00   171.00   181.00     0.00     0.00
  -0.08244 -0.00048 -0.05783  0.01574  0.00000  0.00000
    211.00   281.00   291.00   301.00     0.00     0.00
!-------> Profile Parameters for Pattern #  1
!  Scale        Shape1      Bov      Str1      Str2      Str3    Strain-Model
 0.50456E-05   0.33729  -2.85857   0.00000   0.00000   0.00000       0
   11.00000     0.000     0.000     0.000     0.000     0.000
!      U         V         W         X         Y       GauSiz   LorSiz Size-Model
   1.327712  -0.417573   0.644655   0.000000   0.000000  -0.551711   0.000000    0
    91.000    101.000     0.000     0.000     0.000    111.000     0.000
!     a         b         c        alpha      beta       gamma
   5.523523   5.550351   7.815335  90.000000  90.000000  90.000000
   51.00000   61.00000   71.00000   0.00000    0.00000    0.00000
!  Pref1     Pref2      Asy1      Asy2      Asy3      Asy4
  0.00000  0.00000  0.20873  0.00000  0.00000  0.00000
    0.00     0.00     0.00     0.00     0.00     0.00
```

A.3. PCR file (input file to program Fullprof-2000) of $La_{0.85}Ag_{0.15}MnO_3$

```
   La0.85Ag0.15MnO3
! Current global Chi2 (Bragg contrib.) =      1.589
NPATT     1
W_PAT   1.000
!Nph Dum Ias Nre Cry Opt Aut
  1   0   0   0   0   0   0
!Job Npr Nba Nex Nsc Nor Iwg Ilo Res Ste Uni Cor
  0   5   0   0   0   0   0   0   0   0   0   0
!File names of data(patterns) files
g7ag15r
!
!Mat Pcr NLI Rpa Sym Sho
  0   2   0   0   0   0
!Ipr Ppl Ioc Ls1 Ls2 Ls3 Prf Ins Hkl Fou Ana
  1   0   1   0   0   0   1   0   0   0   0
!
! lambda1 Lambda2    Ratio    Bkpos    Wdt    Cthm     muR   AsyLim   Rpolarz ->Patt# 1
 1.541800 1.541800  1.0000    1.000  3.0000  0.7998  0.0000   40.00    0.0000
!
!NCY  Eps  R_at  R_an  R_pr  R_gl
 3  0.30  0.80  0.80  0.80  0.80
!    Thmin       Step       Thmax    PSD    Sent0  -> Patt#: 1
   20.0200     0.0300    79.9900   0.000   0.000
!
!
     13    !Number of refined parameters
!
! Zero    Code    Sycos    Code   Sysin    Code  Lambda     Code MORE ->Patt# 1
  0.00664  21.00  0.00000   0.00  0.00000   0.00 0.000000    0.00   0
!   Background coefficients/codes  for Pattern#  1
 -25.683      6.9733    -0.27162     0.42747E-02-0.27455E-04 0.47986E-07
     31.000      41.000      51.000       0.000       0.000       0.000
!------------------------------------------------------------------------------
!  Data for PHASE number:   1  ==> Current R_Bragg for Pattern#  1:    10.97
!------------------------------------------------------------------------------
CMR
!
!Nat Dis Ang Jbt Isy Str Furth     ATZ   Nvk More
  4   0   0   0   0   0   0 74757.3672   0   0
!Contributions (0/1) of this phase to the  1 patterns
 1
!Irf Npr Jtyp  Nsp_Ref for Pattern#  1
  0   5   0   0
! Pr1    Pr2    Pr3   Brind.   Rmua   Rmub   Rmuc     for Pattern#  1
  0.000  0.000  1.000  1.000  0.000  0.000  0.000
!
R -3 C                <--Space group symbol
```

```
!Atom Typ      X       Y       Z     Biso      Occ     In Fin N_t Spc /Codes
!   beta11   beta22   beta33   beta12   beta13   beta23  /Codes
LA   LA     0.00000  0.00000  0.25000  0.85327  0.84911   0   0   2    0
            0.00     0.00     0.00     0.00     0.00
   0.00000  0.00000  0.00000  0.00000  0.00000  0.00000
      0.00     0.00     0.00     0.00     0.00     0.00
AG   AG     0.00000  0.00000  0.25000  0.85327  0.15102   0   0   2    0
            0.00     0.00     0.00     0.00     0.00
   0.00000  0.00000  0.00000  0.00000  0.00000  0.00000
      0.00     0.00     0.00     0.00     0.00     0.00
MN   MN     0.00000  0.00000  0.00000  0.96232  0.96204   0   0   2    0
            0.00     0.00     0.00     0.00    0.00
   0.00000  0.00000  0.00000  0.00000  0.00000  0.00000
      0.00     0.00     0.00     0.00     0.00     0.00
O    O      0.55040  0.00000  0.25000  0.67574  1.00000   0   0   2    0
            0.00     0.00     0.00     0.00     0.00
   0.00000  0.00000  0.00000  0.00000  0.00000  0.00000
      0.00     0.00     0.00     0.00     0.00     0.00
!-------> Profile Parameters for Pattern #  1
!  Scale      Shape1      Bov      Str1      Str2      Str3    Strain-Model
 0.27392E-06   2.45100  -0.64272   0.00000   0.00000   0.00000       0
    11.00000     81.000     91.000     0.000     0.000     0.000
!      U         V         W         X         Y       GauSiz   LorSiz Size-Model
   0.522844  -0.337059   0.060235   0.000000   0.000000   0.000000   0.000000    0
      101.000     111.000     121.000     0.000     0.000     0.000     0.000
!    a         b         c        alpha      beta       gamma
   5.524378   5.524378  13.355386  90.000000  90.000000 120.000000
   61.00000   61.00000   71.00000    0.00000    0.00000   61.00000
!  Pref1    Pref2      Asy1     Asy2     Asy3     Asy4
  0.07420  0.00000  0.00757  0.00000  0.00000  0.00000
    131.00     0.00     0.00     0.00     0.00     0.00
```

LIST OF PUBLICATIONS

Papers Published/Communicated in Journals:

1. Metal-insulator transition in electron-doped $Ba_{1-x}La_xMnO_3$ compounds.
   Manoranjan Kar and S. Ravi, PRAMANA-Journal of Physics, **58** (1009-1012) 2002.
2. Study of structural, magnetic, and electrical transport properties in $La_{1-x}Cu_xMnO_3$.
   Manoranjan Kar and S. Ravi, Materials Science & Engineering B, **107** (332-336)2004.
3. Study of magneto-resistivity in $La_{1-x}Ag_xMnO_3$ compounds.
   S. Ravi and Manoranjan Kar, Physica B, **348** (169-176) 2004.
4. Electrical resistivity and ac susceptibility studies in $La_{1-x}Ag_xMnO_3$.
   Manoranjan Kar and S. Ravi, Materials Science & Engineering B, **110** (46-51) 2004.
5. STUDY OF STRUCTURAL, ELECTRICAL TRANSPORT AND MAGNETIC PROPERTIES IN $La_{1-x}Ag_xMnO_3$ COMPOUNDS.
   Manoranjan Kar and S. Ravi, Modern Physics Letters B, **18** (221-231) 2004.

6. Magneto-Resistivity, Ferromagnetism and Charge Ordering in $Ba_{1-x}La_xMnO_3$.
   Manoranjan Kar and S. Ravi (Communicated).
7. Electrical Resistivity and ac Susceptibility Studies in $Sr_{1-x}La_xMnO_3$.
   Manoranjan Kar and S. Ravi (Communicated).
8. Study of electrical transport and ac susceptibility in $LaMn_{1-x}Cu_xO_3$.
   Manoranjan Kar and S. Ravi (Communicated).
9. Study of Electrical Transport and Magnetic Properties in $CaMn_{1-x}Cu_xO_3$.
   Manoranjan Kar, S. M. Borah and S. Ravi (Communicated).

Papers Published in Refereed Conference Proceedings:

1. Electrical Resistivity and Crystal Structure Studies on $Ca(Mn_{1-x}Cu_x)O_3$ Compounds.

   Manoranjan Kar and S. Ravi, Proceeding of DAE Solid State Physics (India), Vol. **44** (473-474) 2001.

2. Electrical Resistivity and ac Susceptibility Studies on $La_{1-x}Ag_xMnO_3$ Compounds.

   Manoranjan Kar and S. Ravi, Proceeding of DAE Solid State Physics (India) **45** (507-508) 2002.

3. Metal-Insulator Transitions in $La_{1-x}Cu_xMnO_3$ Compounds.

   Manoranjan Kar and S. Ravi, Proceeding of DAE Solid State Physics Symposium-2003 (in press).

4. Study of Crystal Structure in $La_{1-x}Ag_xMnO_3$ Compounds.

   Manoranjan Kar and S. Ravi, Proceeding of Seminar on Advanced X-Ray Techniques in Research and Industry, DMRL, Hyderabad (In press 2004).

--------XXX------